

# UNIVERSITY OF BIRMINGHAM



UNIVERSITY OF  
BIRMINGHAM

ENGINEERING AND PHYSICAL SCIENCES

School of Metallurgy & Materials

## **Developing Parametrisation Methods for Physics-based Models of Lithium and Sodium-ion Batteries**

by

**KIERAN BRENDAN O'REGAN**

A thesis submitted to the University of Birmingham for the degree of  
DOCTOR OF PHILOSOPHY

September 2018 to May 2023

(February 2024 Resubmission)

## University of Birmingham Research Archive e-theses repository



This unpublished thesis/dissertation is under a Creative Commons Attribution 4.0 International (CC BY 4.0) licence.

### You are free to:

**Share** — copy and redistribute the material in any medium or format

**Adapt** — remix, transform, and build upon the material for any purpose, even commercially.

The licensor cannot revoke these freedoms as long as you follow the license terms.

### Under the following terms:



**Attribution** — You must give appropriate credit, provide a link to the license, and indicate if changes were made. You may do so in any reasonable manner, but not in any way that suggests the licensor endorses you or your use.

**No additional restrictions** — You may not apply legal terms or technological measures that legally restrict others from doing anything the license permits.

### Notices:

You do not have to comply with the license for elements of the material in the public domain or where your use is permitted by an applicable exception or limitation.

No warranties are given. The license may not give you all of the permissions necessary for your intended use. For example, other rights such as publicity, privacy, or moral rights may limit how you use the material.

Unless otherwise stated, any material in this thesis/dissertation that is cited to a third-party source is not included in the terms of this licence. Please refer to the original source(s) for licencing conditions of any quotes, images or other material cited to a third party.

# Abstract

Lithium-ion batteries have become an important technology in the transition to renewable energy. Improvements in battery performance and cost reductions have led to their adoption in transport and grid storage applications to reduce carbon emissions. Battery models have been an important tool to achieve these improvements. Physics-based models, including the Doyle-Fuller-Newman model provide insight into the mass and charge transport processes within the individual battery components. The application of these battery models in industry and research has been limited by the availability of input parameters and the lack of published methodologies for parameterizing different cell formats and chemistries. Physics-based models have significant potential within industry, from optimising fast charging and battery manufacturing, but the main obstacle for widespread adoption is obtaining the parameters. Numerous parameters relating to the physical, electrochemical, and thermal properties of a battery. This research's experimental approach identifies key battery model parameters, improves methods, and creates accurate models for specific cells, offering insights for industry application and model development. This thesis develops parameterisation methodologies using physical, electrochemical, and thermal characterisation techniques to construct battery models that improve the understanding of battery kinetics/thermodynamics. Techniques including electrochemical impedance spectroscopy, galvanostatic intermittent titration technique, thermal measurement methods, and more are adapted to extract model inputs. This allows battery models that demonstrate high accuracy between simulated and experimental data to be developed. For lithium-ion batteries, a complete parameterisation workflow is developed to capture the thermal-electrochemical behaviour of a high energy commercial cylindrical cell and the property changes that occur during battery operation. This is accomplished by evaluating the dependency of parameters on temperature and state-of-charge. Furthermore, we found that traditional methods can be modified to better parameterise silicon additives, or new chemistries including sodium. Our results demonstrate the importance and complementarity practical methods have in aiding model development and understanding. The novelty of this work lies in its approach to model development, utilizing experiments to identify the limitations of existing battery models and areas where simplifications can enhance utility without compromising the understanding of battery physics. This approach equips theorists with practical tools and insights, enabling significant advancements in the field of battery modelling. These methods have been commercialised and will be developed further to provide the several industries expertise into parameterisation and model development.

## Supervisors

Prof. Emma Kendrick (University of Birmingham) and Dr. Dhammika Widanalage (Warwick Manufacturing Group).

# Impact Statement

Physics-based models are used to accurately predict the performance of batteries, but their accuracy is strongly dependent upon the accuracy of the measured parameters. This thesis provides a parameter set for the thermal-electrochemical behaviour of a commercial cell and outlines a new parameterisation workflow to capture the variability of the kinetic and thermodynamic properties with temperature and state-of-charge (SoC). The methods were further developed to parameterise a sodium-ion battery system, demonstrating that the methodologies developed can be chemistry-agnostic with a few modifications to improve result robustness. The relevancy of this research to industry and academia can be summarised as:

**Research Community** The methodologies developed are being used as a template for further research into the parameterisation and understanding of commercial cell chemistries. Further, the thermal-electrochemical parameter set for the LG M50 commercial cell has become the most widely used parameter in the open-source modelling platform PyBaMM (Python Battery Mathematical Modelling). PyBaMM solves physics-based models by using state-of-the-art automatic differentiation and numerical solvers. This parameter set has been one of few available to the academic community for a high energy cell relevant to automotive applications. This allows researchers to explore topics including new cell formats, fast charging protocols, pack cooling strategies, battery state estimation, and battery degradation. Modelling is important in battery research but increasing relevancy to industry is dependent on information being published for state-of-the-art battery technologies. We published and open-sourced the parameter set and relevant data for the highest energy cell (267 Wh kg<sup>-1</sup>) observed in literature to address this. The parameters outlined for the M50 cell have contributed to the following research papers:<sup>1</sup>

- Tranter *et al.*, *Journal of Electrochemical Society*, 2020, **167**, 110538.<sup>2</sup>
- Brosa Planella *et al.*, *Electrochimica Acta*, 2021, **388**, 138524.<sup>3</sup>
- Ai *et al.*, *Journal of Power Sources*, 2022, **527**, 231142.<sup>4</sup>

**Industry** The methodologies to parameterise physics-based models have been commercialised through a spin-out company between Imperial College London and the University of Birmingham, supported by The Faraday Institution. About:Energy (company number 13583725) is a software company that has developed intellectual property for the parameterisation of batteries. These methods have been used to provide high accuracy models to industry for battery design, application, and prediction. A barrier to industry using models in R&D is parameterisation and model development capabilities. About:Energy centralises this activity and provides equivalent-circuit models and physics-based models to customers across automotive, manufacturing, aerospace, and technology industries.



# Research Contributions

The research in this thesis has contributed to the following publications and developments in battery research.

## Key Publications:

List of publications this thesis has been based upon in chronological order:

1. **Development of experimental techniques for parameterization of multi-scale lithium-ion battery models.** Chang-Hui Chen, Ferran Brosa Planella, Kieran O'Regan, Dominika Gastol, W Dhammika Widanage, and Emma Kendrick, *J. Electrochem. Soc.*, **167**, 080534, (2020).
2. **Review of parameterisation and a novel database (LiionDB) for continuum Li-ion battery models.** Andrew Wang, Simon O'Kane, Ferran Brosa Planella, James Le Houx, Kieran O'Regan, Maxim Zyskin, Jacqueline Sophie Edge, Charles Monroe, Samuel Cooper, David A Howey, Emma Kendrick and Jamie Michael Foster, *Progress in Energy*, **4**, 032004, (2022).
3. **Thermal-electrochemical parameters of a high energy lithium-ion cylindrical battery.** Kieran O'Regan, Ferran Brosa Planella, W. Dhammika Widanage, and Emma Kendrick, *Electrochimica Acta*, **425**, 140700, (2022).
4. **Probing the cause of capacity fade in large-format lithium-ion pouch cells through multimodal characterisation.** Emily Giles, Kieran O'Regan, Abbey Jarvis, Rosie Madge, Alex Sargent, Beatrice Browning, Luke Sweeney, Anton Zorin, Rob Sommerville, Stefan Michalik, Phil Chater, Peter Slater, Phoebe Allan, Dan Reed, Emma Kendrick, Paul Anderson (*submission est. 2024*).
5. **Advancing sodium-ion batteries: electrochemical model parameterisation to understand kinetic limitations,** Kieran O'Regan, Ferran Brosa Planella, Brij Kishore, W. Dhammika Widanage, and Emma Kendrick (*submission est. 2024*)

## Supporting Publications:

List of publications this thesis has contributed towards.

6. **3D microstructure design of lithium-ion battery electrodes assisted by X-ray nano-computed tomography and modelling.** Xuekun Lu, Antonio Bertei, Donal P Finegan, Chun Tan, Sohrab R Daemi, Julia S Weaving, Kieran B O'Regan, Thomas MM Heenan, Gareth Hinds, Emma Kendrick, Dan JL Brett, Paul R Shearing, *Nat Commun*, **11**, 2079, (2020).
7. **Microstructural evolution of battery electrodes during calendaring.** Xuekun Lu, Sohrab R. Daemi, Antonio Bertei, Matthew D.R. Kok, Kieran B. O'Regan, Lara Rasha, Juyeon Park, Gareth Hinds, Emma Kendrick, Dan J.L. Brett, Paul R. Shearing, *Joule*, **4**, 12, 2746-2768, (2020).
8. **Multi-length scale microstructural design of lithium-ion battery electrodes for improved discharge rate performance.** Xuekun Lu, Xun Zhang, Chun Tan, Thomas M. M. Heenan, Marco Lagnoni, Kieran O'Regan, Sohrab Daemi, Antonio Bertei, Helen G. Jones, Gareth Hinds, Juyeon Park, Emma Kendrick, Dan J. L. Brett, and Paul R. Shearing, *Energy Environ. Sci.*, **14**, 5929-5946, (2021).
9. **Frequency domain non-linear characterization and analysis of lithium-ion battery electrodes.** C. Fan, K. O'Regan, L. Li, E. Kendrick, W.D. Widanage, *Journal of Energy Storage*, **36**, 102371, (2021).
10. **Understanding non-linearity in electrochemical systems using multisine-based non-linear characterization.** Fan C, Grandjean TRB, O'Regan K, Kendrick E, Widanage WD, *Transactions of the Institute of Measurement and Control*, (2021).
11. **Lithium-ion battery cathode and anode potential observer based on reduced-order electrochemical single particle model.** Liuying Li, Yaxing Ren, Kieran O'Regan, Upender Rao Koleti, Emma Kendrick, W. Dhammika Widanage, James Marco, *Journal of Energy Storage*, **44**, 103324, (2021).

12. **Formulation and manufacturing optimization of lithium-ion graphite-based electrodes via machine learning.** Stavros Drakopoulos, Azarmidokht Gholamipour-Shirazi, Paul MacDonald, Robert Parini, Carl D. Reynolds, David L. Burnett, Ben Pye, Kieran B. O'Regan, Guanmei Wang, Thomas M. Whitehead, Gareth J. Conduit, Alexandru Cazacu, Emma Kendrick, *Cell Reports Physical Science* **2**, **12**, 22100683, (2021).
13. **From Atoms to Cells: Multiscale Modeling of  $\text{LiNi}_x\text{Mn}_y\text{Co}_z\text{O}_2$  Cathodes for Li-Ion Batteries.** Lucy M. Morgan, Mazharul M. Islam, Hui Yang, Kieran O'Regan, Anisha N. Patel, Abir Ghosh, Emma Kendrick, Monica Marinescu, Gregory J. Offer, Benjamin J. Morgan, M. Saiful Islam, Jacqueline Edge, and Aron Walsh, *ACS Energy Lett.* **7**, **1**, 108–122, (2022).
14. **Data-Driven Identification of Lithium-ion Batteries: A Nonlinear Equivalent Circuit Model with Diffusion Dynamics,** Chuanxin Fan, Liuying Li, Matthew Higgins, Kieran O'Regan, Emma Kendrick, W Dhammika Widanage, *Applied Energy*, **321**, 119336, (2022).
15. **Revealing the rate-limiting electrode of lithium batteries at high rates and mass loadings,** Yongxiu Chen, Julian Key, Kieran O'Regan, Tengfei Song, Yongsheng Han, Emma Kendrick, *Chemical Engineering Journal*, **450**, 138275.
16. **Multiscale Dynamics of Phase Separation and Plating in Graphitic Lithium-ion Battery Anodes Coupling Operando Microscopy and Phase-field Modelling,** Xuekun Lu, Marco Lagnoni, Antonio Bertei, Supratim Das, Rhodri E. Owen, Qi Li, Kieran O'Regan, Aaron Wade, Donal P. Finegan, Emma Kendrick, Martin Z. Bazant, Dan J. L. Brett & Paul R. Shearing, *Nature Communications*, **14**, 5127.
17. **Battery Test Inter-Laboratory Correlation Study – A Repeated Measurements Approach,** Anisha Patel, Alana Zulke, Kieran O'Regan, Emma Kendrick, David Howey, W. Dhammika Widanage (submission est. 2024).

## **Research Grants**

The research in this thesis has been used by the author to further develop research for commercial viability through the award of £920,000 government grants:

1. **The Faraday Institution's Entrepreneurial Fellowship** (£97,500 grant) – to explore business case for battery parameterisation.
2. **Advanced Propulsion Centre's Technology Development Accelerator Programme** (£130,000 grant) – to develop business case and accurate battery thermal characterisation for the automotive industry.
3. **InnovateUK's Faraday Battery Challenge** (£460,000 grant for £960,000 project) – to develop physics-based degradation models used in battery design and improve total cost of ownership and sustainability of electric vehicles.
4. **InnovateUK's Faraday Battery Challenge** (£240,000 grant for £870,000 project) – to develop physics-based degradation models for use in battery management systems to improve health and remaining useful life predictions.

## *PhD – It's a journey.*

*~ Jake Gyllenhal on Donny Darko ~*

*"For me, personally, when approaching the [degree], it was sort of hard to figure out, because there's so many things that [you] get hit with.*

*In the simplest term,  
in the most abstract term  
I could say..  
It's a journey.  
a journey about discovering.*

*And the irony about this whole thing  
is hopefully by the end you have to go back, you have to [do] it  
again.*

*But,  
it's just like this ridiculous, fantastic, completely absurd mixture of  
humour, sadness, madness. It forces you to come to your own  
conclusion about what it is about.*

*It's like an individual experience experiment. It's not about one  
thing, no one can really come to any finite or objective conclusion."*

## Acknowledgements

I owe a great deal of gratitude to Prof. Emma Kendrick for her mentorship throughout my PhD journey. Our initial meeting over coffee nearly six years ago marked the beginning of a collaboration that has since resulted in significant accomplishments, including the publication of 14 research papers, establishing state-of-the-art laboratories, the creation of a spin-out company, and, not least, the shared moments of over beers.

During my PhD, Prof. Kendrick imparted many lessons, but three stand out for shaping my approach to research:

- The Value of Industrial Focus: The true value of science and engineering is realized through its adoption by industry.
- The Necessity of Hard Work: Learning that success is the result of years of dedication and effort.
- Leadership as Impact: Emphasising the importance of building and leading a team of scientists and engineers.

Thank you, Emma, for your patience and resilience in managing me, who, despite often acting impulsively and causing disruptions, brings an undeniable passion for science and a drive for impactful research. My tendency to move quickly is the origin of both the chaos and the progress we achieve.

I'm deeply grateful to my Mum and Dad for their support. You have been a constant source of help. It's common for children to turn to their parents in times of crisis, looking for answers. This rings especially true for PhD students, who often carry the hallmarks of student life into their late 20s. Thank you for always being there for me, providing a home and cooked dinners when I needed to recharge. Love you both!

Thanks to Francesca Long for developing the Faraday Institution training program and community. The Faraday Institution has been instrumental in building a community of researchers whom we can call friends and a training program that has significantly contributed to my professional growth. Fran's efforts have shifted my career focus beyond academia and developed the battery research community's most vital asset—its people.

I had the pleasure of getting to know four exceptional researchers throughout my PhD journey: Brij Kishore, Ferran Brosa-Planella, Alastair Hales, and Dhammika Widanage. Brij, Ferran, and Alastair, as postdoctoral researchers, along with Dhammika, who served as my co-supervisor, have been instrumental to my development as a researcher, covering a wide range of areas including electrochemistry, modelling, and commercialization. Their expertise significantly enriched my research experience. Great PhDs are supported by many talented researchers, motivated by the desire to educate, and help others, and I was fortunate to have such guidance and support from each of them.

Thank you to Gavin and Neil for the support through About:Energy's ideation, commercialization, and growth. Developing a business as a scientist is an incredibly arduous journey, but it is what makes the words in this thesis worth writing. Thanks to both for making this shared journey possible and for your equal commitment to a very impactful future.

Lastly, thank you to Liv, who supported me through some of the most challenging times in this journey. While a PhD involves self-sacrifice, it's the sacrifices made at the expense of others that keep me awake at night.

As I write the final words of this thesis, marking the end of a project that began 2,348 days ago, it's clear that there are two choices in one's career: to feel successful or to be successful. As a scientist, choosing the latter often comes with a repeated feeling of failure, yet this is the essence of the scientific method.

# Contents

<b>Abstract .....</b>	<b>2</b>
<b>Supervisors .....</b>	<b>2</b>
<b>Impact Statement .....</b>	<b>3</b>
<b>Research Contributions .....</b>	<b>4</b>
<b>Acknowledgements .....</b>	<b>7</b>
<b>List of Figures .....</b>	<b>11</b>
<b>List of Tables .....</b>	<b>17</b>
<b>Table of Acronyms .....</b>	<b>19</b>
<b>Research Aims &amp; Thesis Outline .....</b>	<b>20</b>
<b>1 Chapter 1: Background &amp; Introduction .....</b>	<b>22</b>
1.1 Motivation .....	22
1.2 The Lithium-ion Battery .....	23
1.3 Battery Fundamentals .....	25
1.4 Parametric Cell Modelling .....	28
1.4.1 Equivalent Circuit-based Modelling .....	30
1.4.2 Physics-based Models .....	31
1.4.3 Degradation Modelling .....	34
1.5 Next-generation Battery Modelling: Sodium-ion .....	36
1.6 Research Objective .....	38
<b>2 Chapter 2: Literature Review on Parameterisation .....</b>	<b>39</b>
2.1 Electrochemical Parameterisation .....	39
2.2 Thermal Parameterisation .....	46
2.3 Degradation Parameterisation .....	50
2.4 Next-Generation Chemistry Parameterisation .....	52
2.5 Summary .....	53
<b>3 Chapter 3 Methods .....</b>	<b>54</b>
3.1 Teardown .....	54
3.2 Physical Characterisation .....	55
3.3 Electrochemical Characterisation .....	56
3.4 Thermal Characterisation .....	64
3.5 Modelling .....	66

<b>4</b>	<b>Chapter 4: Developing methodologies for parametrisation of lithium-ion batteries ..</b>	<b>67</b>
4.1	Introduction .....	67
4.2	Experimental .....	69
4.2.1	Battery Description .....	69
4.2.2	Sample Extraction and Preparation .....	69
4.2.3	Physical Characterisation .....	70
4.2.4	Chemical Characterisation .....	70
4.2.5	Electrochemical Characterisation .....	70
4.2.6	Validation .....	72
4.3	Results & Discussion .....	72
4.3.1	Physical Characterisation .....	73
4.3.2	Chemical Characterisation .....	77
4.3.3	Electrochemical Characterisation .....	79
4.3.4	Validation .....	91
4.4	Conclusions .....	94
<b>5</b>	<b>Chapter 5: Thermal-electrochemical parameters of a high energy lithium-ion cylindrical battery .....</b>	<b>96</b>
5.1	Introduction .....	96
5.2	Experimental .....	97
5.2.1	Teardown Procedure .....	97
5.2.2	Thermophysical Characterisation .....	97
5.2.3	Thermal-electrochemical Characterisation .....	98
5.2.4	Simulations .....	99
5.3	Results and Discussion .....	99
5.3.1	Cell Structure .....	99
5.3.2	Thermophysical Characterisation .....	102
5.3.3	Thermal-electrochemical Characterisation .....	109
5.3.4	Validation .....	124
5.4	Conclusions .....	128
	Data Availability .....	130
<b>6</b>	<b>Chapter 6 - Advancing sodium-ion batteries: development of parameterisation methods for physics-based models .....</b>	<b>131</b>
6.1	Introduction .....	131
6.2	Experimental .....	133

6.2.1	Materials.....	133
6.2.2	Physical Characterisation .....	133
6.2.3	Electrochemical Characterisation .....	134
6.3	Results & Discussion .....	136
6.3.1	Geometric Properties .....	136
6.3.2	Electrode Properties .....	139
6.3.3	Stoichiometry & Maximum Concentration .....	142
6.3.4	Electrolyte properties .....	151
6.3.5	Validation.....	152
6.4	Conclusions .....	155
6.5	Data Availability .....	156
<b>7</b>	<b>Chapter 7: About:Energy - Exploring the Business Case for Parameterisation and Modelling .....</b>	<b>157</b>
7.1	Problem .....	157
7.2	Solution.....	158
7.3	Technology.....	160
7.4	Market Research .....	161
7.5	Business Model .....	165
7.6	Market Size .....	167
7.7	Outlook .....	169
<b>8</b>	<b>Chapter 8: Conclusions and Future Work.....</b>	<b>171</b>
8.1	Conclusions .....	171
8.2	Future Work.....	172
8.3	Impact.....	173
<b>9</b>	<b>References .....</b>	<b>175</b>
<b>10</b>	<b>Supporting Information .....</b>	<b>187</b>

## List of Figures

Figure 1. Schematic of a lithium-ion battery using a graphite negative electrode and a layered oxide positive electrode, $\text{LiCoO}_2$ .	24
Figure 2. Schematic to show negative and positive potential limits for the electrolyte stability and misconception regarding the electrolyte stability window.	27
Figure 3. Comparison of equivalent circuit-based and physics-based models, two types of parametric models used in battery research.	29
Figure 4. The characteristics of voltage response in a battery can be modelled using two different ways, an electrochemical model relates to processes that happen within a battery, whereas electrical circuit modelling approximates the behaviour using circuit elements such as resistors and capacitors.	29
Figure 5. The electrical circuit to model the internal resistance in a battery.	30
Figure 6. One RC network battery model, known as a Thevenin model. This model allows the prediction of the voltage response for an input current, this response is generated from a network of circuit elements.	31
Figure 7. Schematic to describe domains the DFN model, also known as a pseudo-two-dimensional (P2D) model.	32
Figure 8. Schematic of a sodium-ion battery using a hard carbon negative electrode and a layered oxide positive electrode.	37
Figure 9. ‘LiionDB’ is a parameter database that captures the physical and electrochemical properties of various materials and cells published in literature.	43
Figure 10. Illustration of a three-electrode set-up, the cell shown is a PAT-Cell (left). The reference electrode is in the insulation sleeve as “lithium ring”.	45
Figure 11. Teardown procedure of a discharged LGM50, to illustrate delamination of one side of the electrode coating for electrochemical testing in two- and three-electrode formats.	54
Figure 12. Bragg diffraction: X-rays of the same wavelength and phase are scattered off the atoms in a crystalline material. The lower beam travels a length of $2d\sin\theta$ further.	56
Figure 13. Current input (top) and voltage output (bottom), with CC discharge steps and a CC-CV charge step (bottom). The CC-CV charging step is a compromise between charge time and degradation caused by ohmic heating.	58
Figure 14. Illustration of probe positions for measuring the electronic properties of an electrode.	59
Figure 15. Current response $I_t$ from an excitation signal $E_t$ in a linear system.	60



Figure 16. Nyquist plot illustrating the characteristic series resistance, two semi-circles, and diffusion-limited response at low frequency. These phenomena can be modelled as equivalent circuit elements such as resistors, CPEs and Warburg. These processes have different time constants and the ohmic and SEI are instantaneous processes, whereas charge transfer and diffusion occur over longer durations. ....	61
Figure 17. Differential capacity analysis of an NMC-based lithium-ion electrode. ....	62
Figure 18. Illustration of the transient and steady state regions corresponding to a discharge step during GITT. The flat line corresponds to no applied current. ....	63
Figure 19. Potentiometric profile illustrating the initial SOC change, followed by a long period to attain OCV and a temperature-cycling regime to observe voltage change (left). The entropic term is calculated from the gradient of the OCV points at each temperature (right). ....	66
Figure 20. Summary of the parametrisation requirements for a physics-based model and their categorisations.....	69
Figure 21. Top-view (left) and bottom-view (right) SEM images of the separator illustrating the polymer mesh and ceramic coating respectively. ....	74
Figure 22. Top-view SEM images for graphite-SiO <sub>x</sub> (left) and NMC (right) illustrating the flake and spherical morphologies of these materials. ....	74
Figure 23. Illustration to describe how microstructure has an impact on lithium diffusion pathways within an electrode. Tortuosity ( $L'/L$ ) describes this effect, minimising this value improves lithium transport. ....	76
Figure 24. Simulations of voltage and electrolyte concentration utilising the experimentally derived tortuosities (red solid line) and the theoretically derived tortuosities (blue dotted line) in the positive electrode.....	77
Figure 25. SEM image (left), the shape and particle size of the silicon oxide dopant can be distinguished. Top-view EDS (right) image of the negative electrode illustrating the graphite (red) and silicon oxide (green) content. The colours were obtained in the EDS measurement.....	78
Figure 26. SEM image of the positive electrode surface illustrating presence of carbon fibres to enhance rate performance.....	78
Figure 27. pOCV profiles for graphite-SiO <sub>x</sub> (left) and NMC (right) half cells. ....	79
Figure 28. GITT in half cell configuration for graphite-SiO <sub>x</sub> (left) and NMC (right) allows determination of the open circuit voltages. The graphite-SiO <sub>x</sub> electrode demonstrates significant hysteresis at capacities below 2 mAh cm <sup>-2</sup> , this is attributable to the intrinsic hysteresis of silicon. ....	80
Figure 29. Balancing between three-electrode (blue) and half (red) cell open-circuit voltage curves for the negative (left) and positive electrode (right). ....	81

Figure 30. Mathematical functions used for the positive electrode (left) and negative electrode (right) OCV used in the simulations.....	82
Figure 31. Differential capacity analysis for the NMC-based electrode obtained at C/50 for 3.3-4.3 V in a half cell. ....	83
Figure 32. Differential capacity analysis for the graphite-SiO <sub>x</sub> electrode obtained at C/50 for 0.005-1.5 V (left) in a half cell. For better visualisation the data has been plotted in a narrower range (right).....	83
Figure 33. GITT in a half cell configuration demonstrated that the diffusion coefficients for graphite-SiO <sub>x</sub> (left) and NMC (right) vary significantly as a function as state-of-charge. ....	85
Figure 34. PEIS measurements negative electrode (left) and positive electrode (right)...	87
Figure 35. Equivalent circuit model. ....	88
Figure 36. Comparison of the experimental data (blue line) and the DFN simulations (red circles) and the absolute error between these two datasets. ....	93
Figure 37. Tab locations (left) and a macro-view to illustrate tab positioning (right).....	100
Figure 38. Schematic of an individual electrode layer. ....	101
Figure 39. Specific heat capacities for the NMC composite powder (red), the graphite composite powder (black), and the separator (purple). The specific heat capacities for the NMC powder, graphite powder, and separator are represented by Equations [61]to [63] .....	104
Figure 40. Stoichiometries of the negative (red) and positive electrode (blue) in relation to SOC of the battery (green). ....	110
Figure 41. Process to accurately map stoichiometry from test voltage profile and the OCV 'reference' data set. (1) Observe voltage at each point test was carried out e.g., EIS or GITT, (2) find stoichiometry that corresponds to this voltage from OCV profile (this OCV profile is a function of lithiation, process described in previous Chapter), and (3) plot parameter vs. determined stoichiometry.....	111
Figure 42. Fitted solid-phase diffusivity values of NMC811 positive electrode (top left) and the graphite-SiO <sub>y</sub> negative electrode (top right) as a function of stoichiometry and temperature. Arrhenius dependency for the average solid-phase diffusivity of NMC811 positive electrode (bottom left) and the graphite-SiO <sub>y</sub> negative electrode (bottom right) as a function of temperature.....	114
Figure 43. The solid-phase diffusivity activation energies for the NMC-based (left) and graphite-SiO <sub>y</sub> (right) electrodes measured in a three-electrode configuration .....	115
Figure 44. Exchange current density as a function of lithium concentration for the NMC811 positive (left) and graphite-SiO <sub>y</sub> negative electrode (right) evaluated at 15 °C, 25 °C, 35 °C, and 45 °C.....	116

Figure 45. Equivalent circuit model used for fitting. (R = resistor and CPE = constant phase element).....	116
Figure 46. Exchange current density activation energy as a function of lithium concentration for the positive (left) and negative electrode (right).....	118
Figure 47. Electronic conductivity evaluated for NMC811 extracted from a fully discharged cell. This corresponds to a lithium stoichiometry of approximately $x=0.9$ . These values are plotted versus the inverse of temperature for the positive electrode. The gradient provides the activation energy for NMC. ....	119
Figure 48. Entropic term and polynomial fits for the negative electrode (left) and positive electrode (right). The points in the negative electrode are ignored to achieve a good fit, there is uncertainty in the physics or validation.....	121
Figure 49. Experimental and simulated temperature profiles with the negative electrode entropic term including all data points (left) and excluding the intermediate data points (right). The experimental data was from tests on four cylindrical cells (the cell ID numbers are listed in the legend), while the simulated data was using the fully parameterised DFN model. This data was for a cylindrical cell discharge of 0.5C at 25 °C.....	121
Figure 50. Experimental and simulated voltage (left) and temperature (discharge) profiles for a 0.5C, 1C, and 2C discharge at 25°C. The experimental data was from tests on four cylindrical cells (the cell ID numbers are listed in the legend), while the simulated data was using the fully parameterised DFN model. ....	126
Figure 51. Experimental and simulated voltage (left) and temperature (discharge) profiles for a 1C discharge at 0 °C, 10 °C, 25°C. The experimental data was from tests on three cylindrical cells (the cell ID numbers are listed in the legend), while the simulated data was using the fully parameterised DFN model. ....	127
Figure 52. Simulations for the previous parameter set of the LG M50 (Chen 2020, orange dashed line) and the parameter set that considers parameter-dependencies and thermal behaviour (This work 2021, blue dotted line) compared to the experimental data. The parameters in both cases have been tuned to the data for the 1C discharge and then these same parameters are used for the C/2 simulation to demonstrate that the discharge behaviour and relaxation is captured better for C-rates that deviate from the tuned values. C/2 RMSE (root mean square error) for 0.10 for Chen2020 and 0.14 for this work. ....	128
Figure 53. Doyle-Fuller-Newman model schematic for a Na-ion battery. This model is referred to as a pseudo-2-dimensional (P2D) model due to the battery system being defined in two dimensions with one for the thickness of the electrodes (Cartesian coordinates) and the other for the active material particles (radial coordinates).....	132
Figure 54. XRD pattern of the NMST2488 powder. ....	138

Figure 55. Particle size distributions for NMST2488, the $D_{50}$ is 1.1 $\mu\text{m}$ and specific surface area is 1.58 $\text{m}^2 \text{g}^{-1}$ . The data for the hard carbon was taken from the manufacturer datasheet. ....	138
Figure 56. SEM images of the hard carbon powder (left) and NMST2488 (right) electrodes.....	139
Figure 57. Optical microscopy of hard carbon powder (left) and NMST2488 (right) electrodes. The $D_{50}$ particle sizes of the hard carbon and NMST2488 electrodes are 8.7 $\mu\text{m}$ and 4.5 $\mu\text{m}$ respectively. ....	139
Figure 58. First cycle losses for each electrode during a formation of 15 mA/g of active material, hard carbon (left) and NMST2488 (right). Voltages recorded against Na/Na <sup>+</sup> . ....	140
Figure 59. Gravimetric capacities of the hard carbon (top left) and NMST2488 (top right) electrodes measured in half cell figuration, and the first capacity loss (bottom left) for a three-electrode full cell, with the areal capacity of the second cycle (bottom right). Voltages recorded against Na/Na <sup>+</sup> . ....	141
Figure 60. Three-electrode tests to map the sodium stoichiometry range that the hard carbon (left) and NMST2488 (right) electrodes undergo in a full cell (red) calculated by comparing to the half cell data (red). Voltages recorded against Na/Na <sup>+</sup> . ....	144
Figure 61. Open-circuit voltage of the hard carbon (top left) and NMST2488 electrodes (top right), measured using GITT in a three-electrode full cell. Voltages recorded against Na/Na <sup>+</sup> . The GITT profiles for the hard carbon (bottom left) and NMST2488 (bottom right) illustrate the stability and overpotentials during the measurement. ....	145
Figure 62. Comparison of the OCV and pOCV for the hard carbon (left) and NMST2488 (right) electrodes, measured using GITT in a three-electrode full cell. The voltage is measured against a Na/Na <sup>+</sup> reference.....	146
Figure 63. Sodium solid-phase diffusivity of the hard carbon (left) and NMST2488 electrodes, measured using GITT in three-electrode full cells (top) and three-electrode half cells (bottom). ....	148
Figure 64. Nyquist plot data fitted to an equivalent circuit model for the negative (top left) and positive electrodes (top right), plus the corresponding fitting parameters with errors for the resistance and capacitance values (bottom). ....	150
Figure 65. Exchange current densities measured from EIS as a function of state-of-charge (SOC) for hard carbon (left) and NMST488 (right), measured in half cell configurations. These values are used to observe the parabolic Butler-Volmer behaviour and to evaluate the mean exchange current density. ....	151
Figure 66. Plots for the working and counter simulated and experimental discharges voltage profiles from a three-electrode cell (left) and the root mean square error (RMSE) between the simulated and experimental terminal voltages (right), these voltage profiles were measured at C/20. ....	154

Figure 67. The different stages and costs to extract data and to develop models needed to design better batteries. This data has been obtained from first-hand experience of activities and projects.....	157
Figure 68. The different battery models used, the activities they are used for, and the industries they are used in. ....	158
Figure 69. The practical limitation of battery models is the quality of the input parameters.....	159
Figure 70. Combining intellectual property in the parameterisation of several models with the aim to reduce the cost of turning a physical cell into a battery model by 90%. This activity will be used to populate a database with data and models from commercial cells. ....	159
Figure 71. Analysis of incumbent and emerging companies in the battery software and modelling industries.....	162
Figure 72. Schematic to show the difference between “black-box” and “white-box” models.....	163
Figure 73. Positioning in the market, key differentiators are the different model classes being offered and the “white box” implementation. ....	163
Figure 74. Illustration to show technology map, from data collection to using tools to deliver value.....	164
Figure 75. Global electric vehicle battery production for Q1 2020 (Source data: ev-volumes.com).....	166
Figure 76. “Advanced Datasheet” outlining measured parameters in different categories. ....	167
Figure 77. Top-down analysis: Growth of the battery market size between 2021 and 2030 based on (Source data: Benchmark Mineral Intelligence).....	168
Figure 78. Bottom-up industry analysis, evaluating market size based on number of companies within industry and pricing for each (units in ‘000s). ....	168
Figure 79. Projected revenue for the business divided between the services and software business models. ....	170

## List of Tables

Table 1. Parameter requirements of the DFN model and the techniques used to measure them in this thesis. ....	33
Table 2. Parameter requirements of the thermal model and the techniques used to measure them in this thesis. ....	34
Table 3. The governing equations of the Doyle-Fuller-Newman (DFN) model. <sup>5 60</sup> .....	40
Table 4. The governing equations of the thermal model used in batteries. ....	47
Table 5. A summary of physics-based model parameterisations of commercial cells in literature. ....	50
Table 6. Parameter requirements of the ageing model.....	52
Table 7. Details about the LGM50 cell provided by the manufacturer. ....	69
Table 8. Physical parameters obtained from measuring the cell and its components during teardown.....	73
Table 9. The full parameter set for the Doyle-Fuller-Newman physics-based model. ....	90
Table 10. Comparison of experimentally derived parameter and tuned parameters for 0.5C, 1C, and 1.5C experimental datasets. ....	94
Table 11. Root-mean-squared error and peak error for the output voltage between the DFN simulation and experimental data at 0.5C, 1C, and 1.5C. The RMSE are analysed over the discharge and relaxation regimes, whereas the peak errors are evaluated for the discharge regime only. ....	94
Table 12. Properties and anatomy of the cell. *With electrolyte **Surface area of jellyroll. ....	102
Table 13. Gravimetric and volumetric contributions of components within the cell. *Electrolyte is excluded from volume calculation as it is soaked into the electrodes and separator.....	102
Table 14. Values used to calculate the specific heat capacity of the wetted porous electrodes and separator. ....	106
Table 15. Summary of the thermal diffusivity, specific heat capacity and thermal conductivity values for NMC811 and graphite electrodes as a function of temperature. ....	108
Table 16. Thermophysical properties of the cell components at 25°C (measured values are highlighted in green [m], calculated values in white [c], and literature values in blue [l])......	109

Table 17. Parameters used in our thermal-electrochemical simulations. *Thermophysical properties of wetted components, blue = parameters tuned to obtain agreement for 1C discharge at 25°C.....	123
Table 18. Voltage windows and formation parameters used for the three-electrode or two-electrode formation.....	134
Table 19. Voltage windows and current used for the three-electrode or two-electrode galvanostatic intermittent titration technique (GITT). ....	135
Table 20. Summary of parameterization techniques.....	135
Table 21. Lattice parameters and crystal structure properties of NMST2488 calculated from.....	137
Table 22. Physical and chemical properties of the NMST2488 and hard carbon electrodes.* denotes the particle sizes used in the model.....	138
Table 23. Parameters used to calculate stoichiometry limits for the electrodes in half cell configurations. ....	143
Table 24. The mean solid-phase diffusion coefficients for both materials in the sodium-ion system extracted in three-electrode configurations. These values are provided for both Sodiation and desodiation. ....	147
Table 25. Interfacial resistances ( $RCT$ ) across the stoichiometric range measured in a half cell configuration.....	150
Table 26. Exchange current densities calculated across the stoichiometric range for both electrodes.....	151
Table 27. Physical properties of the separator in the electrolyte domain. 1 = assumed according the Bruggeman relationship. 2 = averaged across both separator materials and weighted as thickness. ....	152
Table 28. Table outlining the tuning of parameters for the physics-based model.....	153
Table 29. Sodium-ion battery parameters required for the Doyle-Fuller-Newman (DFN) model. ....	154

## Table of Acronyms

Acronym	Full Description
BMS	Battery Management System
CC	Constant Current (charging/discharging method)
CPE	Constant Phase Element (in impedance spectroscopy)
CV	Constant Voltage (charging/discharging method)
DCA	Differential Capacity Analysis
DFN	Doyle-Fuller-Newman (a battery model)
DOD	Depth of Discharge (battery usage level)
DSC	Differential Scanning Calorimetry
ECM	Equivalent Circuit Model (for battery modelling)
EDS	Energy Dispersive Spectroscopy
EIS	Electrochemical Impedance Spectroscopy
GITT	Galvanostatic Intermittent Titration Technique
HOMO	Highest Occupied Molecular Orbital
LAM	Loss of Active Material (related to battery degradation)
LCO	Lithium Cobalt Oxide (a type of lithium-ion battery)
LFA	Laser Flash Analysis
LLI	Loss of Lithium Inventory (related to battery degradation)
LUMO	Lowest Unoccupied Molecular Orbital
NCA	Nickel Cobalt Aluminum (a type of lithium-ion battery)
NMC	Nickel Manganese Cobalt (a type of lithium-ion battery)
OCV	Open Circuit Voltage
PyBaMM	Python Battery Mathematical Modelling
SEI	Solid Electrolyte Interface
SEM	Scanning Electron Microscope
SoC	State of Charge (battery charge level)
SoH	State of Health (battery condition)
SPM	Single Particle Model (for battery simulation)
XRD	X-Ray Diffraction



# Research Aims & Thesis Outline

In scientific literature there is a scarcity of available parameters for commercially relevant lithium-ion batteries. The availability of accurately measured parameters is essential for the development of the models that are used to understand and optimise battery technology. Traditionally, parameters from different battery components are taken and assumed to be representative of the cell being modelled. However, battery components and cell performance are significantly influenced by the design and manufacture, which determines structure and composition. This work focusses on developing the theoretical and practical methods to obtain parameters relevant thermal-electrochemical model. Additionally, to validate the application of these methods in different contexts we parameterise the first commercially relevant sodium-ion battery system.

This thesis contains work from published academic journal papers, with the content being incorporated into the thesis with the permission of authors, the content of each chapter is as follows:

- Chapter 1: **Introduction**

The importance of energy storage in the clean energy transition and the relevance of lithium-ion and sodium-ion batteries in this thematic. The landscape of recent battery parameterisation and modelling research.

**Chapter 1** is partly based on “*Progress in Energy*, **4**, 032004, (2022).”<sup>5</sup> and “*ACS Energy Lett.* 2022, **7**, 1, 108–122”.<sup>6</sup>

- Chapter 2: **Literature Review**

Overview of the literature in the field of battery model parameterisation and identifying areas to be developed, setting the scene for the research in this thesis.

- Chapter 3: **Methods**

The theory for the methods used in the thesis, focussing on the assumptions/theory of electrochemical techniques and models used.

**Chapter 2** is partly based on “*Progress in Energy*, **4**, 032004, (2022).”<sup>5</sup>

- Chapter 4: **Electrochemical Parameterisation**

The full parameterisation of a physics-based model for a commercial lithium-ion battery, the LG M50. This chapter outlined the method development to characterise the composition and quantify the physical and electrochemical behaviour. Developing three-electrode tests to map the electrochemical properties more accurately than half cell tests.

**Chapter 3** is based on “*J. Electrochem. Soc.*, **167**, 080534, (2020)”.<sup>1</sup>

- Chapter 5: **Thermal Parameterisation**

The parameter set for the LG M50 was extended to include the thermal properties, this improved the accuracy of the electrochemical model and allowed reversible heat generation to be predicted. A parameterisation workflow to capture variability of the transport and thermodynamic properties with temperature and state-of-charge (SoC) was also developed.

**Chapter 4** is based on “*Electrochimica Acta*, **425**, 140700, (2022).”<sup>7</sup>

- Chapter 6: **Parameterisation of Next-Generation Batteries**

The developed parameterisation methodology was modified to be less sensitive to material choice and to develop additional understanding in sensitivity of the testing methods, providing a material and cell agnostic testing process. The first commercially relevant electrochemical model of a sodium-ion was evaluated to aid the development of next-generation battery systems.

- Chapter 7: **Commercialisation of Research**

The market research and technologies involved in commercialising the research in this thesis. Parameterisation is an important tool to solve industry challenges, the research contributed to the spin-out company being formed between University of Birmingham and Imperial College London. About:Energy pivoted from a parameterisation consultancy to a battery data and software company aiming to become an industry tool for cell selection, benchmarking, and system development

**Chapter 8** is based on “[www.aboutenergy.io](http://www.aboutenergy.io)”.

- Chapter 8: **Conclusions**

The conclusions drawn from this work with a consideration to future directions for this research. Discussion of the importance of open-sourcing data and the wider impact this thesis had had on battery research.

# Chapter 1: Background & Introduction

## 1.1 Motivation

Climate change is one of the most significant challenges faced by society. The rise in average global temperature has been primarily attributed to the increase of carbon dioxide concentration in the atmosphere. This relationship has been recognised by scientists since the late-1800s.<sup>8</sup> There have been severe predictions of the socioeconomic cost and loss of life associated with a 2.0 °C rise in global temperature. In spite of the early observation of this phenomenon and its implications, there has yet to be effective global strategy from government to find a solution and mitigate effects. The 1.5 °C rise targeted by the IPCC requires countries to adopt a net zero strategy, and achieving this requires changes in governance and the development of new technologies. Amongst these sustainable technologies, those that enable the decarbonisation of our transport and energy sectors are critical.

Energy storage has been critical for reducing society's reliance on fossil fuels, these non-renewable fuels have been used for electricity generation for decades. Energy storage technologies vary considerably in scale, cost, storage duration, and energy/power density. For example, pumped-hydro reservoirs provide energy storage to balance the grid on a MWh scale, pumping water up into a reservoir when energy is abundant and then using this potential energy to generate electricity when demand is higher. Pumped-hydro is suited for long-duration energy storage, in the order of several days.

As governments seek to further decarbonise, new technologies are needed for short-term duration and to electrify new applications. Reducing transport emissions relies on similar technologies. Batteries have become the favoured solution in this context, being used to power vehicles with electricity or hydrogen (fuel cell vehicles use batteries) and to reduce problems associated with the intermittency of renewable energy power sources. There are many commercially-viable battery chemistries, including secondary (rechargeable) batteries such as lead-acid and nickel-metal-hydride. These chemistries do not meet the performance-requirements for mass-market electric vehicles (EVs), because the application requires more energy/power dense batteries to achieve long-range. The lithium-ion battery has been popularised as the technology to be used for a variety of energy storage application including EVs due to its favourable energy density, cost, and safety. The carbon footprint of a battery's life cycle is critical to its effectiveness in driving a transition to sustainable energy. Batteries are considered polluting due to their reliance on critical materials and factory-scale manufacturing processes. Improving the sustainability of this technology is reliant on maximising the energy-power trade-off, improving longevity, and developing novel materials. This requires understanding the physics of the processes, for example evaluating the kinetic and thermodynamic properties provide insight into how to improve, control and enhance battery performance.

## 1.2 The Lithium-ion Battery

Lithium-ion batteries were first discovered at University of Oxford by John Goodenough in the 1980s, and this led to Sony commercialising the technology in 1991. Major developments towards the commercialisation of lithium-ion batteries were also made by Stan Whittingham and Akira Yoshino, the three academics winning the 2019 Nobel Prize in Chemistry. Since then, lithium-ion batteries have been used widely for energy storage applications due to favourable cost and performance.<sup>9</sup>

Since the commercialisation of the lithium-ion battery research has focussed on lowering cost to below \$100/kWh for a battery pack.<sup>10</sup> This price is claimed to be the point to enable a technological shift away from combustion vehicles. Lowering battery cost has seen a collective effort from academia and industry to solve challenges in manufacturing, battery design, recycling, and other areas. However, the improvements of battery technology in these areas have largely been through lab-based experiments and physical prototyping.

A global battery supply chain with a capacity of over 400 GWh has been built to date, this is estimated to scale to 4.3 TWh by 2030 to cater to global battery demand. The scaling of manufacturing capacity and improvements in technologies has seen the price of lithium-ion batteries fall from 668\$/kWh in 2013 to 137\$/kWh in 2020.<sup>10</sup> Commercial lithium-ion batteries have traditionally comprised of a layered oxide material as the positive electrode. This layered oxide material has traditionally been a mix of different transition metals to form  $\text{Li}[\text{Ni}_{1-x-y}\text{Mn}_x\text{Co}_y]\text{O}_2$  (NMC),  $\text{Li}[\text{Ni}_{1-x-y}\text{Co}_x\text{Al}_y]\text{O}_2$  (NCA), and  $\text{LiCoO}_2$  (LCO). NMC has been popularised as the cathode material of choice in Europe and the US due to its energy density and stability in comparison to LCO, the nickel content has been increased to tailor batteries with higher energy. Graphite has been the material predominately used in the negative electrode.<sup>11</sup> Nickel, manganese, cobalt, natural graphite and lithium have been added to the critical materials list by the European Commission due to the volumes of these materials needed for a sustainable energy transition, the difficulty building supply, and the geopolitical risk the supply chains pose.<sup>12</sup> Other battery materials have been developed and popularised to realise new applications, this includes increased deployment of the cheap and safe  $\text{LiFePO}_4$  (LFP) in Asia. The battery market primarily consists of these two chemistries, accounting for >95% of capacity. Next-generation materials including the use of silicon-containing materials as a negative electrode additive to increase energy density have been commercialised more recently.<sup>13</sup>

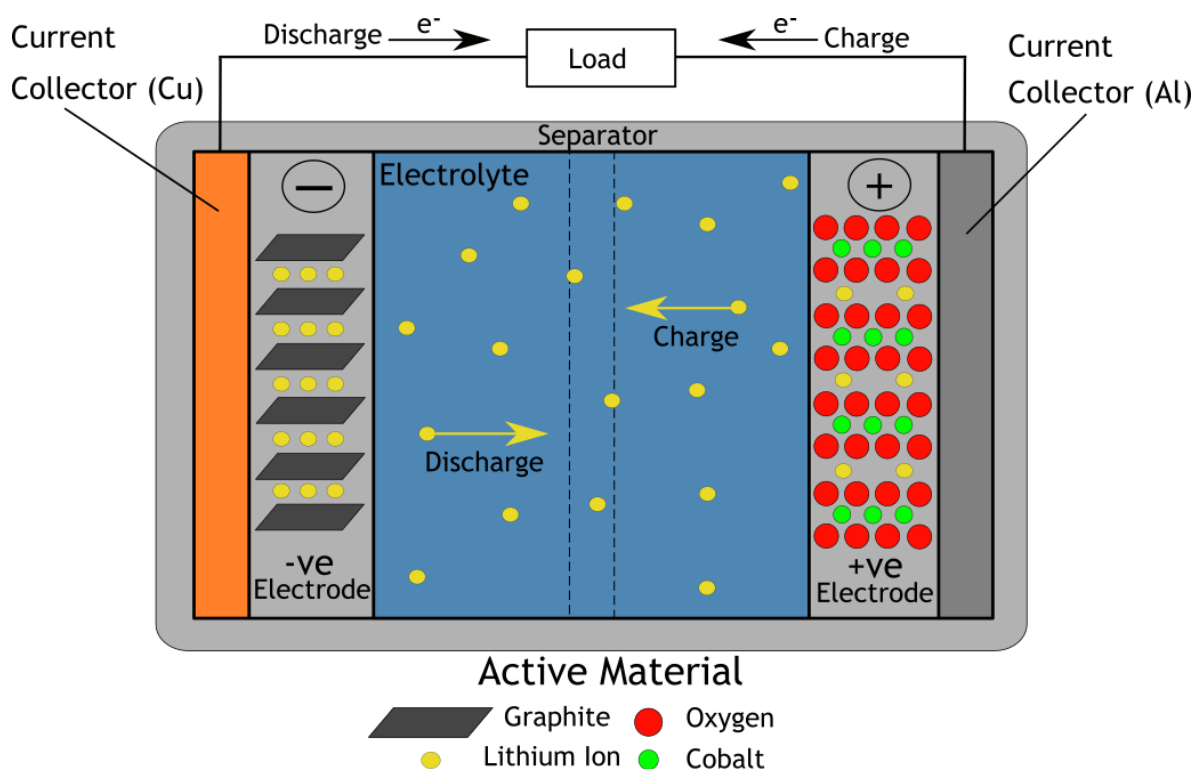


Figure 1. Schematic of a lithium-ion battery using a graphite negative electrode and a layered oxide positive electrode,  $\text{LiCoO}_2$ .

There has been significant academic and commercial interest in improving lithium-ion technologies. Developments within the automotive industry primarily relate to the development of lower cost and more energy dense batteries.<sup>14,15</sup> Innovative ways to optimise battery technology have been devised to improve performance at the material, electrode, cell, and pack level. Research at the material level has focussed on developing higher energy density materials, such as high-nickel NMC and using pure silicon as a negative electrode additive.<sup>16–18</sup> The electrode microstructure has been tailored to enhance ion and electron transport.<sup>19,20</sup> Cell design has been improved by introducing new form factors to improve energy density and by tailoring structure to improve thermal properties.<sup>21,22</sup> Novel battery pack architectures have been designed to lower resistance, improving fast charging and reducing mechanical degradation during operation.<sup>23,24</sup>

Holistic battery development that encompasses both simulation-based virtual design and physical experimentation, is needed more in science and moves beyond traditional trial-and-error methods. This can be achieved using models with greater physical insight that enable predictions to be made relating to the thermodynamic or kinetic limitations of a battery, these predictions are based upon the electrochemical properties and internal states.

Lithium-ion batteries comprise of a positive electrode, a negative electrode, and a separator soaked in an electrolyte.<sup>25</sup> The separator acts as a barrier to prevent the electrodes coming into contact (thus causing a short circuit), while allowing ion transport between the electrodes to complete the battery circuit. Electrochemical testing commonly utilises this two-electrode configuration to replicate the behaviour of

commercial cells. The positive and negative electrodes chemistries commonly utilised in commercial cells are transition metal oxides/phosphates and graphite. There have been significant contributions in the development of these materials and compatible electrolyte systems. Despite substantial research there is a knowledge gap between academia and industry in developing state-of-the-art chemistries for practical applications, relating to topics such as cell design and manufacturing.<sup>26</sup>

Mathematical modelling has been critical to optimise battery technology, from active materials to battery packs. Models are used to understand battery performance by making predictions across various timescales and length-scales.<sup>27</sup> Models reduce the need to run a practical experiment for every scenario by enabling many pathways and outcomes for battery operation to be simulated virtually. There are four main categories of model, (i) atomistic models used for material discovery, (ii) continuum models, that can be physics-based or described by electrical used to optimise cell performance, and (iii) techno-economic models used to estimate the cost and environmental impacts of batteries, (iv) or machine learning models that are driven by large datasets.<sup>27</sup> This thesis outlines research relating to the improvement of continuum models through the development of novel parameterisation methodologies to evaluate the electrochemical properties of a battery more accurately. Parameteric cell models, those that require parameters to be evaluated through practical experiments, have been a focus of interest for in research due to the predictive power about battery performance.

### 1.3 Battery Fundamentals

The thermodynamic properties of a battery mean it can generate electrical energy from chemical reactions being driven between two electrodes of polar charge. These reactions have an electrochemical potential, this thermodynamic property involves storing energy in the form of a chemical potential. In an electrochemical cell, the chemical reactions take place at each electrode and can be represented by:<sup>28</sup>



These equations define the reduction (Eq. [1]) and oxidation (Eq. [2]) reactions happening at each electrode. For reversible cells, the half-cell reactions give the overall reaction in the cell (Eq. [3]). The change in the standard free energy,  $\Delta G^0$ , of this reaction is:

$$\Delta G^0 = -nFE^0 \quad [4]$$

where  $F$  is Faraday's constant and  $E^0$  is the standard electrode potential. The standard electrode potential measures the likelihood of a chemical species gaining or losing

electrons. The standard state is defined by ions at an effective concentration of 1 mol dm<sup>-3</sup>. If conditions deviate from the standard state, the potential of the cell,  $E_{\text{cell}}$ , is measured using the Nernst equation:

$$E_{\text{cell}} = E_{\text{cell}}^0 - \frac{RT}{nF} \ln \left( \frac{\alpha_B^i \alpha_D^i}{\alpha_A^i \alpha_C^i} \right) \quad [5]$$

where  $\alpha^i$  is the activity of the relevant species (A, B, C, D represent chemical species participating in the electrochemical reaction),  $R$  is the gas constant, and  $T$  is temperature. For a system comprised of two electrodes, the operating voltage of a cell is limited by the open-circuit voltage,  $E^0$ , which is the potential difference across the electrodes at equilibrium:

$$E^0 = -\frac{1}{nF} (\alpha_A^i - \alpha_C^i) \quad [6]$$

Here  $(\alpha_A^i - \alpha_C^i)$  is the difference in the chemical potential of the negative electrode or anode (A) and the positive electrode or cathode (C),  $n$  is the number of electrons involved in the reaction. The energies associated with the electronic and ionic transfer determined the nominal voltage of the cell. The work function (minimum quantity of energy required to remove an electron to infinity from the surface of a metal) determines the energy of electron transfer, whereas the crystal structure determines that of ion transfer (Figure 2). The magnitude of  $E^0$  is constrained to less than 5 V due to the attainable difference  $\alpha_A^i - \alpha_C^i$  of the electrochemical potentials, but also by the thermodynamic potential window of the electrolyte, referring to the range which the electrolyte does not decompose during electrochemical reactions.

Previously, there has been the misconception of equating energy difference between the highest unoccupied molecular orbital (HOMO) and lowest unoccupied molecular orbital (LUMO) with the electrochemical stability window. The terms HOMO and LUMO should be avoided when referring to electrolyte stability.<sup>29</sup> This misconception arises because the HOMO-LUMO gap pertains to electronic transitions within molecules, while the electrochemical stability window is determined by the potential range in which the electrolyte remains neither oxidized nor reduced, a process governed by different chemical and physical principles.

Another relevant aspect that Figure 2 illustrates is Fermi levels. These are described with the red and blue shaded areas in the Figure, representing the chemical potential for electrons in a solid. In molecular orbital theory, the Fermi level is an approximation of the electron's chemical potential, aligning closely with the energy of the HOMO in a reduction or the LUMO in an oxidation process. It predicts whether an electron transfer will occur, indicating the propensity for a molecule to gain or lose electrons during electrochemical reactions.

The Butler-Volmer equation is another fundamental relationship that describes the kinetics of an electrochemical reaction, explaining how the flow of electric current in an electrode is influenced by the difference in voltage between the electrode and the surrounding electrolyte for a straightforward, single-molecule oxidation-reduction process:

$$J = j_o \cdot \left\{ \exp \left[ \frac{\alpha_a z F \eta}{RT} \right] - \exp \left[ - \frac{\alpha_c z F \eta}{RT} \right] \right\} \quad [7]$$

In this expression,  $J$  symbolizes the current density (the electric current flowing per unit area of electrode surface),  $j_o$  represents the exchange current density,  $\alpha$  denotes the charge transfer coefficient,  $\eta$  the activation overpotential, while  $R$  and  $F$  are the constants of ideal gas and Faraday correspondingly. The Butler-Volmer equation assumes equilibrium between concentrations at the electrode and in the electrolyte, expressing current density as a function of potential. However, this holds mainly under steady-state, moderate reaction rates; rapid reactions or marked concentration polarization disrupt this equilibrium, impacting reaction kinetics. Put differently, it assumes that the rate of mass transfer greatly surpasses the rate of the chemical reaction, with the latter being predominantly governed by the slower chemical reaction rate.

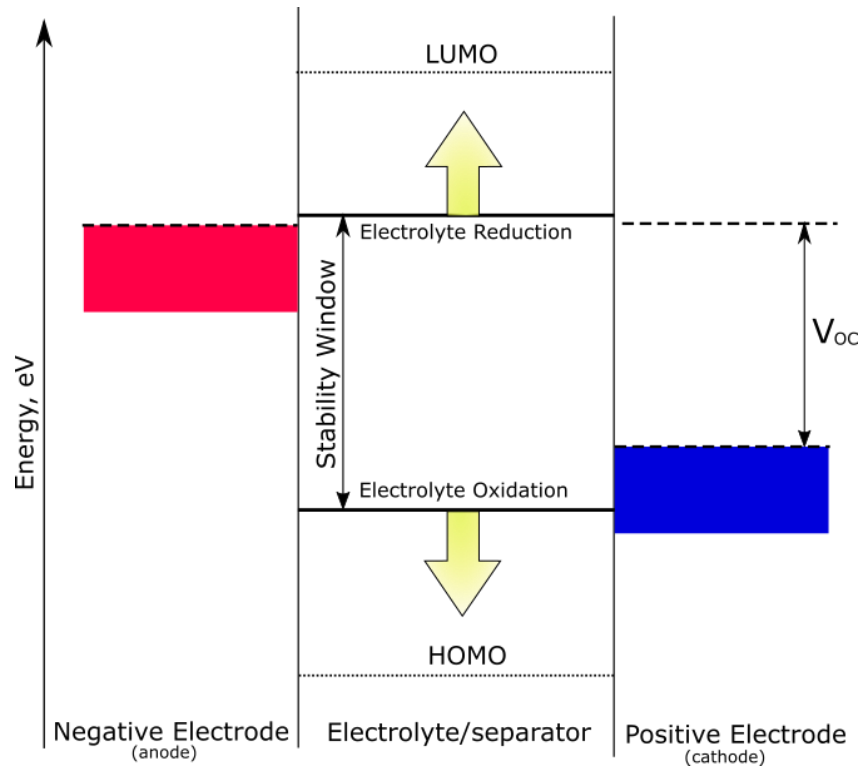


Figure 2. Schematic to show negative and positive potential limits for the electrolyte stability and misconception regarding the electrolyte stability window.

Parametric battery models capture the thermodynamic and kinetic properties of a battery.<sup>30</sup> These models aim to capture charge transfer and polarisation either through



electrical circuit elements or physics-based equations. The latter employing the Butler-Volmer reaction kinetics in Eq. [7] to describe the intercalation of lithium ions at the interface between the electrode and the electrolyte, thereby linking these phenomena.<sup>30</sup> They also account for the thermodynamics of the system and phase changes through an open-circuit voltage curve.

## 1.4 Parametric Cell Modelling

Models have been used widely in the application, design, and prediction of battery technology. Models are an effective tool to reduce the time and cost of R&D, they reduce the reliance on expensive testing facilities or resource intensive experiments. There are many classes of models, but parametric approaches have received the most attention from research and industry. These models are governed by a finite number of parameters, in contrast to non-parametric models (also known as data-driven models) that have an (potentially) infinite number of parameters. Figure 3 illustrates two examples of parametric models used in battery research, electrical and electrochemical. In these models, the parameters are numerical or measurable variables that define a system, in the case of this thesis, the system studied is a battery. The most used commercially-implemented parametric battery models are equivalent circuit-based, but physics-based are beginning to be explored commercially.

These models have different uses owing to their computational expense and fidelity. Equivalent-circuit models assume that the batteries behave like a specific electric circuit and by suitably fitting the parameters it can provide accurate predictions relating to electrical properties, whereas physics-based models enable the determination of the internal states of a lithium-ion battery; allowing, for example, the observation of electrode potentials and lithium concentrations (Figure 4).

To simulate battery behaviour, models require input parameters that capture the electrochemical, thermal, and ageing properties of a battery. The values of these parameters are unique to each battery type and depend significantly on the format and chemistry of the cell. Parametrisation is the process of quantifying the properties of a battery to provide a set of values in the equations that govern the model. It is only with these values can the battery behaviour be simulated in different operating conditions.

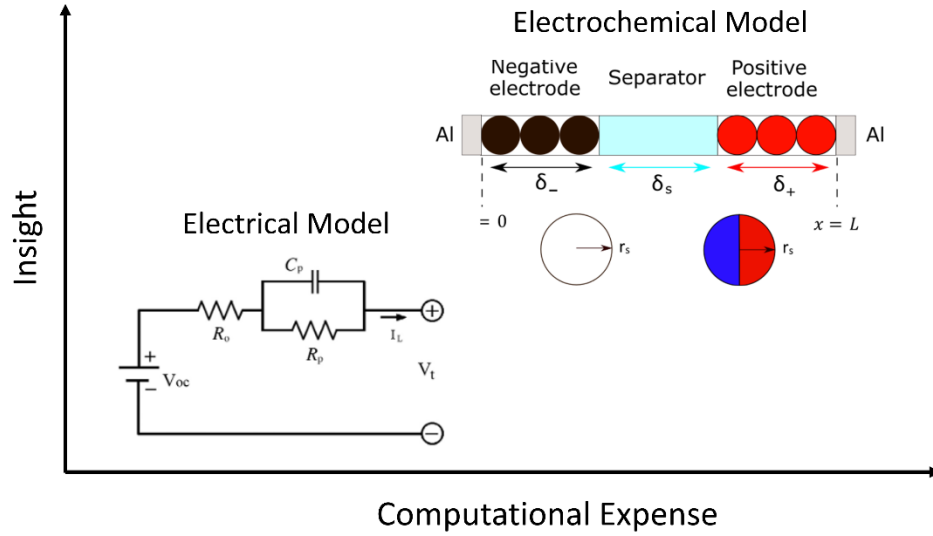


Figure 3. Comparison of equivalent circuit-based and physics-based models, two types of parametric models used in battery research

Equivalent circuit-based models are commonly used in battery management systems (BMS) due to the low computational expense required to solve them. This makes them suitable to be used in on-board applications. The safe and efficient use of a battery system is reliant on the BMS: the BMS protects a rechargeable battery, by preventing it from overcharging, monitoring its state, and balancing cell voltages. To optimise performance and prolong longevity, accurate estimation of battery state-of-charge (SoC) and prediction of the battery state-of-health (SoH) is critical.

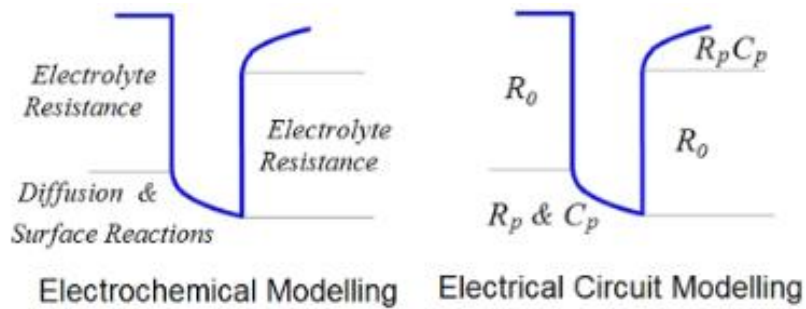


Figure 4. The characteristics of voltage response in a battery can be modelled using two different ways, an electrochemical model relates to processes that happen within a battery, whereas electrical circuit modelling approximates the behaviour using circuit elements such as resistors and capacitors.

Physics-based models are another type of model popular in academic research. The model class was first introduced for batteries in 1975 by Newman and Tiedemann,<sup>30</sup> eventually taking the eponymous form researchers are familiar with today: The Doyle-Fuller-Newman (DFN) model.<sup>31</sup> In the subsequent decades there were several notable

developments by these researchers.<sup>32–35</sup> These models utilise equations based on conservation laws that describe processes such as lithium diffusion and intercalation, and therefore require extensive parameterisation relating to the physics of the battery, including the thermodynamic and kinetic processes in the electrodes and electrolyte. The parameter requirements of physics-based models are therefore considerably more involved than equivalent circuit-based.

#### 1.4.1 Equivalent Circuit-based Modelling

Equivalent circuit models allow the behaviour of a two-terminal battery to be explained simply by circuit elements. These models have low fidelity but are fast and accurate enough to run in real-time. In the case of lithium-ion batteries, more complex equivalent circuits are needed to approximate non-linear behaviour. Battery behaviour can be replicated by assembling a network of resistors, capacitors, and voltage sources.<sup>36</sup> The simplest battery model can be modelled by an ideal voltage source and a resistance (Figure 3). The addition of an element comprised of a resistor and a capacitor in parallel (RC) increases the model accuracy by considering the effect of polarisation in a battery (Figure 6). The RC elements model the behaviour of intercalation/deintercalation of lithium into the porous electrode. In engineering this circuit is called a Thevenin model, utilized for simplifying and analyzing general electrical networks. In contrast with a Randles model, specifically designed for electrochemical systems, used for impedance analysis.

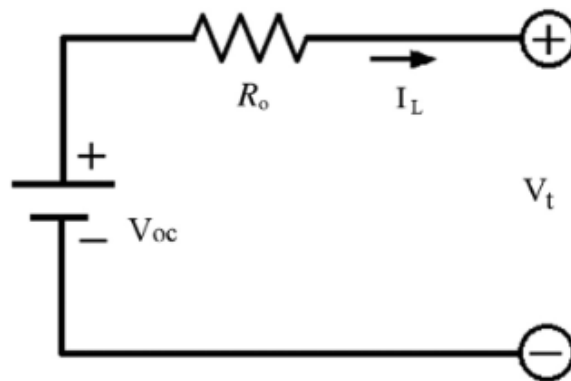


Figure 5. The electrical circuit to model the internal resistance in a battery.

These models have been favoured in practical applications due to, not only their ability to produce fast and robust predictions, but their reliance on few parameters that must be determined experimentally. The limitation of Thevenin battery models is that the parameter values are constant, but in battery applications parameter values depend on SOC, temperature, and SOH.<sup>37</sup> However, lookup tables that outline the Thevenin model parameters can be evaluated, this allows the model to depend on SOH, SOC, and temperature.<sup>38</sup>

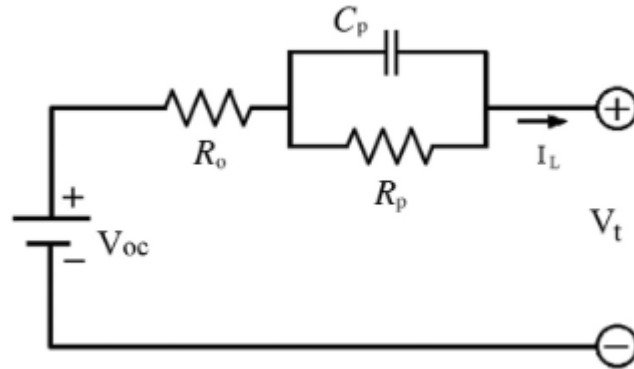


Figure 6. One RC network battery model, known as a Thevenin model. This model allows the prediction of the voltage response for an input current, this response is generated from a network of circuit elements.

Despite their computational efficiency and adaptability for online estimation in battery management systems, there has been increased interest in models that provide better insight into the operation of a battery. Informational limitations arise for the equivalent circuit model as it can only predict current-voltage behaviour and not internal states. Equivalent circuit models provide good approximation to the short-term behaviour, though they fail making predictions at processes such as diffusion that occur on longer timescales. Physics-based models are being popularised in industry for their physically relevant parameters and the ability to observe the internal states of the battery.

#### 1.4.2 Physics-based Models

Physics-based models of batteries are used to understand and predict the behaviour of battery systems.<sup>39</sup> These models consider the electrochemical reactions occurring within the battery, the movement of ions through the electrolyte, and the transport of electrons through the electrodes. By simulating these processes, physics-based models can provide insights into the performance and degradation of batteries, as well as guide the design of new battery technologies.

##### 1.4.2.1 Electrochemical Modelling

The most popular battery electrochemical model is the Doyle-Fuller-Newman (DFN) model (Figure 7).<sup>30,40</sup> Since its development, the DFN model has been accepted as the most reliable physics-based model.<sup>41</sup> However, the model has several assumptions that need to be considered. The most critical is the assumption of a spherical particle geometry and that the effective transport properties are obtained using an empirical relation that depends only on the electrode porosity, known as electrolyte volume fraction. In practice, battery electrodes feature non-spherical particle shapes that exhibit polydispersity. The morphology of the active material significantly contributes to the effective properties. Despite these assumptions, lithium-ion transport can be captured at the microscopic length scales. The computational expense of the DFN renders it impractical as a predictive tool at system level. This has led to the development of simplified versions of the DFN model that are less computationally expensive and do not

lead to significant loss of information, for example the single particle model with electrolyte (SPMe).<sup>42</sup>

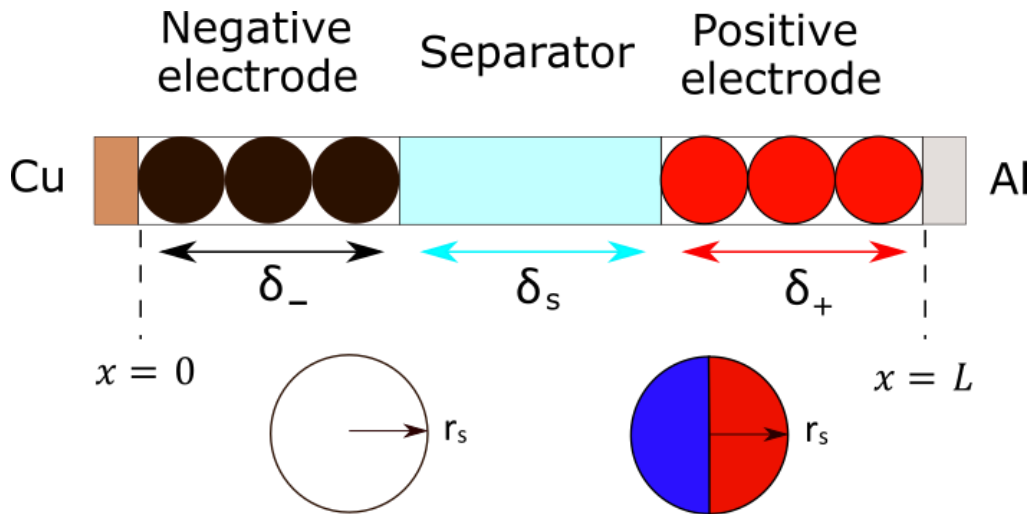


Figure 7. Schematic to describe domains the DFN model, also known as a pseudo-two-dimensional (P2D) model.

The methods commonly used to measure the parameters relevant in an electrochemical model are outlined in Table 1. These values relate to the individual components, many of which can only be measured through cell teardown and post-mortem analysis. This can be an obstacle to the practical use of the model in both academia and industry due to the lab facilities and experimental expertise needed. Fuller explanations of these parameters, the equations governing them, and the measurement techniques are included in the subsequent chapters.

Table 1. Parameter requirements of the DFN model and the techniques used to measure them in this thesis.

	Parameter	Symbol	Units	Technique
Electrode Properties	Maximum Li <sup>+</sup> concentration in particle	$c_{s,k}^{max}$	mol m <sup>-3</sup>	Galvanostatic cycling
	Initial Li <sup>+</sup> concentration in electrolyte	$c_{e0}$	mol m <sup>-3</sup>	Manufacturer
	Initial Li <sup>+</sup> concentration in particle	$c_{s,k}^0$	mol m <sup>-3</sup>	Galvanostatic cycling
	Solid-phase diffusivity	$D_{s,k}$	m <sup>2</sup> s <sup>-1</sup>	Galvanostatic intermittent titration technique
	Open-circuit voltage	$U_k(D_{s,k})$	V	Galvanostatic intermittent titration technique
	Exchange current density	$j_{0,k}$	A m <sup>-2</sup>	Electrochemical impedance spectroscopy
	Reaction rate constant	$k_k$	mol m <sup>-2</sup> s <sup>-1</sup>	Electrochemical impedance spectroscopy
	Electrode and separator thickness	$L_k$	m	Geometric measurement
	Particle radius	$r_k$	m	Microscopy
	Electrode stoichiometry	$\theta_k$	-	Galvanostatic cycling
	Solid-phase electronic conductivity	$\sigma_k$	S m <sup>-1</sup>	Electronic probe
	Electrolyte volume fraction (porosity)	$\varepsilon_k^b$	-	Gravimetric measurement
Electrolyte Properties	Li <sup>+</sup> transference number	$t_+^0$	-	Literature
	Thermodynamic factor	$1 + \frac{\partial \ln f_{\pm}}{\partial \ln c_e}$	-	Literature
	Charge transfer coefficients	$\alpha_{ak}$ or $\alpha_{ck}$	-	Literature
	Electrolyte diffusivity	$D_{e,k}$	m <sup>2</sup> s <sup>-1</sup>	Literature
	Electrolyte ionic conductivity	$\sigma_{e,k}$	S m <sup>-1</sup>	Literature

#### 1.4.2.2 Thermal Modelling

Thermal equations can be coupled to an electrochemical model to improve its accuracy and to predict heat transport/generation within a battery system. The thermal performance becomes an important consideration for high power cells and battery packs.<sup>43</sup> However, new equations require new parameters. These parameters relate to the temperature dependence of the electrochemical properties, specific heat capacity, entropy, and thermal conductivity.<sup>44</sup>

The methods commonly used to measure the parameters relevant in a thermal model are outlined in Table 2. These values relate to the thermal properties of individual components, which often require breaking down the cell into its constituent parts for accurate determination. Fuller explanations of these parameters, the equations governing them, and the measurement techniques are included in the subsequent chapters.

Table 2. Parameter requirements of the thermal model and the techniques used to measure them in this thesis.

Parameter	Symbol	Units	Technique
Specific heat capacity	$C_p$	$\text{J kg}^{-1} \text{K}^{-1}$	Differential scanning calorimetry
Thermal conductivity	$k$	$\text{W m K}^{-1}$	Laser flash analysis
Entropic term	$\frac{\partial U}{\partial T}$	$\text{V K}^{-1}$	Potentiostatic method
Density	$\rho_k$	$\text{kg m}^{-3}$	Gravimetric methods
Diffusivity	$D_k(T)$	$\text{m}^2 \text{s}^{-1}$	Galvanostatic intermittent titration technique
Exchange current density activation energy	$J_k(T)$	$\text{A m}^{-2}$	Electrochemical impedance spectroscopy
Electronic conductivity	$\sigma_k(T)$	$\text{S m}^{-1}$	Four-point probe

Including the thermal equations accounts for the irreversible and reversible heat generated by the ohmic drop in the battery and the entropy of the materials, respectively. The heating caused by the ohmic drop is caused by the internal resistance of the cell, named Joule heating. Reversible heat generation dominates at low currents in a battery, this is because the Joule heating at low currents becomes comparable to the heat caused by the entropy changes in materials. Thermal transport becomes important in larger battery systems, as the thermal conductivity and heat capacity of the materials govern how well heat is dissipated.<sup>45</sup> A thermal electrochemical model is established by integrating an internal heat transfer framework that includes the structure of the cell, enabling assessment of anisotropy and temperature-dependent properties. The approach defines thermal electrochemical models by elucidating the thermal attributes specific to each constituent component. This approach leads to inaccuracies in the thermal performance of multi-cell systems because summing the individual components' thermal properties do not account for the thermal contact resistances between the layers.

#### 1.4.3 Degradation Modelling

Understanding and mitigating the causes of battery ageing is considered one of the most important challenges in energy storage research. Battery degradation refers to several processes that lower the usable capacity and increase the internal resistance of the cell. Researchers have focussed on optimising battery chemistry, design, or management to mitigate ageing, significantly lowering the cost and carbon footprint of a battery during its lifetime. Ageing occurs at the various length-scales of a battery, within the crystal structure, the active material particle, and the microstructure.<sup>6</sup> These processes are categorised into loss of active material and loss of lithium inventory.<sup>46</sup>

- Loss of active material (LAM) – Capacity fade occurs when the active material degrades and can no longer intercalate lithium, either through particle cracking or the blocking of active sites by surface layers. These processes also lead to power fade by increasing the contact resistance within the electrode structure.

- Loss of lithium inventory (LLI) – Capacity fade occurs when lithium ions available for intercalation are consumed by reactions, including SEI formation, decomposition, and lithium plating. The growth of surface films on the active materials also increases resistance, leading to power fade.

The operating conditions of a battery can significantly affect the rate of ageing, these factors include temperature, SOC, and the current profile. These stress factors have been connected to different underlying ageing processes.<sup>47</sup> For example, charging the battery at low temperatures (below 10 °C) results in significant lithium plating and capacity fade. Lithium plating occurs when lithium ions fail to intercalate into the anode during charging and form metallic lithium on the surface. This process reduces the ability to store energy (leading to capacity fade) but also poses safety risks.<sup>48</sup> Predicting battery lifetime under specific conditions is important to understand its operation in an application, meaning the management system can control the environment to mitigate significant ageing. Lifetime prediction is also important from a techno-economic perspective to evaluate the first-life duration of a cell (characterised by its capacity reaching 80%).

Degradation models can then be used to estimate the practical lifetime of the cell and its economic value for a second-life application. However, predicting the lifetime of batteries under conditions that have not been empirically validated can be challenging due to a phenomenon known as non-linear ageing, also referred to as the "knee point".<sup>49</sup> Non-linear ageing is characterized by a significant change in the material's coulombic efficiency, which leads to sudden capacity fade. This phenomenon occurs when the efficiency with which the battery can accept and release charge dramatically decreases, often after a period of relatively stable performance, resulting in an abrupt decline in the battery's ability to hold a charge. This phenomenon significantly reduces the lifetime of the battery. New modelling approaches that predict future fade for new operating scenarios have been proposed, these models can capture the linear and non-linear behaviour with high accuracy.<sup>50</sup> Although accurate lifetime estimations still require ageing data to tune the parameters relating to ageing processes.

There are three types of ageing models used to predict battery lifetime, empirical, machine-learning, and physics-based.<sup>51</sup> Empirical models require data from large-scale battery ageing experiments, constructing these models is resource-intensive. Empirical models cannot be generalised to different chemistries/formats, limiting predictions to the specific type and operational environment seen in the experiment. Machine learning models use a black box approach. This means that the modelling framework is not based upon physical processes such as lithium plating or particle cracking. They are similar to empirical models as they require many cells to be tested under different conditions, although the machine learning algorithm provides greater adaptability and accuracy. Physics-based ageing models use differential algebraic equations to describe degradation mechanisms, these models are extensions of the DFN and SPM that capture the electrochemical behaviour of the system.

To ensure reliability and optimal performance over the lifetime of the cell, degradation models need to be applicable across a wide range of temperatures, current rates, SoCs,



and depths-of-discharge (DoD). To reduce the computational expense, DFN degradation models can be simplified to SPM and combined with the parasitic reactions associated with each ageing mechanism.<sup>52</sup> State-of-the-art degradation modelling aims to accurately predict one of several mechanisms, SEI growth, lithium plating, gas evolution, or crack propagation. Combining these mechanisms into a single model has thus far not been possible as it would come at a computational expense that prohibits practical implementation. The parameterisation of these degradation processes is an important part of the model construction.

## **1.5 Next-generation Battery Modelling: Sodium-ion**

Lithium-ion batteries are not the most suitable technology for every energy storage application due to both performance and supply chain aspects. The lifetime and energy density of lithium-ion batteries have limitations for specific applications, such as aerospace. Additionally, the constraints of lithium supply and the availability of other critical materials make them less economically viable.<sup>53,54</sup> This has led to the commercialisation of new battery chemistries. Next-generation technologies address several issues with existing lithium-ion batteries, including the availability of raw materials, cost and safety. The price of lithium chemicals including lithium carbonate have increased by 437% in 2021 reaching an all-time high. It takes 2 to 3 years to build a gigafactory and 6 to 15 years to build a mine, so analysts predict this price environment to continue throughout the decade. This presents an opportunity for the adoption of new chemistries, including sodium-ion batteries.

Sodium-ion batteries are being popularised, despite having a lower energy density than lithium-ion. The specific energy density of lithium-ion batteries typically ranges from 100 to 265 watt-hours per kilogram (Wh/kg), while that of sodium-ion batteries ranges from 80 to 120 Wh/kg.<sup>55</sup> Therefore, lithium-ion batteries have a higher energy density than sodium-ion batteries by about 20-50%. The potential in cost reductions makes them suitable for applications that do not have weight constraints such as grid-storage and light electric vehicles. Sodium-ion batteries could be cheaper as the chemistries being commercialised are lithium, cobalt, and copper free. Reducing the reliance on lithium is important for the cost competitiveness of any new technology. The total lifetime cost of the battery is also reduced due to the safety benefits, due to the ability to transport batteries at 0 V and a lower energy density reduces the chance of thermal runaway. However, cost competitiveness of these batteries is reliant on GWh-scale manufacturing.

Similar to lithium-ion batteries, sodium systems are comprised of intercalation materials, the positive electrode composition is most commonly a layered transition metal oxide (Figure 8).<sup>55</sup> The main difference between these two chemistries is the difference in ion size, the larger sodium-ion cannot intercalate into ordered materials such as graphite. Instead, amorphous materials such as hard carbon need to be used so that reversible intercalation is possible.

Several companies are seeking to commercialise this technology, including emerging companies like Faradion, LiNa, and Altris, but also industry incumbents such as CATL.

CATL has announced the first-generation of its batteries will be available in 2023. Despite commercial interest in sodium-ion batteries as an alternative solution for energy storage, the research community has largely focussed on addressing fundamental material-level science, rather than engineering challenges.<sup>55</sup> This research has focussed on the computational discovery of new materials, the development of electrode materials, and improvement of the solid-electrolyte interphase layer.<sup>55,56</sup>

Sodium-ion is similar to existing lithium-ion technologies. This means that decades of learning relating to the manufacture, synthesis, and design can be applied to these materials. However, nuances exist that mean previous knowledge be applied in its entirety and existing methods will have to be optimised to maximise the performance/cost of this chemistry.

To be competitive with lithium-ion, improvements in manufacturing and battery management will need to be achieved. Traditional manufacturing methods will need to be adapted due to the instability of certain materials in air, for example, the conditions during mixing and coating may need to be controlled to ensure the longevity of layered oxide materials.<sup>57</sup> Lithium-ion battery development has been aided by modelling investigations, although sodium-ion commercialisation has been primarily focussed on empirical lab-based research. The development and understanding of sodium-ion systems using models represent a significant opportunity in research. Models are underutilised beyond atomistic modelling and material development. Engineering-focused models, in particular, have a great opportunity to improve performance and reduce the time to market for these new materials. By leveraging these models, researchers can better predict and optimize the behaviour of sodium-ion batteries, advancing more efficient and cost-effective energy storage solutions.

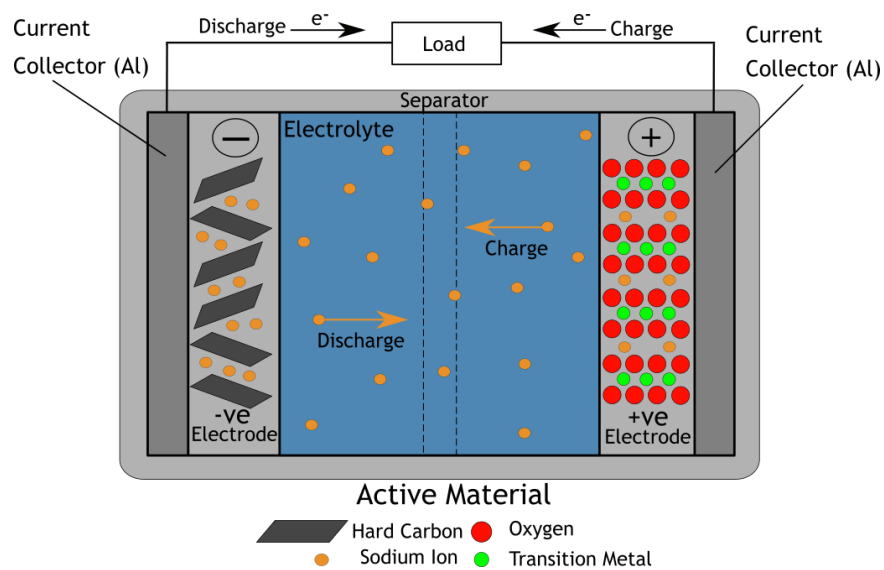


Figure 8. Schematic of a sodium-ion battery using a hard carbon negative electrode and a layered oxide positive electrode.

## 1.6 Research Objective

This thesis aims to address the significant challenge of parameterising lithium-ion battery models through the development of comprehensive methodologies. By leveraging physical, electrochemical, and thermal characterization techniques, the research aims to identify critical model parameters, enhance experimental approaches, and create accurate models for specific cell chemistries and formats. The utilisation of advanced techniques, such as electrochemical impedance spectroscopy, galvanostatic intermittent titration technique, and thermal measurement methods, is central to achieving this. This approach enables the construction of battery models that closely align simulated data with experimental observations, offering a robust tool for industry application and model development.

The objective of this work was to develop a complete parameterization workflow tailored to high-energy commercial cylindrical cells. This involves capturing the intricate thermal-electrochemical behaviour of lithium-ion batteries and understanding the property changes that occur during battery operation, with a particular focus on the dependency of parameters on temperature and state-of-charge. Additionally, this thesis explores the modification of traditional methods to better parameterise emerging technologies, such as silicon additives and new chemistries including sodium.

The novelty of this research lies in its methodological approach, which not only identifies the limitations of existing battery models but also proposes areas where simplifications can enhance utility without compromising the intricate understanding of battery physics. By equipping theorists and practitioners with practical tools and insights, this thesis aims to facilitate significant advancements in the field of battery modelling.

The structure of this thesis is designed to systematically guide the reader through the research process, from the initial identification of the problem and the development of methodologies to the practical application of these methods in model development and industry implementation. Through this journey, the thesis underscores the importance of a comprehensive experimental approach to battery model parameterization, setting the stage for future innovations in battery technology and modelling.

## Chapter 2: Literature Review on Parameterisation

This chapter reviews relevant literature to provide the research context for this thesis, topics include: (i) electrochemical parameterisation, (ii) thermal parameterisation, (iii) degradation parameterisation, and (iv) parameterisation of next-generation batteries. Each section on ‘parameterisation’ outlines the wider research themes that this thesis seeks to contribute to, summarising the main electrochemical, physical, and thermal experimental techniques used to develop a model, for the thermal and electrochemical models, outlining the governing model equations and key assumptions.

### 2.1 Electrochemical Parameterisation

#### Model

The Doyle-Fuller-Newman (DFN) model is one of the most used frameworks in the field of battery modelling and research, predicting the behaviour of lithium-ion batteries under various conditions.<sup>31,58,59</sup> Developed by Doyle, Fuller, and Newman, this electrochemical model integrates coupled, nonlinear differential equations to simulate the dynamic interactions within a battery cell. It predicts the voltage and current as functions of time across the electrodes and electrolyte, thereby offering insights into the performance, efficiency, and longevity of battery systems. The DFN model is characterised by its pseudo two-dimensional (P2D) approach, which treats the battery as one-dimensional in terms of the active material particles (assumed to be spherical) and one-dimensional across the electrodes.<sup>60</sup> This setup enables the model to capture the complex interplay of mass and charge transfer processes along the radial axis ( $r$ ) for lithium intercalation into electrode particles and unidirectionally across the cell layers ( $x$ -axis), thus accounting for the spatial distribution of processes that occur within the battery.

The equations governing the DFN model (Table 3) describe various key processes: mass conservation in the electrodes and electrolyte (Equations [8] and [10]), charge conservation (Equations [9] and [11]), reaction kinetics (Equation [12]), exchange current density (Equation [13]), and overpotential (Equation [14]). These equations are intricately connected, modelling the lithium-ion concentration in the solid ( $c_s$ ), and liquid ( $c_e$ ) phases, the solid-phase potential ( $\phi_s$ ), and the liquid-phase potential ( $\phi_e$ ). For instance, mass conservation in the electrodes (Equation [8] and electrolyte (Equation [10]) is crucial for determining  $c_s$ , and  $c_e$ , respectively, with boundary conditions that ensure physical viability at the interfaces. Charge conservation equations (Equations [9] and [11]) are vital for calculating  $\phi_s$  and  $\phi_e$ , integrating the conductivity within the solid and liquid phases to account for the electrical flow. Reaction kinetics (Equation [12]) and the associated exchange current density (Equation [13]) describe the electrochemical reactions at the electrode-electrolyte interface, crucial for understanding the rate of lithium intercalation and deintercalation.

Table 3. The governing equations of the Doyle-Fuller-Newman (DFN) model.<sup>5 60</sup>

Description	Equation	Boundary conditions
<b>Electrodes</b>		
Mass conservation [8]	$\frac{\partial c_{s,k}}{\partial t} = \frac{1}{r^2} \frac{\partial}{\partial r} \left( r^2 D_{s,k} \frac{\partial c_{s,k}}{\partial r} \right)$	$\frac{\partial c_{s,k}}{\partial r} \Big _{r=0} = 0, -D_{s,k} \frac{\partial c_{s,k}}{\partial r} \Big _{r=R_k} = \frac{J_k}{a_k F}$
Charge conservation [9]	$\frac{\partial}{\partial x} \left( \sigma_{s,k} \frac{\partial \phi_{s,k}}{\partial x} \right) = J_{k(x,y,z,t)}$	$\begin{aligned} -\sigma_{s,n} \frac{\partial \phi_{s,n}}{\partial x} \Big _{x=0} &= -\sigma_{s,p} \frac{\partial \phi_{s,p}}{\partial x} \Big _{x=L} = i_{app} \\ -\sigma_{s,n} \frac{\partial \phi_{s,n}}{\partial x} \Big _{x=L_n} &= -\sigma_{s,p} \frac{\partial \phi_{s,p}}{\partial x} \Big _{x=L-L_p} = 0 \end{aligned}$
<b>Electrolyte</b>		
Mass conservation [10]	$\varepsilon_k \frac{\partial c_{e,k}}{\partial t} = \frac{\partial}{\partial x} \left( \varepsilon_k^b D_e \frac{\partial c_{e,k}}{\partial x} \right) + (1 - t^+) \frac{J_k}{F}$	$\frac{\partial c_{e,n}}{\partial x} \Big _{x=0} = \frac{\partial c_{e,p}}{\partial x} \Big _{x=L} = 0$
Charge conservation [11]	$\frac{\partial}{\partial x} \left( \varepsilon_k^b \sigma_{e,k} \left( \frac{\partial \phi_{e,k}}{\partial x} - \frac{2(1-t^+)RT}{F} \frac{\partial \log c_{e,k}}{\partial x} \right) \right) = -J_k$	$\frac{\partial \phi_{e,n}}{\partial x} \Big _{x=0} = \frac{\partial \phi_{e,p}}{\partial x} \Big _{x=L} = 0$
<b>Reaction kinetics</b>		
Butler-Volmer [12]	$J_k = \begin{cases} a_k j_{0,k} \sinh \left( \frac{1}{2} \frac{RT}{F} \eta_k \right), & k \in \{n,p\}, \\ 0, & k = s. \end{cases}$	
Exchange current [13]	$j_{0,k} = k_k \sqrt{c_{e,k} c_{s,k} (c_{s,k}^{\max} - c_{s,k})} \Big _{r=R_k}$	
Overpotential [14]	$\eta_k = \phi_{s,k} - \phi_{e,k} - U_k \left( c_{s,k} \Big _{r=R_k} \right), \quad k \in \{n,p\}$	
<b>Initial conditions</b>		
Initial conditions [15]	$c_{s,k} = c_{k0}, c_{e,k} = c_{e0}$	
<b>Terminal voltage</b>		
Terminal voltage [16]	$V = \phi_{e,p} \Big _{x=L} - \phi_{e,n} \Big _{x=0}$	

In the DFN model, alongside key variables like  $c_s$ ,  $c_e$ ,  $\phi_s$ , and  $\phi_e$ , the radial position  $r$  is crucial for lithium-ion diffusion in active material particles. Solid-phase diffusivity ( $D_{s,k}$ ) is the transport of lithium ions within the electrode particles, it directly affects the rate at which ions can move through the electrode material, featured in Equation [8]. Boundary conditions at  $r=0$  and  $r=R_k$  define ion movement limits. The current density  $J_k$  links electrochemical reactions with transport phenomena, features in both mass and charge conservation equations (Equations [8], [9], and [10]). The exchange current density ( $j_{0,k}$ ) and overpotential  $\eta_k$  detail the reaction kinetics, are specified in Equations [13] and [14], respectively. The transference number ( $t^+$ ), indicating the share of total current by the ion, plays a role in the electrolyte charge conservation equation (Equation [11]). Porosity ( $\varepsilon_k$ ) impacts electrolyte transport, addressed in Equation [10], while conductivity ( $\sigma_{s,k}$  for solids and  $\sigma_{e,k}$  for the electrolyte) is essential for charge conservation, appearing in Equations [9] and [11].<sup>5</sup>

The assumptions underlying the DFN model are critical for its application and interpretation:

- **Pseudo Two-Dimensional Geometry:** one-dimensional representation of spherical active material particles within the electrodes with a one-dimensional plane across the electrodes. This assumption simplifies the complex three-dimensional structure of a battery, directly impacting the interpretation of mass and charge transfer processes as described by Equations [8] and [9] for mass and charge conservation in the electrodes.
- **Spherical Active Material Particles:** the active material particles are spherical (relevant to Equation [8]), simplifying the diffusion process of lithium ions into a radial problem. This assumption is crucial for applying Fick's law of diffusion to model the solid-phase lithium-ion concentration ( $c_s$ ) and its change over time and space.
- **Unidirectional Mass and Charge Transfer:** that mass and charge transfer processes are unidirectional along the r-axis for lithium intercalation and across the cell layers (x-axis), as indicated in Equations [8] and [9] for mass conservation and charge conservation, respectively.
- **Homogeneous Phase Properties:** homogeneous distributions within each phase (solid and liquid), facilitating the use of Ohm's law and the Stefan-Maxwell equations to describe charge conservation (Equation [9] for the solid phase and Equation [11] for the electrolyte). This assumption enables the model to treat properties like conductivity ( $\sigma_{s,k}$ ) and diffusivity ( $D_e$ ) as constants over each domain, simplifying the calculations of  $\phi_s$  and  $\phi_e$ .
- **Butler-Volmer Reaction Kinetics:** The electrochemical reactions at the electrode-electrolyte interfaces are modelled using the Butler-Volmer equation (Equation [12]), with the assumption that the exchange current density ( $j_{0,k}$ ) can be represented by straightforward expressions relating to the concentrations of lithium in the solid ( $c_s$ ) and liquid ( $c_e$ ) phases.

The simplifications are designed to make complex battery behaviours computationally manageable while capturing the essential physics.

### Parameterisation

Physical models' ability to estimate the internal states of a battery makes them a powerful tool for design and understanding, leading to these models to become widely used in the research community to predict ageing through physical mechanisms, optimise fast charging protocols by mitigating lithium plating, and to enhance battery design by studying structure-property relationships.<sup>19,50,58</sup> The DFN model requires over 30 parameters that describe the physical, chemical, and electrochemical properties of a battery, Chapter 4 outlines the methods and results for the parameterisation of this model. Different parameters need to be evaluated for the extension of this model to include thermal and ageing behaviours, these are described in Chapters 5 and 6.

Battery technology is changing quickly, and new cell chemistries and formats are commercialised each year. This means that, to solve industrial and academic research questions relevant to state-of-the-art technologies, parameter sets must be made available at a similar pace. This has led to recent research that specifically focus on parameterising automotive batteries.<sup>59,60</sup> Because battery materials and components are unique to each cell they are non-translatable to different models, changes in microstructure or chemical composition significantly affect the performance.<sup>61</sup> Ecker *et al.* developed the first complete physics-based model parameterisation methodology, this paper details the determination of parameters necessary to fully parameterize a physico-chemical model for a 7.5 Ah cell produced by Kokam, comparing these parameters with existing literature, and outlining the procedures for their measurement, including porosity, particle radius, and electrode tortuosity through mercury-porosimetry, as well as electrolyte conductivity and electrode charge transfer kinetics. It introduces a physico-chemical model and validates the measured parameter set by comparing model predictions with experimental results, underscoring the importance of accurate parameterization in understanding battery internal states.<sup>61</sup> There have been subsequent investigations that have adapted the methodology to include new cell formats and techniques.<sup>62,63</sup> However, the model was only parametrised and validated at room temperature limiting its practical use. To be accurate electrochemical models need the parameters to depend on temperature as the temperature of a battery changes during operation.

For emerging battery chemistries including lithium-sulphur, lithium metal, and sodium-ion, physics-based parameter sets are extremely rare.<sup>36</sup> The development of these battery technologies have been primarily by lab-based experiments and physical prototyping, whereas models can be used to reduce cost and timelines to commercialisation. There is a significant disconnect between the performance of novel chemistries in academia and industry, but the modelling research community has made significant contributions by contributing to the understanding and prediction of battery technologies.<sup>26</sup>

Another limitation in parameterisation research is the accuracy of measured parameter values. There is often disagreement between simulated and experimentally-measured data, model predictions are significantly reliant on the accuracy of these values. These inaccuracies often come from intrinsic error in all experimental techniques, but also the fact that physics-based models also have their own assumptions to be consistent with parameterisation techniques or to reduce the complexity of the model itself.

Understanding the assumptions and limitations of physics-based models and their parameterisation is important in their application. Wang *et al.* provided an extensive review of DFN model parameterization to prevent researchers from using parameter values or techniques inconsistent with the intended operating conditions.<sup>64</sup> Not all parameters hold equal importance; each contributes differently to the sensitivity of model predictions. The electrolyte is not considered a highly sensitive parameter in the model primarily because its variations have a comparatively minor effect on the key

performance indicators of a battery, such as capacity and power output. While the electrolyte plays a crucial role in ion transport between electrodes, the predictions are often more significantly influenced by parameters related to electrode materials and design. This is because the electrode characteristics directly affect the electrochemical reactions, making them more critical to model accuracy and performance. Other parameters have to be manually optimised to provide reasonable predictions in the model,<sup>1</sup> Tuning refers to the process of optimising the measured parameter values into ones that provide better agreement with the experimental data. Electrolyte characterisation is often not directly included in the parameterisation workflow due the low sensitivity of the parameters to the model and difficulty extracting electrolyte.<sup>59</sup>

### Data Availability

Data availability has been a focus within academic research, a theme especially relevant to the physics-based modelling research community. Modelling research groups often do not have the experimental expertise to obtain the necessary parameterisation and validation data. Finding parameter values in literature is difficult and time-consuming, often these parameter values are not outlined in the correct format or for a complete cell. This has led researchers to publish parameters values and validation data in repositories for specific cells. There have been significant efforts to reduce the time of finding relevant parameters: for example, LiionDB, created by Wang et al. is an interactive database of DFN-type battery model parameters that makes it easier to find this information.<sup>5</sup> LiionDB contains information relating to the electrode, electrolyte, and separator properties. Other efforts including BatteryArchive contain ageing data for different cell chemistries being tested under a variety of operational conditions that can be used as validation data for ageing models.

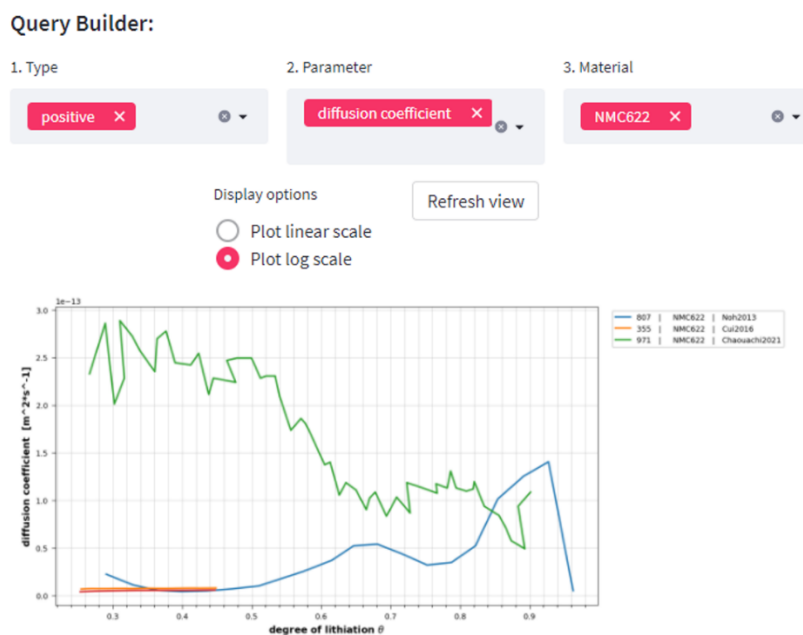


Figure 9. ‘LiionDB’ is a parameter database that captures the physical and electrochemical properties of various materials and cells published in literature.



Developing parameterisation methodologies is motivated by the need to improve model robustness and reliability. Recent developments include capturing volume expansion or microstructural inhomogeneities in active materials, using a reference electrode to eliminate the over-potentials caused by lithium metal counter electrodes (three-electrode testing), and machine learning algorithms to find suitable parameter values from voltage-current data.<sup>65</sup>

These approaches improve the prediction of the thermodynamics and kinetics of a battery, describing properties such as the solid-phase diffusivity, exchange current density, and open-circuit voltage. These properties have to be accurately and efficiently captured in parameterisation methodologies; recent works have provided electrochemical protocols to measure these parameters directly from including galvanostatic intermittent titration technique (GITT).<sup>66</sup> The subsequent chapters of this thesis present improvements to electrochemical protocols used when parameterising in a three-electrode setup. These improvements allow for a more accurate evaluation of the thermodynamic and kinetic properties of a battery. This includes using formation processes to stabilize the materials before conducting electrochemical measurements and mapping the dependency of parameters on lithium concentration.

### Methodologies

Commonly in research, two electrode configurations of batteries are tested, these are known as “half cells” or “full cell”. “Full cells” resemble the composition of a commercial cell and are used in R&D to replicate the behaviour. However, this configuration does not allow the kinetic and thermodynamic behaviour of the individual electrodes to be measured. Using a lithium metal (counter) electrode is an example of a “half cell”, this configuration is used to measure the properties of an electrode of interest (working electrode).<sup>67</sup> This lithium metal electrode replaces one of the porous electrodes that would be present in a traditional battery. This configuration is known as a “half cell”. Half cells allow the deconvolution of individual electrode behaviour to obtain information on thermodynamics and capacity. However, this configuration is not like a commercial cell, for example the lithium supply is not limited. This means the kinetics and degradation mechanisms observed within the cell are completely different from those observed in a full cell using the electrode material.

To address this challenge, a third electrode, known as a “reference electrode,” is employed to isolate and analyse the behaviour of individual electrodes without the constraints of using a lithium counter electrode. The counter electrode serves as the opposite pole to the working electrode during electrochemical reactions, while the reference electrode provides a stable voltage point, enabling precise measurement of the working electrode's behaviour. (Figure 10). This configuration is known as a “three-electrode cell”. The “three-electrode” configuration is like a full cell, but it has a third electrode that can act as an observer (not current carrying) to measure the positive and negative electrode voltages. Reference electrodes can vary considerably in geometry and chemistry depending on the requirements of the experiment.<sup>67</sup> This reduces the issues that make half cells less suitable for measuring rate capability and diffusion coefficients

i.e. reducing the overvoltage measured on each electrode.<sup>65,68</sup> In this set-up the lithium electrode is a ring to ensure geometric stability for better electrochemical stability.<sup>67</sup>

Reference electrodes eliminate the large overvoltage present in a half cell to obtain more accurate thermodynamic information by minimising the intrinsic hysteresis of the cell. In a half cell large hysteresis is often seen due to high resistance of lithium metal. The presence of significant overvoltage, alongside the chemical reactivity of lithium metal and the growth of dendrites, renders the half-cell a poor model for lithium-ion batteries compared to a three-electrode setup. Dendrites are needle-like structures that form on the lithium metal surface during charging, which can lead to short circuits and battery failure.<sup>65</sup>

The challenge of three-electrode testing is attempting to deconvolute the behaviours of the electrodes, the negative electrode often exhibits electrochemical artefacts that make it difficult to analyse. This effect is characterised by a loop appearing on a Nyquist diagram, deviating from the typical semicircular shape. A Nyquist diagram is a graphical representation used in electrochemistry to display the complex impedance of a system, revealing details about its resistive and capacitive behaviour. The loop formation is attributed to impedance distortions arising from geometrical or electrochemical asymmetries, such as electrode misalignment or varying impedance responses between electrodes.<sup>69</sup> Developing methods to reduce the effect of induction loops this issue has been the focus of much research.<sup>70</sup>

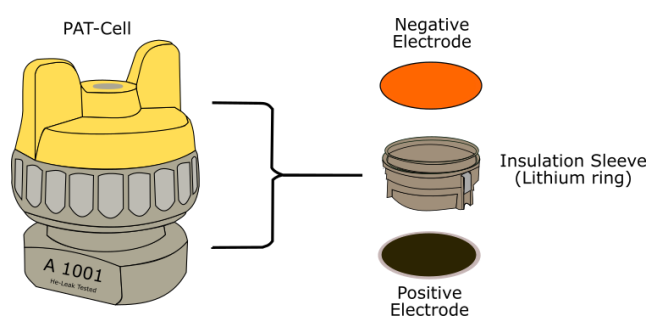


Figure 10. Illustration of a three-electrode set-up, the cell shown is a PAT-Cell (left). The reference electrode is in the insulation sleeve as “lithium ring”.

In battery manufacturing, an important step is the electrochemical process known as formation.<sup>71</sup> This ensures that there is controlled growth of a passivating film on each of the battery electrodes. This film, the solid-state electrolyte interface (SEI), is formed by the electrolyte system reacting with the electrodes. If the SEI is not formed in a controlled way, it limits the lifetime of the battery. The Solid Electrolyte Interphase (SEI) layer should ideally be electronically insulating to prevent electrons from moving through it, while still being ionically conductive to allow lithium ions to pass. However, in practice, the SEI film sometimes permits electron transport. This electron flow can lead to further decomposition of the electrolyte and cause the SEI layer to thicken, which is undesirable as it can affect the battery's performance and longevity. SEI growth is the largest contributor to capacity fade in batteries as the lithium inventory is depleted throughout the life of the battery.

Formation is a critical part of parameterisation and is not always carried out effectively in academic research. This step stabilises the SEI and therefore the thermodynamic and kinetic properties of a battery, if this is excluded from a test protocol, parameters are evaluated when these properties are dynamic. For the post-mortem analysis of commercial cells this step is still important because it reconditions the electrodes to the new electrolyte being used.

Understanding the impact of formation on battery performance is important for next-generation such as sodium-ion batteries, this is because high first cycle loss makes it more difficult to map stoichiometry and calculate the maximum concentrations of the electrodes. The methodologies to evaluate these parameters to consider the irreversible loss of sodium or lithium inventory.

This thesis and related research contribute to the improvement of parameterisation methodologies in four key areas: (i) developing new experimental methodologies, (ii) parameterising new battery chemistries, (iii) providing an understanding into the limitations of the model and parameterisation, and (iv) building repositories for cell parameters and data. Contributions include publishing a parameter set of a high energy 21700 cylindrical cell, the LG M50, considered a state-of-the-art automotive cell. The data for the electrochemical model was made available in PyBaMM and has been used extensively by the research community to model phenomena including the prediction of non-linear ageing, the optimisation of fast charging by understanding lithium plating, and enhancing battery design by studying structure-property relationships.<sup>19,50,58</sup>

## 2.2 Thermal Parameterisation

### Model

The thermal model predicts heat behaviours within a battery system, this is critical to the performance and safety of a battery. This model quantifies how heat is generated, transported, and dissipated in batteries, a process influenced by kinetic and thermodynamic properties. The model includes evaluating the temperature dependence of electrochemical parameters and those relating to heat generation and transport, which are vital since batteries often operate at non-ambient temperatures, generating heat as a by-product of the electrochemical reactions and internal resistance. Temperature influences the capacity, efficiency, self-discharge, and internal resistance of a battery.<sup>72</sup> This thermal dependence is due to the kinetic and thermodynamic properties.<sup>63</sup> Low temperature operation is very important too, state estimation at these temperatures contributes to the inaccuracy of most models, parameterising across a wide range of temperatures is important as electric vehicles operate in extreme climates (below 0 °C and above 60 °C).

The thermal model employs several connected equations: Energy conservation (Equation [17]) is the foundational equation, describing how heat is conducted within the battery and the sum of heat contributions, denoted as  $q_{tot}$  (Equation [18]), which includes reversible heat ( $q_{rev}$ , Equation [19]), linked to entropy change ( $\Delta S$ , Equation [20]), Joule heat ( $q_j$ ) Equation [21]), and reaction heat ( $q_r$ , Equation [22]). These terms account for

the various sources of heat due to electrochemical reactions and resistive losses within the battery. Joule heat, for instance, is particularly relevant as it models heat generated due to the internal resistance, which is crucial at both high and low operating temperatures.

Table 4. The governing equations of the thermal model used in batteries.

Description	Equation
Energy conservation [17]	$\rho C_p \frac{\partial T}{\partial t} = \nabla \cdot (k \nabla T) + q_{tot}$
Total battery heat [18]	$q_{tot} = q_{rev} + q_j + q_r$
Reversible heat [19]	$q_{rev} = \frac{\int_0^{l_n+l_s+l_p} J_k \left( \frac{\partial U}{\partial T} \right) dx}{l}$
Entropy change [20]	$\Delta S = nF \frac{\partial U}{\partial T}$
Joule heat [21]	$q_j = \frac{\int_0^{l_n+l_s+l_p} \left[ \sigma_{eff} \left( \frac{\partial \phi_s}{\partial x} \right)^2 + k_{eff} \left( \frac{\partial \phi_e}{\partial x} \right)^2 + \frac{2k_{eff}RT}{F} (1 - t_+^0) \frac{\partial(\ln c_e)}{\partial x} \frac{\partial \phi_e}{\partial x} \right] dx}{l}$
Reaction heat [22]	$q_r = \frac{\int_0^{l_n+l_s+l_p} J_k (\phi_s - \phi_e - U) dx}{l}$
Convection boundary condition [23]	$-k \frac{\partial T}{\partial n} = h(T - T_{amb})$

For the thermal model, the assumptions are:

- **Homogeneous Material Properties:** uniform material properties like thermal conductivity ( $\sigma_k$ ) across the battery.
- **Constant Surface Heat Transfer Coefficient:** the surface heat transfer coefficient ( $h$ ) is assumed constant, as seen in the convection boundary condition (Equation [23]).
- **Uniform Temperature Gradient:** a uniform temperature gradient along the battery, relevant for the conduction term in Equation [17].
- **Electrochemical Parameter Stability:** electrochemical parameters remain stable across the operational temperature range.
- **Isotropic Heat Generation:** heat generation within the battery is assumed to be isotropic, simplifying the heat generation terms in Equations [19], [22], and [[22].

The thermal model is coupled with the DFN model to extend its capabilities in capturing heat generation ( $q_{tot}$ ) and heat transport mechanisms. This coupling is critical for a more comprehensive simulation of battery behaviour, as the DFN model accounts for mass/charge transport that directly affects heat generation through reaction heat ( $q_r$ ) and Joule heating ( $q_j$ ), with parameters measured across a range of temperatures to ensure accuracy for electric vehicles operating in extreme climates. The equations that describe these processes are summarised in Table 4. These equations involve new

parameters that need to be measured, these are outlined in Table 2, requiring different technologies and methodologies to be developed.

Three main limitations in the accuracy and robustness of existing thermal models in literature are: (i) temperature dependence of electrochemical parameters, (ii) measuring parameters needed to predict heat generation and transport within a battery pack, and (iii) measuring thermal properties at component level rather than cell level. To effectively expand predictions to include new models discussed in literature, it is essential to incorporate certain key parameters that are frequently overlooked. These include internal cell anatomy, which details the structural and material composition within the cell, and thermal conductivity, which is crucial for understanding how heat is distributed and managed within the cell. These parameters are vital for a comprehensive understanding of the model's behaviour under various conditions:

- 0D Thermal: Focuses on basic thermal properties without spatial differentiation, including activation energy, entropic terms, and overall heat capacity of the system.
- 1D Thermal: Extends to linear spatial variation, incorporating thermal conductivity, specific heat capacities, and characteristics specific to 1D cell geometry alongside the basic thermal parameters.
- 2D Thermal: Involves two-dimensional spatial variation, accounting for 2D cell geometry while integrating the previously mentioned thermal parameters.
- 3D Thermal: Encompasses three-dimensional spatial variation, considering 3D cell geometry, positions of electrical tabs, internal structure, and all thermal parameters.

High accuracy thermal models require the heat generation and transport properties to be mapped completely. Thermal models always account for the irreversible heat generation caused by current flow and resistance within the cell; however, reversible heat generation is often not included.<sup>63</sup> Reversible heat generation is described by the entropic term and involves energy being produced from material phase changes, this term is particularly important at low currents. At low currents, the reversible heat generated can be on the order of milliwatts or even lower, while the irreversible heat due to factors like internal resistance may range from several milliwatts to watts, depending on the specific battery technology and conditions.<sup>73</sup> The exact magnitudes can vary widely based on the battery type, size, and operational parameters. Heat capacity and thermal conductivity are important too.

### Parameterisation

Popular electrochemical models used in literature including those by Ecker *et al.* and Schmalstieg *et al.*<sup>61,62</sup> do not capture the temperature dependence of the electrochemical properties. Kinetic parameters including the diffusivity, exchange current, and electrode conductivity are dependent on temperature as higher temperatures make transport more facile, while the thermodynamic open-circuit voltage is also impacted by temperature, the entropic term maps the change in voltage due to temperature.<sup>61,62</sup>

Table 5 summarises the literature for thermal model parameterisation, these papers often miss information that would enable a 3D cell thermal model to be constructed. Parameters relating to a 3D cell thermal model are important for assessing the performance of new cell formats or designing thermal management systems for packs.

Identifying prior literature in Table 5, it is evident that the scope of thermal model parameterisation in existing literature varies significantly. For example, Chen 2020 and Zulke 2021 focus solely on the electrochemical aspects for LG cylindrical 21700 and a 4.8 Ah cylindrical 21700 cells, respectively, providing no thermal modelling parameters beyond the basic level. Similarly, Ecker 2015 discusses a 7.5 Ah Kokam pouch cell but also limits the discussion to electrochemical parameters without venturing into thermal aspects.

In contrast, Schmalstieg 2019 and Liebig 2020 extend their analyses to include 1D thermal modelling for NMC111 graphite prismatic cells, offering a slightly broader perspective on thermal behaviour. Sturm 2019 provides a more comprehensive approach for a 3.35 Ah LG cylindrical 18650 cell, including both electrochemical and 1D thermal parameters, yet stops short of exploring higher-dimensional thermal models.

This work offers a full spectrum of parameterisation across all dimensions, including 0D, 1D, 2D, and 3D thermal models for a 5 Ah LG cylindrical 21700 cell. This comprehensive approach not only bridges the gap left by prior studies but also sets a new standard for thermal model parameterisation, facilitating advanced analysis and design of thermal management systems for battery packs.

Error is often introduced into models as thermal properties such as the specific heat capacity and thermal conductivity are measured at a component level, rather than the cell level.<sup>63</sup> Electrochemical behaviour is described at a cell level, while thermal behaviour is described at a battery level, because heat transport occurs between cells in a larger systems.<sup>3</sup> Specific heat capacity is more accurately measured at cell level as the electrolyte heat retention of each component, while measuring thermal conductivity at the component level ignores the thermal contact resistances between components that impact heat transport.

Table 5. A summary of physics-based model parameterisations of commercial cells in literature.

Paper	Properties		Chemistry	Electrochemical	Thermal			
	Cell Type	Wh/kg		DFN	0D	1D	2D	3D
ORegan2022 <sup>7</sup>	5 Ah LG cylindrical 21700	267	NMC811 graphite -SiO <sub>y</sub>	☑	☑	☑	☑	☑
Chen 2020 <sup>1</sup>	5 Ah LG cylindrical 21700	267	NMC811 graphite -SiO <sub>y</sub>	☑				
Ecker 2015 <sup>74</sup>	7.5 Ah Kokam pouch	173	NMC111 Gr	☑				
Schmalstieg 2018 <sup>62</sup>	28 Ah prismatic	-	NMC111 graphite	☑	☑			
Liebig 2019 <sup>63</sup>	40 Ah prismatic	-	NMC111 graphite	☑	☑			
Sturm 2019 <sup>75</sup>	3.35 Ah LG cylindrical 18650	211	NMC811 graphite -SiO <sub>y</sub>	☑	☑			
Zulke 2021 <sup>76</sup>	4.8 Ah cylindrical 21700	256	NCA graphite -SiO <sub>y</sub>	☑				

This thesis outlines a parameterisation workflow to capture temperature dependency with the information needed to construct a 3D thermal-electrochemical model of the cylindrical cell. This is the first parameterisation of a commercial cell that can be used to model the 3D behaviour of a cell. The heat transport properties of the electrodes and separator are also evaluated so that temperature gradients within the cell can be predicted—important for understanding the trade-offs of larger format cell designs. Temperature is important to predict battery behaviour in the order of minutes but also over months, it is the main contributor to ageing and has significant impact on the severity of degradation mechanisms.<sup>47</sup> Understanding the interplay between the electrochemical, thermal, and ageing properties provides insight into how the entire battery lifecycle can be improved, from design to operation.

## 2.3 Degradation Parameterisation

The performance of batteries worsens over their lifetime due to ageing. Ageing limits the usable lifetime of a battery, and it also impacts the thermal and electrochemical properties. There are four main degradation mechanisms that contribute to ageing: (i) lithium plating, (ii) particle cracking, (iii) SEI growth, and (iv) loss of active material.

There are several papers that discuss various mechanisms that contribute to the ageing of lithium-ion batteries. Many papers discuss different mechanisms, this includes Campbell *et al.* describe lithium plating and Jin *et al.* list paper on SEI growth.<sup>77,78</sup> These mechanisms can be modelled using the equation described in each paper to predict the capacity and power fade in a battery. However, it can be difficult to directly measure the parameters required for these equations, such as the plating exchange current density and reduction potential, diffusion coefficient, and reaction rate for electrolyte degradation, these parameters are listed in Table 6.

As described in previous sections, electrochemical methods have been extensively developed for physics-based models to capture charge, mass, and heat transport.<sup>1,61,79</sup> However, creating degradation models is more difficult as the physical parameters relate to hard to measure reactions including lithium plating and electrolyte decomposition reactions. For commercial cells it is difficult to parameterise lithium plating kinetics and the electrolyte decomposition reaction as the composition is unknown. Often these parameters can be identified by using literature values or optimisation techniques.<sup>47</sup> Electrochemical tests are often used to quantify these processes and help construct degradation models as they are able to probe the chemical processes that contribute to battery ageing. Solid electrolyte interface growth (SEI) can be quantified using electrochemical impedance spectroscopy or hybrid pulse power characterisation to monitor the resistance changes due to solid electrolyte interface growth, although this method is limited because it cannot quantify solid electrolyte interface growth without knowledge of its composition. The solid electrolyte interface is a thin layer that forms on the electrode surface in a battery, acting as a barrier that regulates ion flow while preventing direct contact between the electrode and the electrolyte..<sup>80</sup> Lithium plating/stripping can be detected by using differential voltage analysis and to estimate the irreversible loss of lithium inventory (LLI) owing to plating.<sup>77</sup> Methodology development for evaluating battery degradation using post-mortem, operando techniques, and large ageing datasets have been a focus of research.

Large DOE (design of experiment) studies are often used to develop degradation models and understand the connection between environmental factors and ageing. Previous research includes a study using sixty large capacity pouch cells, then testing them under five different conditions to develop an empirical model to predict battery lifetime.<sup>81</sup> DOE studies are resource-intensive, leading researchers to develop accelerated ageing characterisation to reproduce realistic automotive cell aging in a short time.<sup>82</sup> Studying changes in the voltage behaviour of batteries is also an important tool for constructing degradation models. Analysis of the OCV and its change due to aging allows the identification of aging mechanisms, including loss of mobile ions or loss of active material.<sup>83</sup> DVA (differential voltage analysis) can be used to reveal significant differences in the aging behaviour and state of homogeneity of cells that cannot be obtained by solely analysing capacity and power fade. This allows inhomogeneous distributions of lithium to be mapped across large format cells showing local lithium plating.<sup>84</sup> Investigating the ageing of batteries in operando does not provide insight into the property changes of the negative and positive electrode, and more importantly they do not allow accurate decoupling of the individual ageing mechanisms. Post-mortem analysis means dismantling the cell to characterise the internal components. Extracting electrodes whilst ensuring the SEI remains intact from a commercial cell is challenging and requires best practice for accurate analysis of automotive cells.<sup>85</sup>



Table 6. Parameter requirements of the ageing model.

Parameter	Symbol	Units
SEI partial molar volume	$\bar{V}_{SEI}$	$\text{m}^3 \text{mol}^{-1}$
SEI resistivity	$\rho_{SEI}$	$\Omega \text{m}$
Initial SEI thickness	$L_{SEI,0}$	$\text{m}$
Initial crack length	$l_{cr,0}$	$\text{m}$
Initial crack width	$\omega_{cr}$	$\text{m}$
Solvent diffusion activation energy	$E_{sol}$	$\text{m}$

However, for commercially available cells it is very difficult to deconvolute which degradation mechanisms are the primary contributors to battery ageing. To glean this information the disassembly and post-mortem analysis of a cell is required.

Degradation presents a complex challenge in battery modelling, where the electrochemical and thermal performance of a battery significantly depends on its state of health. While characterizing this aspect was beyond the scope of this thesis, it was thoroughly investigated in the accompanying PhD research to support further studies on recycling and battery management systems. This thesis does not directly investigate degradation but offers a methodology to dismantle commercial cells and probe their ageing mechanisms through electrochemical techniques. Post-mortem analysis allows the deconvolution of changes in the thermodynamic and kinetic properties of each electrode. These properties can be spatially resolved across each electrode to observe whether components including the tab locations and the cell geometry influence the ageing of the cells. The electrochemical, thermal, and ageing behaviours of lithium-ion have been mapped extensively over the last three decades to understand battery operation. This knowledge is relevant to but does not completely capture next-generation battery chemistries, presenting a new opportunity to apply parameterisation to improve the understanding of emerging technologies. Degradation models and DOE is now part of a collaborative researcher project that includes the experimental methods, this includes teardown and electrochemical characterisation to provide insight into multi-scale degradation of lithium-ion batteries used in automotive applications.

## 2.4 Next-Generation Chemistry Parameterisation

There has been little research into physics-based modelling of sodium-ion battery materials, despite simulation tools being useful for cell design and manufacturing. The lack of literature in this area can be attributed to the availability of parameter sets for sodium-ion materials. Previously, parameters relevant to physics-based models have been outlined for sodium-ion electrolytes and for a half cell configuration.<sup>86,87</sup> However, until 2022 no parameter sets for a physics-based model had been outlined for a complete sodium-ion system.

A physics-based model of a complete sodium-ion system would highlight whether the DFN model is applicable, or if the governing equations need to be changed to consider new electrochemical effects such as sodium plating within hard carbon. Chayambuka *et al.* outlined the first physics-based model parameterisation for a complete sodium-ion system.<sup>88,89</sup> The battery comprised of a  $\text{Na}_3\text{V}_2(\text{PO}_4)_2\text{F}_3$  (NVPF) cathode and a hard carbon

anode, the parameterisation helped identify the diffusion mass transport limitations and ohmic losses for these materials. This work demonstrated that a DFN model could be used to provide good agreement to experimental and simulated data with no modification to the governing equations.

The availability of parameter sets is crucial for the development of sodium-ion batteries, as models enable the study of various cell designs. Different cell designs necessitate distinct studies because they exhibit significantly different performance characteristics and parameters, underlining the importance of tailored approaches in battery research and development. Research into systems using different cathodes is needed, Chayambuka *et al.* studied an NVPF cathode. This material has two characteristic voltage plateaus, exhibiting a similar behaviour to LFP.<sup>88</sup> However, the low energy density and the voltage response making it difficult to estimate state-of-charge, means the material is less favourable for use in automotive applications.

This thesis outlines the first parameter set for a commercially relevant sodium-ion system, using a layered oxide cathode,  $\text{Na}[\text{Ni}_{1/2}\text{Mn}_{1/4}\text{Sn}_{1/8}\text{Ti}_{1/8}]\text{O}_2$  (NMST2488). The data has been made publicly available in PyBaMM, being the first complete sodium-ion DFN model on the platform. The research introduces a methodology that is slightly adapted from Chen *et al.*, serving as a template. It demonstrates that these techniques can be applied agnostically, meaning they are independent of the battery's chemistry.<sup>1</sup> The model is then used to understand the kinetic limitation of the materials by simulating the IR drops and equilibrium potentials in the sodium electrodes, the insight can be used to inform cell design for fast charging,

## 2.5 Summary

In conclusion, the battery parameterization methods discussed in this literature review have focused on a variety of approaches that cover the electrochemical, thermal, and degradation behaviours of the battery. The literature reviewed provides context for the practical and theoretical improvements needed in parameterisation to improve the accuracy and application of battery models.

## Chapter 3 Methods

This section outlines the details and theory of methods that are common throughout several chapters. These techniques are used to evaluate the parameters that relate to the various properties of a battery, specifically the disassembly of cells for subsequent physical, electrochemical, and thermal characterisation.

### 3.1 Teardown

Teardown is used within Chapters 4 and 5 to extract components for characterisation from a cylindrical battery. To characterise the individual components within a cell, disassembly and post-mortem analysis is required (Figure 11). To ensure safe disassembly, cells must be discharged to 0% state of charge (SOC), for lithium-ion batteries this is often 2.5 V.<sup>90</sup> Cells are then disassembled in a glovebox under an argon atmosphere to prevent chemical changes occurring in the presence of moisture and oxygen. The double-sided electrodes are then removed from the cell, with one side removed for electrochemical testing. These electrodes can now be built in electrochemical test cells.

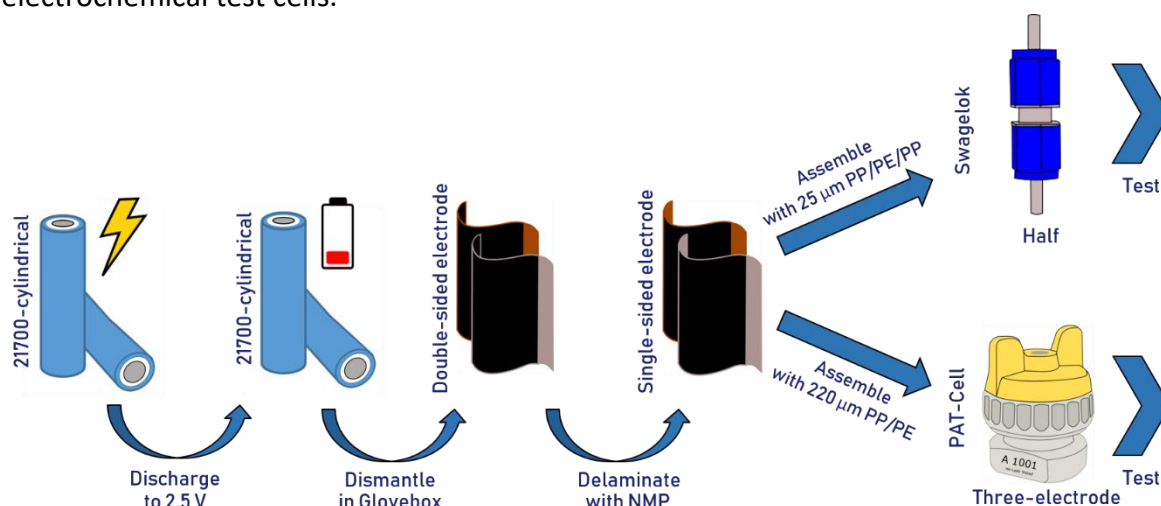


Figure 11. Teardown procedure of a discharged LGM50, to illustrate delamination of one side of the electrode coating for electrochemical testing in two- and three-electrode formats.

## 3.2 Physical Characterisation

### Scanning Electron Microscopy (SEM)

Scanning Electron Microscopy (SEM) is used to analyse particle size and morphology of materials in Chapters 4 and 6 for both lithium-ion and sodium-ion materials. SEM uses an electron beam to scan a sample, these electrons interact with atoms on the sample surface. Secondary electrons are emitted by the atoms excited by the electron beam, these electrons are ejected from the K-shell of the atom by inelastic scattering. A machine detects tiny electric signals from different spots on a sample. These signals are used to understand the sample's appearance and composition, creating a picture where different colours represent the strength of the electric signals at each spot. This method reveals details of the sample's surface and its elements. X-rays from the sample identify precisely what elements make up the battery parts, by observing how the sample responds to the X-rays.

### X-ray Diffraction (XRD)

X-ray diffraction (XRD) is used to characterise the crystallinity and phases of battery active materials of a sodium-ion material in Chapter 7. A diffractometer produces X-rays at a fixed wavelength, this wavelength is determined by the radiation source e.g. Cu-K $\alpha$ . Crystalline materials have repeating units of atoms with an atomic spacing close to the wavelength of X-rays, this allows the crystal lattice to act like a diffraction grating. When the atoms diffract incident X-rays, constructive interference occurs at specific angles depending on the distance between the atoms. This appears as a peak and represents a certain lattice plane that can be characterised by a Miller index. The diffraction from a specific lattice plane in different crystallites lies on a cone with a specific Bragg angle, characterised by  $2\theta$ .<sup>91</sup> A diffractometer measures the intensities of these cones as a function of  $2\theta$ . Because the wavelength of the radiation and the incident and reflected angles are known, the interatomic spacings ( $d_{hkl}$ ) can be calculated according to Bragg's Law:

$$\frac{n\lambda}{2d} = \sin \theta \quad [24]$$

where  $n$  is the number of reflections,  $\lambda$  is the wavelength of the incident X-ray beam,  $d$  is the distance between near atomic planes, and  $\theta$  is half the diffracted angle (Figure 12).

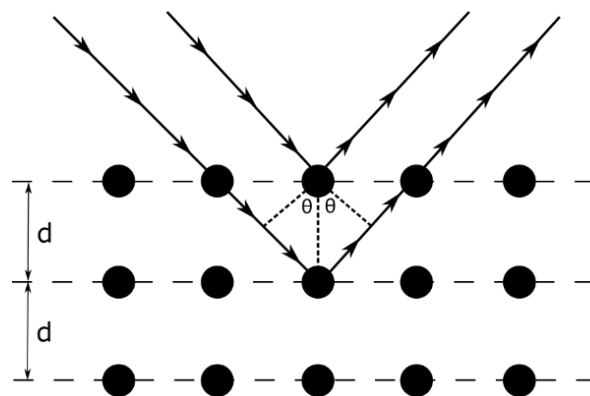


Figure 12. Bragg diffraction: X-rays of the same wavelength and phase are scattered off the atoms in a crystalline material. The lower beam travels a length of  $2d \sin \theta$  further.

The principle of Powder X-ray Diffraction (XRD) hinges on the assumption of a randomly distributed sample, meaning adequate quantity of each crystal structure plane will be suitably aligned for X-ray diffraction. However, occasionally in practical scenarios, sample rotation is required to counteract texturing and achieve sample randomness.

Furthermore, the locations (which reflect lattice distances) and the comparative intensity of the lines in a diffraction pattern serve as markers for a particular phase and substance. Information on the morphology of the material can also be elucidated; the width of diffraction lines can be attributed to the distribution of crystallite size because of a phenomenon known as Scherrer broadening.<sup>92</sup> The Scherrer equation can be used to calculate the crystallite domain size of a material:

$$D = \frac{K\lambda}{B \cos \theta} \quad [25]$$

where  $D$  is the domain size,  $K$  is the shape factor, and  $B$  is the line broadening at full width half maximum (FWHM). This FWHM can be evaluated by Rietveld refinement. The shape factor considers the crystallite domain shape. A spherical crystallite ( $K = 0.9$ ) is often assumed for convenience, calculating the exact domain shape is difficult.

### 3.3 Electrochemical Characterisation

#### Galvanostatic Cycling

Galvanostatic cycling is the main method to test battery performance, this was used in Chapter 4, 5 and 6 to probe the electrochemical properties of cells and materials. It can be used to measure properties such as columbic efficiency and capacity of materials. Galvanostatic cycling involves applying a constant current to the battery to observe how it charges and discharges, providing insights into its efficiency and how much charge it can hold. Battery cycling protocols often contain two different current regimes: constant current (CC) and constant voltage (CV). These terms are self-identifying, constant current refers to the application of a fixed current (allowing voltage to change) and constant voltage refers to fixing the potential (allowing the current to change). The CV step is characterised by the decay of current, this voltage is held until the current decays beyond

a pre-determined limit. CC and CV steps are used in combination to improve battery performance and safety while charging (Figure 13).

Applying both CC and CV steps during charging allows constant current to be applied, and then when the voltage reaches its upper limit (a constraint imposed by the electrolyte voltage limit and safety precaution) a CV step can be used to hold the potential and continually delithiate the positive electrode in order to attain a higher battery SoC than would otherwise be achieved if a CC step was used exclusively. If only a CC step was used it would require the selection of a very low current to ensure that when the upper voltage limit is reached most of the lithium has been removed from the cathode. The C-rate represents the measure of current related to the time required to charge or discharge a battery. For instance, a 1C rate for a 5 Ah battery implies a discharge current of 5 A over 1 hour, while a C/20 rate indicates a discharge current of 0.25 A over 20 hours. On the other hand, if only a CV step was used (i.e. a single potential step) this would result in too much current flow and cause irreversible damage to the battery due to the heat generated.<sup>93</sup> The CC-CV regime could be applied during battery discharge but it would not serve practical purpose, the output power during the CV step could not be controlled (due to the decaying current), additionally a fully discharged battery could cause irreversible damage to the negative electrode due to copper dissolution at high potentials.<sup>90</sup> A CV hold is employed during the charging of batteries to regulate and limit the voltage applied, preventing overcharging and associated safety risks. During discharging, such voltage control is not needed, as the goal is to extract energy from the battery rather than add it.

### Potentiostatic Cycling

In electrochemical testing, potentiostatic cycling is used to investigate the performance and behaviour of batteries and other electrochemical systems. Unlike galvanostatic cycling, which focuses on maintaining a constant current, potentiostatic cycling revolves around maintaining a constant voltage while allowing the current to vary accordingly.<sup>94</sup> This technique is particularly useful for examining the charge or discharge characteristics of a battery, as it provides insights into the stability and efficiency of the electrode materials under constant voltage conditions. It helps in understanding how the electrode materials interact with the electrolyte and react to prolonged voltage exposure.

A potentiostatic technique that is widely employed in battery research is cyclic voltammetry. This technique involves sweeping the potential of a working electrode in a cyclic manner, allowing analysis of the redox reactions occurring within the battery. This method is essential for understanding the electrochemical properties of battery materials, such as their oxidation and reduction potentials, reaction kinetics, and the reversibility of electrochemical processes. It can be used to evaluate the capacity, stability, and efficiency of new electrode materials.

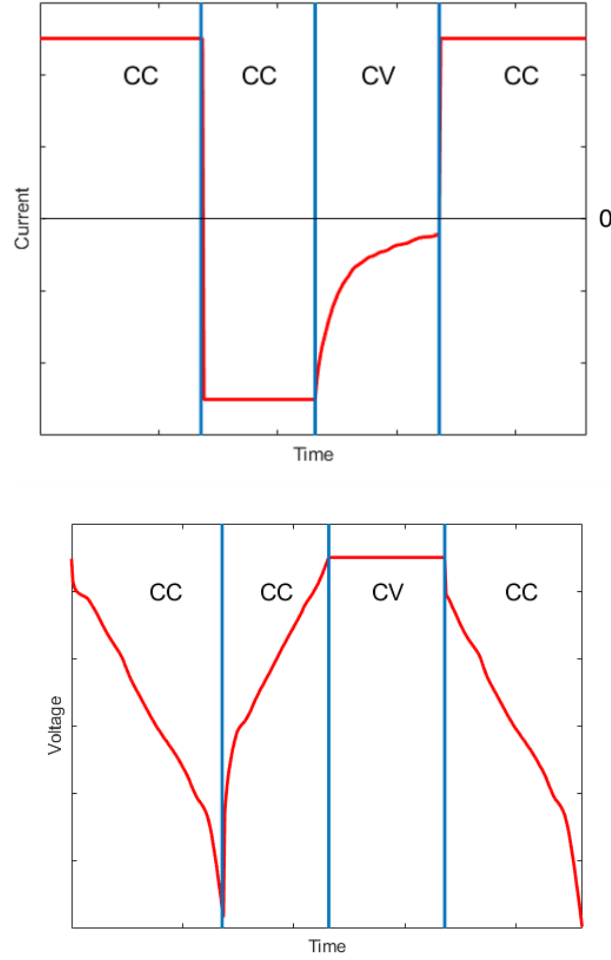


Figure 13. Current input (top) and voltage output (bottom), with CC discharge steps and a CC-CV charge step (bottom). The CC-CV charging step is a compromise between charge time and degradation caused by ohmic heating.

#### Four-point Probe Measurement

The four-point probe technique allows the electronic transport properties of electrodes to be measured.<sup>95</sup> To measure electronic transport properties in battery electrodes using the four-point probe technique, the current collector must be removed. This is because the current collector, typically made of conductive materials like copper or aluminium, significantly affects electrical conductivity measurements, making it difficult to isolate the electrode material's intrinsic properties. The four-point probe applies a current to the two outer probes and measures the voltage drop between the two inner probes (Figure 14). This eliminates the contact and wire resistances compared to two-point probe measurements. The four-point probe enables the resistivity of an electrode to be calculated using the following relationship:

$$\rho = \frac{\pi L}{\ln 2} \left( \frac{V}{I} \right) \quad [26]$$

Here  $\rho$  is the resistivity,  $L$  is the electrode coating thickness,  $I$  is the applied current, and  $V$  is the measured voltage during this technique. The electronic conductivity  $\sigma$  can then be calculated as the inverse of the resistivity:

$$\sigma = \frac{1}{\rho} \quad [27]$$

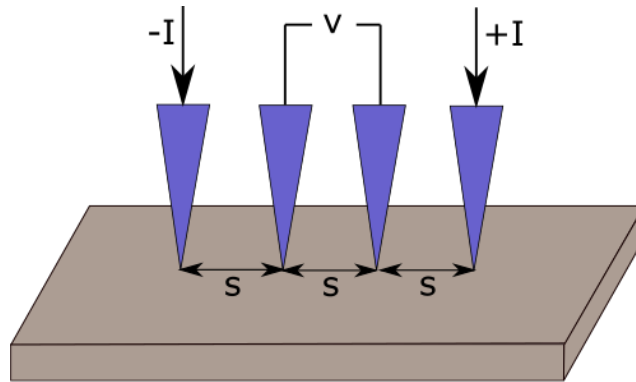


Figure 14. Illustration of probe positions for measuring the electronic properties of an electrode.

#### Electrochemical Impedance Spectroscopy (EIS)

Electrochemical impedance spectroscopy (EIS) is used to evaluate cell performance, characterise degradation, or to parametrise models.<sup>96</sup> This technique was used in Chapters 4, 5 and 6 to measure the kinetics and related activation energies of different materials. The electrical resistances within a battery can be measured by applying an alternating potential and measuring the current response in the cell. This sinusoidal excitation has its frequency swept across a predetermined range to produce a corresponding alternating current (AC) signal (Figure 10). The response in a battery is not always linear i.e. the current output is also a sinusoidal signal with the same frequency as the input. It is possible to choose an excitation signal with a small enough potential (amplitude <10 mV) to ensure the cells response is linear and can be easily analysed. This type of system is referred to as pseudo-linear.



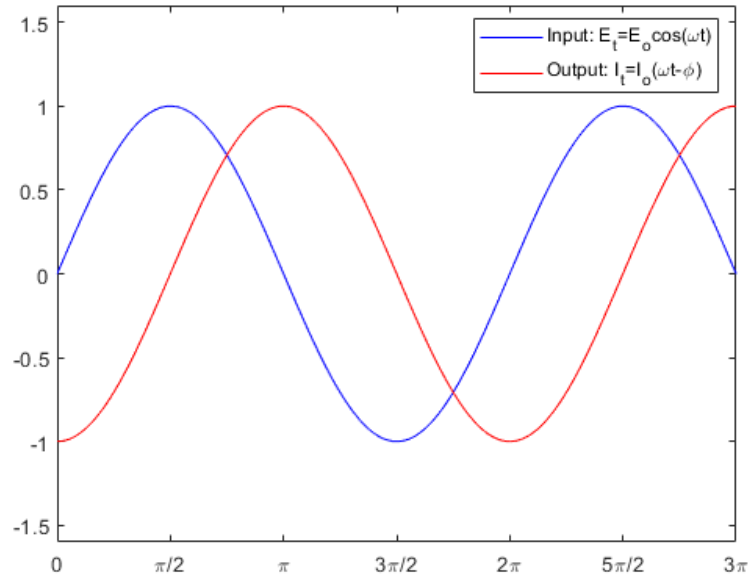


Figure 15. Current response  $I_t$  from an excitation signal  $E_t$  in a linear system.

The excitation signal, expressed as a function of time has the

$$E_t = E_0 \sin(\omega t). \quad [28]$$

Here  $E_t$  is the potential as a function of time  $t$ ,  $E_0$  is the amplitude of the signal, and  $\omega$  ( $2\pi f$ ) is the radial frequency. In a linear system, the response signal,  $I_t$ , is shifted in phase ( $\phi$ ) and has a different amplitude than  $I_0$ :

$$I_t = I_0 \sin(\omega t + \phi). \quad [29]$$

An expression analogous to Ohm's Law allows the calculation of the impedance of the system as:

$$Z = \frac{E_t}{I_t} = \frac{E_0 \sin(\omega t)}{I_0 \sin(\omega t + \phi)} = Z_0 \frac{\sin(\omega t)}{\sin(\omega t + \phi)} \quad [30]$$

With Euler's formula, it is possible to express the impedance as a complex function,  $Z(\omega)$ . This expression has real and imaginary components. Plotting the imaginary vs the real components construct a Nyquist plot (Figure 16). Analysis of the Nyquist plot enables deconvolution of the components that contribute to resistance within a cell: (i) ohmic, (ii) SEI, (iii) charge transfer, and (iv) diffusion. These components are probed by different frequencies depending on the time constants of these processes. These phenomena

resistances and capacitances of these phenomena can be evaluated by fitting the data to an equivalent circuit model (ECM).

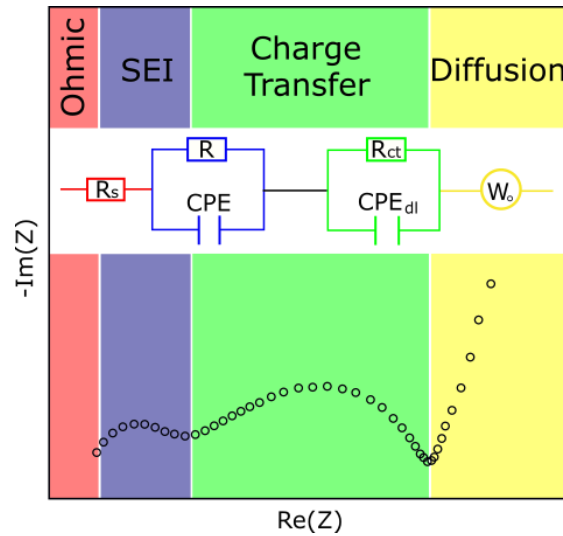


Figure 16. Nyquist plot illustrating the characteristic series resistance, two semi-circles, and diffusion-limited response at low frequency. These phenomena can be modelled as equivalent circuit elements such as resistors, CPEs and Warburg. These processes have different time constants and the ohmic and SEI are instantaneous processes, whereas charge transfer and diffusion occur over longer durations.

The electrochemical response of a battery can be described by as circuit elements such as resistors and constant phase elements. The constant phase element (CPE) is an imperfect capacitor that models the behaviour of the electrode double layer. By building a circuit model using these elements it is possible to determine:

- $R_s$ , the ohmic resistance models the voltage drop across the electrolyte.
- $R_{ct}$ , the charge transfer resistance models the voltage drop over the electrode-electrolyte interface.
- $C_{dl}$ , the double-layer capacitance models the effect of charges building up in the electrolyte at the surface.
- $W_o$ , the Warburg impedance models diffusion of lithium ions in the electrodes.

EIS data can also be linearized when integrated into the Doyle-Fuller-Newman (DFN) battery model, simplifying the impedance data for modelling purposes.<sup>97</sup> EIS primarily operates in the frequency domain with small amplitude voltage perturbations, and while time-domain modelling is, it is less common. In the DFN model, the Solid-Electrolyte Interphase (SEI) is treated as a passivation layer, affecting ion transport. Changes in SEI properties over cycling can be accounted for in the DFN model to simulate its evolving impact on battery performance. To develop a detailed model for predictive simulations, linearization may be preferable. However, for quick insights and characterizations, Nyquist plot analysis is a valuable tool.

### Differential Capacity Analysis

Differential capacity analysis (or DCA, or  $dQ/dV$ ) is a technique used in Chapter 4 to characterise materials and understand phase changes. This technique was pioneered by DuBarry *et al.* over the past two decades.<sup>98–100</sup> DCA allows deconvolution of degradation mechanisms and changes in the electrode active material chemistry in greater detail than properties such as capacity fade and coulombic efficiency.

This technique has been employed to characterize capacity fade and assist in elucidating phase transitions by observing peak positions in the output. The phase transitions relate to the thermodynamics of the material, indicating how its structure changes with varying charge and discharge states. Specifically, peaks in the output correspond to significant events within the battery, such as the formation or dissolution of phases, providing critical insights into thermodynamics. (Figure 17) DCA tracks an electrochemical system's capacity increase on charge or decreases in discharge as a function of voltage. Plotting differential capacity versus voltage creates an electrochemical “fingerprint” that can be tracked. Instead of plotting current with respect to voltage for voltammetry, the differential capacity over voltage ( $dQ/dV$ ) is plotted against voltage. The DCA method allows observation of shifts in clearly identifiable peaks over the lifetime of a battery to deconvolute the type of degradation.

In a full cell this technique is unable to determine the behaviour of the negative electrode (in this case graphite). To elucidate these behaviours in commercial cell chemistries a reference electrode needs to be inserted, or the electrodes extracted via a cell teardown to enable half-cell or three-electrode testing.

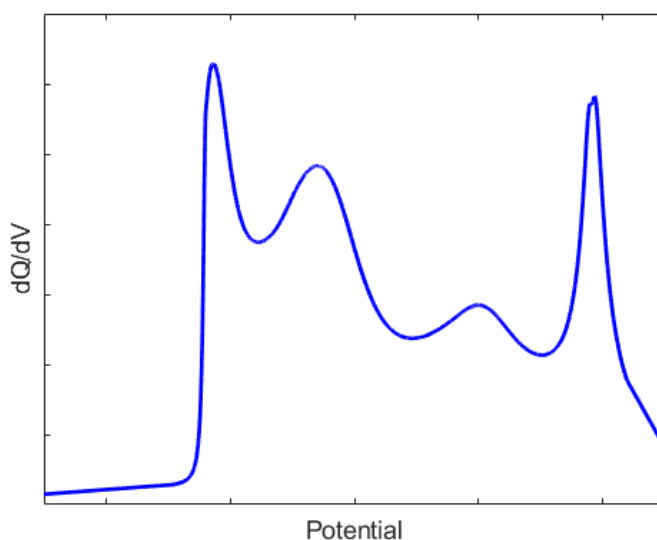


Figure 17. Differential capacity analysis of an NMC-based lithium-ion electrode.

### Galvanostatic Intermittent Titration Technique (GITT)

GITT was a technique used in Chapter 4, 5, and 6 to measure the solid-phase diffusivity of lithium-ion and sodium-ion materials. This technique was introduced by Weppner and Huggins, it is an electrochemical titration technique to measure the thermodynamic and kinetic properties of an electrochemical system.<sup>28</sup> GITT involves applying a short transient

current to change the SOC of the system followed by a relaxation period where no current flows. The final voltage during this relaxation is the open circuit voltage at that SOC. This process is repeated until the voltage cycles through the complete window. These voltages are then plotted as a function of the state-of-charge (SoC) to obtain the open circuit voltage (OCV) profile. An OCV profile is a graph that shows the voltage of a battery when it is not connected to any external circuit or load, indicating its intrinsic voltage at various states of charge. This allows accurate determination of the open circuit voltage of an electrochemical system by ignoring contributions from overpotentials, therefore the evaluation of the intrinsic hysteresis of battery materials.<sup>101</sup>

This technique can also be used to ascertain the diffusion coefficients of an electrochemical system by observing the voltage change that occurs in the transient and relaxation periods (Figure 18) during and after applying current. From the voltage change during the transient,  $\Delta E_t$  and the steady-state period  $\Delta E_s$ , the solid-phase diffusion coefficients,  $D_s$ , can be calculated using the following equation:

$$D_s = \frac{4}{\pi t} \left( \frac{m_{AM} V_M}{M_{AM} A} \right)^2 \left[ \frac{\Delta E_s}{\Delta E_t} \right]^2 \quad [31]$$

Here  $t$  is the duration of the transient,  $m_{AM}$  is the molar mass of active material,  $V_M$  is the molar volume of active material,  $M_{AM}$  is the atomic weight of the active material, and  $A$  is the geometric area of the electrode.

The parameters chosen for this technique have a significant effect on the kinetic information obtained, and therefore have to be chosen appropriately:

- The charge passed during each titration step ( $I \cdot t$ ) must be low enough so that concentration gradients do not influence the diffusion-controlled reaction.
- The relaxation period must be sufficient so that the true-OCV is reached, otherwise the measured diffusion coefficients will be lower.

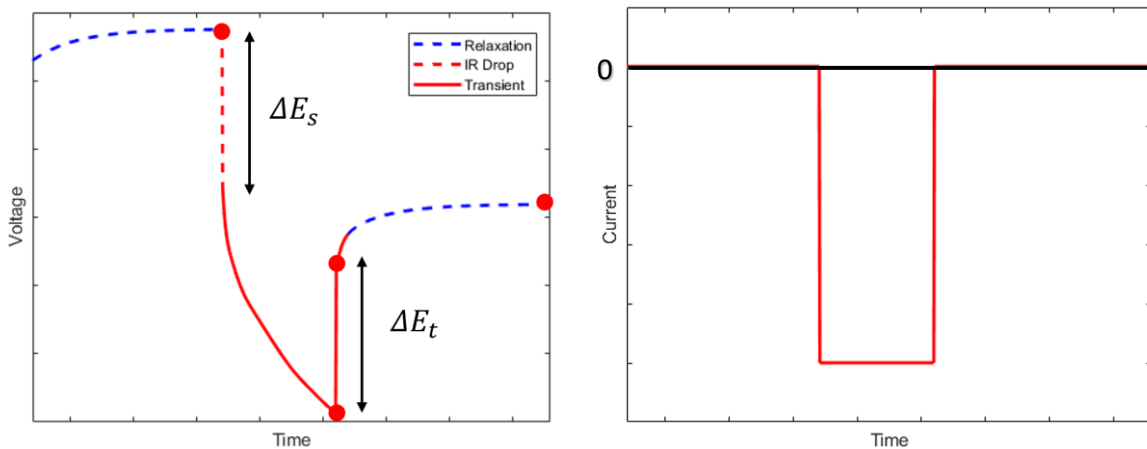


Figure 18. Illustration of the transient and steady state regions corresponding to a discharge step during GITT. The flat line corresponds to no applied current.

The traditional Weppner and Huggins approach evaluates the voltage change during the relaxation and transient periods by only fitting two points, thus during analysis it can be hard to discern clear trends as noise arises.<sup>1</sup> Fitting only two points assumed that the system reaches true-OCV. To provide a more reliable method to extract diffusion coefficients we have developed a new approach using the Sand Equation.

From the Sand equation we know the evolution of the lithium concentration  $c_{surf}$  in time at the surface of the particles under a constant current, this behaviour is described by Bard and Faulkner in the following expression:<sup>102</sup>

$$c_{surf} = c_0 + 2 \frac{I}{SFL\sqrt{D_s\pi}} \sqrt{t}, \quad [32]$$

By observing current density  $i$  rather than current  $I$  and using the following relationship to convert Equation [32] into:

$$c_{surf} = c_0 + 2 \frac{i}{aF\sqrt{D_s\pi}} t. \quad [33]$$

Here  $S$  is the electrode-electrolyte surface area and  $a$  is the surface area per unit volume. This expression describes the evolution of lithium surface concentration with time when a constant current is applied. In this measurement voltage is not measured directly, but the voltage of the electrode against the lithium counter. Given that the variation of concentration at the surface is small, we can linearize the expression for terminal voltage equation to obtain:

$$V = U(c_0) + (c_{surf} - c_0)U'(c_0) - R_{IR}i, \quad [34]$$

Here  $U$  is the OCV as a function of concentration. Combining Equations [32] and [34] we obtain:

$$V = U(c_0) - R_{IR}I + 2 \frac{U'(c_0)i}{aFL\sqrt{D_s}} \sqrt{t}, \quad [35]$$

Therefore, the voltage (and therefore concentration) evolves as proportionally with  $\sqrt{t}$ . To determine the diffusion coefficient, for each pulse we fit the coefficient in front of  $\sqrt{t}$  to the experimental value. Then the diffusion coefficient can be calculated as:

$$D_s = \frac{4}{\pi} \left( \frac{I}{aFL} \frac{U'(c_0)}{dV/d\sqrt{t}} \right)^2 \quad [36]$$

### 3.4 Thermal Characterisation

#### Differential Scanning Calorimetry (DSC)

DSC can be used to measure the specific heat capacity of individual components within a battery or the battery itself.<sup>103</sup> This technique was used in Chapter 5 to measure the heat capacity of individual components in a battery. DSC quantifies the heat quantity needed

to raise the temperature of a sample and a reference as a function of temperature. The experiment always maintains an equal temperature for both the sample and the reference. The temperature scheme is devised to ensure that the sample holder's temperature increases linearly with time. The principle of this method dictates that when the sample experiences a physical change, like a phase transition, heat must be transferred to the sample relative to the reference to preserve a uniform temperature across both. Depending on whether heat must flow to the sample depends on whether the process is endothermic or exothermic respectively. In addition to evaluating the enthalpy of phase transitions, it is possible to determine the temperature at which the transition takes place.

#### Laser Flash Analysis (LFA)

LFA is used to indirectly measure the thermal conductivity of different battery components.<sup>104,105</sup> This technique was used to measure the thermal properties of electrodes in Chapter 6.<sup>7</sup> The thermal conductivity describes the ability of a material to conduct heat and heat transport within the cell. This is influenced significantly by the anisotropic structure of a cell and means that the thermal conductivities of the individual components can be evaluated to predict thermal gradients. The thermal conductivity  $\lambda$  is not able to be directly measured so the thermal diffusivity  $\alpha$  must be evaluated:<sup>106</sup>

$$\lambda = \alpha \rho C_p. \quad [37]$$

Here  $C_p$ , is the specific heat capacity and  $\rho$  is the density.

#### Potentiometric Method

The entropic term is a property that relates to the reversible heat generation in the electrode. During cycling of battery material, thermodynamic phase changes occur and this causes heat to be released/absorbed depending on its magnitude. This property can be measured by evaluating the dependency of OCV on temperature (Figure 19).<sup>107</sup> The temperature is changed at each lithium concentration, this provides the OCV at different temperatures for the material. The entropic term can be calculated from the gradient of a line through the points. It can take many hours to attain OCV at a particular lithium stoichiometry and temperature, therefore the thermal stability of the electrolyte needs to be considered when choosing the temperature regime. This is because at high temperatures it is more difficult to attain OCV, due to electrochemical instability and particularly at the graphite interface.<sup>108</sup> Choosing a lower temperature regime avoids instabilities, while allowing the thermodynamic behaviour to be measured. The change in entropy  $\Delta S$  can be determined through the slope of the OCV with temperature:<sup>73</sup>

$$\Delta S = \frac{-\Delta G}{T} = nF \left( \frac{E}{T} \right). \quad [38]$$

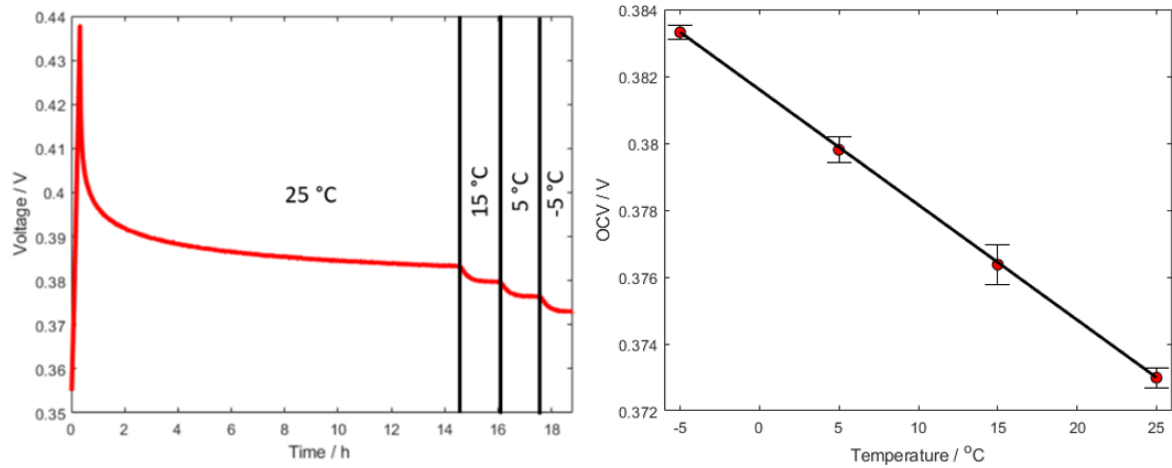


Figure 19. Potentiometric profile illustrating the initial SOC change, followed by a long period to attain OCV and a temperature-cycling regime to observe voltage change (left). The entropic term is calculated from the gradient of the OCV points at each temperature (right).

### 3.5 Modelling

#### Python Battery Mathematical Modelling (PyBaMM)

The PyBaMM software package was used to conduct simulations in this thesis.<sup>109</sup> PyBaMM was chosen for validation in battery modelling due to its open-source nature, which encourages the addition of parameters by a wider community, fostering collaborative improvements and extensions. Its robust code base offers a solid foundation for exploring new modelling problems, making it an ideal tool for comprehensive and innovative battery research. PyBaMM solves physics-based electrochemical models by using state-of-the-art methods, including automatic differentiation of a system of differential-algebraic equations (DAEs) and efficient numerical solvers. PyBaMM uses the method of lines to solve the equations (which means it discretises in space, but not in time, and then the solver integrates in time). The discretisation used is finite volumes.

## Chapter 4: Developing methodologies for parametrisation of lithium-ion batteries

The author's contributions from the following paper have been included and rewritten: **Development of experimental techniques for parameterization of multi-scale lithium-ion battery models.** Chang-Hui Chen, Ferran Brosa Planella, Kieran O'Regan, Dominika Gastol, W Dhammika Widanage, and Emma Kendrick, J. *Electrochem. Soc.*, **167**, 080534, (2020).

### 4.1 Introduction

Physics-based models need accurate parameter values to give meaningful predictions. Model definitions can be applied to any lithium-ion battery of a given type (irrespective of chemistry/format) whereas the parametrisation must be carried out for each specific cell under consideration to enable reliable predictions.<sup>110</sup> Lithium-ion battery modelling focusses on commercial chemistries due to their relevance in industry and use in real-world scenarios.<sup>111,112</sup> However, determining the parameter that represent the behaviour of a commercial cell proves challenging as limited information is provided by the manufacturer; the composition of electrodes, electrolyte, and separator is often unknown. Elucidating the composition of these components relies on experimental methods that do not always provide robust results.<sup>113</sup> Similar to the equivalent circuit model, for physics-based models, it is possible to elucidate several parameters from current-voltage data, but not all the parameters can be derived electrochemically.<sup>114,115</sup> Therefore, in addition to the electrochemical experiments, the complete parametrisation requires cell teardown and post-mortem characterisation. Dimensional parameters, including thicknesses and porosity, are relatively easy to measure after teardown, but parameters describing electrode microstructure including tortuosity and particle radius, prove difficult to measure and require use of microscopy and other image-based techniques.<sup>116,117</sup>

Limitations arise when attempting to quantify the behaviours of the electrodes post-mortem due to the physical and electrochemical changes that occur during the extraction and cell reassembly processes. The extraction process can induce physical stress to the materials during cell disassembly, washing, and cutting of electrodes.<sup>118</sup> The electrodes are exposed to moisture and oxygen which cause chemical changes to the active materials and the SEI, this can also occur in a glovebox environment where ppm concentrations of these contaminants exist. Reassembling the electrodes into a cell for electrochemical testing relies on the use of components different compared to those found in the commercial cell, this means the information obtained is not entirely representative of the original environment. It is critical to develop teardown and characterisation methodologies that ensure there is minimal damage to the electrodes, the electrochemical configuration closely resembles the original cell environment, and that the characterisation techniques provide accurate information. These factors are essential to obtaining a robust parameter set. In this investigation we have focussed on an experimental design that minimise these variables.



Despite the practical difficulties, the laboriousness, and the required multi-disciplinary approach, there have been several notable parametrisation efforts on commercial cell chemistries.<sup>62,63,119</sup> Similar to these parameterisations, we focus on the Doyle-Fuller-Newman (DFN) model definition, but in contrast, we emphasise the importance determining many of the parameters *in situ* using a three-electrode set-up. The use of a reference electrode enables the observation of individual electrode potentials, this enabled direct measurement of stoichiometries and open circuit voltages without voltage hysteresis contributions from the lithium metal counter electrode. To our knowledge, three-electrode testing has not been used explicitly for DFN parameterisations, we demonstrate it as a powerful tool in this context. Additionally, EIS and GITT in half cells allowed calculation of the maximum lithium concentrations (dependent on material composition, structure, and electrochemical design), reaction rates, and diffusion coefficients. To calculate the diffusion coefficients for the negative electrode we accounted for the volume expansion of the active materials during lithiation. Through EDS analysis, the negative electrode was observed to be comprised of two active materials, graphite and  $\text{SiO}_x$ , the latter exhibits significant volume change during electrochemical cycling.<sup>13</sup> To our knowledge, this is the first time a methodology has been outlined to calculate diffusion coefficients for a bi-component electrode system.

This chapter presents the autopsy of a commercially available 21700 cylindrical cell, the LGM50. In this work, we detail an autopsy process that comprises of a teardown, followed by the physico-chemical and electrochemical characterisation of the cell components. The derived parameters can be categorised into the domains that the DFN model is defined in, positive electrode, separator, and negative electrode. In cases where the parameters cannot be derived explicitly from the experiments we provide theory-based derivations and relevant discussion. In all, there are over 30 parameters that describe the various components of a battery (Figure 20). To demonstrate the validity of this parameter set we have compared experimentally derived data with simulations using the DFN model.

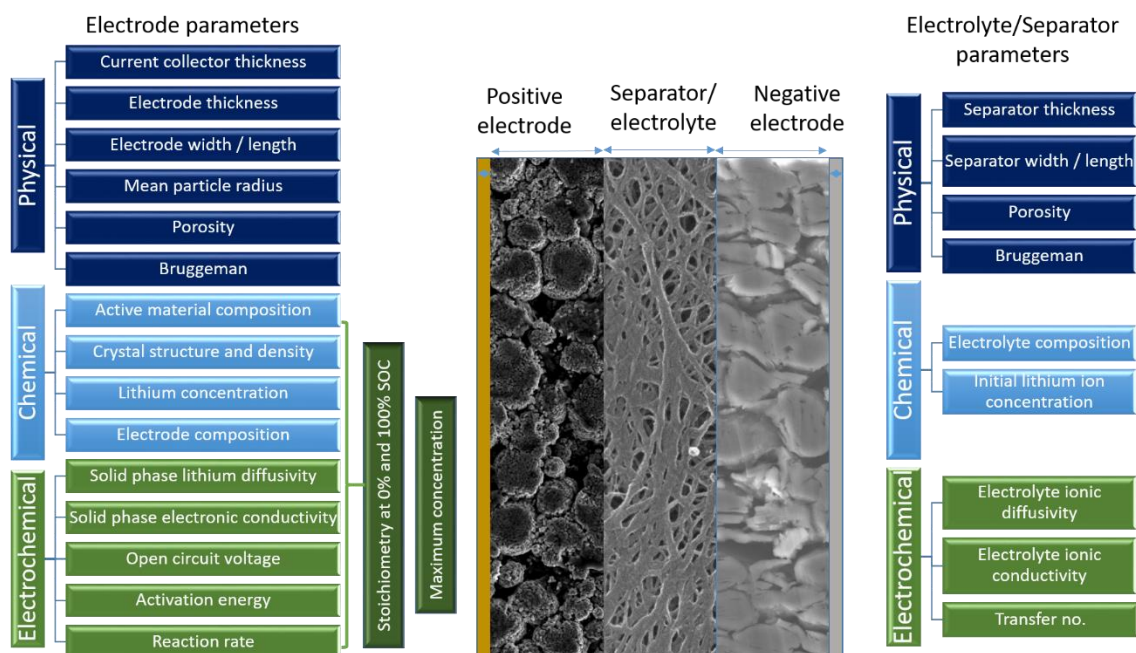


Figure 20. Summary of the parametrisation requirements for a physics-based model and their categorisations.

## 4.2 Experimental

### 4.2.1 Battery Description

The cell investigated was the M50 (LG Chem), a 21700 cylindrical cell designed for energy applications. The cell was received from the manufacturer with information on the characteristics and operating conditions (Table 7). The cell has a nominal capacity of 5 Ah, with a recommended voltage window of 2.5-4.2 V, providing a nominal voltage of 3.63 V.

Table 7. Details about the LGM50 cell provided by the manufacturer.

Property	Description
Nominal energy	18.20 Wh
Nominal voltage	3.63 V
Max. voltage	4.2 V
Min. voltage	2.5 V
Standard charge	0.3C (1455 mA)
Standard discharge	0.2C (970 mA)
Optimal Operating temperature	0 – 45 °C

### 4.2.2 Sample Extraction and Preparation

To parameterise the behaviours of the individual electrodes, they had to be extracted from the cell. This process involved fully discharging the cell, dismantling in a glovebox, washing the electrodes to remove residual electrolyte, and then removing one side of the electrode lamina to ensure compatibility in the battery reassembly process.

The cells were discharged at C/50 to 0% state of charge (SOC) to ensure safe disassembly, this corresponded to 2.5 V. Discharging to 0 V, despite being safer, would have caused irreversible changes to the electrodes.<sup>90</sup> The cells were disassembled in a glovebox under an argon atmosphere to prevent the chemical changes that occur due to the presence of moisture and oxygen. After cell opening, the tab between the electrode roll and the outer casing was cut with a ceramic scalpel. The double-sided electrodes and the

separator were removed from the cell and soaked separately in dimethyl carbonate (DMC) overnight. This was to remove any electrolyte salt residue. The samples were stored in an inert atmosphere and characterised within days of disassembly to prevent quality deteriorating.<sup>120</sup> This was to minimise changes to the electrode materials, as the active lithium content will react readily.

There were no further modifications to the electrodes before physical and chemical characterisation.

### **4.2.3 Physical Characterisation**

#### **4.2.3.1 Geometrical Data Measurements**

The thickness of the electrodes and separator were measured using a digital length gauge (Heidenhain).

#### **4.2.3.2 Scanning Electron Microscopy (SEM)**

Top-view images of the electrodes were captured using an XL30 ESEM FEG (Phillips) with an accelerating voltage of 20 kV and a secondary electron detector. ImageJ software was used to analyse the mean particle radius of the electrodes. This analysis was carried out for a region of 100  $\mu\text{m}$  x 65  $\mu\text{m}$  for both the positive and negative electrode.

### **4.2.4 Chemical Characterisation**

#### **4.2.4.1 Energy-dispersive X-ray spectroscopy (EDS)**

Energy-dispersive X-ray spectroscopy (Oxford instruments) was used to analyse the elemental make-up of the electrodes, this allowed the composition of electrodes to be elucidated.

### **4.2.5 Electrochemical Characterisation**

To prepare the electrodes for electrochemical characterisation, one side of the double-sided electrode was delaminated using N-methyl-2-pyrrolidone (NMP) heated to 50 °C. The NMP was heated to increase the solubility of the binder.<sup>121</sup> Then the electrodes were heated at 50 °C under vacuum to remove any NMP. The electrodes were then assembled into a two- or three-electrode format. This process was carried out under inert atmosphere.

The two-electrode configuration adopted a perfluoroalkoxy alkane (PFA) Swagelok®-type configuration. This cell comprised of a positive electrode, a negative electrode, and a 25  $\mu\text{m}$  thick Celgard 2325 (PP|PE|PP, Celgard) separator, and R&D 281 electrolyte (1 mol  $\text{dm}^{-3}$   $\text{LiPF}_6$  in 3:7, v:v, ethylene carbonate (EC): diethyl carbonate (DEC), +1%wt vinylene carbonate (VC), Soulbrain). This configuration utilised 330  $\mu\text{m}$  thick lithium metal (Sigma) as the counter electrode i.e. a half cell.

The three-electrode configuration adopted a PAT-Cell (EL-Cell) configuration. This cell comprised of a positive electrode, a negative electrode, a 220  $\mu\text{m}$  FS-5P (PP fibre|PE, EL-Cell) separator, and R&D281 electrolyte (Soulbrain). This configuration utilised a lithium ring electrode that provided geometrical symmetrical electrode stack, improving lifetime by limiting corrosion of the reference.

The dimensions of electrode/separator, volume of electrolyte, and voltage windows used for each configuration were as follows:

- **Swagelok half cells:** comprised of the extracted negative or positive electrode (12 mm), separator (12.8 mm), a lithium metal counter electrode (12 mm), and 50  $\mu$ l electrolyte. This is a test cell that uses Swagelok plastic components, it enables precise testing of new battery materials.
  - Graphite-SiO<sub>x</sub> E<sub>cell</sub>: 0.005-1.5V
  - NMC E<sub>cell</sub>: 3.3-4.3 V
- **PAT-Cell three-electrode:** comprised of a negative electrode (18 mm), a positive electrode (18 mm), FS-5P separator, a lithium ring reference electrode, and 100  $\mu$ l of electrolyte.
  - E<sub>cell</sub>: 2.5-4.2V

The lower voltage windows were chosen to ensure full practical lithiation of each electrode, this corresponded to 2.8 V for the NMC half cell and 0.005 V for the graphite-SiO<sub>x</sub> half cell. For the graphite-SiO<sub>x</sub> half cell, choosing a voltage lower than 0.005 V can cause dendrites to form without intercalating more lithium.<sup>122</sup>

The electrochemical measurements were performed on BCS battery cyclers or VMP-3 potentiostats (Bio-logic). For deviating temperatures, a programmable climate chamber (Temperature Applied Sciences) was used. After cell assembly, the cells were subject to a conditioning step to restore the SEI and ensure its compatibility with the new electrolyte. This step comprised of a 12-hr resting period to allow proper electrolyte wetting of the separator and electrodes.<sup>123</sup> Two C/20 (current to achieve a rate where the battery is fully charged or discharged in 20 hours) constant CC-CV charge and CC discharge cycles. The voltage was held at upper voltage limit (or lower voltage limit for graphite-SiO<sub>x</sub> half cell) during the CV step until the current decayed below C/50.

The negative electrode has a higher areal capacity than the positive electrode to inhibit lithium plating during cell operation. This means that the cell capacity is limited by the positive electrode. The C-rates applied to the cells, including half cells, were based upon the practicable capacity (1C = 4.55 mA cm<sup>-2</sup>) of the positive electrode to replicate the current both electrodes experience in the cylindrical cell.

#### 4.2.5.1 Galvanostatic Intermittent Titration Technique (GITT)

To obtain kinetic and thermodynamic information of the electrodes a C/10 current transient was applied for 150 sec followed by a resting period that lasted until the rate of change of the potential with time decayed below 0.1 mV h<sup>-1</sup>. This was carried out until the resting period potential was above the upper voltage limit for the charge and below the lower voltage limit for the discharge. This was carried out for three-electrode and half cell configurations.

#### 4.2.5.2 Quasi-Open Circuit Voltage (pOCV)

The voltage profiles of graphite-SiO<sub>x</sub> and NMC were measured by a C/50 CC charge/discharge in half cell configuration.

#### **4.2.5.3 Potentiostatic Electrochemical Impedance Spectroscopy (PEIS)**

Impedance measurements were obtained by applying a sinusoidal wave in the frequency range 100 kHz – 10 mHz. The measurement was preceded by a 30 min rest period to ensure the system was at steady state. This test was carried out for half cell configurations at 50% SoC. Analysis of the resulting Nyquist plots was carried out using ZView® (Ametek).

#### **4.2.5.4 Differential Capacity Analysis (dQ/dV)**

Differential capacity plots were obtained by analysis of a C/50 CC cycle in half cell configuration in half cell configuration.

#### **4.2.5.5 Four-point Probe Measurement**

To measure the electronic conductivity of the electrode materials a four-point probe (Ossila Instruments) was used. The electrode lamina was removed from the current collector by strong-adhesive tape. This was to ensure the measurement was for the electrode only, not the current collector. The maximum voltage for the measurement was chosen such that it did not exceed the normal operating voltages for each electrode, this was 4.0 V for the positive electrode, and 1.0 V for the negative electrode. The voltage was stepped in 0.02 V increments until a target current of 0.03 mA and 10 mA was reached for the positive and negative electrode respectively. The conductivity was measured in three different places on the electrode, and an average value was taken.

#### **4.2.5.6 Electrochemical Validation**

To obtain experimental data to compare to the simulations the cylindrical cell was cycled. This involved charging the cell to 100% SoC at C/2 CC-CV (C/50 cut-off), then the discharging to 2.5 V at C-rates of C/2, C, and 1.5C, followed by a 2 hr relaxation period.

#### **4.2.6 Validation**

Model validation is crucial to ensure that the parameterized model accurately represents the real-world system it is intended to simulate. By comparing initial simulations from the model with experimental data, developers can assess the model's accuracy and reliability, identifying and correcting discrepancies. This process enhances the model's predictive capabilities, making it a more effective tool for forecasting, decision-making, and understanding complex systems. The Python Battery Mathematical Modelling (PyBaMM) software package was used to run simulations using the Doyle-Fuller-Newman model and our parameter set.<sup>109</sup> This is an open-source software where our parameter set 'Chen2020' has been made available. Instructions on how to use this software package and how to access our parameter set can be found on GitHub at <https://github.com/pybamm-team/PyBaMM>. The validation experiments comprised of C/2, C, and 1.5C cell discharge to 2.5 V, followed by a 2 hr relaxation period. For these simulations we used the default settings, further information on the default solvers, meshes, and differential algebraic equations can be found on the GitHub.

### **4.3 Results & Discussion**

To parametrise physics-based battery models the physical, chemical and electrochemical behaviours must be quantified. For this purpose, we have identified 35 parameters

(Figure 20) outlined in the equations that govern the DFN model Chapter 2. This requires use of a variety of characterisation techniques, the following section will describe the experiments and relevant analyses to obtain this parameter set.

#### 4.3.1 Physical Characterisation

The components of the cell were separated after teardown to allow measurement of the electrode and separator dimensions (Table 8). The electrode coating on the positive electrode covered both sides of the current collector equally, 79 cm length by 6.5 cm width (Figure S1 in the Supporting Information). This corresponded to a total electrode area of 1027 cm<sup>2</sup>. The coating on the negative electrode was asymmetrical, the coating covered 77.5 cm on one side of the current collector and 83.5 cm on the other (Figure S2). The negative electrode had a width of 6.5cm, this corresponded to a total electrode area of 1046.5 cm<sup>2</sup>.

Table 8. Physical parameters obtained from measuring the cell and its components during teardown.

Property	Unit	Positive Electrode	Negative Electrode	Separator
Length (side 1 / 2)	cm	79 / 79	77.5 / 83.5	-
Width	cm	6.5	6.5	-
Area	cm <sup>2</sup>	1027	1046.5	-
Current collector thickness	μm	16.3	11.7	-
Electrode coating thickness	μm	75.6	85.2	12
Electrode Loading	mg cm <sup>-2</sup>	24.69	14.85	
Average particle size	cm	5.22	5.86	-
Electrolyte volume fraction	%	31	23	-
Tortuosity	μm	5.8	9.0	-
Bruggeman exponent	μm	1.5	1.5	-

The thickness of the lamina and current collector for both electrodes was calculated by comparing the differences between the bare foil and an electrode with one-side coated. The positive electrode lamina was measured to be 75.6 μm and coated onto 16.3 μm aluminium foil. The negative electrode lamina was measured to be 85.2 μm and coated onto 11.7 μm copper foil. The thickness of the separator was measured to be ~12 μm, the approximation was due to ±2 μm difference across the membrane. The density of the separator was much higher than polyolefin (C<sub>n</sub>H<sub>2n</sub>) membranes are typically, this corroborated with the SEM images that showed the presence of a ceramic coating on one side. These ceramic coatings have been commonly utilised to improve the thermal stability of the separator.<sup>124</sup>

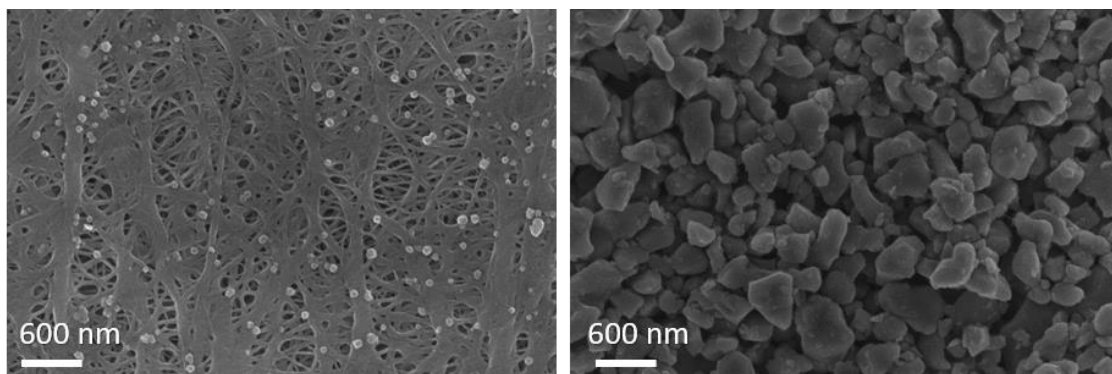


Figure 21. Top-view (left) and bottom-view (right) SEM images of the separator illustrating the polymer mesh and ceramic coating respectively.

The microstructural information of both the electrodes was ascertained using SEM, the particle size of the active material could be determined from the top-view images (Figure 22). The images captured information from over 100 particles on the electrode surface, this analysis provides an underestimation of particle size as it is known that gravitational settling of larger particles occurs during coating.<sup>125,126</sup> This factor can be overcome by using 3D image-based methods, however the small sample size may not be representative of the entire electrode. This has led to the development of electrochemical methods to measure particle size more accurately. For our analysis, the particles were assumed to be spherical, this assumption is consistent with the DFN model. The average particle size for the positive and negative electrode active materials were calculated to be 5.22  $\mu\text{m}$  and 5.86  $\mu\text{m}$ , information on the particle size distribution has been published elsewhere.<sup>1</sup>

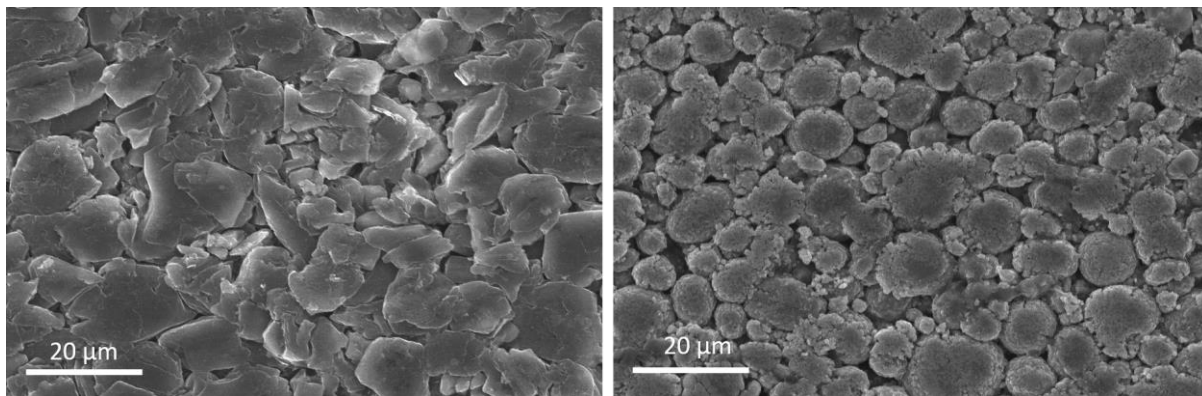


Figure 22. Top-view SEM images for graphite-SiO<sub>x</sub> (left) and NMC (right) illustrating the flake and spherical morphologies of these materials.

The electrolyte volume fraction (porosity) can be determined using X-ray and electron imaging techniques, the electrode structure can be reconstructed in 3D using software to evaluate this property.<sup>117,127</sup> These methods are time-consuming and can be inaccurate due to difficulty resolving the boundary between the active material and the carbon binder domain.<sup>128</sup> Instead, we calculate the electrolyte volume fraction,  $\varepsilon$ , from the theoretical density (assuming no porosity) and observed mass loadings of each electrode:

$$\varepsilon = 1 - \varepsilon_{act} = 1 - \frac{M_{coat}}{L\rho} \quad [39]$$

Here  $\varepsilon_{act}$  is the active material volume fraction,  $M_{coat}$  is the electrode coating mass per unit area,  $L$  is the lamina thickness, and  $\rho$  is the theoretical density of the electrode.  $M_{coat}$  was measured to be 24.69 mg cm<sup>-2</sup> and 14.85 mg cm<sup>-2</sup> for the positive and negative electrode respectively. Here we assume that the contribution of the inactive component is 3% for each the polymer binder and conductive carbon components i.e. a ratio of 94: 3: 3. The selection of a 3% contribution for both the polymer binder and conductive carbon components in battery electrodes is a compromise aimed at maintaining mechanical stability and electrical conductivity without compromising the energy density of the battery. This assumption is consistent with the cell being designed for energy applications, implying that the inactive component would have been reduced to maximise the energy density. The crystal densities of NMC 811 (4.95 g cm<sup>-3</sup>),<sup>129</sup> graphite (2.26 g cm<sup>-3</sup>), polyvinylidene fluoride (1.78 g cm<sup>-3</sup>) and C65 (1.9 g cm<sup>-3</sup>) were used in the calculation. The elucidation of the electrode chemistry can be found in the next section. From Eq. [39] electrolyte volume fractions of 31% for the positive electrode and 23% for the negative electrode were obtained. The porosities for these electrodes have been measured in Chen et al. using FIB-SEM, for this method values of 35% for the positive electrode and 27% for the negative electrode were obtained.<sup>1</sup> In the final parameter set an average value was taken from both of these sets of measurements (Table 9).

To further detail the physical properties of the electrode we quantified a parameter that describes the decrease in effective electrolyte conductivity due to microstructure, this parameter is known as tortuosity,  $\tau$  (Figure 23).<sup>130</sup> It is important that tortuosity is minimised in the design of electrode architectures, this leads to improved electronic and ionic transport.<sup>131</sup> The tortuosity can be obtained from its relationship with porosity:

$$\tau = \varepsilon^{1-\beta} \quad [40]$$

The Bruggeman constant  $\beta$  correlates these two microstructural parameters. The Bruggeman constant is not explicitly outlined in the DFN model, though it is accounted for in the theoretical derivation of tortuosity and the expression for effective parameters.<sup>132</sup>

$$\Psi_{eff} = \Psi \frac{\varepsilon}{\tau} \quad [41]$$

here  $\Psi$  is arbitrarily chosen to illustrate the effective relationship for a given parameter. The Bruggeman exponent makes it possible to evaluate the tortuosity of an electrode with a known porosity. For battery models, this exponent is typically set to 1.5.<sup>31</sup> Tortuosity values of electrodes have previously been found to be significantly higher than those predicted by the Bruggeman correlation (Eq. [40]), suggesting that this assumption is not valid and tortuosity should be derived from experimental methods.<sup>133,134</sup> Practical methods to obtain tortuosity, such as X-ray tomography,<sup>117</sup> FIB-SEM,<sup>135</sup> and EIS<sup>136</sup> are



experimentally and/or computationally expensive.<sup>137</sup> Additionally, for image-based techniques, being able to sufficiently resolve the electrode microstructure can prove challenging due to the size and attenuation of active material particles.<sup>116</sup>

The tortuosities of the M50 electrodes have been measured previously using FIB-SEM to image and reconstruct the 3D structure.<sup>1</sup> Through computational analysis, tortuosity values were calculated to be 4.8 for the positive electrode and 14 for the negative electrode using Taufactor, an open-source software for analysing microstructural properties.<sup>1,138</sup> These values were used in simulations of cell discharge and the results proved unrealistic: the electrolyte was depleted too quickly at the negative electrode, this meant the cell did not reach the lower voltage limit before the lithium was depleted (Figure 24). The values for the tortuosity that had been derived using the Bruggeman correlation were also used in the simulations, these were 1.7 and 2 for the positive and negative electrode respectively. The theoretical tortuosity values (based on  $\beta=1.5$ ) provided more accurate simulations of cell behaviour i.e. the lower voltage window could be reached during discharge. This illustrates the need for more robust techniques to experimentally derived tortuosity values are regarded as robust for model parametrisation. For the final parameter set we assume the Bruggeman correlation applies to the electrodes and exclude the experimentally derived values (Table 8).

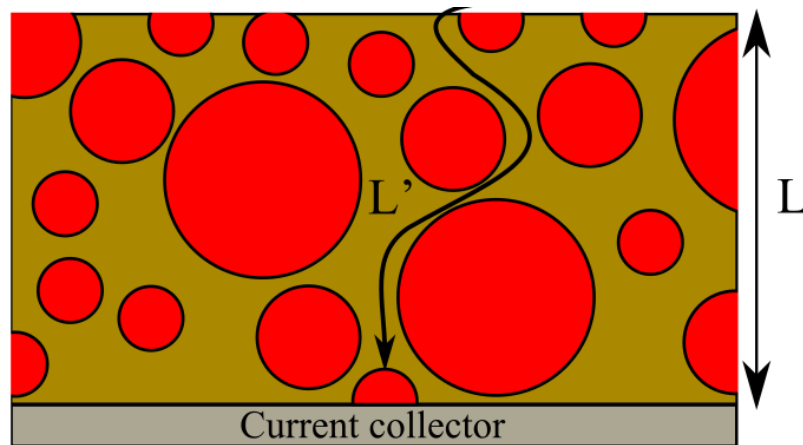


Figure 23. Illustration to describe how microstructure has an impact on lithium diffusion pathways within an electrode. Tortuosity ( $L'/L$ ) describes this effect, minimising this value improves lithium transport.

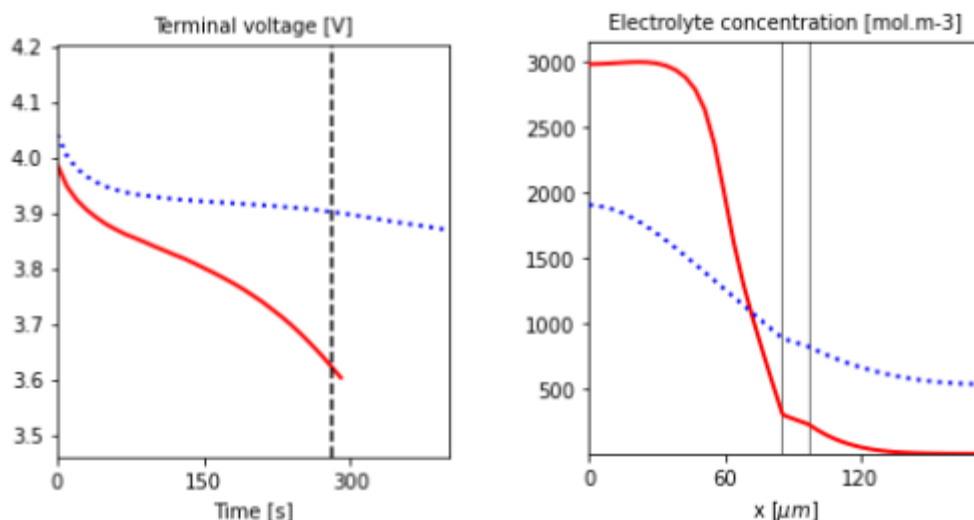


Figure 24. Simulations of voltage and electrolyte concentration utilising the experimentally derived tortuosities (red solid line) and the theoretically derived tortuosities (blue dotted line) in the positive electrode.

#### 4.3.2 Chemical Characterisation

Energy dispersive X-ray spectroscopy (EDS) was used to determine the elemental constituents of each electrode. This analysis enabled the elucidation of the positive and negative electrodes (Figure 25) active materials. From EDS analysis of the negative electrode, the active material was determined to be graphite doped with silicon, present as silicon oxide.<sup>1</sup> Silicon oxides are a promising anode material without the severe volume change of silicon-based anodes that can limit battery lifetime. The distribution of the silicon content across the surface implies that the silicon oxide particles were mixed homogeneously and inserted into the graphitic layers. In the positive electrode, nickel, manganese and cobalt concentrations were observed (Figure S3). The atomic ratio was calculated to be Ni: Co: Mn = 7.5: 1.0: 0.6, like a stoichiometry of NMC811. This is consistent with positive electrode chemistries designed for automotive applications (mostly) being composed of high nickel  $\text{Li}[\text{Ni}_{1-x-y}\text{Mn}_x\text{Co}_y]\text{O}_2$  due to high energy density.<sup>139</sup>

Magnified SEM images of the  $\text{Li}[\text{Ni}_{1-x-y}\text{Mn}_x\text{Co}_y]\text{O}_2$  surface indicated the active material particles were intermixed with carbon fibres (Figure 26). These fibres improve the poor intrinsic electronic conductivity (hence rate capability)  $\text{Li}[\text{Ni}_{1-x-y}\text{Mn}_x\text{Co}_y]\text{O}_2$  layered oxides.<sup>140</sup>

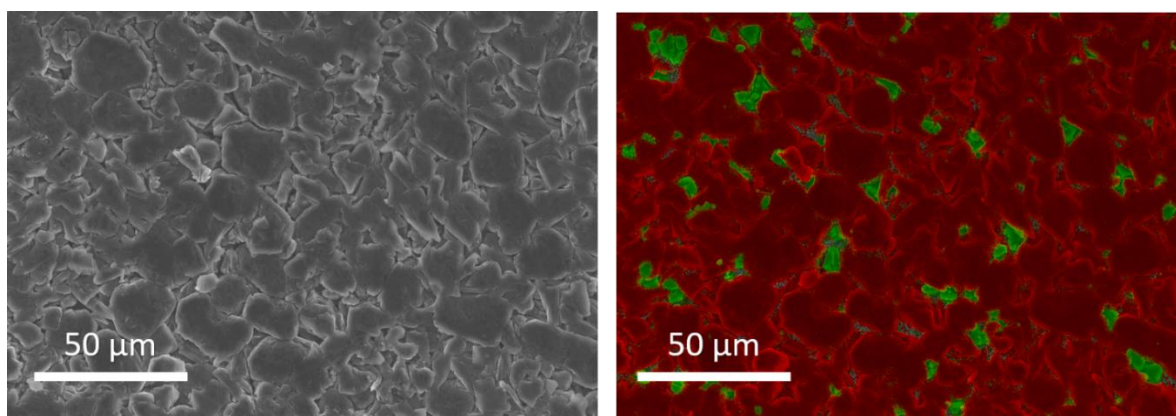


Figure 25. SEM image (left), the shape and particle size of the silicon oxide dopant can be distinguished. Top-view EDS (right) image of the negative electrode illustrating the graphite (red) and silicon oxide (green) content. The colours were obtained in the EDS measurement.

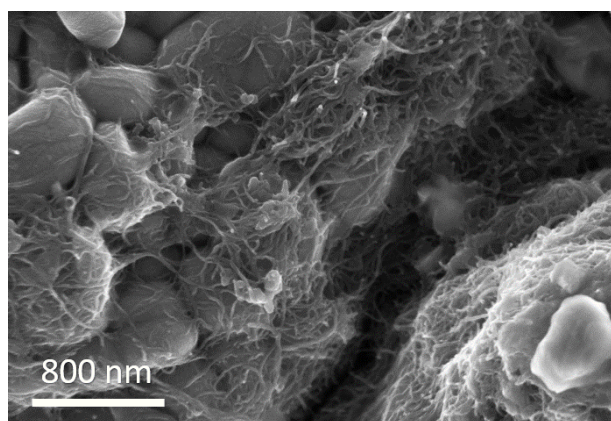


Figure 26. SEM image of the positive electrode surface illustrating presence of carbon fibres to enhance rate performance.

### 4.3.3 Electrochemical Characterisation

#### Quasi Open Circuit Voltage (pOCV)

The practicable capacity of the graphite-SiO<sub>x</sub> and NMC-based electrodes were evaluated at C/50 between 0.005-1.5 V and 3.3-4.3 V respectively (Figure 27). The capacities were determined to be 5.24 mAh cm<sup>-2</sup> and 4.55 mAh cm<sup>-2</sup>. This corresponds to a 15% higher capacity for the negative electrode. The rated capacity of the cylindrical cell is 5 Ah, with a positive electrode area of 1027 cm<sup>2</sup>, this normalises to 4.87 mAh cm<sup>-2</sup>. This value is within 7% of the positive electrode capacity we have determined, confirming that our electrode extraction and delamination process has only a small impact on the electrochemical performance.

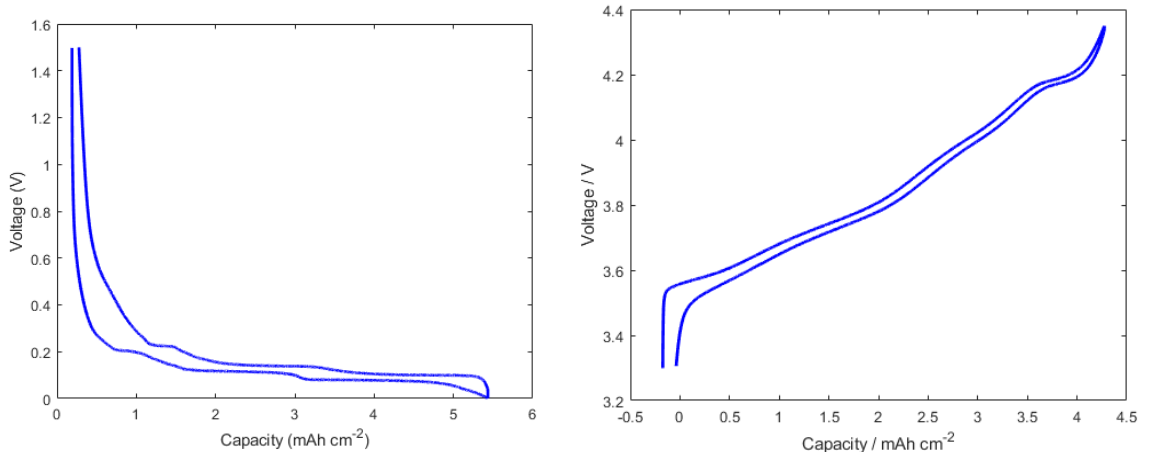


Figure 27. pOCV profiles for graphite-SiO<sub>x</sub> (left) and NMC (right) half cells.

To obtain meaningful modelling predictions it is critical to find the representative functions for the electrode equilibrium potentials, otherwise known as the open circuit voltage (OCV). The pOCVs profiles do not provide a reliable representation of the OCV due to a phenomenon known as voltage hysteresis. Hysteresis is observed for both graphite-SiO<sub>x</sub> and NMC-based electrodes.<sup>101</sup> Hysteresis in electroactive materials is influenced by thermodynamic factors, especially through phase transitions that involve energy barriers and changes in material structure. However, it is not solely due to thermodynamics; kinetic factors, such as reaction rates and ion diffusion, also contribute.<sup>141</sup> Hysteresis is significant in the negative electrode due to the presence of graphite and silicon.<sup>142</sup> The hysteresis observed in the pOCV profiles has additional contributions caused by current flow, these are known as an overpotentials:<sup>143</sup>

$$V_{cell} - V_{OCV} = \mu_{ohmic} + \mu_{f,pos} + \mu_{f,neg} + \mu_{pol,pos} + \mu_{pol,neg} + \mu_{diff} \quad [42]$$

Here  $V_{cell}$  represents the cell voltage,  $V_{OCV}$  represents the open circuit voltage without an applied current,  $\mu_{ohmic}$  is the pure ohmic voltage drop,  $\mu_f$  is the voltage drop due to passivation film or layers on each electrode respectively,  $\mu_{pol}$  is the polarisation voltage drop caused by interfacial charge-transfer reactions at each electrode,  $\mu_{diff}$  is related to particle diffusion. The primary contribution to hysteresis is the ohmic drop, this is observed as an instantaneous voltage change when current is applied, mainly

attributable to electrolyte resistance.<sup>144</sup> It is possible to eliminate these overpotentials by introducing rest periods into the cell (dis)charge.

### Open Circuit Voltage (OCV) & Stoichiometry

Galvanostatic intermittent titration technique (GITT) allows voltage hysteresis to be reduced, providing the OCV profiles of the individual electrodes.<sup>28</sup> These potentials were determined in half cell configuration, as this allowed mapping beyond the normal stoichiometric range the electrodes would exhibit during cell operation i.e. 2.5-4.2 V (Figure 28). GITT involves determining the voltage corresponding to the electromotive force at various SOC's by waiting sufficient time. The points corresponding to the system reaching dynamic equilibrium can be interpolated to obtain the voltage profile.<sup>1</sup> As the system is at OCV, there are no contributions from overpotentials, Eq. [43] can be rewritten as:

$$V_{cell} = V_{OCV} = U_{pos} - U_{neg} \quad [43]$$

Hence  $V_{cell}$  is solely defined by the voltage contributions from the electrodes, this is evidenced by the reduction in voltage hysteresis in the OCV profiles compared to the pOCV. The DFN model requires these profiles to be defined as functions dependent on the lithium content in the electrodes i.e. stoichiometry.

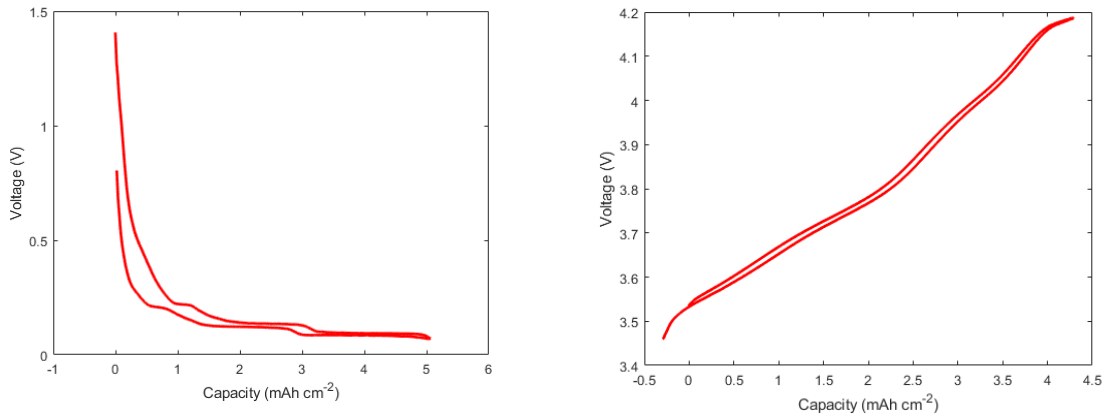


Figure 28. GITT in half cell configuration for graphite-SiO<sub>x</sub> (left) and NMC (right) allows determination of the open circuit voltages. The graphite-SiO<sub>x</sub> electrode demonstrates significant hysteresis at capacities below 2 mAh cm<sup>-2</sup>, this is attributable to the intrinsic hysteresis of silicon.

To define the stoichiometric range the maximum lithium concentration of each electrode needs to be calculated. This quantity will allow us to determine the lithium content in the negative and positive electrode corresponding to 0% and 100% SoC. The stoichiometry,  $x$ , is defined as:

$$x = \frac{c_s}{c_s^{max}}. \quad [44]$$

Here  $c_s$  is the lithium concentration and  $c_s^{max}$  is the maximum lithium concentration of the electrode. To determine the stoichiometric range of the positive and negative electrode we compared the OCVs obtained from half cell and three-electrode tests. Using this data, we overlayed the data sets and shift the half cell profile to match the features on the three-electrode profile, this fit was improved by minimising the least squares error (Figure 29). In theory the half cell should be cycled through the full stoichiometric range of the electrode. This is true for graphite-SiO<sub>x</sub>, we observe full lithiation/delithiation in the half cell test. For the positive electrode this is not possible, we are unable to cycle through the entire stoichiometric range due to electrolyte oxidation occurring above 4.2 V.<sup>145</sup> Therefore we will have to extrapolate the data to calculate the complete range.

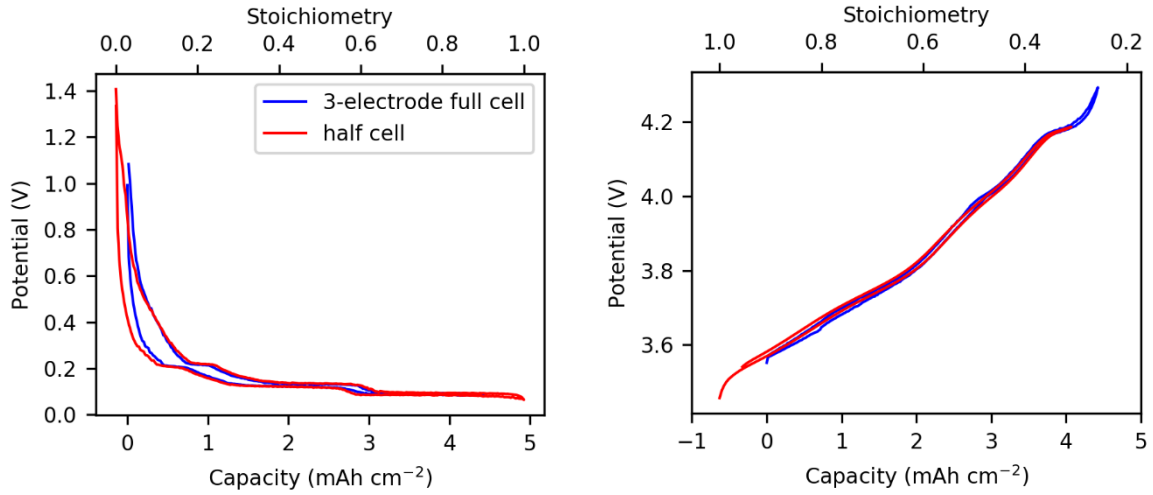


Figure 29. Balancing between three-electrode (blue) and half (red) cell open-circuit voltage curves for the negative (left) and positive electrode (right).

For the graphite-SiO<sub>x</sub> (Li<sub>1-z</sub>CSi) electrode we defined the half cell upper and lower voltage limits as lithium stoichiometries of 1.0 and 0.0 respectively (Figure 29). From the fitting of the two voltage profiles, it can be observed that the stoichiometric range the graphite-SiO<sub>x</sub> electrode is cycled through in the three-electrode cell (2.5-4.2 V) is 0.0279 to 0.9014, these values correspond to 0% and 100% SoC respectively.

As previously stated, it was not possible to fully delithiate the positive electrode. To ascertain the stoichiometric range, we need to find the corresponding capacity for a lithium content of 0. The half cell test exhibited a capacity of 4.7 mAh cm<sup>-2</sup>, this corresponds to 1.75·10<sup>-4</sup> mol cm<sup>-2</sup> of lithium being removed from the electrode:

$$Q = \frac{nF}{3.6} \quad [45]$$

Here  $Q$  is capacity and  $F$  is the Faraday constant. The mass loading of the NMC-based (NMC811,  $M_w = 95.63$  g mol<sup>-1</sup>) electrode was 24.69 mg cm<sup>-2</sup>, this corresponds to an estimated lithium content of 2.54·10<sup>-4</sup> mol cm<sup>-2</sup>. Therefore 1.75·10<sup>-4</sup> mol cm<sup>-2</sup> of lithium removed equates to a stoichiometry of 0.321 being reached in the half cell being

discharged to 4.3 V. For this calculation we have ignored the binder and conductive carbon components as we are not able to easily determine the mass they contribute to the electrode. Similar to the graphite-SiO<sub>x</sub> electrode, we rescale the OCV profiles, thereby ascertaining that the positive electrode cycles through a stoichiometry range of 0.2567 to 0.9072 in the three-electrode cell i.e. lithium concentrations of  $6.31 \cdot 10^{-5} \text{ mol cm}^{-2}$  and  $2.34 \cdot 10^{-4} \text{ mol cm}^{-2}$  respectively.

The OCV curves cannot be accurately represented by a constant, therefore we need to find a function that best describes these from interpolation (Figure 29). Fitting the three-electrode data provides the exact voltage windows the electrodes would experience in the commercial cell, this contrasts to previous research that has fitted half cell data to obtain these curves.<sup>119</sup> In the simulations we focus explicitly on the discharge process, therefore we fit functions to the OCV profiles that correspond to the delithiation of the negative electrode and lithiation of the positive electrode. Defining the stoichiometry of the electrode  $x$  as in [44], the OCV profiles can be represented by:

$$U_+(x) = -0.7991x + 4.5337 - 0.0416 \tanh(18.6490(x - 0.5496)) - 21.0988 \tanh(14.717(x - 0.2943)) + 20.8930 \tanh(14.8461(x - 0.2948)) \quad [46]$$

$$U_-(x) = 1.9793e^{-39.361x} + 0.2482 - 0.0909 \tanh(29.8538(x - 0.1234)) - 0.04478 \tanh(14.9159(x - 0.2769)) - 0.0205 \tanh(30.4444(x - 0.6103)) \quad [47]$$

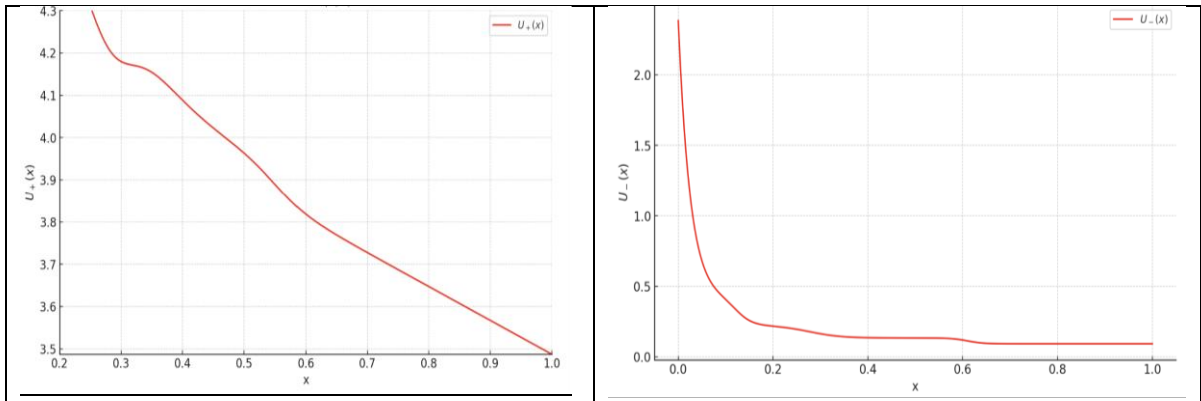


Figure 30. Mathematical functions used for the positive electrode (left) and negative electrode (right) OCV used in the simulations.

### Differential Capacity Analysis (dQ/dV)

Differential capacity (dQ/dV) analysis illustrates the voltage hysteresis more clearly for the positive (Figure 31) and negative (Figure 32) electrodes. The peaks in these graphs correspond to the voltages at which lithium is intercalated or deintercalated. The NMC-based electrode exhibited an average hysteresis of 15 mV, whereas the graphite-SiO<sub>x</sub> electrode exhibited a 40 mV hysteresis. This hysteresis can be directly related to the voltage efficiency, the existence of an overpotential means less energy is recovered than

thermodynamics predicts.<sup>146,147</sup> This energy is lost as heat. The comparison of the dQ/dV analysis for pOCV and OCV profile for this cell chemistry can be found elsewhere.<sup>1</sup>

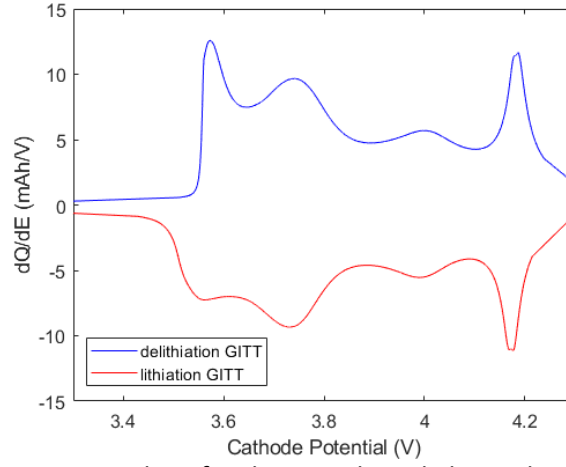


Figure 31. Differential capacity analysis for the NMC-based electrode obtained at C/50 for 3.3-4.3 V in a half cell.

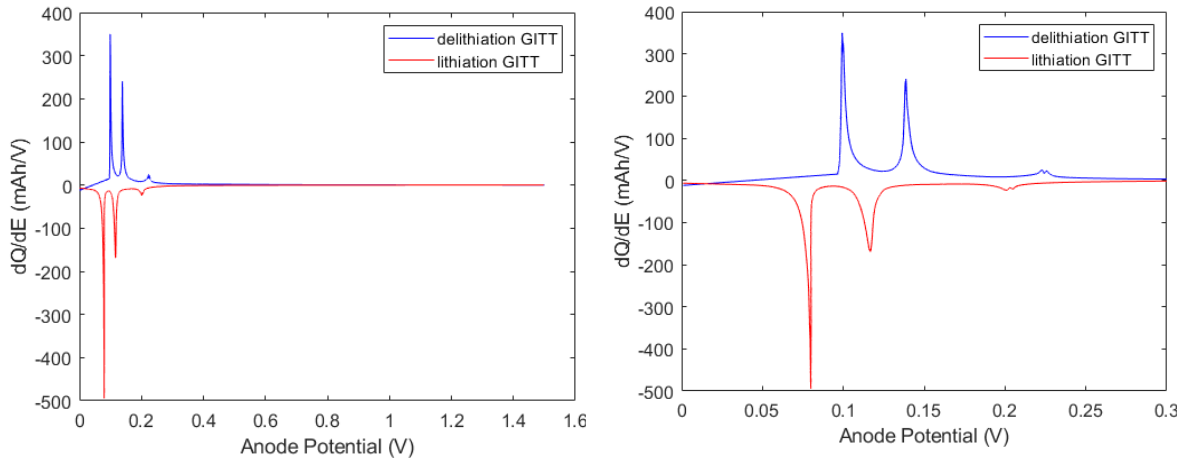


Figure 32. Differential capacity analysis for the graphite-SiO<sub>x</sub> electrode obtained at C/50 for 0.005-1.5 V (left) in a half cell. For better visualisation the data has been plotted in a narrower range (right).

### Maximum Lithium Concentration

The maximum lithium concentration at 100% SoC needs to be calculated for each electrode. This process is different for the positive and negative electrode due to the latter being a bi-component electrode i.e. containing both graphite and SiO<sub>x</sub> as active materials. These concentrations can be evaluated for the positive and negative electrodes according to Equations [48] and [49] respectively. For the positive electrode  $c_s^{max}$  can be calculated from:

$$c_s^{max} = \frac{M_{coat}Z}{M_w L \varepsilon_{act}}. \quad [48]$$



Here  $M_{coat}$  is the mass loading (24.69 mg cm<sup>-2</sup>),  $z$  is the fraction of Li<sup>+</sup> per mole of LiNi<sub>1-x-y</sub>Mn<sub>x</sub>Co<sub>y</sub>O<sub>2</sub> (which is 0.9072 for 100% SoC),  $M_w$  is the molecular mass of the lithiated active material (95.63 g mol<sup>-1</sup>),  $L$  is the electrode thickness (75.6 μm), and  $\epsilon_{act}$  is the active material volume fraction (0.665). For the negative electrode  $c_s^{max}$  can be calculated from:

$$c_s^{max} = \frac{Q}{FL\epsilon_{act}}. \quad [49]$$

Here  $Q$  is the areal capacity (5.07 mAh cm<sup>-2</sup>),  $L$  is the electrode thickness (85.2 μm), and  $\epsilon_{act}$  is the active material volume fraction (0.75). These yield values of 46420 mol m<sup>-3</sup> and 29603 mol m<sup>-3</sup> for the positive and negative electrodes respectively. The positive electrode maximum concentration is almost twice that of the negative electrode, this is compensated by the positive electrode being cycled in a narrower stoichiometry range and that there is more volume of the negative electrode in the cylindrical cell.

### Diffusion Coefficients

The solid-state diffusion coefficient,  $D_s$ , describes lithium transport within the particles. It can be determined as a function of lithiation using GITT for the active materials. These values were obtained for most of the stoichiometric range of each electrode in half cell configuration (Figure 33). To obtain the diffusion coefficients, the voltage profile from GITT was evaluated using an expression derived from the Sand equation (further details can be found in Chapter 2):

$$D_s = \frac{4}{\pi} \left( \frac{I}{aFL} \frac{U'(c_0)}{m_{fit}} \right)^2 \quad [50]$$

To calculate  $D_s$  this expression relies on the surface area of the particles. For the positive electrode this calculation does not pose a challenge as the active material is composed of spherical particles. However, the negative electrode diffusion coefficient calculation is less certain due to three factors. Firstly the electrode is composed of two active materials, graphite and SiO<sub>x</sub> that will have different diffusion coefficients. Secondly, the graphite is flake-like in nature, meaning calculating the surface area based on a spherical particle size provides a poor approximation. Finally, the volume expansion of these active materials had to be considered: graphite and SiO<sub>x</sub> both undergo volume expansion during lithiation, previous work has demonstrated expansion of 10% and 118% respectively.<sup>13,148</sup> LiNi<sub>1-x-y</sub>Mn<sub>x</sub>Co<sub>y</sub>O<sub>2</sub> active materials do not demonstrate appreciable volume expansion.

These factors are taken into consideration for the calculation of the surface area. Firstly, we take an effective particle radius between the graphite particles (5.86 μm) and SiO<sub>x</sub> (1.2 μm) this equates to 5.4 μm if we assume the electrode is composed of 90% graphite and 10% SiO<sub>x</sub>. Secondly, to consider the volume expansion that these particles undergo we apply a function across the diffusion coefficient values that takes into account the surface area change from a particle radius 5.4 μm (0% lithiation) to 20.0 μm (100%

lithiation). The detailed description of this process can be found in our previous work.<sup>1</sup> Incorporating a fitting factor to account for the varying particle size in silicon oxide significantly altered the calculated diffusion coefficient, highlighting the sensitivity of this parameter to physical changes in the material. However, the value required further adjustment for the model validation due to inaccuracies encountered in GITT analysis.

The observed values for the diffusion coefficients are in strong agreement with values reportedly previously for NMC and graphite electrodes,  $10^{-15}$ - $10^{-11}$   $\text{cm}^2 \text{s}^{-1}$  and  $10^{-12}$ - $10^{-9}$   $\text{cm}^2 \text{s}^{-1}$  respectively.<sup>149,150</sup> For the graphite-SiO<sub>x</sub> electrode the observed displacement between the lithiation and delithiation branches is due to the voltage hysteresis. Typically, diffusion coefficients values are in the range  $10^{-12}$ - $10^{-10}$   $\text{cm}^2 \text{s}^{-1}$ , though features at intermediate lithium concentrations exhibit values in the range  $10^{-15}$ - $10^{-14}$   $\text{cm}^2 \text{s}^{-1}$ . The diffusion values observed for NMC811 demonstrate less variability, values were  $\sim 10^{-11}$   $\text{cm}^2 \text{s}^{-1}$  across most of stoichiometric range, although as the electrode is completely lithiated the diffusion coefficient values falls to  $10^{-14}$   $\text{cm}^2 \text{s}^{-1}$ .

Solid-phase diffusivity can vary greatly, often by several orders of magnitude, primarily due to differences in the microstructural properties of the material, such as particle size, porosity, and crystallinity. Additionally, the operating conditions, like temperature and state of charge, significantly influence the mobility of ions within the solid, further contributing to this wide variation in diffusivity values. Despite this the simulations take an averaged diffusion coefficient; this is a gross simplification and it is possible to define non-constant diffusion across the SoC range.<sup>63</sup> This simplification proves inaccurate as it does not account for the considerable change in magnitude at various states of lithiation. The limitation of this assumption is clear at low SoCs where diffusion in the positive electrode is critically low. Finding these functions is beyond the scope of this chapter, therefore we report averaged diffusion coefficients of  $1.48 \cdot 10^{-15}$   $\text{m}^2 \text{s}^{-1}$  and  $1.74 \cdot 10^{-15}$   $\text{m}^2 \text{s}^{-1}$  for the positive and negative electrodes respectively.

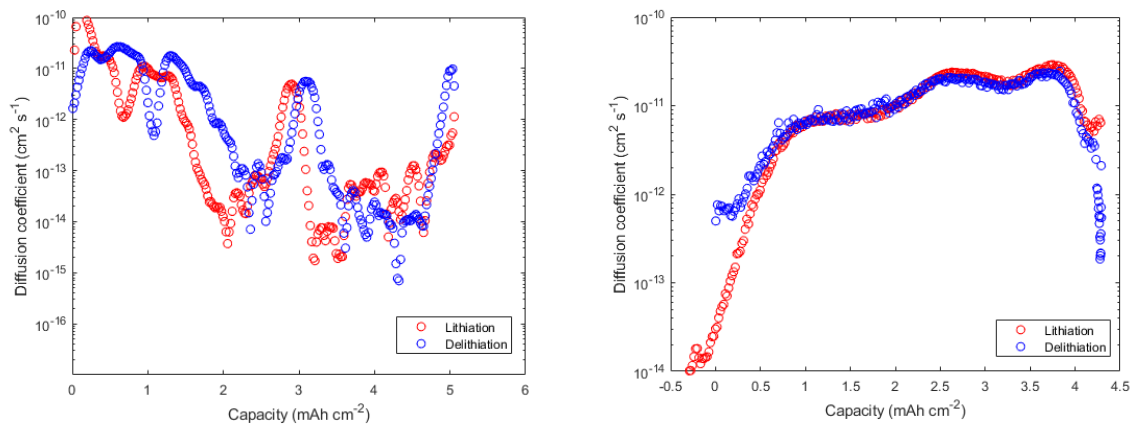


Figure 33. GITT in a half cell configuration demonstrated that the diffusion coefficients for graphite-SiO<sub>x</sub> (left) and NMC (right) vary significantly as a function as state-of-charge.

### Electronic Conductivity

The electronic conductivities of the positive and negative electrode were determined to be  $0.18 \text{ S m}^{-1}$  and  $215 \text{ S m}^{-1}$  respectively. These were averaged values. The variability in the measurements was attributed to microstructural damage that occurs during delamination and heterogeneity of the electrode.<sup>151</sup> The conductivity of the graphite-SiO<sub>x</sub> electrode is 1000 times larger than the NMC-based electrode. This is significantly low conductivity of NMC is attributed to semiconducting behaviour at low lithium concentrations, therefore inhibiting lithium conduction significantly.<sup>152</sup>

### Exchange Current Density

The DFN model requires a quantity to describe the electron transfer as the ions migrate between the electrolyte and the electrode, the exchange current density,  $j_0$ . The Butler-Volmer equation relates the applied electrochemical current density,  $j$ , the overpotential,  $\eta$ , for the electrode reactions:<sup>153</sup>

$$j = j_0 \left( \exp \left[ \frac{(1 - \alpha)F\eta}{RT} \right] - \exp \left[ -\frac{\alpha F\eta}{RT} \right] \right) \quad [51]$$

This expression assumes that the lithium concentration in the bulk is the same as at the electrode surface. Therein,  $\alpha$  is the charge transfer coefficient,  $F$  is the Faraday constant,  $R$  is the ideal gas constant. When the overpotential is very small and the electrochemical system is at equilibrium, expression [51] can be linearised to:

$$j = j_0 \frac{F}{RT} \eta. \quad [52]$$

The definition of the charge transfer resistance  $R_{ct}$  is:<sup>154</sup>

$$\eta = jSR_{ct} \quad [53]$$

Here  $S$  is the electrode-electrolyte surface area. Eqs. [52] and [53] can be transformed into:<sup>155</sup>

$$R_{ct} = \frac{RT}{j_0 SF}. \quad [54]$$

The surface area can be calculated from the total volume of the electrode and the electrode-electrolyte interface per unit volume. Here we assume the particles are spherical, as this is an existing assumption of the DFN model. Subsequently,  $S$  can be evaluated from:

$$S = \frac{3\varepsilon_{act}}{r} V \quad [55]$$

Here  $V$  is the geometrical volume of the electrode used in the electrochemical test (not the cylindrical cell total volume). The electrode is a porous structure so  $S$  will be significantly larger than  $V$ . From Eqs. [54] and [55] it is possible to calculate the exchange current density of the positive and negative electrode if  $R_{ct}$  is known. PEIS measurements were utilised to obtain the charge transfer resistance.

From the PEIS experiments (Figure 34), two characteristic regions will be analysed, and the corresponding resistance values calculated. These two regions describe the dynamic behaviour of the battery:<sup>156</sup>

- $R_0$  at  $-\text{Im}(Z)=0$ : The impedance crosses the x-axis frequency i.e. the inductive behaviour is compensated by the capacitive behaviour. Therefore, the impedance at this point is the pure ohmic resistance of the battery.
- $R_{ct}$  at  $\min(-\text{Im}(Z))$ : The negative imaginary part of the impedance spectrum shows a local minimum at the end of a large semicircle at low frequencies. This semicircle is associated with the charge transfer reactions and the double layer capacitance.

The impedance spectrum was evaluated at various states of charge across the given frequency range 100 kHz to 10 mHz and ZView was used to find the values of resistances by fitting the data to an Equivalent Circuit Model (Figure 35). Evaluating  $R_{ct}$  at 50% SOC yielded  $1.8 \Omega$  and  $14.72 \Omega$  for the positive and negative electrodes respectively. These values yielded exchange current densities of  $0.280 \text{ mA cm}^{-2}$  and  $0.0295 \text{ mA cm}^{-2}$  and are agreeable to previously reported values.<sup>155</sup> These are with respect to the geometric surface area. The fitted Nyquist plots of this material are described in the Supporting Information.

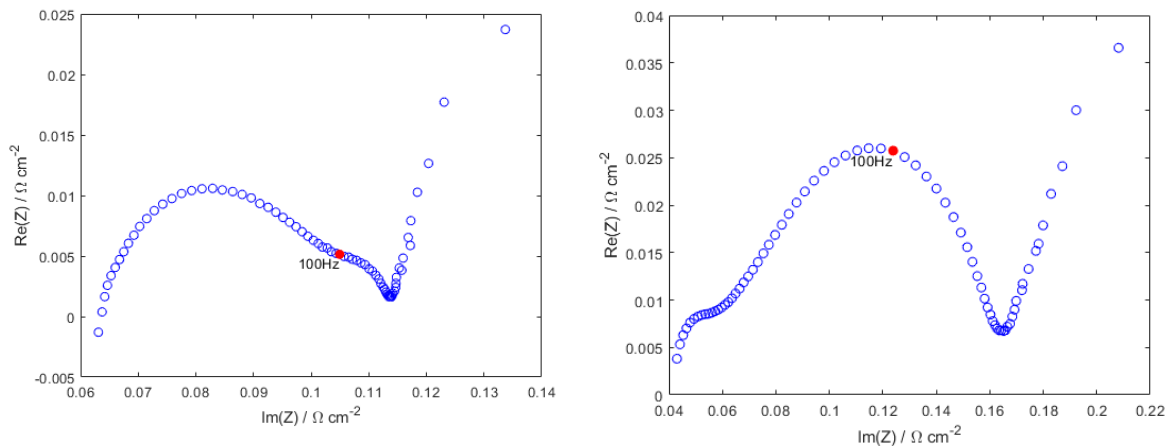


Figure 34. PEIS measurements negative electrode (left) and positive electrode (right).

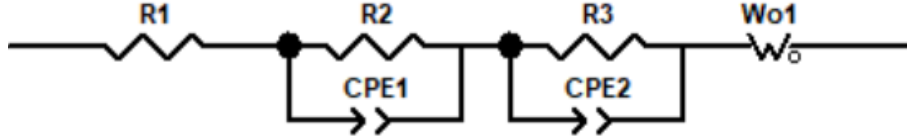


Figure 35. Equivalent circuit model.

Similar to several other parameters, the exchange current density varies as a function of SoC follows a semi-circular profile with a maximum corresponding to a lithium stoichiometry of 0.5.<sup>119</sup> The reason for evaluating the exchange current density at only 0.5 stoichiometry is that this allows a trivial calculation to obtain the reaction rate.

### Reaction Rate

In the DFN model it is assumed that the exchange current density is not obtained directly, and takes the form (if we assume the electrode activity coefficient  $\alpha=0.5$ ):<sup>157</sup>

$$j_0 = k\sqrt{c_e c_s (c_s^{max} - c_s)}. \quad [56]$$

Here  $k$  is the reaction rate,  $c_e$  is the electrolyte concentration,  $c_s$  is the electrode surface concentration, and  $c_s^{max}$  is the maximum electrode concentration. Given that we have evaluated  $j_0$  at a stoichiometry of 0.5,  $c_s$  can be assumed to be equal to  $\frac{c_s^{max}}{2}$ . Thus, the reaction rate can be calculated from:

$$k = \frac{2j_0}{c_s^{max}\sqrt{c_e}} \quad [57]$$

Taking the initial electrolyte concentration as  $1 \text{ mol dm}^{-3}$ , we find that the reaction rates are  $3.59 \cdot 10^{-6} \text{ A m}^{-2}$  and  $6.48 \cdot 10^{-7} \text{ A m}^{-2}$  for the positive and negative electrode respectively.

### Electrolyte Properties

For commercial cells we have no knowledge of the electrolyte composition, methods to ascertain the constituents have been described previously. However, it is difficult to obtain reliable results for the type and volumetric ratio of carbonate solvents, salt concentration, and the additives present. For cell testing we utilised an electrolyte comprised of  $1 \text{ mol dm}^{-3} \text{ LiPF}_6$  in EC:EMC (3:7, v:v) with 1wt% VC. This electrolyte is commonly utilised for research and has been parametrised previously.<sup>158</sup> Nyman *et al.* have provided fitted expressions and plots of their experimental results for the electrolyte diffusion coefficient, electronic conductivity, and the  $\text{Li}^+$  transference number.

The electrolyte diffusion coefficient is defined as follows:<sup>158</sup>

$$D_{l,k}(c_{l,k}) = 8.794 \cdot 10^{-11} c_{l,k}^2 - 3.972 \cdot 10^{-10} c_{l,k} + 4.862 \cdot 10^{-10} \quad [58]$$

The  $\text{Li}^+$  transference number  $t_0^+$ , is the fraction of total electrical current carried in an electrolyte by a given ionic species, and is defined as follows:<sup>158</sup>

$$t_0^+(c_{l,k}) = -0.1287 \cdot c_{l,k}^3 + 0.4106 \cdot c_{l,k}^2 - 0.4717 \cdot c_{l,k} + 0.4492 \quad [59]$$

The electrolyte conductivity is defined as follows:

$$\sigma_{l,k}(c_{l,k}) = 0.1297 \cdot c_{l,k}^2 - 2.51 \cdot c_{l,k}^{1.5} - 0.3229c_{l,k} \quad [60]$$

These expressions are described by functions depending on lithium concentration, but for the numerical simulations we will set  $t_0^+$  to a constant by evaluating Equation [60]. This is because a non-constant transference number is not supported by the software used. For a concentration of  $1 \text{ mol dm}^{-3}$  this yields a value of 0.2594.

The charge transfer coefficient,  $\alpha$ , is usually set to 0.5 for battery modelling, so we make that assumption here too.<sup>159</sup>

### Parameter Summary

Through experimental methods, theoretical derivations, and subsequent analysis we have evaluated over 30 parameters that had been identified for the DFN model. In addition to these parameters, we have provided values for the stoichiometries at 0% and 100% SoC. These values can act as initial conditions in the model, some of the parameters identified are also defined as a function of stoichiometry by the requirements of the model (Table 9). In this investigation we observe only the discharge phenomena in the simulations, therefore we use the stoichiometry at 100% as the initial condition.

Table 9. The full parameter set for the Doyle-Fuller-Newman physics-based model.

	Parameter	Symbol	Unit	Positive Electrode	Separator	Negative Electrode	Reference
Design Specifications	Domain Thickness	$L$	m	$75.6 \cdot 10^{-6}$	$12 \cdot 10^{-6}$	$85.2 \cdot 10^{-6}$	Table 8
	Electrode Plate Area	$A$	m <sup>2</sup>	$1.027 \cdot 10^{-1}$	-	$1.047 \cdot 10^{-1}$	Table 8
	Electrode Active Volume	$V$	m <sup>3</sup>	$7.76 \cdot 10^{-6}$	-	$89.2 \cdot 10^{-6}$	Table 8
	Particle Radius	$r_k$	m	$5.22 \cdot 10^{-6}$	-	$5.86 \cdot 10^{-6}$	Table 8
	Electrolyte Volume Fraction	$\epsilon_{l,k}$	%	33.5	-	25	Eq. [39]
	Active Material Volume Fraction	$\epsilon_{s,k}$	%	66.5	-	75	Eq. [39]
	Bruggeman Exponent	$\beta$	-	1.5	1.5	1.5	Eq. [40]
Electrode	Solid Phase Lithium Diffusivity	$D_{s,k}$	m <sup>2</sup> s <sup>-1</sup>	$1.48 \cdot 10^{-15}$	-	$1.74 \cdot 10^{-15}$	Eq. [50]
	Solid Phase Electronic Conductivity	$\sigma_{s,k}$	S m <sup>-1</sup>	0.18	-	215	-
	Maximum Concentration	$c_{s,k}^{max}$	mol m <sup>-3</sup>	48313	-	29583	Eq. [48] and [49]
	Stoichiometry at 0% SoC	-	-	0.9072	-	0.0279	[44]
	Stoichiometry at 100% SoC	-	-	0.2567	-	0.9014	[44]
Electrolyte	Electrolyte Ionic Diffusivity	$D_{l,k}$	m <sup>2</sup> s <sup>-1</sup>	See Eq. [58][50]			Ref [158]
	Electrolyte Ionic Conductivity	$\sigma_{l,k}$	S m <sup>-1</sup>	See Eq. [60]			Ref [158]
	Transference Number	$t_0^+$	-	0.2594			Ref [158]
	Initial Electrolyte Concentration	$c_{l,ini}$	mol m <sup>-3</sup>	1000			Assumed
Reaction	Open Circuit Voltages	$U_k$	V	Equation [46]	-	Equation [47]	Eq. [46] and [47]
	Activation Energy	-	J mol <sup>-1</sup>	$17.8 \cdot 10^3$	-	$35.0 \cdot 10^3$	Eq. [56]
	Reaction Rate	$K_k$	A m <sup>-2</sup>	$3.59 \cdot 10^6$	-	$6.48 \cdot 10^6$	Eq. [57]
	Charge Transfer Symmetry Factor	$\alpha$	-	0.5	-	0.5	Ref [159]

The experimental methodologies in this investigation have been designed with the aim of achieving a robust parameter set that accurately represents the behaviour of the commercial cell. However, even for the most prudently designed experiments there will always be limiting factors. From this perspective it is important that we state the practical limitations of this investigation:

- Inherent changes in the physical and chemical properties of electrodes that occur in the extraction and delamination process.
- The electrolyte used in this investigation likely has a different composition than the one used in the commercial cell, the electrolyte parameters and OCVs will be different.
- Tortuosity was approximated using the Bruggeman correlation due to inaccuracies that arise in the analysis of image-based techniques to deconvolute this parameter.
- Electrode sampling was random meaning potential non-uniformity in the jelly roll was not captured in a systematic manner.
- Several of the parameters were derived based on the assumption that particles are spherical.

#### **4.3.4 Validation**

Using the parameters we have elucidated it is possible to run simulations based on the DFN model definition (Table 9). An underlying assumption for the DFN model is that the porous electrode can be modelled as a homogenous matrix of spherical particles. This is contrary to the fact that electrodes have non-uniform structure comprised of particles that vary in size and morphology. This gross simplification has significant implications on the transport properties of the electrode but including these intricacies in state-of-the-art models would make the computational expense impractical.<sup>160</sup> With this assumption it is reasonable to expect some of the parameters will need their values tuning to observe better agreement between the simulations and experimental datasets. This tuning process involved systematically tuning individual parameters; the parameters that required tuning were chosen by observing key regions in the voltage profile. Further details of this process can be found elsewhere.<sup>1</sup>

The five parameters adjusted were the diffusion coefficients, the maximum concentrations, and the 100% SOC stoichiometry in the positive electrode (Table 10). These parameters were tuned by comparing the simulations of the discharge process at different C-rates (C/2, 1C, 1.5C) to the experimental data. Note that the parameters adjusted are related to the porous electrode. The solid-state diffusion coefficients do not depend on the current, however, in this case as we use an effective diffusion coefficient, the coefficient needs to capture the variation caused by changes in the concentration. Therefore, the effective diffusion coefficient needs to be adjusted for the individual C-rate to consider its variation caused by changes in concentration. This adjustment needed to be carried out for the negative electrode only as its diffusion was more sensitive to changes in current than the positive electrode. The significant variation



between the experimentally derived values and those used in simulation can be attributed to the assumptions made when calculating the diffusion coefficients. Spherical particles, constant volume fractions, and constant particle size contribute to this disparity. Although we have accounted for volume expansion in the  $\text{SiO}_x$  and graphite this fitting factor does not provide a perfect description of the volume expansion due to lithiation.

The simulation results based on the updated parameter set demonstrate a good approximation to the experimental datasets for all the C-rates (Figure 36). The experimental dataset is obtained from tests on the cylindrical cell undergoing a CC discharge followed by an open-circuit voltage period. The voltage error does not show any significant difference across the three C-rates, confirming the parameters are valid under various discharge conditions. The most noticeable distinction is that the 1.5C C-rate had the lowest peak error during the discharge regime, this error was 480 mV (Table 11). The largest error during the profile was during the relaxation period. The behaviour during the relaxation period is dependent on electrode diffusion so any inaccuracy is likely due to the use of constant parameters.

The agreement observed between experimental and simulated datasets is notable considering that only five of the experimentally derived parameters had to be tuned. The model accurately captures the discharge and the final voltage after relaxation, the disparity between the datasets occurs during the beginning of the relaxation period. The deviations between the experimental and simulated electrochemical data might be attributed to the following limitations in the model:

- Inadequate description for ionic transport on longer time scales i.e. diffusion. These limitations are borne from modelling with a constant diffusion coefficient despite the variation over four orders of magnitude. This limitation was particularly evident as the positive electrode diffusion coefficient dropped significantly at low SOC and due to the required 1800% tuning of the negative electrode diffusion coefficient (Table 10). This significant tuning highlights the inaccuracy of traditional GITT analysis.
- Detailed microstructural information was elucidated in the experiments but is not accounted for in the model. The simulations in this investigation rely on the assumption that electrodes are homogenous and made up of monodisperse spherical particles. More sophisticated models can account for polydispersity, multiple active materials, and electrode heterogeneity, although their utility may be limited due to computational expense.

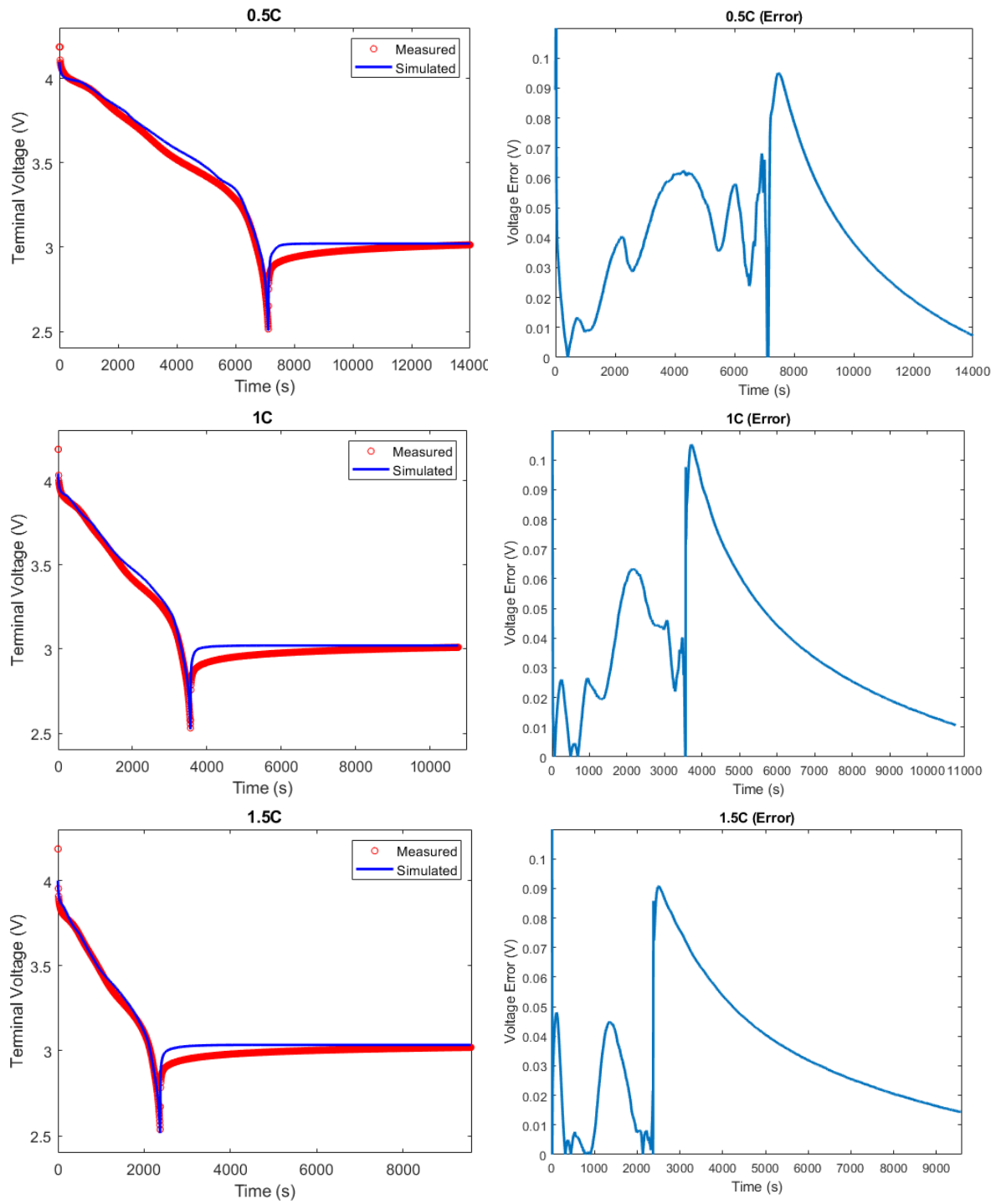


Figure 36. Comparison of the experimental data (blue line) and the DFN simulations (red circles) and the absolute error between these two datasets.

Table 10. Comparison of experimentally derived parameter and tuned parameters for 0.5C, 1C, and 1.5C experimental datasets.

\*The negative diffusion coefficient was tuned to a different value for to provide better fits for the 0.5C/1C/1.5C discharge profiles.

	Symbol	Units	Experiment	Simulation	Variation (%)
Positive Electrode Diffusion Coefficient	$D_{s,p}$	$\text{m}^2 \text{s}^{-1}$	$1.48 \cdot 10^{-15}$	$4.0 \cdot 10^{-15}$	170
Negative Electrode Diffusion coefficient	$D_{s,n}$	$\text{m}^2 \text{s}^{-1}$	$1.74 \cdot 10^{-15}$	$*1.3/3.3/6.3 \cdot 10^{-14}$	1797
Positive Electrode Maximum Concentration	$c_{s,p}^{max}$	$\text{mol m}^{-3}$	48313	63104	31
Negative Electrode Maximum Concentration	$c_{s,n}^{max}$	$\text{mol m}^{-3}$	29583	33133	12
Positive Electrode 100% Stoichiometry	-	-	0.2567	0.26	1.3

Table 11. Root-mean-squared error and peak error for the output voltage between the DFN simulation and experimental data at 0.5C, 1C, and 1.5C. The RMSE are analysed over the discharge and relaxation regimes, whereas the peak errors are evaluated for the discharge regime only.

C-rate	RMSE (mV)	Peak Error (mV)
0.5C	25.5	625
1C	24.4	630
1.5C	27.5	480

## 4.4 Conclusions

This chapter enhances understanding and simulation results of commercial lithium-ion cells. Adopting both physical experimentation and modelling, a comprehensive parameter set for a commercial cell has been elucidated for a physics-based model. Out of the complete parameter set, only 5 required tuning to align the simulations of the Doyle-Fuller-Newman (DFN) model with experimental observations, achieving a low error margin. This demonstrates the precision of our parameterisation, which has significantly contributed to the field, as evidenced by its extensive use in literature, including research to improve fast charging, thermal modelling and cell design.

This chapter addressed the critical challenge of parameter determination, a process that is time-consuming. By employing teardown and gravimetric techniques, we successfully extracted cell materials with minimal degradation. This approach, combined with three-electrode testing, provided precise measurements of open-circuit voltages for individual electrodes across their full stoichiometric ranges.

The simulations conducted at 0.5C, 1C, and 1.5C discharge rates, along with their relaxation profiles, demonstrated good accuracy across most conditions, particularly in transient behaviours and at the relaxation's end. However, the initial relaxation phase presented challenges, signalling the need for variable diffusion coefficients—a hypothesis further supported by the requirement to adjust the negative electrode diffusion coefficient for enhanced model fidelity. This adaptation, while necessary, reflects broader limitations inherent in both experimental and theoretical frameworks, such as

those encountered in galvanostatic intermittent titration technique (GITT) and electrochemical impedance spectroscopy (EIS) methods, as well as assumptions within the DFN and Butler-Volmer equations.

These assumptions, especially the constant diffusion coefficients and the independence of electrochemical kinetics from stoichiometry, result in significant discrepancies between model predictions and experimental data. Such assumptions fail to account for the dynamic nature of battery materials, whose properties change with lithium concentration and operating conditions. By integrating non-isothermal behaviours and the dependence of key parameters on stoichiometry, this chapter identifies these issues as limitations of the current research. Meanwhile, the following chapter aims to enhance theoretical modelling and practical measurement techniques by addressing these effects.

In conclusion, this chapter has established a foundational framework for the accurate simulation of lithium-ion batteries, marking substantial progress in parameter determination and model validation. However, it also highlights areas for future research. There is a critical need for advancements in experimental techniques and the development of more sophisticated theoretical models that can account for the complex, variable behaviour of battery materials. Further efforts are essential to incorporate the nuanced dependencies of battery performance on state of charge, temperature, and microstructural characteristics, aiming for an increasingly accurate approximation of real-world battery behaviour.

# Chapter 5: Thermal-electrochemical parameters of a high energy lithium-ion cylindrical battery

Based on **Thermal-electrochemical parameters of a high energy lithium-ion cylindrical battery**. Kieran O'Regan, Ferran Brosa Planella, W. Dhammika Widanage, and Emma Kendrick, *Electrochimica Acta*, **425**, 140700, (2022).<sup>7</sup>

## 5.1 Introduction

Research has previously compared differences in energy and power cells, investigating their physical and electrochemical properties.<sup>161,162</sup> These works highlight the need to include the thermal performance in modelling, battery performance is strong dependent on temperature. Additionally, the research that has parameterised both thermal and electrochemical behaviours in batteries has often not involved measuring the specific heat capacities and thermal conductivities of the individual materials needed to describe thermal performance, this is known as a lumped thermal model. A lumped battery thermal model simplifies the complex thermal behaviour of a battery into discrete components to predict temperature distribution.<sup>63,163</sup>

In this chapter we parameterise the LG M50, a cell that with a high energy density of  $267 \text{ Wh kg}^{-1}$ , attributed to high electrode coat weight and its composition of  $\text{Li}[\text{Ni}_{1-x-y}\text{Mn}_x\text{Co}_y]\text{O}_2$  (NMC) and  $\text{SiO}_y$  materials. To our knowledge, this is to date the highest energy cell reported in literature, for which parameterisation has been performed, and the only cell to have the thermal characteristics for the electrodes and cell ( $267 \text{ Wh kg}^{-1}$ ). The parameterisation provides the modelling community with the data to predict thermal inhomogeneities within the cell by detailing the cell anatomy and the thermal transport properties required to extend to 3D. Including the information allows better predictions about battery performance to be made, therefore allowing more efficient thermal management systems to be designed.

The M50 has become popular in the academic battery modelling community. The thermal parameters for this cell have not been outlined, meaning research has neglected the thermal behaviour or used properties not specific to the M50.<sup>1,3,164</sup> Presently, the influence of temperature on the electrochemical behaviour has not been included or these properties required have been taken from a different cell.<sup>2</sup> This work details the complete experimental design for a thermal-electrochemical parameterisation of a 21700 cylindrical cell to evaluate the geometric, electrochemical, and thermal properties of the electrodes, separator, and current collectors. In addition to providing the information necessary for a 3D thermal model, the lithium concentration and temperature parameter dependencies are documented to enable more accurate model predictions by accounting for the local variability in performance during cell operation. Models often neglect the effect of lithium concentration and temperature on cell properties,<sup>115,165</sup> despite the parameters being significantly influenced by these variables.<sup>62</sup> This includes the experimental methodology and the mathematical analysis

to assess these parameter-dependencies, which can be applied to commonly used NMC and graphite materials.

The parameter requirements were based on the most utilised electrochemical model developed by Doyle, Fuller, and Newman (DFN) outlined in Table 3<sup>31</sup>. This chapter focusses on presenting parameters relevant to capture 3D thermal behaviour, with equations outlined in Table 4. However, to validate the parameters against experimental data, a pseudo-two-dimensional (P2D) electrochemical coupled to a lumped (0D) thermal model was used.

## **5.2 Experimental**

### **5.2.1 Teardown Procedure**

The battery investigated was a 5 Ah M50 21700 cylindrical cell manufactured by LG Chem. This cell utilises nickel-rich NMC811 and SiO<sub>2</sub>-graphite active materials. To extract the components the cell was discharged and disassembled in a glovebox. The teardown methodology has been described previously and detailed chemical and physical composition can be found in Table S1 in the Supporting Information.<sup>1</sup>

During the teardown the gravimetric and volumetric contribution of each component was measured: the jellyroll was weighed immediately after disassembly, and again after the electrolyte had been evaporated to evaluate solvent content. The anatomy of the cell was detailed, and the components were separated for individual analysis. To evaluate the mass of electrode coating the current collectors were delaminated. The positive electrode was soaked in N-methyl-2-pyrrolidone (NMP) and sonicated at 70 °C to remove the coating. The negative electrode coating was removed using water. The measured weight of the bare current collectors was used to calculate the total black mass for each electrode. The electrode black mass was used to measure specific heat capacity. For further characterisation, a pristine cell was dismantled, and fresh electrodes extracted. For the electrochemical testing, one side of the coating had to be removed and to measure the thermal conductivity the double-sided electrode was left intact.

### **5.2.2 Thermophysical Characterisation**

#### **Differential Scanning Calorimetry (DSC)**

The specific heat capacities of the dried composite powders and the separator were evaluated by applying a continuous method on a DSC 1 from Mettler Toledo between 25 °C and 100 °C. The heating rate was set at 10 K min<sup>-1</sup> with a sampling interval of 0.1 s. Three repeats of the blank pans, sapphire reference, and the samples were measured. The sample weights were approximately 10 mg.

#### **Laser Flash Analysis (LFA)**

The through-plane thermal diffusivity was measured for the electrodes using laser flash analysis (LFA 467 HyperFlash, Netzsch). This measurement was carried out at temperatures of -5 °C, 10 °C, 25 °C, 40 °C, and 55 °C using a nitrogen purge gas. For this

measurement samples of 20 mm x 20 mm were used, each sample was measured five times at each temperature.

### 5.2.3 Thermal-electrochemical Characterisation

To deconvolute the behaviours of the negative and positive electrode a three-electrode configured PAT-Cell (EL-Cell) and a perfluoroalkoxy alkane Swagelok™ half-cell (using lithium metal as the counter electrode) were utilised for the electrochemical testing. The three-electrode cell was comprised of an 18 mm negative and positive electrode, a 21.6 mm double layered separator comprised of 180  $\mu\text{m}$  polypropylene woven layer and a 38  $\mu\text{m}$  polyethylene membrane (EL-Cell), with 100  $\mu\text{l}$  of electrolyte. The half-cell was comprised of a 11 mm working electrode, a 12 mm lithium counter electrode, 12.8 mm Celgard 2325 tri-layer separator (polypropylene/polyethylene/polypropylene) and 50  $\mu\text{l}$  of electrolyte. The electrolyte used was 1  $\text{mol dm}^{-3}$   $\text{LiPF}_6$  in ethylene carbonate: ethylmethylcarbonate (3:7, v:v, Soulbrain). The electrochemical protocols were programmed on a VMP3 potentiostat (Bio-Logic). Electrochemical testing was preceded by two cycles of C/20 CC CV charge (CV cut-off was C/50) and CC discharge between 2.5 V and 4.2 V. The C-rate was based upon the discharge capacity for the second cycle. For temperature control a programmable climatic chamber (Temperature Applied Sciences) with an accuracy of  $\pm 1$   $^{\circ}\text{C}$  and a fan i.e. forced convection.

### Galvanostatic Intermittent Titration Technique (GITT)

GITT was conducted at temperatures of 5  $^{\circ}\text{C}$ , 15  $^{\circ}\text{C}$ , 25  $^{\circ}\text{C}$ , 35  $^{\circ}\text{C}$ , and 45  $^{\circ}\text{C}$  in a three-electrode cell between 2.5 V and 4.2 V. Transients were C/10 CC for 150 seconds and the relaxation period was limited to a duration of 2 hours or when the voltage decay with time was  $dE/dt < 0.1 \text{ mV h}^{-1}$ .

### Entropy Determination (Potentiostatic method)

OCV measurements were carried out at temperatures of 25  $^{\circ}\text{C}$ , 15  $^{\circ}\text{C}$ , 5  $^{\circ}\text{C}$ , -5  $^{\circ}\text{C}$  at SoCs between 0% and 100% (10% intervals) in a three-electrode cell. The cell was initially charged to 100% SoC with C/5 CC CV (C/50 cut-off), then was discharged for 1 h by a C/10 CC step at 25  $^{\circ}\text{C}$  i.e. to 90% SoC. The battery was subsequently allowed to relax for 15 h at the same temperature, after which the thermal cycle (15 $^{\circ}\text{C}$ , 2 h; 5  $^{\circ}\text{C}$ , 2 h; -5  $^{\circ}\text{C}$ , 2 h) was applied. This process was repeated until a final SoC of 0% was attained.

### Potentiostatic Electrochemical Impedance Spectroscopy (PEIS)

PEIS measurements were conducted at SoCs between 10% and 100% for temperatures 15  $^{\circ}\text{C}$ , 25  $^{\circ}\text{C}$ , 35  $^{\circ}\text{C}$ , and 45  $^{\circ}\text{C}$  in a Swagelok half-cell. The sinusoidal current applied had an amplitude of 10 mV and a 10 mHz – 100 kHz frequency range. The data was analysed by fitting to an equivalent circuit model in Zview (Ametek).

### Four-point Probe

The electronic conductivity of the positive electrode was evaluated at temperatures 15  $^{\circ}\text{C}$ , 20  $^{\circ}\text{C}$ , 25  $^{\circ}\text{C}$ , 30  $^{\circ}\text{C}$ , and 35  $^{\circ}\text{C}$  using a four-point probe (Ossila Instruments). The positive electrode coating was delaminated using liquid gallium to dissolve the aluminium current collector and obtain the electrode coating undamaged. Small quantities of 1  $\text{mol dm}^{-3}$  hydrochloric acid and deionised water were used to remove the

gallium alloy. This methodology has been described in detail previously.<sup>166</sup> To measure the electronic conductivity of the positive electrode a target current of 100  $\mu\text{A}$  was used, the voltage was stepped by 0.1 V until the target current had been reached.

### Model Validation

The thermal-electrochemical model was validated for discharge rate capability tests at various temperatures, the temperature during these experiments was monitored to validate the heat generation component of the model. The heat generation was measured using an external thermocouple on the cylindrical cell. Before the experiment there is a two hour rest period to record the initial state. Then the cell was charged at 0.3C with a C/100 current cut-off for the CV step, and discharged at C/10, C/2, 1C, and 2C using a Maccor battery tester. The voltage window used was 2.5 V - 4.2 V. Between each charge and discharge there was a two hour rest period. The testing protocol was carried out at 0 °C, 10 °C, and 25 °C with the chamber temperature being measured throughout the experiment.

#### 5.2.4 Simulations

Simulations were conducted in the Python Battery Mathematical Modelling (PyBaMM) software package (using v0.4.0).<sup>109</sup> The equations for the thermal-electrochemical model are summarised in Table 3 and Table 4. In order to solve the model a finite volume scheme was used, with 30 grid points for each electrode and the separator, and 150 grid points for each particle; resulting in a system of 9092 ODEs and 150 algebraic equations. An exponential mesh was used to help with the convergence of the solver. In order to solve the system, a CasADI solver was used.<sup>167</sup> Each simulation of discharge plus relaxation takes 10 to 20 minutes using an Intel Core i7-7660U (2.50GHz) processor and 16 GB RAM. This is because the nonlinear diffusion takes the solver many iterations to converge. The computational time could be reduced by using more sophisticated numerical methods, but this is out of the scope of this work. It should be noted that reduced models such as the thermal single particle model with electrolyte (TSPMe)<sup>3</sup> yield very similar results with a significant reduction of the computational time. TSPMe simplifies the Doyle-Fuller-Newman (DFN) model by not considering electrode thickness, offering a simplified approach.

## 5.3 Results and Discussion

### 5.3.1 Cell Structure

The cell structure describes the geometry and the anatomy, this information is needed to resolve a 3D thermal model.<sup>168</sup> The structure can be used to build a complex model to predict inhomogeneities due to detail relating to the internal cell layered structure, including tab location, winding structure, and gravimetric contributions.

The cell is comprised of a of high nickel  $\text{Li}[\text{Ni}_{1-x-y}\text{Mn}_x\text{Co}_y]\text{O}_2$  positive electrode material and a  $\text{SiO}_y$ -graphite negative electrode, with a ceramic-coated polyolefin separator.<sup>1</sup> This information and the specifications provided by the manufacturer are summarised in Table S1 in the Supporting Information. The dimensions of the cell, including tab locations, are illustrated in Figure 37, with the tabs are located at opposite ends; from



the top view, the positive tab is positioned 90° clockwise from the negative tab. The positive tab is 7.0 cm in length and is visible from both sides, whereas the negative tab is 5.0 cm in length and only visible from the side that has the electrode coating facing the inside of the jellyroll. Photographs of these tabs can be found in the Figure S4 with their dimensions are outlined in Table 12.

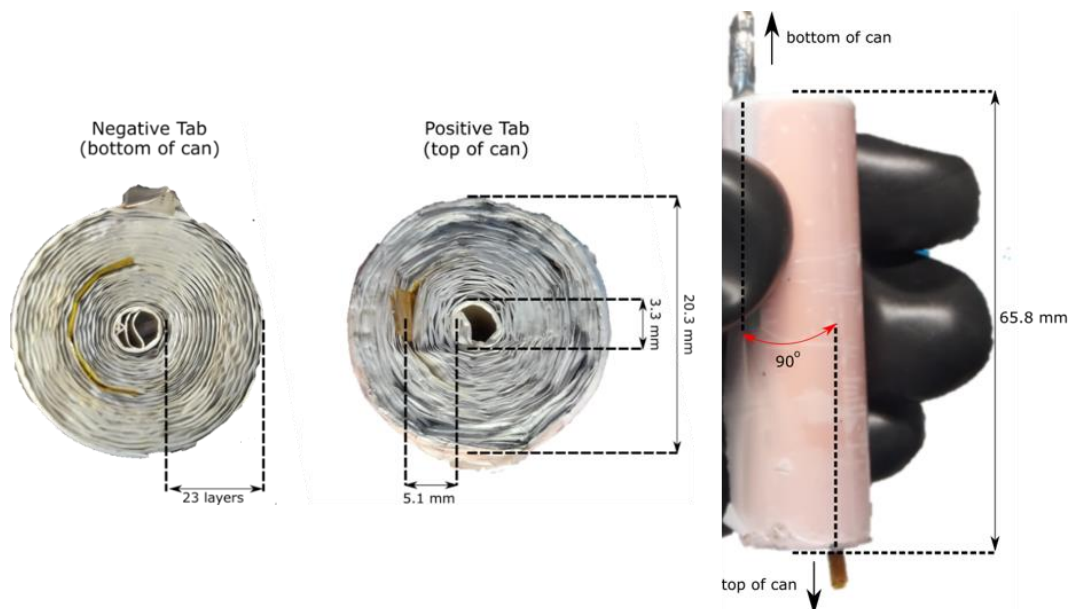


Figure 37. Tab locations (left) and a macro-view to illustrate tab positioning (right).

The cell jellyroll is electrically isolated from the cell casing by a thin plastic layer (thickness 20  $\mu\text{m}$ ) in the radial direction. In the axial direction, there is a thick plastic disc (thickness 0.22 mm) at the bottom and a perforated fibrous membrane (thickness 0.2 mm) at the top (Figure S4 in the Supporting Information). These components significantly lower the axial thermal conductivity by forming a barrier for heat conduction through the current collectors to the casing. The jellyroll is comprised of an electrode stack of two separators, a double-side coated positive electrode, and a double-side coated negative electrode. The copper current collector was not completely coated (Figure S4 in the Supporting Information). The jellyroll consisted of ca. 23 windings of the electrode stack, with the schematic of a single stack illustrated in Figure 38.

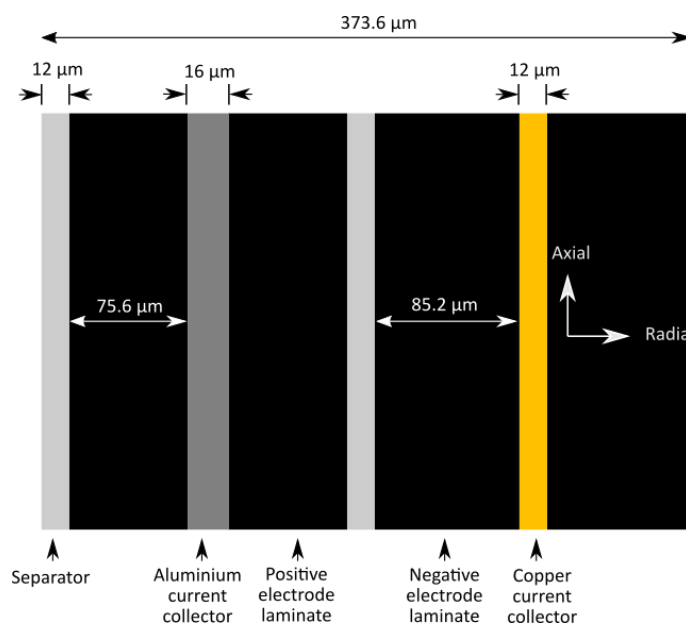


Figure 38. Schematic of an individual electrode layer.

The gravimetric and volumetric contributions of the components are summarised in Table 13. Immediately after disassembly, all the components of the cell were measured to account for solvent lost via evaporation. The jellyroll mass included any electrolyte still present and that lost during disassembly. The remaining solvent was evaporated to obtain a total electrolyte mass of 3.33 g. For the electrolyte assumed in this investigation,  $1 \text{ mol dm}^{-3} \text{ LiPF}_6$  in 3:7 EC:EMC (v:v), this corresponded to a salt content of 0.47 g, and a total electrolyte mass of 3.80 g. It was assumed this salt content was equally distributed within the separator and electrode coatings; these contributions were subtracted from the components. The mass of the separator, positive electrode, and negative electrode windings were 1.96 g, 28.96 g, and 22.36 g. After delaminating the coatings, the black mass of the individual components was evaluated. The volumetric contribution of each component could then be calculated, these are outlined in Table 13, with the densities of copper, aluminium, the stainless-steel cell casing, and the electrolyte taken from literature.<sup>169,170</sup>

Table 12. Properties and anatomy of the cell. \*With electrolyte \*\*Surface area of jellyroll.

Property	Unit	Value
Volumetric energy density	Wh L <sup>-1</sup>	752
Specific energy density	Wh kg <sup>-1</sup>	267
Jelly roll width/height	m	$2.03 \cdot 10^{-2}$ / $6.58 \cdot 10^{-2}$
Jelly roll volume	m <sup>3</sup>	$2.13 \cdot 10^{-5}$
Jelly roll surface area**	m <sup>2</sup>	$4.84 \cdot 10^{-3}$
Cell width / length	m	$2.1 \cdot 10^{-2}$ / $71 \cdot 10^{-2}$
Casing thickness	m	$3.4 \cdot 10^{-4}$
Cell volume	m <sup>3</sup>	$2.43 \cdot 10^{-5}$
Negative tab width / length / thickness	m	$4.00 \cdot 10^{-3}$ / $5 \cdot 10^{-2}$ / $1 \cdot 10^{-4}$
Negative tab position	-	Figure S5
Positive tab width / length / thickness	m	$3.5 \cdot 10^{-3}$ / $7 \cdot 10^{-2}$ / $1 \cdot 10^{-4}$
Positive tab position	-	Figure S5
Mass of cell	kg	$6.83 \cdot 10^{-2}$
Mass of jellyroll*	kg	$5.71 \cdot 10^{-2}$

Table 13. Gravimetric and volumetric contributions of components within the cell. \*Electrolyte is excluded from volume calculation as it is soaked into the electrodes and separator.

Component	Weight / g	Volume / cm <sup>3</sup>
Negative electrode coating	16.51 (24.2%)	9.49 (41.2%)
Copper foil	5.85 (8.6%)	0.66 (2.9%)
Positive electrode coating	26.09 (38.3%)	7.98 (35.1%)
Aluminium foil	2.87 (4.2%)	1.06 (4.7%)
Separator	1.96 (2.9%)	2.07 (9.1%)
Electrolyte (incl. LiPF <sub>6</sub> )	3.80 (5.6%)	3.12*
Casing	10.64 (15.6%)	1.35 (5.9%)
Other	0.39 (0.6%)	0.10 (0.4%)
Jellyroll	57.08	21.3
Cell	67.25	24.2

### 5.3.2 Thermophysical Characterisation

This section outlines the properties needed to accurately predict thermal transport and local temperature inhomogeneities in a cell. Information including the specific heat capacities and thermal conductivity of each material is often not outlined or measured in cell parameterisations.<sup>62,74</sup> This information can be combined with details of cell anatomy to construct an accurate 3D thermal model. Table 16 describes the thicknesses, densities, specific heat capacities, and thermal conductivities for all the individual cell components. This allows model to capture this detail rather than using macro-properties for thermal transport.

The specific heat capacity of the active materials was measured from the composite powders, whereas the thermal conductivity could not be measured directly so thermal diffusivity is measured first to calculate it. The thermal properties of the components should be considered with the presence of electrolyte as the commercial cell is comprised this way and the electrolyte significantly effects thermal transport.<sup>104,171</sup> However, due to the volatility of the electrolyte, ex situ measurements could not be carried out for the separator or electrode and in situ measurements do not allow the deconvolution of the thermal properties of individual components—this is needed to enable physics-based models to predict thermal inhomogeneities. Here we outline a method to calculate the thermal properties of the wetted electrode using experimental data from the extracted electrodes.

It is important to directly measure the thermal properties of the electrodes as microstructure significantly effects heat transport and generation within the battery.<sup>172,173</sup> However, due to difficulty extracting any usable quantity of electrolyte, the thermal properties of a known electrolyte 1 mol dm<sup>-3</sup> LiPF<sub>6</sub> in 1:1:1 EC:EMC:DMC (v:v) was used (this is dissimilar from the electrolyte used in the electrochemical tests and model which is 1 mol dm<sup>-3</sup> LiPF<sub>6</sub> in 3:7 EC:EMC (v:v)).<sup>174</sup> The heat capacity and thermal conductivity of this electrolyte were used in the following section as LiPF<sub>6</sub> in carbonate electrolytes are assumed to have similar properties and the model is not significantly sensitive to electrolyte parameters, the information is summarised Table 16. Li et al., in their parameter sensitivity analysis of an electrochemical model-based study, observed that for a commercial cylindrical (21700) lithium-ion cell with NCA/Gr-SiOx chemistry, the parameters concerning the separator and electrolyte, derived from several papers, demonstrated insensitivity in relation to this specific cell type.<sup>64</sup>

The following measurements were carried out on materials extracted from a cell fully discharged to 2.5 V i.e. 0% SoC. The effect of lithiation on the thermal properties such as specific heat capacity and thermal conductivity, was not considered here due to the difficulty in maintaining air stability at higher states of charge. It should be noted that the state of lithiation does significantly influence heat transport properties as described in a previous work, it was shown that the thermal diffusivity only changed by 15% for LiNi<sub>1-x-y</sub>Mn<sub>x</sub>Co<sub>y</sub>O<sub>2</sub> across the whole lithium stoichiometry range.<sup>175</sup> In practice, the change would be less significant as the materials are never fully lithiated/delithiated.

### Specific Heat Capacity

The specific heat capacity describes the heat energy required to raise a material by a unit of energy, this relates to how easily the temperature rises within a cell and helps the model to predict temperature gradients. Selection of materials with a high specific heat capacity means more energy is needed to raise the internal temperature of a cell reducing the presence of internal gradients. This property was measured for the delaminated electrode powders and the separator as it is not dependent on microstructure (Figure 39). The values for the black masses provide an aggregate heat capacity for the active material, binder, and carbon black. The reported specific capacities corroborate the values reported previously for an NMC/graphite battery.<sup>171</sup>

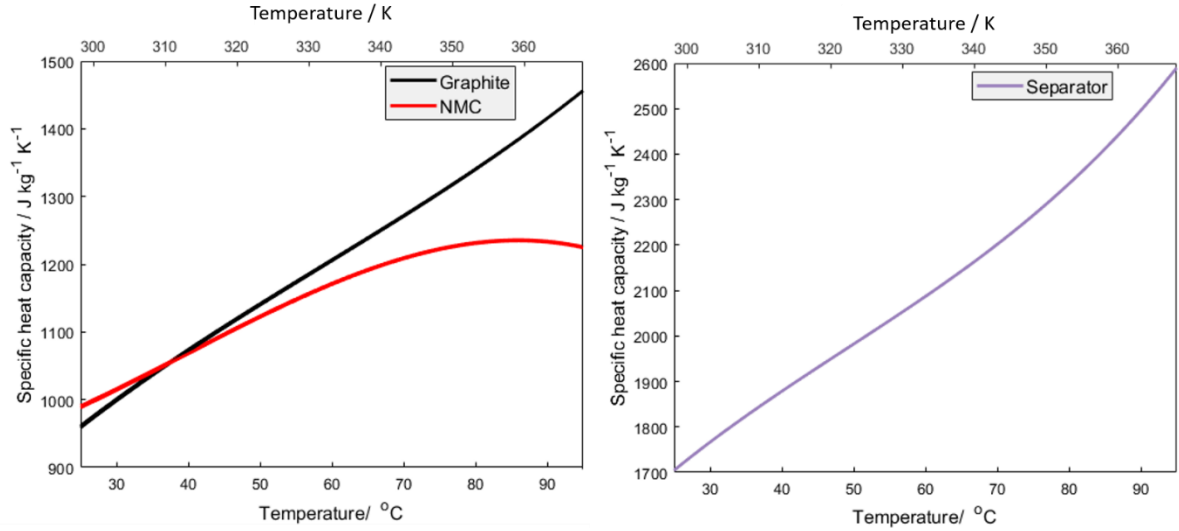


Figure 39. Specific heat capacities for the NMC composite powder (red), the graphite composite powder (black), and the separator (purple). The specific heat capacities for the NMC powder, graphite powder, and separator are represented by Equations [61] to [63]

To capture the change in specific heat capacity due to temperature in the model a function is needed to describe this relationship. The Debye theory of specific heat states that the specific heat of solids is proportional to  $T^3$  if the temperature is below the Debye temperature, which is reported to be 141 °C for graphite and between 136 °C - 204 °C for the transition metals in NMC.<sup>176</sup> We can therefore fit the specific heat capacity against temperature data using third order polynomial according to Debye theory ( $R^2 > 0.997$  in [61] to [65]):

$$\text{NMC} \quad -0.0008414 \cdot T^3 + 0.7892 \cdot T^2 - 241.3 \cdot T + 2.508 \cdot 10^4 \quad [61]$$

$$\text{Graphite-} \quad 0.0004932 \cdot T^3 - 0.491 \cdot T^2 + 169.4 \cdot T - 1.897 \cdot 10^4 \quad [62]$$

$$\text{SiO}_y$$

$$\text{Separator} \quad 0.001494 \cdot T^3 - 1.444 \cdot T^2 + 475.5 \cdot T - 5.13 \cdot 10^4 \quad [63]$$

It is important to capture these phenomena using scientifically robust descriptions rather than arbitrary functions. The fits for the electrode powders and separator are illustrated in Figure 39, with the comparison to raw data in Figure S3, found in the Supporting Information.

The current collectors also make a notable proportion of the cell mass (>7%) so the variability of the specific heat capacities can also be captured to better predict local inhomogeneities in temperature. The heat capacities across the normal temperature operating range of a battery for aluminium and copper were taken from literature and fitted to third order polynomials to capture the parameter-dependency using Debye theory (where  $T$  is in Kelvin and units are  $\text{J kg}^{-1} \text{K}^{-1}$ ). These relationships are outlined in Equations [64] and [65]<sup>177</sup>

$$\text{Aluminium} \quad 4.503 \cdot 10^{-6} \cdot T^3 - 0.006256 \cdot T^2 + 3.281 \cdot T + 355.7 \quad [64]$$

$$\text{Copper} \quad 1.445 \cdot 10^{-6} \cdot T^3 - 0.001946 \cdot T^2 + 0.9633 \cdot T + 236 \quad [65]$$

The decreasing NMC specific heat capacity above 80 °C could be due to decomposition of the binder within the sample, as there are no phase transitions within this range.<sup>178</sup> However, this is beyond the normal operating range of a battery cell so this information would not be captured by the simulations.

The effect of the electrolyte is included by calculating the volumetric heat capacity for the wetted electrode from the volumetric heat capacities of each bulk material as shown in Equation [66]:

$$\bar{\theta} = \rho_s \cdot C_{p,s} \cdot \varepsilon_s + \rho_l \cdot C_{p,l} \cdot \varepsilon_l. \quad [66]$$

$\bar{\theta}$  is the averaged volumetric heat capacity; while  $\rho$ ,  $C_p$ , and  $\varepsilon$  are the density, gravimetric heat capacity and volume fraction for the electrode and electrolyte, respectively. The densities and the specific heat capacities of the electrolytes and the dry electrodes can be found in Table 16, and the electrolyte volume fraction in the positive and negative electrode is 0.335 and 0.25 respectively. Similarly, the averaged density  $\bar{\rho}$  of the saturated electrodes can be calculated from the densities of the electrode solid and liquid components:

$$\bar{\rho} = \rho_s \cdot \varepsilon_s + \rho_l \cdot \varepsilon_l. \quad [67]$$

The volumetric heat capacity for the wetted positive electrode and wetted negative electrode are  $3340000 \text{ J m}^{-3} \text{ K}^{-1}$  and  $1740000 \text{ J m}^{-3} \text{ K}^{-1}$ . Then the gravimetric heat capacity of the wetted electrodes is calculated by dividing the averaged volumetric heat capacity (calculated above) by the averaged density of the saturated electrodes ( $3700 \text{ kg m}^{-3}$  and  $2060 \text{ kg m}^{-3}$  for positive and negative electrode). This provides a gravimetric heat capacity of  $900 \text{ J kg}^{-1} \text{ K}^{-1}$  and  $845 \text{ J kg}^{-1} \text{ K}^{-1}$  for the wetted positive electrode and negative electrode (without the current collectors) at 25 °C. As the specific heat capacity of the dry electrode bulk (powder) varies with temperature, this dependency can be included for the wetted electrode:

$$\overline{C_p} = \frac{\bar{\theta}}{\bar{\rho}}. \quad [68]$$

Here  $\bar{\theta}$  and  $\bar{\rho}$  are calculated from [66] and [67] respectively, the other values are summarised in Table 15.

Table 14. Values used to calculate the specific heat capacity of the wetted porous electrodes and separator.

Parameter	NMC811	Graphite-SiO <sub>y</sub>	Separator
Density of porous material ( $\rho_s$ ) / kg m <sup>-3</sup>	3270	1740	946
Heat capacity of bulk material ( $C_{p,s}$ ) / kg m <sup>-3</sup>	Eq. [61]	Eq. [62]	Eq. [63]
Density of electrolyte ( $\rho_l$ ) / kg m <sup>-3</sup>	1280	1280	1280
Heat capacity of electrolyte ( $C_{p,l}$ ) / J K <sup>-1</sup> kg <sup>-3</sup>	229	229	229
Electrolyte volume fraction ( $\varepsilon_l$ )	0.335	0.25	0.47
Density of wetted material ( $\rho_{s+l}$ ) / kg m <sup>-3</sup>	3700	2060	1620

### Thermal Conductivity

The thermal conductivity describes the ability of a material to conduct heat, representing how quickly heat can pass through the material, whereas thermal diffusivity quantifies the rate at which heat spreads through a material, combining the effects of conductivity, density, and specific heat capacity. While conductivity focuses on the flow of heat, diffusivity considers how rapidly temperature changes within the material occur due to that heat flow. In this paper we use, laser flash to measure the thermal diffusivity of the electrodes by observing the time it takes for a pulse of laser energy to cause a temperature change on the opposite side of a sample. These properties are influenced significantly by the anisotropic structure of a cell and means that the thermal conductivities of the individual components can be evaluated to predict thermal gradients. For the electrode materials the thermal conductivity  $\lambda$  was obtained from the following Equation [69]:<sup>106</sup>

$$\lambda = \alpha \rho C_p. \quad [69]$$

Here  $C_p$ , is the specific heat capacity,  $\rho$  is the density, and  $\alpha$  is the thermal diffusivity. It was not possible to measure the thermal diffusivity of the separator as it is too thin to be characterised using laser flash analysis (LFA). The electrolyte volume fraction of traditionally used PP/PE/PP separator does significantly affect the thermal conductivity, therefore the thermal diffusivity is assumed to be similar across commercially used separator materials.<sup>179</sup> The thermal conductivity of a wetted separator with similar properties is taken from literature, this is 0.3344 W m<sup>-1</sup> K<sup>-1</sup>.<sup>180</sup> The density and the volumetric specific heat capacity of the wetted separator can be evaluated using Eq. [66]. At 25 °C,  $\rho$ ,  $C_p$ , and  $\varepsilon_l$  are 946 kg m<sup>-3</sup>, 1700 J kg<sup>-1</sup> K<sup>-1</sup> and 0.47 for the dry separator. The volumetric heat capacity is 1745970 J m<sup>-3</sup> K<sup>-1</sup>. This corresponds to a density and gravimetric specific heat capacity of 1620 kg m<sup>-3</sup> and 1080 J kg<sup>-1</sup> K<sup>-1</sup> for the wetted separator. Therefore, the heat capacity for the wetted separator is represented by Equation [66], where  $C_{p,s}$  is defined by Equation [63], and the other values are summarised in Table 14.

For the electrodes, this property cannot be determined from the powder as it is influenced by microstructure.<sup>181</sup> Instead, the through-plane thermal diffusivity of the double-side coated electrode is measured. The through-plane thermal diffusivity and calculated specific heat capacities of the double-sided electrodes are illustrated in Table 15. The overall specific heat capacity of the electrodes were calculated using the heat capacities and mass fractions (Figure 39) of the black mass and current collectors. The area density of the positive electrode was attributed to 8.1% aluminium and 91.9% NMC coating, whereas the area density of the negative electrode was attributed to 26.6% copper and 73.4% graphite coating.

The thermal diffusivity decreases with temperature for both electrodes, although as the specific heat capacity relationship with temperature is inversely proportional, the thermal conductivity does not change significantly with temperature. The through-plane thermal conductivity of the graphite-SiO<sub>y</sub> electrode increases slightly, whereas the NMC electrode decreases slightly.

The thermal diffusivity and the specific heat capacity of the double-sided electrodes are used to calculate the overall thermal conductivity for the positive and negative electrode respectively. As the electrode is a layered material the conductivity of the electrode lamina can be deconvoluted. The conductivity in the in-plane direction is the harmonic average of the conductivities (weighted by their thickness). In this case, there were three layers, two layers of the electrode lamina and one layer of the current collector. Therefore, the thermal conductivity perpendicular to the electrode can be written as:<sup>182</sup>

$$\lambda_{total} = \frac{L_{e1} + L_{cc} + L_{e2}}{\left(\frac{L_{e1}}{\lambda_{e1}} + \frac{L_{cc}}{\lambda_{cc}} + \frac{L_{e2}}{\lambda_{e2}}\right)} = \frac{2L_e + L_{cc}}{\left(\frac{2L_e}{\lambda_e} + \frac{L_{cc}}{\lambda_{cc}}\right)}. \quad [70]$$

The thickness of the electrode  $L_e$  and current collector  $L_{cc}$ , the conductivity of the current collector  $\lambda_{cc}$  and the total conductivity  $\lambda_{total}$  are known, therefore the conductivity of the electrode lamina  $\lambda_e$  can be calculated. This corresponds to 0.807 W m<sup>-1</sup> K<sup>-1</sup> and 3.793 W m<sup>-1</sup> K<sup>-1</sup> at 25 °C for the NMC811 and graphite composite laminas respectively, values measured between -5 °C and 55 °C are reported in Table 15. These thermal conductivities are in a similar range to reported values of 1.31 to 2.62 W m<sup>-1</sup> K<sup>-1</sup> and 0.68 to 2.62 W m<sup>-1</sup> K<sup>-1</sup> for NMC811 and graphite respectively.<sup>183</sup>

The thermal conductivity measurements were for the dry porous electrode, although the properties of the wetted electrode are required. The measurement included the contribution of the nitrogen purge gas and not the electrolyte, however N<sub>2</sub> exhibits similar thermal conductivity (0.025 W m<sup>-1</sup> K<sup>-1</sup>) to the electrolyte (0.03 W m<sup>-1</sup> K<sup>-1</sup>) so the thermal conductivity of the wetted and dry electrode are assumed the same. The graphite and NMC thermal conductivities were fitted as interpolants in the model as low order polynomials did not provide good agreement.

The thermal conductivity for aluminium and copper current collectors were taken from literature as in batteries they appear in their pure elemental form and the thermal



properties do not vary. The thermal conductivity of aluminium does not change appreciably within the operating range of the battery so the constant value of 237 in  $\text{W m}^{-1} \text{K}^{-1}$  is used. However, the thermal conductivity for the copper decreases with temperature. The dependency of thermal conductivity on temperature is fitted to a third-degree polynomial to capture this change in the model (where  $x$  is in Kelvin and in  $\lambda$  is in  $\text{W m}^{-1} \text{K}^{-1}$ ):<sup>177</sup>

$$-5.409 \cdot 10^{-7} \cdot T^3 + 0.0007054 \cdot T^2 - 0.3727 \cdot T + 463.6 \quad [71]$$

These measurements allow prediction of thermal inhomogeneity within a cell but combining these values do not provide an accurate value for the overall cell thermal conductivity. This is because of the cumulative error in measuring several materials separately and by not accounting for the thermal contact resistances between the layers in a cell. For accurate 3D thermal models and to predict the performance of larger battery systems the macro-thermal properties need to be measured. Cylindrical cells are a composite and not a pure material, therefore the conductivity of each cell type must be measured to improve prediction of the cell temperature.

Table 15. Summary of the thermal diffusivity, specific heat capacity and thermal conductivity values for NMC811 and graphite electrodes as a function of temperature.

	Thermal Diffusivity / $\alpha$ / $\text{mm}^2 \text{s}^{-1}$				
Temperature / K	268.15	283.15	298.15	313.15	328.15
Positive electrode (2-sided)	0.305	0.292	0.282	0.27	0.259
Negative electrode (2-sided)	2.508	2.355	2.266	2.148	2.028
	Specific Heat Capacity / $C_p$ / $\text{J kg}^{-1} \text{K}^{-1}$				
Temperature / K	268.15	283.15	298.15	313.15	328.15
Positive electrode (2-sided)	897	925	983	1057	1130
Negative electrode (2-sided)	585	709	809	892	967
	Thermal Conductivity / $\text{W m}^{-1} \text{K}^{-1}$				
Temperature / K	268.15	283.15	298.15	313.15	328.15
Positive electrode (2-sided)	0.880	0.868	0.892	0.918	0.941
NMC811 coating (wetted porous)	0.796	0.785	0.807	0.830	0.851
Negative electrode (2-sided)	3.249	3.696	4.058	4.243	4.339
Graphite-SiO <sub>y</sub> coating (wetted porous)	3.037	3.455	3.793	3.967	4.056
Aluminium	233	235	237	239	241
Copper	394	398	401	405	408

## Effective Thermal Properties

Lumped thermal models require the effective thermal properties of the jellyroll. The thermal properties of the jellyroll can be measured directly, or they can be calculated using the individual heat capacities of the components. In this model the jellyroll is a homogenous material so it has a uniform temperature, and the thermal conductivity can be neglected. The jellyroll excludes the casing and the miscellaneous components such as the hard plastic and perforated fibrous membrane at the axial sites. An overall specific heat capacity of  $887 \text{ J kg}^{-1} \text{ K}^{-1}$  ( $2.38 \cdot 10^6 \text{ J K}^{-1} \text{ m}^{-3}$ ) was calculated using the gravimetric contributions and the heat capacities of the individual components in Table 16. The 2-sided electrodes relate to the whole double-sided coating, including the current collector and both coated electrodes, whereas the coatings relate to the single sided coating thickness only (not including the current collector). The total specific heat capacity is similar to value reported previously,  $850 \text{ J kg}^{-1} \text{ K}^{-1}$  for a jellyroll with density  $2400 \text{ kg m}^{-3}$ .<sup>184,185</sup>

Table 16. Thermophysical properties of the cell components at 25°C (measured values are highlighted in green [m], calculated values in white [c], and literature values in blue [l]).

Material	Thickness / $\mu\text{m}$	$\rho$ / $\text{kg m}^{-3}$	$C_p$ / $\text{J kg}^{-1} \text{ K}^{-1}$	$\Theta$ / $\text{J m}^{-3} \text{ K}^{-1}$	$\alpha$ $\text{mm}^2 \text{ s}^{-1}$	$\lambda$ / $\text{W m}^{-1} \text{ K}^{-1}$
NMC811 coating (dry porous)	75.6 <sup>m</sup>	3270 <sup>m</sup>	990 <sup>c</sup>	3237300 <sup>c</sup>	0.249 <sup>c</sup>	0.807 <sup>c</sup>
NMC811 coating (dry bulk)	75.6 <sup>m</sup>	4918 <sup>c</sup>	990 <sup>m</sup>	4868120 <sup>c</sup>	-	-
NMC811 coating (wetted porous)	75.6 <sup>m</sup>	3699 <sup>c</sup>	902 <sup>c</sup>	3335495 <sup>c</sup>	0.242	0.807 <sup>c</sup>
Positive electrode (2-sided)	167.2 <sup>m</sup>	3216 <sup>c</sup>	983 <sup>c</sup>	3162202 <sup>c</sup>	0.282 <sup>m</sup>	0.892 <sup>c</sup>
Graphite-SiO <sub>y</sub> coating (dry porous)	85.2 <sup>m</sup>	1740 <sup>m</sup>	960 <sup>c</sup>	1670400 <sup>c</sup>	2.271 <sup>c</sup>	3.793 <sup>c</sup>
Graphite-SiO <sub>y</sub> coating (dry bulk)	85.2 <sup>m</sup>	2320 <sup>c</sup>	960 <sup>m</sup>	2227200 <sup>c</sup>	-	-
Graphite-SiO <sub>y</sub> coating (wetted porous)	85.2 <sup>m</sup>	2060 <sup>c</sup>	846 <sup>c</sup>	1743680 <sup>c</sup>	2.175 <sup>c</sup>	3.793 <sup>c</sup>
Negative electrode (2-sided)	182.4 <sup>m</sup>	2213 <sup>c</sup>	809 <sup>c</sup>	1790697 <sup>c</sup>	2.266 <sup>m</sup>	4.058 <sup>c</sup>
Aluminium foil <sup>177</sup>	16 <sup>m</sup>	2702 <sup>l</sup>	876 <sup>l</sup>	2366952 <sup>l</sup>	100 <sup>l</sup>	237 <sup>l</sup>
Copper foil <sup>177</sup>	12 <sup>m</sup>	8933 <sup>l</sup>	383 <sup>l</sup>	3421339 <sup>l</sup>	117 <sup>l</sup>	401 <sup>l</sup>
Separator (dry porous) <sup>186</sup>	12 <sup>m</sup>	946 <sup>m</sup>	1700 <sup>m</sup>	1608200 <sup>c</sup>	0.208 <sup>c</sup>	0.3344 <sup>l</sup>
Separator (wetted porous)	12 <sup>m</sup>	1548 <sup>c</sup>	1128 <sup>c</sup>	1745966 <sup>c</sup>	0.192 <sup>c</sup>	0.3344 <sup>c</sup>
Electrolyte (EC:EMC:DMC, 1:1:1) <sup>174</sup>	-	1280 <sup>l</sup>	229 <sup>l</sup>	293120 <sup>l</sup>	0.1 <sup>l</sup>	0.03 <sup>l</sup>
Jellyroll	-	2682 <sup>c</sup>	887 <sup>c</sup>	-	-	-
Casing (SS Type 304) <sup>177</sup>	340 <sup>m</sup>	7900 <sup>l</sup>	477 <sup>l</sup>	-	3.87 <sup>l</sup>	15 <sup>l</sup>
						Measured <sup>m</sup>
						Calculated <sup>c</sup>
						Literature <sup>l</sup>

### 5.3.3 Thermal-electrochemical Characterisation

In this section, the temperature dependencies of the parameters were outlined to capture the influence of temperature on electrochemical behaviour, batteries undergo self-heating even at moderate C-rates so this information is essential to accurately predict these changes. These dependencies were modelled using an Arrhenius relationship:

$$n(T) = n_{ref} \cdot e^{\frac{E_n^{act}}{R} \left( \frac{1}{T_{ref}} - \frac{1}{T} \right)} \quad [72]$$

Here  $n$  represents a temperature dependent parameter,  $n_{ref}$  is its value at reference temperature namely  $T_{ref}$ ,  $E_n^{act}$  is the activation energy,  $R$  is the gas constant, and  $T$  is the temperature in Kelvin. The activation energy can be evaluated by finding the slope  $c$  of plot  $\ln(n)$  vs.  $1/T$ :

$$c = E_n^{act}/R. \quad [73]$$

To describe the heat generation of the cell, the entropic coefficients were measured to capture the reversible heat and the irreversible heat is accounted for in the DFN model definition. The effect of voltage hysteresis is often not considered in models, these properties are therefore evaluated during cell discharge only i.e., positive electrode lithiation and negative electrode delithiation. It has been observed that the hysteresis effect is minimal for parameters including the entropic coefficients and diffusion.<sup>1,187</sup>

The properties are mapped as a function of lithium concentration, the stoichiometric ranges were mapped previously using half-cells.<sup>1</sup> For the positive electrode this corresponds to crystal lattice lithium concentrations of  $x=0.2567$  to  $0.9072$  and for the negative electrode,  $x=0.0279$  to  $0.9014$  (Figure 40). However, when a battery is discharged and current is no longer applied lithium diffuses in/out of the active materials, therefore the stoichiometry changes. To correct for this, the open circuit voltages during the test procedure were aligned to the OCV data (Figure 41). It should be noted, that the capacity of the negative electrode is oversized to the positive electrode for safety, reducing lithium plating and ensuring enough capacity for the lithium removed from the positive electrode.<sup>188</sup> The positive electrode capacity is not defined by the complete stoichiometric range, but a lithium content which is reversible in the voltage window specified, e.g.  $\text{Li}_x\text{MO}_2$  where  $0.26 \leq x \leq 0.91$ . In this case NMC811 has a practical upper voltage of 4.4 V.<sup>16</sup>

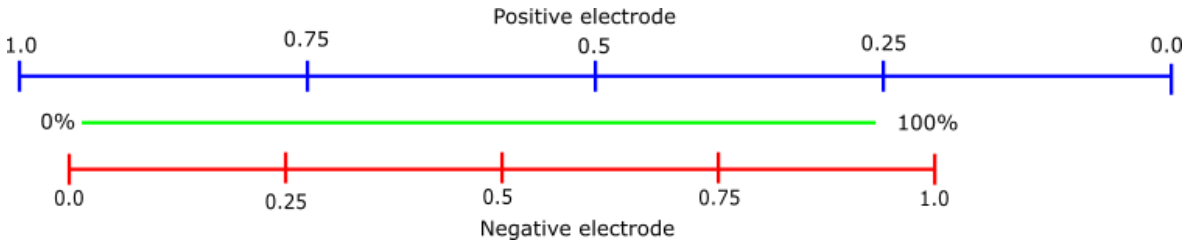


Figure 40. Stoichiometries of the negative (red) and positive electrode (blue) in relation to SOC of the battery (green).

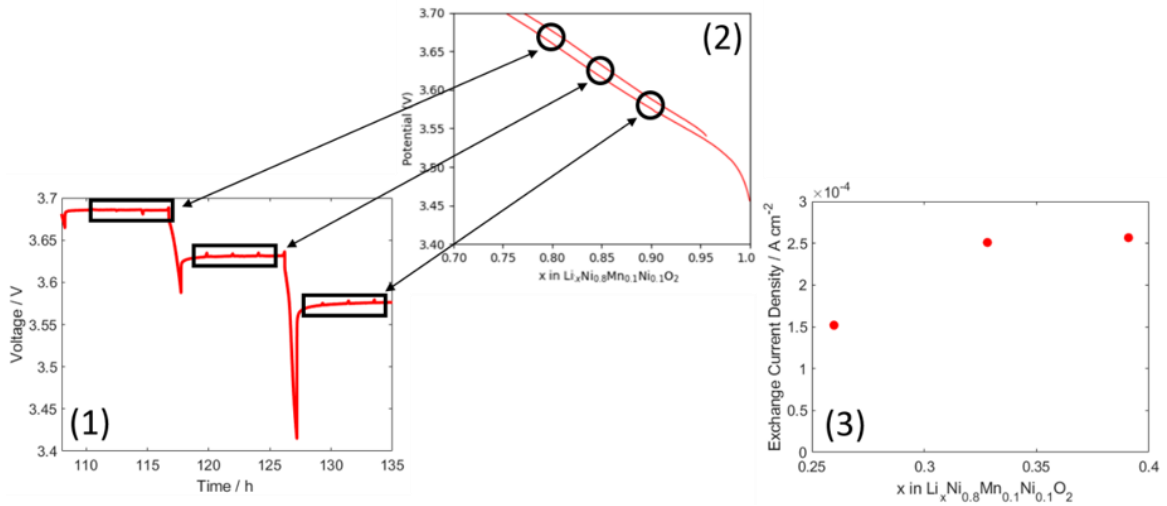


Figure 41. Process to accurately map stoichiometry from test voltage profile and the OCV 'reference' data set. (1) Observe voltage at each point test was carried out e.g., EIS or GITT, (2) find stoichiometry that corresponds to this voltage from OCV profile (this OCV profile is a function of lithiation, process described in previous Chapter), and (3) plot parameter vs. determined stoichiometry.

### Diffusion

The activation energy of solid-phase diffusion can be calculated by repeating GITT at different temperatures.<sup>18,189</sup> This allows us to determine the dependency of solid-phase diffusivity on concentration and temperature within the active material. The diffusion coefficients were analysed from the transients and steady-phase regions during GITT. The analytical approach involves evaluating changes in lithium concentration at the particle surface as a function of time. This can be described by an expression relating to the Sand equation:<sup>190</sup>

$$D_s = \frac{4}{\pi} \left( \frac{I}{FS c_s^{\max}} \frac{\frac{\partial U}{\partial x}}{\frac{\partial V}{\partial \sqrt{t}}} \right)^2. \quad [74]$$

Here  $I$  is the applied current,  $F$  is the Faraday constant,  $S$  is the effective area of the porous electrode-electrolyte interface, and  $c_s^{\max}$  is the maximum concentration in the electrode.  $S$  can be calculated from the total number of particles in the electrode and the average surface area of a particle:

$$S = n \cdot S_{\text{particle}} = \frac{\varepsilon_{\text{act}} \cdot V_{\text{electrode}}}{V_{\text{particle}}} S_{\text{particle}}. \quad [75]$$

$\varepsilon_{\text{act}}$  is the active material volume fraction,  $V_{\text{electrode}}$  is the electrode volume,  $V_{\text{particle}}$  is particle volume,  $S_{\text{particle}}$  is the particle surface area. For this the average particle sizes of 5.22  $\mu\text{m}$  and 5.86  $\mu\text{m}$  were used for the positive and negative electrode respectively,

these parameters were measured previously using SEM.<sup>1</sup> For the analysis of the positive electrode diffusivity it is assumed  $S$  remains unchanged as NMC volume expansions is negligible, but for the negative electrode we account for the volume expansion of the graphite-SiO<sub>y</sub>.<sup>1,191,192</sup> This involves applying a linear scaling factor across the diffusivity to capture the 4x volume expansion across the lithiation range of the battery.<sup>1</sup> The size of particles in batteries do not increase linearly with lithiation, as the process is influenced by complex electrochemical interactions, so this is a simplification. The solid-phase diffusion coefficients were measured using GITT in a three-electrode cell comprising of the NMC811 positive electrode and the graphite-SiO<sub>y</sub> negative electrode (Figure 42). The three-electrode set-up probed a limited stoichiometric range for each electrode, which was near equivalent to that observed under operation in the cylindrical cell. The diffusion coefficients vary significantly with lithium concentration, distinct regions can be identified in these profiles and attributed to distinct thermodynamic phases.<sup>193</sup> For the NMC-based electrode these phases relate to the different crystal structures of LiNi<sub>0.8</sub>Mn<sub>0.2</sub>Co<sub>0.2</sub>O<sub>2</sub> e.g. hexagonal and monoclinic.<sup>16,194</sup> For graphite-SiO<sub>y</sub>, the Li insertion stages of graphite are responsible for the changes in solid-phase diffusivity e.g. I to IV.<sup>195,196</sup> For the temperature range 5 °C to 45 °C, the diffusivity of the NMC811 was approximately 10<sup>-10</sup> cm<sup>2</sup> s<sup>-1</sup> to 10<sup>-11</sup> cm<sup>2</sup> s<sup>-1</sup> and for graphite-SiO<sub>y</sub> it was 10<sup>-14</sup> cm<sup>2</sup> s<sup>-1</sup> to 10<sup>-10</sup> cm<sup>2</sup> s<sup>-1</sup>, see Figure S4 and S5 respectively for the raw data. The solid-phase diffusion coefficients for graphite-SiO<sub>y</sub> between 10<sup>-14</sup> cm<sup>2</sup> s<sup>-1</sup> to 10<sup>-12</sup> cm<sup>2</sup> s<sup>-1</sup> are underestimates due to difficulty observing the minor voltage changes that occur during the transient and relaxation periods of GITT for the plateau regions in graphite. In plateau regions the reaction overpotentials dominate and produce inaccuracies for the solid-phase diffusivity.

The diffusion coefficients of NMC materials have been reported in the range of 10<sup>-10</sup> cm<sup>2</sup> s<sup>-1</sup> to 10<sup>-8</sup> cm<sup>2</sup> s<sup>-1</sup> previously, corroborating fairly well with the results here.<sup>152,197</sup> However, the diffusion values for SiO<sub>y</sub> and graphite have had values reported much higher than observed here, between 10<sup>-11</sup> cm<sup>2</sup> s<sup>-1</sup> to 10<sup>-8</sup> cm<sup>2</sup> s<sup>-1</sup> and 10<sup>-10</sup> cm<sup>2</sup> s<sup>-1</sup> to 10<sup>-8</sup> cm<sup>2</sup> s<sup>-1</sup> for the materials respectively.<sup>150,192,198</sup> Diffusion coefficients are often reported over several orders of magnitude due to differences in experimental set-ups and analysis. The solid-phase diffusivity often must be tuned to a higher value to provide reasonable simulation values as if the low diffusivity values are included in the fits, the simulations either do not converge or provide unrealistic results. This tuning was carried out here and the fitted profiles are illustrated in Figure 42.

Equation [76] was used to account for the dependency of solid-phase diffusivity on stoichiometry, this equation is illustrated in Figure 42. The equation is a linear combination of Gaussian functions and captures the features of the profile accurately, meaning non-linear solid-phase diffusivity can be captured by the simulations (the fitting parameters can be found in Table S2):

$$\log_{10} D_s(x) = a_0 \cdot x + b_0 + c_0 + a_1 \cdot \exp\left(-\frac{(x - b_1)^2}{c_1}\right) + a_2 \cdot \exp\left(-\frac{(x - b_2)^2}{c_2}\right) + a_3 \cdot \exp\left(-\frac{(x - b_3)^2}{c_3}\right) + a_4 \cdot \exp\left(-\frac{(x - b_4)^2}{c_4}\right). \quad [76]$$

These fits are later used in the model and shown in Figure Figure S7 and Figure S8. Figure 42 also describes the change in diffusivity across the measured stoichiometric range as a function of temperature, demonstrating the Arrhenius-type behaviour of this parameter. The average value of solid-phase diffusivity of the ‘fitted’ curves for the graphite-SiO<sub>y</sub> is lower than the experimental average for about a factor of three, because we are fitting to the  $\log_{10}(D)$  rather than  $D$ . The reason not to fit to  $D$  directly is because that would not capture the features in low diffusivity zones, plus adds the risk of obtaining negative values for diffusivity. Fitting to the  $\log_{10}(D)$  ensures diffusivity is always positive and captures the features at different orders of magnitude, at the expense of underestimating the average diffusivity (especially in the negative electrode). Therefore, a scaling factor of 3.03 for the graphite-SiO<sub>y</sub> diffusivity was introduced in the diffusivity used in the final model so the fitted average diffusivity matched the experimental average diffusivity across all temperatures, as shown in Figure 42 (bottom right).

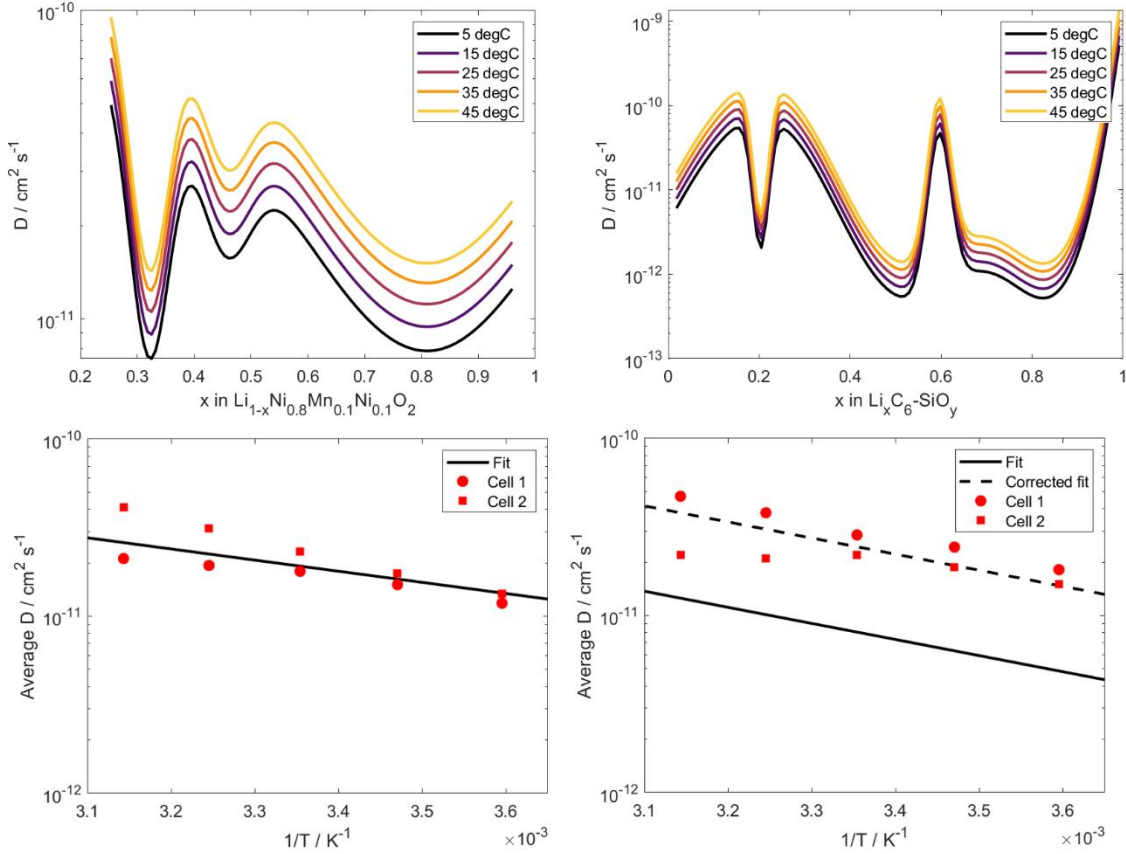


Figure 42. Fitted solid-phase diffusivity values of NMC811 positive electrode (top left) and the graphite-SiO<sub>y</sub> negative electrode (top right) as a function of stoichiometry and temperature. Arrhenius dependency for the average solid-phase diffusivity of NMC811 positive electrode (bottom left) and the graphite-SiO<sub>y</sub> negative electrode (bottom right) as a function of temperature.

An Arrhenius relationship (Eq. [72]) can be used to find the activation energies across the stoichiometric range of each electrode (Figure 43). Similarly to the solid-phase diffusivity, the activation energies are influenced by thermodynamic phases and their transitions. For NMC the activation energy is in the range of 10 kJ mol<sup>-1</sup> to 20 kJ mol<sup>-1</sup>. This compares to reported values of 15 kJ mol<sup>-1</sup> to 30 kJ mol<sup>-1</sup> for the lower nickel content NMC electrodes.<sup>199</sup> For graphite-SiO<sub>y</sub> the activation energy has a wider range of 5 kJ mol<sup>-1</sup> to 60 kJ mol<sup>-1</sup>. Similar to values up to 50 kJ mol<sup>-1</sup> for graphite reported by Ecker *et al.*<sup>74</sup> For graphitic materials the consensus is that values are generally between 20 kJ mol<sup>-1</sup> and 40 kJ mol<sup>-1</sup>.<sup>200–202</sup> The range in reported values is attributed to the variability and high uncertainty for the analytical approaches used in determining the diffusion coefficients.<sup>196</sup> Significant temperature dependence is observed for the diffusivity between stoichiometries of  $x=0.3$  to  $0.5$  and at approximately  $x=0.8$ , corresponding to the plateau regions of graphite.

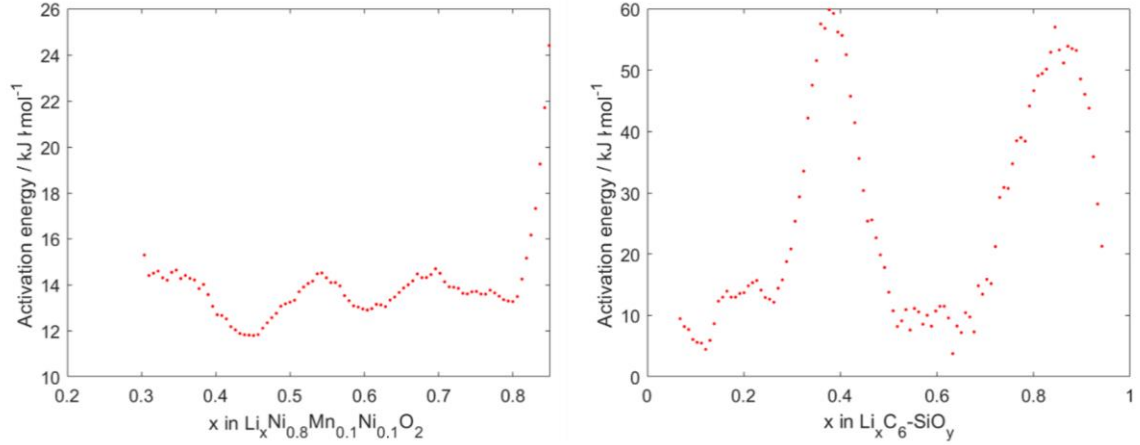


Figure 43. The solid-phase diffusivity activation energies for the NMC-based (left) and graphite-SiO<sub>y</sub> (right) electrodes measured in a three-electrode configuration.

### Exchange Current

Previously the exchange current density and its activation energy were evaluated at a single stoichiometry.<sup>1</sup> Here, the exchange current density and its dependency were mapped on temperature and lithium concentration at various stoichiometries using a half cell (Figure 44). The exchange current density  $j_o$  can be evaluated by measuring the charge-transfer resistance  $R_{ct}$  during EIS:

$$R_{ct} = \frac{RT}{j_o S F}. \quad [77]$$

Here  $R$ ,  $S$ , and  $F$  are the gas constant, the electrode-electrolyte interfacial area, and the Faraday constant respectively. For these calculations  $S$  was calculated from the geometrical electrode volume  $V$ , the active material volume fraction  $\varepsilon_{act}$ , and particle radius:

$$S = \frac{3\varepsilon_{act}}{r} V. \quad [78]$$

This was determined to be  $3.27 \cdot 10^{-3} \text{ m}^2$  and  $4.16 \cdot 10^{-3} \text{ m}^2$  for the positive and negative electrode respectively. The Nyquist plot for the positive electrode only shows one semi-circle that can be attributed to the charge transfer process. This is because the SEI resistance shares a similar time constant with the double layer and therefore is difficult to visually discern the phenomena (see Figure S9 in the Supporting Information).. However, two RC elements should be included in the equivalent circuit model to account for the charge transfer and SEI resistance. The Nyquist plots are fitted to an equivalent circuit model (Figure 45) to evaluate  $R_{ct}$  and then used to determine  $j_o$  from Eq. [77].



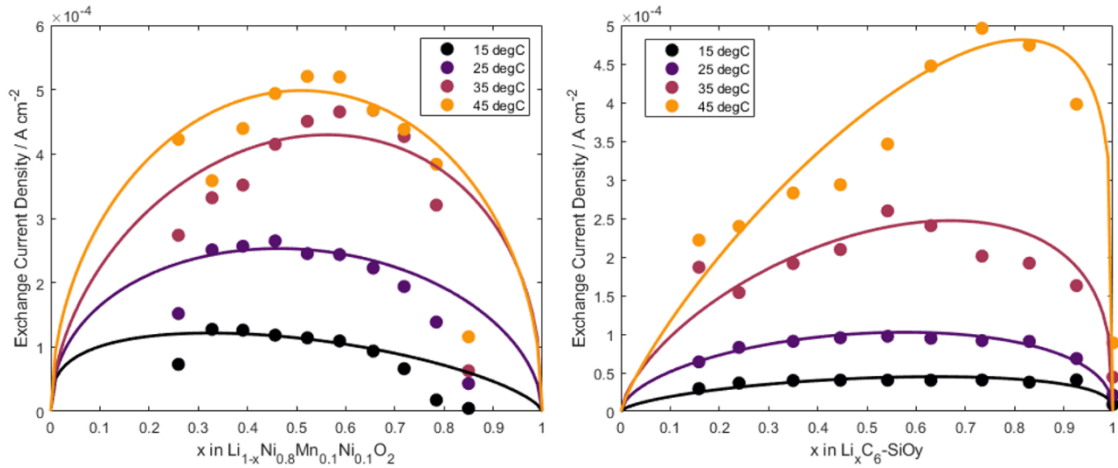


Figure 44. Exchange current density as a function of lithium concentration for the NMC811 positive (left) and graphite-SiO<sub>y</sub> negative electrode (right) evaluated at 15 °C, 25 °C, 35 °C, and 45 °C.

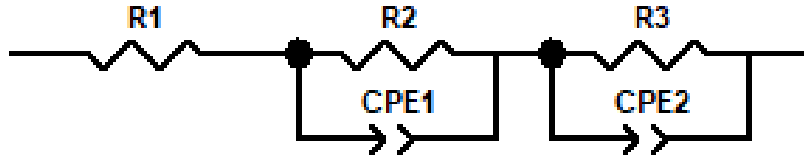


Figure 45. Equivalent circuit model used for fitting. (R = resistor and CPE = constant phase element).

The exchange current density demonstrates a dependency on lithium concentration that can be described by a form of the Butler-Volmer equation (see Figure 44):<sup>74</sup>

$$j_0 = k_0 \cdot \left(1 - \frac{c_s}{c_{s,max}}\right)^{1-\alpha} \cdot \left(\frac{c_s}{c_{s,max}}\right)^\alpha \cdot \left(\frac{c_e}{c_{e0}}\right)^{1-\alpha}. \quad [79]$$

Here  $c_s$  and  $c_e$  refer to lithium concentration in the solid lattice and electrolyte, respectively,  $c_{s,max}$  is the maximum concentration in the electrode particles and  $c_{e0}$  is the reference concentration in the electrolyte. The parameter  $k_0$  is the reference current of the reaction. As shown in Figure 44, the exchange current density for the NMC811 positive electrode was measured at 25 °C between  $0.5 \cdot 10^{-4} \text{ A cm}^{-2}$  and  $3.0 \cdot 10^{-4} \text{ A cm}^{-2}$  with a mean value of  $2.01 \cdot 10^{-4} \text{ A cm}^{-2}$ . For the graphite-SiO<sub>y</sub> electrode the exchange current density was measured at 25 °C between  $2.0 \cdot 10^{-5} \text{ A cm}^{-2}$  and  $9.0 \cdot 10^{-5} \text{ A cm}^{-2}$  with a mean value of  $7.1 \cdot 10^{-5} \text{ A cm}^{-2}$ . The observed trends are similar to the results reported by Ecker *et al.* who reported a value of  $2.23 \cdot 10^{-4} \text{ A cm}^{-2}$  and  $7.05 \cdot 10^{-5} \text{ A cm}^{-2}$  corresponding to  $x=0.5$  in  $\text{Li}_x(\text{Ni}_{0.4}\text{Co}_{0.6})\text{O}_2$  and  $\text{Li}_x\text{C}_6$ .<sup>74</sup> The Butler-Volmer equation (Eq. [79]) fits the negative electrode exchange current density vs stoichiometry well, this fit is worse for the positive electrode ( $R^2=0.63$ ) and a semi-ellipse with an exchange current value of 0 at stoichiometries at  $\sim 0.2$  and  $0.9$  (at 25 °C) provides a better fit ( $R^2=0.9$ , Figure S9 in the

Supporting Information). The question arises whether using the stoichiometry of 0 to 1 to represent degree of lithiation with respect to the molar lithium concentration within the crystal structure is the correct assumption to use in the model. There is most probably 'inactive' or non-mobile lithium below  $x=0.2$  in this case as observed in Figure 9, where it is impractical for  $\text{Li}_x\text{Ni}_{0.8}\text{Mn}_{0.1}\text{Co}_{0.1}\text{O}_2$  to be delithiated further due to collapse of the crystal structure.<sup>203</sup> There is little sensitivity in this particular parameter,<sup>204</sup> and therefore have assumed Butler-Volmer kinetics over the entire lithium stoichiometry in this work which is consistent with the model inputs.

The activation energy of the exchange current density was evaluated using an Arrhenius relationship (Equation [72]) across the stoichiometric range of each electrode (Figure 46). The activation energies for the positive electrode range between  $20 \text{ kJ mol}^{-1}$  to  $50 \text{ kJ mol}^{-1}$  and for the negative electrode between  $45 \text{ kJ mol}^{-1}$  to  $65 \text{ kJ mol}^{-1}$ . The mean values for the Ni-rich and graphite-based electrodes were  $31.1 \text{ kJ mol}^{-1}$  and  $54.8 \text{ kJ mol}^{-1}$  respectively. Ecker *et al.* reported activation energies of  $43.6 \text{ kJ mol}^{-1}$  for  $\text{Li}(\text{Ni}_{0.4}\text{Co}_{0.6})\text{O}_2$  and  $53.4 \text{ kJ mol}^{-1}$  for graphite.<sup>74</sup> Jow *et al.* reported activation energies for graphite and NCA as  $68 \text{ kJ mol}^{-1}$  and  $50 \text{ kJ mol}^{-1}$  respectively.<sup>205</sup> Smart *et al.* reported activation energies for graphite and  $\text{Li}(\text{Ni}_{0.8}\text{Co}_{0.2})\text{O}_2$  with different electrolyte systems in the ranges  $45 \text{ kJ mol}^{-1}$  to  $60 \text{ kJ mol}^{-1}$  and  $-34 \text{ kJ mol}^{-1}$  to  $48 \text{ kJ mol}^{-1}$ .<sup>206</sup> Similar ranges have been reported for graphite and  $\text{Li}(\text{Ni}_{0.5}\text{Mn}_{0.3}\text{Co}_{0.2})\text{O}_2$ , these were  $56 \text{ kJ mol}^{-1}$  to  $72 \text{ kJ mol}^{-1}$  and  $58 \text{ kJ mol}^{-1}$  to  $69 \text{ kJ mol}^{-1}$ .<sup>207</sup>

Previously reported values activation energies for this cell were  $17.8 \text{ kJ mol}^{-1}$  and  $35 \text{ kJ mol}^{-1}$  for NMC and graphite respectively.<sup>1</sup> However, these activation energies are appreciably lower than the values reported here and for similar materials. In this case, the parameter table is updated with the newly evaluated activation energies that have been measured at various lithium stoichiometries and corroborate with literature. The dependency of the exchange current density on temperature and lithium concentration can be described as:

$$j_0(c, T) = k_0 \cdot \left(1 - \frac{c_s}{c_{s, \max}}\right)^{1-\alpha} \cdot \left(\frac{c_s}{c_{s, \max}}\right)^\alpha \cdot \left(\frac{c_e}{c_{e0}}\right)^{1-\alpha} \exp\left(-\frac{E_a}{R} \cdot \left(\frac{1}{T} - \frac{1}{298.15}\right)\right). \quad [80]$$

Here  $k_0$  is the reference current,  $\alpha$  is the activity coefficient, and  $E_a$  is the activation energy; and the variables are the stoichiometry and temperature. Because the stoichiometry is defined as  $x = \frac{c_s}{c_{s, \max}}$ , this equation combines Butler-Volmer (Eq. [79]) and Arrhenius behaviours (Eq. [72]). These values are outlined in Table S3 in the Supporting Information.

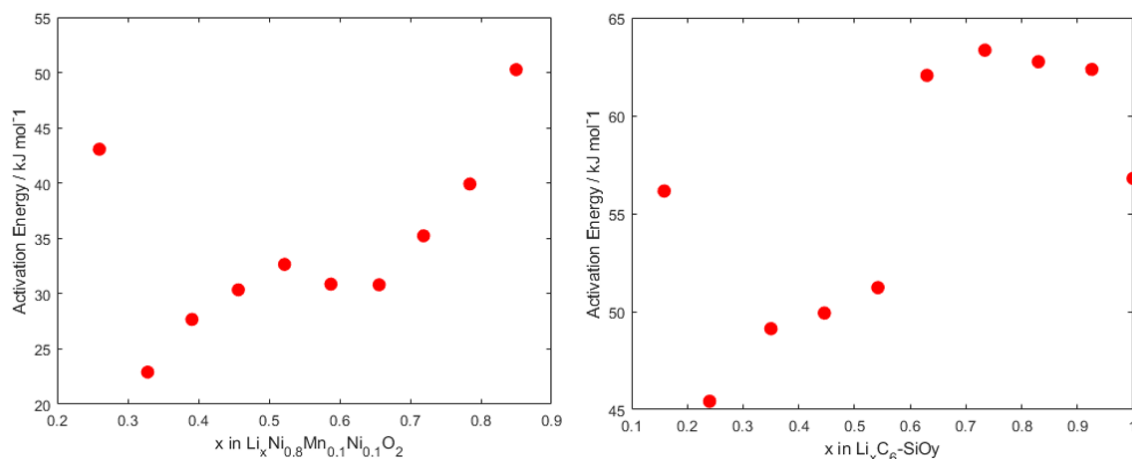


Figure 46. Exchange current density activation energy as a function of lithium concentration for the positive (left) and negative electrode (right).

### Electronic Conductivity

The electronic conductivity is also a temperature-dependent property, however intrinsic material properties determine whether there is a corresponding activation energy. The semi-metallic properties of graphite relate to an inversely proportional relationship with temperature and electronic conductivity. However, in the normal operating temperature range of a battery, the change in graphite electronic conductivity is considered negligible. In contrast, NMC exhibits semiconducting properties (owing to its non-zero band gap energy) this causes electron conduction to be significant dependent on temperature. As the electron conduction in NMC is a thermally activated process the corresponding activation energy can be evaluated using an Arrhenius type relationship (Equation [72]).<sup>208</sup>

The NMC811 electrode was extracted from a cell that was discharged to 2.5 V. This relates to a lithium content of approximately  $x=0.9$ . At this state of lithiation, the solid-phase electronic conductivity was evaluated to be  $0.847 \text{ S m}^{-1}$  at  $25^\circ\text{C}$ . This value is four times higher than the  $0.18 \text{ S m}^{-1}$  calculated by Chen *et al.* This could be since using liquid gallium to delaminate the electrode, rather than adhesive tape, preserves the electrode structure. The corresponding activation energy for the positive electrode electronic conductivity was determined to be  $3.5 \text{ kJ mol}^{-1}$  (Figure 47). The effect of lithium concentration was not evaluated due to the stability of the partially lithiated NMC materials in ambient conditions. Elsewhere, this relationship has been investigated previously by Amin *et al.* by pelletizing the pure active material and conducting EIS measurements in a battery.<sup>209</sup>

Amin *et al.* studied NMC532 and NMC111 at lithium stoichiometries between  $x=0.25$  and  $x=1.0$ .<sup>209</sup> For these materials the activation energy of the electronic conductivity decreased from  $40 \text{ kJ mol}^{-1}$  to  $4.8 \text{ kJ mol}^{-1}$  and  $46.3 \text{ kJ mol}^{-1}$  to  $9.6 \text{ kJ mol}^{-1}$  respectively. The latter values for the lithiated materials are similar to the value reported in this chapter. For states of lithiation below  $x=0.25$  the material exhibits metallic properties and electronic conduction is not thermally activated. The electronic conductivity is the

least sensitive parameter in the DFN model and therefore it is less critical to describe its dependency on lithium concentration.

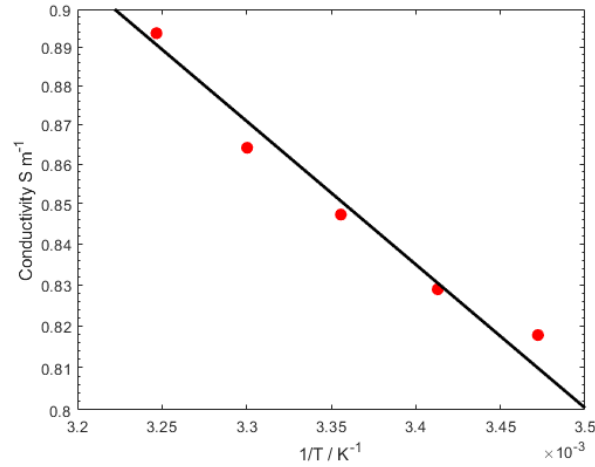


Figure 47. Electronic conductivity evaluated for NMC811 extracted from a fully discharged cell. This corresponds to a lithium stoichiometry of approximately  $x=0.9$ . These values are plotted versus the inverse of temperature for the positive electrode. The gradient provides the activation energy for NMC.

### Entropic Term

There are several sources of heat generation in batteries,<sup>172</sup> This includes irreversible and reversible heat components.<sup>210</sup> For high C-rates (most scenarios) more than half of the heat generation can be ascribed to irreversible heat, known as ohmic heat loss.<sup>211</sup> At low C-rates (1C or less) the reversible heat contribution from the material phase changes becomes more significant, this heat generation is due to the entropy changes that occur as a result of intercalation reactions, and this property depends on the internal temperature and OCV of the system. The entropy change can account for over half the total heat generated at the rates typically used in electric vehicles.<sup>212,213</sup> Parameterisations that outline activation energies do not characterise the reversible heat of the battery, this is important to predict temperature and the influenced electrochemical performance correctly.<sup>63,74</sup>

The change in entropy  $\Delta S$  can be determined through the slope of the OCV with temperature:<sup>73</sup>

$$\Delta S = \frac{-\Delta G}{T} = nF \left( \frac{E}{T} \right). \quad [81]$$

It can take many hours to attain OCV at a particular SOC and temperature, therefore the thermal stability of the electrolyte needs to be considered when choosing the temperature regime. This is because at high temperatures due to electrochemical instability, particularly at the graphite interface, it is more difficult to attain OCV.<sup>108</sup> Choosing a lower temperature regime avoids instabilities, while allowing the thermodynamic behaviour to be measured.

Using a three-electrode configuration for the experiment allows us to measure the entropic terms for SoCs between 0% and 100%, see Figure 48. This means that the entropic term for both electrodes is mapped at the same state of charge (SoC) for both electrodes. At low states of lithiation the graphite OCV decreases as temperature increases, this corresponds to a  $\Delta S < 0$ . As the graphite electrode is delithiated the entropic term becomes positive. This change occurs at  $x = 0.6$ . These observations agree with research by Reynier *et al.* on a pure graphite electrode.<sup>214</sup> This suggests that less than 10wt% of  $\text{SiO}_y$  has a minimal effect on the entropic term. These results are also consistent with the entropic term of a silicon-graphite material that was reported for lithium stoichiometries less than 0.7.<sup>215</sup>

The entropic term of the NMC electrode is negligible at several states of lithiation. For the other states of lithiation it does not show an appreciable value. This means the full cell behaviour is dominated by the negative electrode and the trend is the same, although the opposite magnitude. This is due to the definition of the full cell potential ( $E_{\text{cell}} = E_{\text{we}} - E_{\text{ce}}$ ). The reversible heat generation in the cell is determined by the graphite-based electrode. These values are in good agreement with published results; the entropic term of NMC-type electrodes have been shown to be negligible in comparison to other positive electrode chemistries.<sup>216</sup>

The variation of entropic term with stoichiometry has been captured by fitting functions to the experimental data. For the negative and positive electrode these functions are (fitting parameters outlined in Table S4 in Supporting Information):

$$\frac{\partial U_p}{\partial T}(x) = a_1 \cdot \exp\left(-\frac{(x - b_1)^2}{c_1}\right) + a_2 \cdot \exp\left(-\frac{(x - b_2)^2}{c_2}\right), \quad [82]$$

$$\frac{\partial U_n}{\partial T}(x) = a_0 \cdot x + b_0 + a_1 \cdot \exp\left(-\frac{(x - b_1)^2}{c_1}\right). \quad [83]$$

However, the function for the negative electrode entropic term was chosen to exclude the points at intermediate stoichiometries. This is because including these points inadequately describes heat generation at 0.5C, see Figure 49. This is despite the values reported here being similar as previously reported for this material, it is not clear why a discrepancy arises when the negative entropic coefficients for the negative electrode are included.<sup>163</sup>

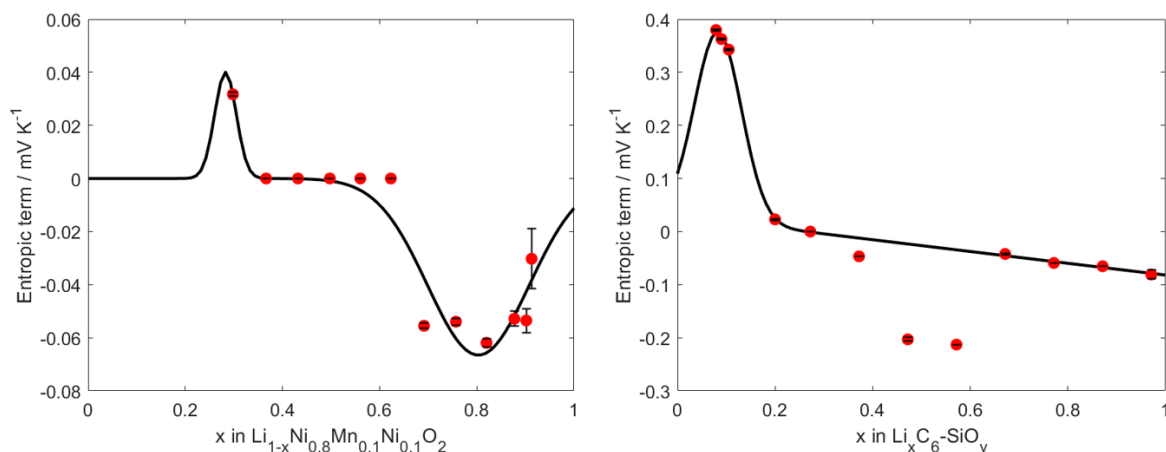


Figure 48. Entropic term and polynomial fits for the negative electrode (left) and positive electrode (right). The points in the negative electrode are ignored to achieve a good fit, there is uncertainty in the physics or validation.

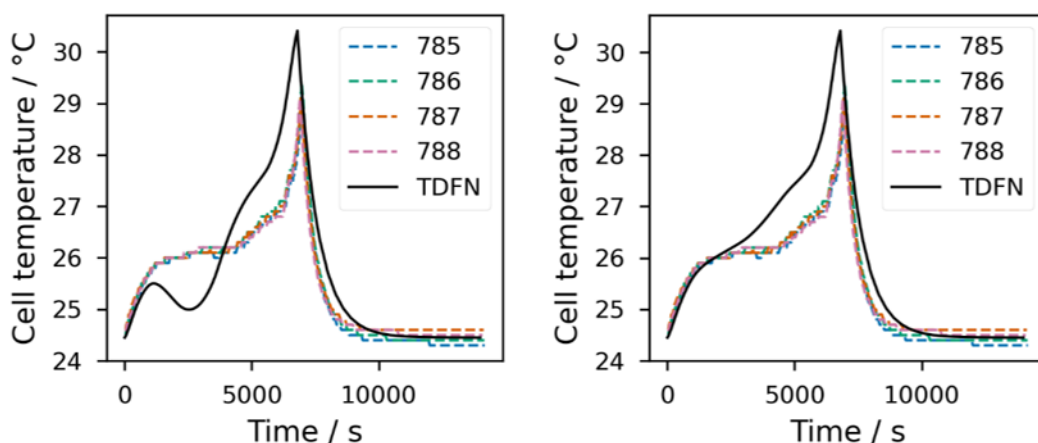


Figure 49. Experimental and simulated temperature profiles with the negative electrode entropic term including all data points (left) and excluding the intermediate data points (right). The experimental data was from tests on four cylindrical cells (the cell ID numbers are listed in the legend), while the simulated data was using the fully parameterised DFN model. This data was for a cylindrical cell discharge of 0.5C at 25 °C.

This term has been represented by high order even polynomial functions in the past, however this fitting is often inadequate outside the stoichiometric range.<sup>217</sup> It is difficult to predict the entropic term value outside the measured range, for this reason it is assumed the parameter tends to zero, rather than assigning it a non-zero value that may overestimate heat generation.

This section provides the information needed to construct an accurate thermally coupled electrochemical model by outlining the activation energies and the reversible heat of the battery. This information is often not measured in parameterisations and is critical to predicting the internal temperature and its influence on thermal performance.<sup>62,74</sup> The methodologies also describe the experimental and mathematical approach to quantify the parameter-dependencies of several electrochemical parameters, enabling the

changes in performance during battery operation to be documented. The methods can be applied similarly to the widely used materials, graphite and NMC.

### Electrolyte Properties

Ion-transport models for concentrated binary electrolyte solutions depend on the ionic conductivity, ionic diffusivity, and the transference number.<sup>218</sup> The thermodynamic factor (TDF) is also required to describe the thermodynamic behaviour of the electrolyte system, this parameter is dependent on the mean molar activity coefficient. The Thermodynamic Factor (TDF) quantifies the variation of the chemical potential of a species in an electrolyte system with its concentration, reflecting the driving forces behind mass transport and ion distribution. To be consistent with the electrochemical parameterization of this cell it is assumed the electrolyte was 1 mol dm<sup>-3</sup> LiPF<sub>6</sub> in EC:EMC (3:7, v:v).<sup>1</sup> These electrolyte properties were assumed due to difficulty obtaining electrolyte from the commercial cell for characterisation, this electrolyte has been well characterised in literature.

The temperature and concentration dependence of the electrolyte properties has been determined previously by Gasteiger *et al.*<sup>219</sup> The dependencies for the ionic conductivity, ionic diffusivity, thermodynamic factor, and the transference number can be described as the following empirically-derived relationships:

$$\kappa(T, c) = p_1 \cdot (1 + (T - p_2)) \cdot \frac{(1 + p_3 \cdot \sqrt{c} \cdot p_4 \cdot (1 + p_5 \cdot \exp(\frac{1000}{T})))}{1 + c^4 \cdot (p_6 \cdot \exp(\frac{1000}{T}))} \frac{\text{mS}}{\text{cm}}. \quad [84]$$

$$D_{\pm}(T) = p_1 \cdot \exp(p_2 \cdot c) \cdot \exp\left(\frac{p_3}{T}\right) \cdot \exp\left(\frac{p_4}{T} \cdot c\right) \cdot 10^{-6} \frac{\text{cm}^2}{\text{s}}. \quad [85]$$

$$TDF(T) = p_1 + p_2 \cdot c + p_3 \cdot T + p_4 \cdot c^2 + p_5 \cdot T + p_6 \cdot T^2 + p_7 \cdot c^3 + p_8 \cdot c^2 + p_9 \cdot c \cdot T^2 \quad [86]$$

$$t_+(T) = p_1 + p_2 \cdot c + p_3 \cdot T + p_4 \cdot c^2 + c \cdot p_5 \cdot T + p_6 \cdot T^2 + p_7 \cdot c^3 + p_8 \cdot c^2 + p_9 \cdot c \cdot T^2 \quad [87]$$

The fitting parameters values  $p_i$  have been outlined elsewhere.<sup>219</sup> These functions have been previously included in the PyBaMM software used for the simulations.

Table 17. Parameters used in our thermal-electrochemical simulations. \*Thermophysical properties of wetted components, blue = parameters tuned to obtain agreement for 1C discharge at 25°C.

	Parameter	Unit	Positive electrode ( $k = p$ )	Separator ( $k = s$ )	Negative electrode ( $k = n$ )
Electrode	Active material type		$\text{LiNi}_{1-x-y}\text{Mn}_x\text{Co}_y\text{O}_2$	Ceramic coated polyolefin	Graphite + $\text{SiO}_y$
	Current collector thickness	m	$16 \cdot 10^{-6}$	-	$12 \cdot 10^{-6}$
	Electrode thickness ( $L_k$ )	m	$75.6 \cdot 10^{-6}$	$12 \cdot 10^{-6}$	$85.2 \cdot 10^{-6}$
	Mean particle radius ( $R_k$ )	m	$5.22 \cdot 10^{-6}$	-	$5.86 \cdot 10^{-6}$
	Electrolyte volume fraction ( $\varepsilon_k$ )	%	33.5	47	25
	Active material volume fraction ( $\varepsilon_{\text{act},k}$ )	%	66.5	-	75
	Bruggeman exponent ( $b$ )	-	1.5	1.5	1.5
	Solid-phase lithium diffusivity ( $D_{s,k}$ )	$\text{m}^2 \text{s}^{-1}$	Eq. [76]	-	Eq. [76]
	Exchange current density ( $j_0$ )	$\text{A cm}^{-2}$	Eq. [80]	-	Eq. [80]
	Maximum concentration ( $c_{s,k}^{\text{max}}$ )	$\text{mol m}^{-3}$	$51765^1$	-	$29583^1$
	Density ( $\rho_s$ )*	$\text{kg m}^{-3}$	625	1620	1740
	Current collector density	$\text{kg m}^{-3}$	2702	-	8933
	Specific heat capacity ( $C_p$ )*	$\text{J kg}^{-1} \text{K}^{-1}$	Eq. [66]	Eq. [66]	Eq. [66]
	Current collector specific heat capacity	$\text{J kg}^{-1} \text{K}^{-1}$	Eq. [S4]	-	Eq. [S5]
	Thermal conductivity ( $\lambda$ )*	$\text{W m}^{-1} \text{K}^{-1}$	Table 15	$0.334^{186}$	Table 15
	Current collector thermal conductivity	$\text{W m}^{-1} \text{K}^{-1}$	237	-	Eq. [S6]
	Open Circuit Voltages ( $U_k$ )	V	Eq. [S7] <sup>1</sup>	-	Eq. [S8] <sup>1</sup>
	Entropic term ( $\frac{dU}{dT}$ )	$\text{V K}^{-1}$	Eq. [82]	-	Eq. [83]
	Solid-phase electronic conductivity ( $\sigma_{s,k}$ )	$\text{S m}^{-1}$	0.847	-	$215^1$
	Electronic conductivity activation energy	$\text{kJ mol}^{-1}$	3.5	-	-
Cell	Effective heat transfer area of jellyroll	$\text{m}^2$	$4.84 \cdot 10^{-3}$		
	Effective heat transfer area of cell	$\text{m}^2$	$5.31 \cdot 10^{-3}$		
	Jellyroll volume	$\text{m}^3$	$2.13 \cdot 10^{-5}$		
	Cell volume	$\text{m}^3$	$2.42 \cdot 10^{-5}$		
	Jellyroll effective heat capacity	$\text{J kg}^{-1} \text{K}^{-1}$	866		
Electrolyte	Ionic diffusivity ( $D_e$ )	$\text{m}^2 \text{s}^{-1}$	Eq. [85] <sup>219</sup>		
	Ionic conductivity ( $\kappa$ )	$\text{S m}^{-1}$	Eq. [84] <sup>219</sup>		
	Transference number ( $t^+$ )	-	Eq. [86] <sup>219</sup>		
	Thermodynamic factor (TDF)	-	Eq. [87] <sup>219</sup>		
	Density ( $\rho_l$ )	$\text{kg m}^{-3}$	$1280^{174}$		
	Specific heat capacity	$\text{J kg}^{-1} \text{K}^{-1}$	$229^{174}$		
	Thermal conductivity	$\text{W m}^{-1} \text{K}^{-1}$	$0.03^{174}$		



### 5.3.4 Validation

The parameters outlined in Table 17 have been made available in PyBaMM and can be used as inputs for different physics-based models to predict battery behaviour in various conditions. To validate the determined parameters, we compared experimental data to simulations using the DFN model coupled to a thermal model. These equations are outlined in Table 3 and Table 4. The model was used to predict the voltage and temperature profiles at C-rates of 0.5C, 1C, and 2C, at 0 °C, 10 °C and 25 °C. These 9 datasets are available in a data repository, however for this chapter we study five cases: (i) 0.5C|25 °C, (ii) 0.5C|0 °C, (iii) 0.5C|10 °C, (iv) 1C|25 °C, and (v) 2C|25 °C.<sup>220</sup>

The initial concentrations for the positive and negative electrodes were set to 13975 mol m<sup>-3</sup> and 28866 mol m<sup>-3</sup>, respectively, which correspond to stoichiometries of 0.27 and 0.98. Note that the initial concentrations can vary significantly from cell to cell, so their values were determined by manually adjusting the rest voltage at the beginning of the simulation to the experimental data. To achieve good agreement between the simulated and experimental data adjusting of a few other parameters values is needed. This was initially carried out based on the voltage profile of the 1C|25 °C case, for this only one parameter needed manual tuning: the positive electrode diffusivity. This tuning was done manually by trial and error by setting a multiplicative factor to the diffusivity function (illustrated in Figure S8 in the Supporting Information) until a good qualitative agreement was observed with the experimental data. We found that a factor of 2.7, the same as used in a previous work,<sup>1</sup> gave good agreement with experimental data, and even though this can seem a significant adjustment, note that it is within the typical variability between different cells. The negative electrode diffusivity, on the other hand, was adjusted but instead of manual tuning we used the factor of 3.03 found earlier, which gives a good agreement with experimental data. This contrasts to the previous electrochemical parameterisation for this cell, requiring the negative electrode diffusion coefficient to be increased 1800% from the experimentally determined value, which demonstrates the improvement in simulated data when parameter value variability is considered and not taken to be a constant.<sup>1</sup> The temperature profiles for the 1C and 2C cases demonstrated good agreement, although as the 0.5C is dominated by reversible heat it is more sensitive to entropic term. Therefore, in the 0.5C|25 °C case the negative electrode entropic term had to be tuned. This adjustment involved excluding the lower entropic term values, see Figure 48. In summary, the values of three parameters had to be adjusted to achieve good agreement for the temperature and voltage profiles.

The quality of tuning was confirmed by comparing agreement of the different C-rates at 25 °C, see Figure 50. Since the parameters were tuned based on the 1C case there is excellent agreement here, the voltage profiles for 0.5C and 2C have disagreement for the final voltage during relaxation. However, this could be improved by adjusting the electrode diffusivities explicitly for these cases—tuning is likely needed depending on the operational conditions being used in the simulation. Next, we compare the data for the 1C case at various temperatures, see Figure 51. This allows us to observe whether the temperature dependencies of the electrochemical parameters have been mapped adequately. The comparison at 10 °C and 25 °C illustrates good agreement for both the

voltage and temperature profiles. The agreement between experimental and simulated data worsens at 0 °C, primarily because this temperature falls outside the range of measured parameter values. Consequently, there is likely an interplay of different effects, indicating that the Arrhenius relationship may not be applicable across the entire operating temperature range. Additionally, this discrepancy could also stem from unaccounted variables or complexities in the system that emerge at lower temperatures due to lithium plating. The heat transfer coefficient was adjusted manually to a value of  $15 \text{ W m}^{-2} \text{ K}^{-1}$ , which is within the expected range of values.

To verify the improvement in simulations accounting for the parameter-dependencies and thermal behaviour for the M50, the simulations were compared to a C-rate discharge that the parameters were not tuned to. The diffusivity needs tuning due to underestimation in the solid-state coefficient during GITT, and in this case we have tuned to 1C for both the Chen *et al.* parameter set and those outlined in this chapter, they both provide good agreement for this C-rate, see Figure 52. However, if these simulations are used to observe cell behaviour under various C-rates then it is not possible to tune to each C-rate, to observe how these parameters compare to the experimental data for those C-rates not specifically tuned for we repeat the simulations at C/2 and compare to the experimental data. For this case the new parameter set reduces the RMSE (root mean square error) by 27% (RMSE is 0.14 for Chen2020 parameter set and 0.10 for ORegan2021 parameter set). This demonstrates that including these parameter dependencies improves the prediction under conditions that could not be specifically tuned to. This relaxation can also be captured better in the simulation by capturing particle size distributions in the simulations.<sup>221</sup> Reducing the number of parameters needed to be tuned and reducing the magnitude of tuning needed by including non-constant values. There is always deviation between the experimentally measured parameters and the values needed to provide agreement with simulations, so tuning is a necessary step. This is due to errors introduced by the unknown cell composition, damage to materials during teardown, errors introduced in the analysis and the simplicity and assumptions of the models in capturing the full kinetic and thermodynamic data.

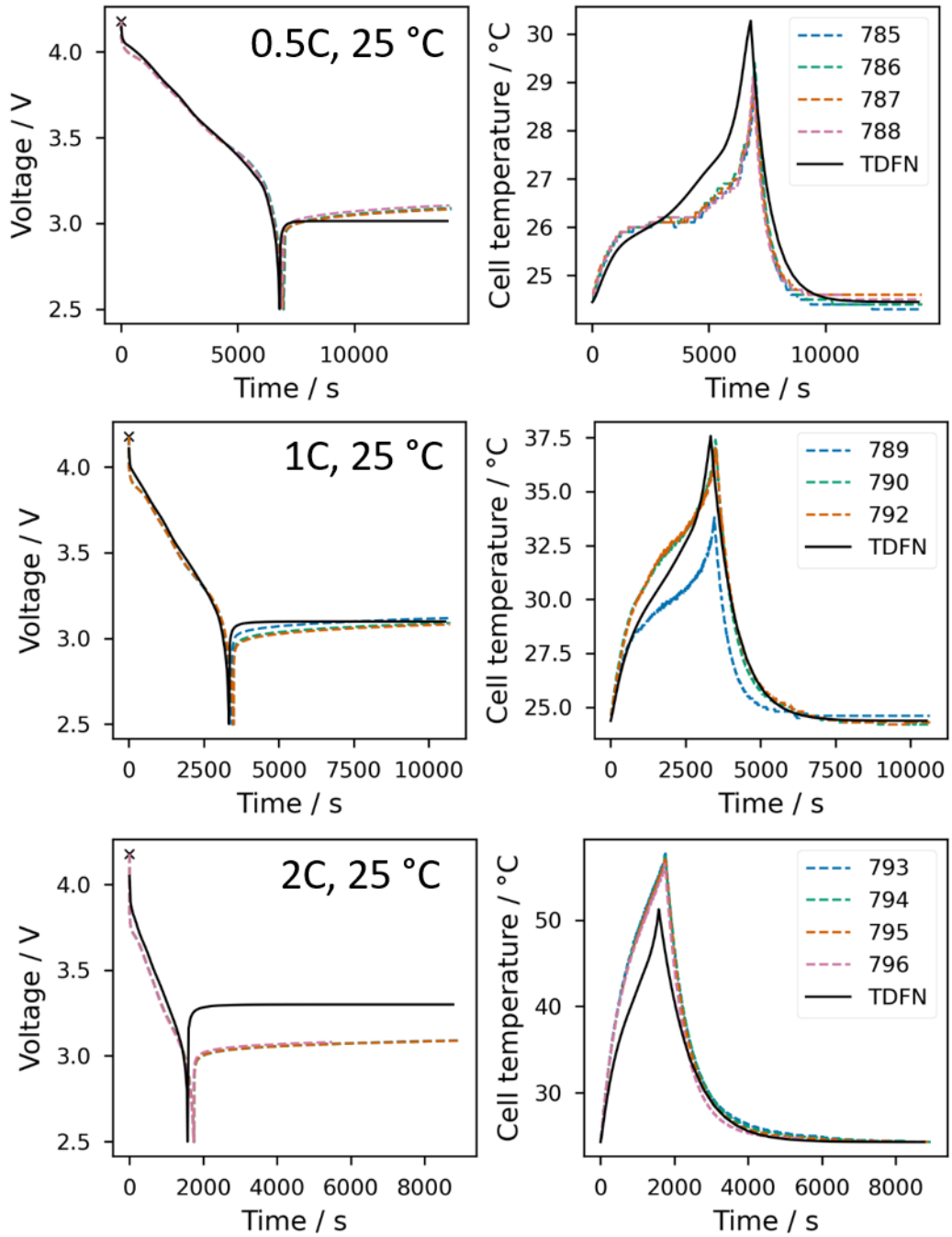


Figure 50. Experimental and simulated voltage (left) and temperature (discharge) profiles for a 0.5C, 1C, and 2C discharge at 25°C. The experimental data was from tests on four cylindrical cells (the cell ID numbers are listed in the legend), while the simulated data was using the fully parameterised DFN model.

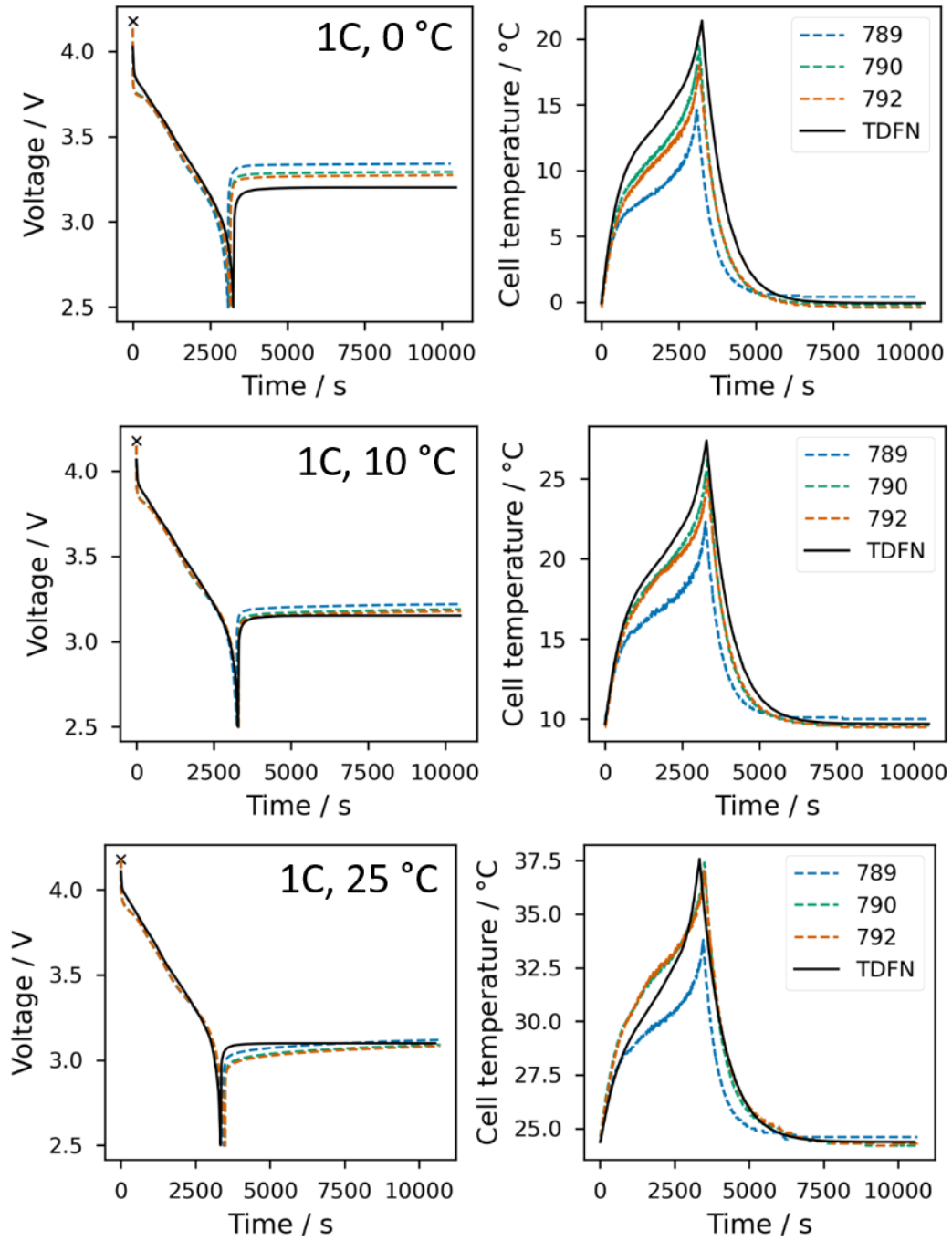


Figure 51. Experimental and simulated voltage (left) and temperature (discharge) profiles for a 1C discharge at 0 °C, 10 °C, 25 °C. The experimental data was from tests on three cylindrical cells (the cell ID numbers are listed in the legend), while the simulated data was using the fully parameterised DFN model.

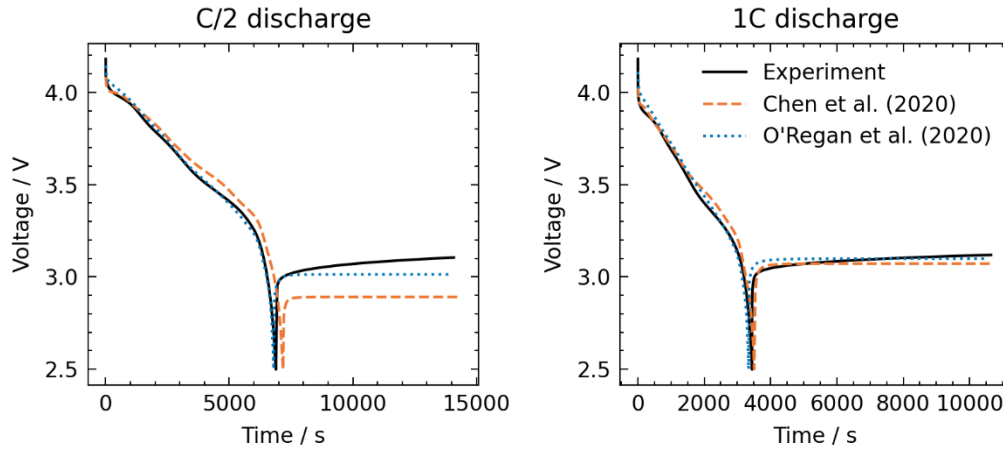


Figure 52. Simulations for the previous parameter set of the LG M50 (Chen 2020, orange dashed line) and the parameter set that considers parameter-dependencies and thermal behaviour (This work 2021, blue dotted line) compared to the experimental data. The parameters in both cases have been tuned to the data for the 1C discharge and then these same parameters are used for the C/2 simulation to demonstrate that the discharge behaviour and relaxation is captured better for C-rates that deviate from the tuned values. C/2 RMSE (root mean square error) for 0.10 for Chen2020 and 0.14 for this work.

Future work to improve the accuracy of the parameterisation includes mapping the lithium concentration of the thermal parameters (e.g. specific heat capacity and thermal conductivity), rather than at a single stoichiometry. This relationship was not considered here due to the stability of active materials in ambient conditions. *In situ* methods that allow measurement as a function of lithium concentration would allow the changes in these parameters that occur during battery operation to be captured. Additionally, the requirement to increase the solid-phase diffusivity value of each electrode highlights limitations in the analytical approach and DFN theory. It is assumed that particles are spherical and monodisperse despite the electrode microstructure being heterogeneous. Ignoring these effects in parameter evaluation and the model is one of the main reasons for disagreement with experimental data. Accounting for electrode inhomogeneity will improve model accuracy, for example including size distribution and non-spherical morphologies.

## 5.4 Conclusions

This chapter outlines the parameterisation methodology for a 3D thermal-electrochemical model for a high-energy lithium-ion battery. The electrochemical and thermal relationships in a high energy density cylindrical cell (21700) and the electrodes have been mapped through electrochemical testing at different temperatures, to provide diffusivity, exchange current and electronic conductivity profiles. Additional thermal properties, specific heat capacity, thermal conductivity and the entropic terms are measured using thermal characterisation techniques.

In this paper, we detail parameters for 0D to 3D models for use in future research. While thermal and electrode parameters support the creation of 3D to 0D models respectively,

our focus is on a 0D electrochemical-thermal model. This model, developed with our parameters, aligns well with cell validation data. Although expanding to a 3D model could improve accuracy, it necessitates further modelling efforts beyond our current scope.

The physical parameters of the negative and positive electrode are very similar, the positive electrode had slightly lower thickness, at 76  $\mu\text{m}$  rather than 84  $\mu\text{m}$ , a higher pore volume of 33,5% compared to 25% and a slightly lower mean particle radius of 5.2  $\mu\text{m}$  rather than 5.9  $\mu\text{m}$ . Whereas the thermal properties are also very similar with the Specific heat capacity ( $C_p$ ) at 990 and 950  $\text{J kg}^{-1} \text{K}^{-1}$  respectively, thermal diffusivity, ( $\alpha$ ) is 0.282 compared to 2.266  $\text{mm}^2 \text{s}^{-1}$  and the thermal conductivity 0.892 compared to 4.058 for the dry electrodes at room temperature, which corresponds to the difference in electronic conductivity of 0.847 and 215  $\text{Sm}^{-1}$ . Indicating that the thermal and electronic conductivities can be linked.

The negative electrode likely limits the maximum power observed by the cell, as observed from the lower diffusion coefficient and current exchange density compared to the positive electrode over the full SOC window. At stoichiometries of  $\text{Li}_x\text{C}_6$ , where  $x=0.45$  and 0.85 activation energies of up to 60  $\text{kJ K}^{-1}$  and low diffusion coefficients of  $5 \times 10^{-13} \text{cm}^2 \text{s}^{-1}$  at 25  $^\circ\text{C}$  were observed. Some of these limitations may be compensated for at 45  $^\circ\text{C}$  as the exchange current in the negative electrode surpasses that of the positive electrode and the diffusion coefficient increases in the negative by an order of magnitude to  $2 \times 10^{-12} \text{cm}^2 \text{s}^{-1}$ . Whereas for the positive electrode the lowest diffusion coefficients were observed for  $\text{Li}_x\text{MO}_2$ , at  $x=0.32$  and 0.81, which are just within the full cell cycling window ( $0.26 \leq x \leq 0.91$ ),  $7 \times 10^{-12} \text{cm}^2 \text{s}^{-1}$  was obtained at room temperature which increased to  $2 \times 10^{-11}$  at 45 $^\circ\text{C}$ , above stoichiometry of  $x=0.8$  the activation energy also doubled to 24  $\text{kJ K}^{-1}$ . The changes in temperature change the ionic transport by orders of magnitude and the reaction rates increase.

In terms of application to the modelling, the incorporation of state of charge or stoichiometry and temperature variable conductivities and diffusivities have improved the model fit before tuning. The electrochemical parameters tuning was reduced from four parameters: diffusivities and maximum concentrations, to only the solid-phase diffusivities. The magnitude of tuning was also reduced, the tuning needed of the negative electrode diffusivity was decreased by 303%. The diffusivity of the negative electrode is key to improving the models for high energy cells, large changes in magnitude of the diffusivity with temperature variation with only small changes in SOC, cause difficulties in fitting. To improve the fits at higher rates, the effect of the ohmic resistance and heating must be taken into consideration. As observed by the fit of the 2D discharge and relaxation, the actual observed voltage is significantly lower than the estimated. This is likely because the diffusion coefficient is being underestimated and Ohmic heating is causing faster movement of the lithium ions in the solid, resulting in more lithium transport over that time frame.

In summary, a parameterisation methodology is outlined, which uses electrochemical and thermal techniques, illustrating the parameter variability caused by local and global changes in temperature or lithium concentration. This methodology is chemistry and

format-agnostic and can be applied to different cell types to increase the availability of 3D thermal-electrochemical parameters. Insight into the diffusion and reaction rate kinetics show the limiting electrodes. Further work with these parameters would be to design, predict and validate faster charging and discharging protocols, through understanding the changes in rate kinetics at different states of charge and with temperature.

## **Data Availability**

The parameter set in Table 17 has been made available in the PyBaMM software package. This open-source software is a development platform for physics-based modelling tools.<sup>222</sup> Further information can be found at <https://www.pybamm.org/>.

The data repository with parameter values for the electrode solid-phase diffusivity, entropic term, exchange current density, electronic conductivity, specific heat capacity, and thermal conductivity can be found at Zenodo (<https://zenodo.org/>) under the DOI 10.5281/zenodo.5171874. The data repository containing the validation data for cells tested under different operating conditions can be found at Zenodo under the DOI 10.5281/zenodo.4864437.

# Chapter 6 - Advancing sodium-ion batteries: development of parameterisation methods for physics-based models

Partly based on **Thermal-electrochemical parameters of a high energy lithium-ion cylindrical battery**. Kieran O'Regan, Ferran Brosa Planella, W. Dhammika Widanage, and Emma Kendrick, *Electrochimica Acta*, **425**, 140700, (2022).<sup>7</sup>

## 6.1 Introduction

For lithium-ion battery systems electrochemical models are essential to optimise cell design, predict lifetime, and design fast charging algorithms. For sodium-ion batteries to be successful it is critical that similar models are developed to increase longevity and safety. It is unclear whether traditional electrochemical models developed for lithium-ion batteries can be applied directly to sodium-ion systems. These battery chemistries are both Group 1 alkali metals that can form ions that intercalate into different materials. These materials do exhibit kinetic and thermodynamic differences due to the size of the sodium ion, the structure of hard carbon, and the intercalation of sodium into the materials. The exact structure of hard carbon is not known, as it depends on the precursor and carbonisation conditions, meaning sodium is stored in many ways depending on synthesis.

The most widely used electrochemical model is the Doyle-Fuller-Newman (DFN) model (Figure 53). As the DFN model is underpinned by fundamental theories that describe the electrochemistry such as concentrated solution theory and porous electrode theory allowing the internal states of a battery. The internal states include the sodium concentrations and potential, both electrodes and electrolyte. The DFN model states that lithium-ion transport in the electrodes and electrolyte is governed according to Fick's law of diffusion. However, the exact sodiation mechanism into hard carbon is still unknown and may need new theories to describe this mechanism.<sup>223</sup> In graphite lithium intercalates according to Fick's law of diffusion, but sodium transport into hard carbon happens by both intercalation and plating. Different electrochemical models need to be combined with the DFN to model the deposition and dissolution of a metallic sodium phase in the three-dimensional microstructure.<sup>224,225</sup> This was confirmed by Bray *et al.* used NMR imaging to reveal chemical signals for both metallic and solvated Na, which are linked to sodium transport.<sup>5</sup>



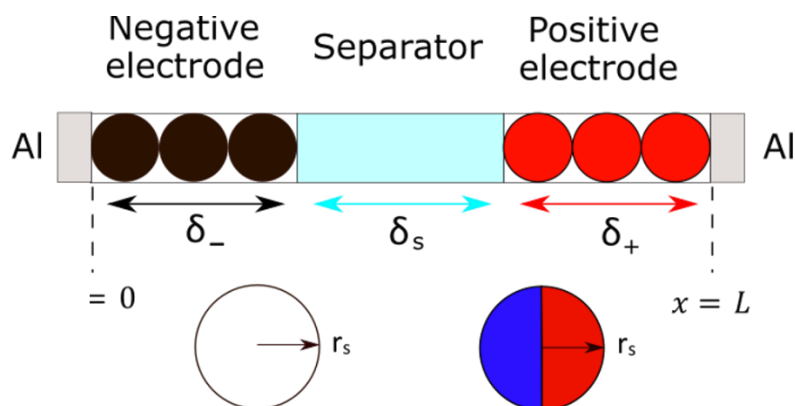


Figure 53. Doyle-Fuller-Newman model schematic for a Na-ion battery. This model is referred to as a pseudo-2-dimensional (P2D) model due to the battery system being defined in two dimensions with one for the thickness of the electrodes (Cartesian coordinates) and the other for the active material particles (radial coordinates).

There have been many studies into benchmarking the kinetic and thermodynamic performance of novel sodium-ion batteries. These investigations were aimed to rationalise material properties and phase changes, and few were motivated to parameterise electrochemical models. Chayambuka et al. outlined the first physics-based model parameterisation for a complete sodium-ion system.<sup>88,89</sup> The battery comprised of a  $\text{Na}_3\text{V}_2(\text{PO}_4)_2\text{F}_3$  (NVPF) cathode and a hard carbon anode, the parameterisation helped identify the diffusion mass transport limitations and ohmic losses for these materials. This work demonstrated that a DFN model could be used to provide good agreement to experimental and simulated data with no modification to the governing equations. Research into systems using different cathodes is needed, Chayambuka et al. studied an NVPF cathode with two characteristic voltage plateaus, like LFP.<sup>88</sup> However, the low energy density and the voltage response making it difficult to estimate state-of-charge, means the material is less favourable for use in automotive applications.

In this chapter, the first electrochemical parameterisation of a sodium-ion battery system comprising of hard carbon and a layered oxide material is presented. The aim for this investigation was to adapt to sodium-ion a previously published parameterisation strategy developed for a commercial lithium-ion battery.<sup>1</sup> This sodium-ion system was manufactured in-house and with known active materials, knowledge of chemical and physical parameters for the active materials improves parametrised accuracy as less assumptions have to be made. The methodology has been adapted to tailor to a different chemistry and challenges due to the higher variability of in-house manufactured materials. This system was chosen due to a high potential energy density, enabling the understanding of design limitations of the current technology to steps for future optimisation. The electrochemical model parameters were validated by comparing model and experimental data, with the results being published so that the model can be used to further accelerate sodium-ion development.

## 6.2 Experimental

### 6.2.1 Materials

The active materials used to manufacture the positive and negative electrodes were  $\text{Na}[\text{Ni}_{1/2}\text{Mn}_{1/4}\text{Sn}_{1/8}\text{Ti}_{1/8}]\text{O}_2$  (NMST2488) and hard carbon (Type I Kuranode, Kuraray). NMST2488 cathode material was prepared via solid-state reaction, by mixing stoichiometric proportions of  $\text{Na}_2\text{CO}_3$ ,  $\text{Ni}(\text{NO}_3)_2 \cdot 6\text{H}_2\text{O}$ ,  $\text{MnCO}_3$ ,  $\text{SnO}_2$  and  $\text{TiO}_2$ . The powders were milled in isopropanol for 2 days on a roller mill, using 50% by volume 10mm Zirconia milling media. Additional isopropanol was added to the above mixture to ensure good viscosity during mixing. The precursor mix was dried overnight in a vacuum chamber maintained at 70 °C, and then transferred into a crucible for heat treatment in a muffle furnace. The materials were heated to 650°C from room temperature for 2 h before increasing the temperature to 900 °C for 12 h. The temperature ramping rate was 2 °C min<sup>-1</sup>. The annealed sample was transferred to a glovebox while hot at 230 °C to keep the sample moisture free. It was then jet-milled at 30000 rpm to obtain dark brown powder which was further used for cathode slurry preparation.

Hard carbon and NMST2488 slurries were mixed in a Thinky mixer with all steps carried out at 1500 rpm. The NMST2488 electrode slurry was made using wt% ratio of 89:5:5:1 for the active material, conductive carbon (C65), polyvinylidene fluoride (PVDF), and oxalic acid. The oxalic acid was dissolved for 2 min, then the NMST and C65 were added and mixed for 5 mins, then the 8 wt% PVDF in N-Methyl-2-pyrrolidone (NMP) was mixed in for 5 mins. The mixes were carried out at 1500 rpm. Oxalic acid is used in battery electrode slurries as a dispersing agent, pH controller, viscosity optimizer, and adhesion promoter. It ensures a homogeneous mixture of active materials, binders, and conductive additives, leading to improved electrochemical performance and processing of the electrode coatings.

The hard carbon electrode slurry was made using a wt% ratio of 90:5:5 for the active material, C65, and PVDF. The PVDF (8 wt% in NMP) and hard carbon were mixed in the Thinky mixer for 5 min, then hard carbon was mixed in for 5 mins, then NMP was mixed in in several subsequent 5 minute steps to obtain the correct consistency for coating— 5.0 g, 2.0 g, 1.0 g, 1.0 g, and 1.0 g. The mixes were carried out at 1500 rpm.

The electrodes were coated onto 16 µm aluminium current collectors using a 200 µm doctor blade on a draw-down coater. The electrodes were initially dried on a hot-plate at 60 °C to remove the NMP. The electrodes were then further dried overnight in a vacuum oven at 60 °C

### 6.2.2 Physical Characterisation

#### 6.2.2.1 Geometric and gravimetric measurements

Thicknesses of the electrodes and current collector were measured using a digital length gauge (Heidenhain), the mass loadings of the electrodes were evaluated by cutting out a 10 cm<sup>2</sup> electrode area using a cutting tool (James Heal), the particle size distribution of the NMST2488 powder was measuring using a particle size classifier and diluting the

material to a solution with an optical concentration of 20%. A small quantity of the powder was dispersed in water in a vial using the dispersant available (2 drops). A few drops of the dispersed colloidal solution were put in the instrument such that the concentration was ~18%. Several repeats were done to get a stable and concurrent value.

#### 6.2.2.2 X-ray Diffraction

The XRD was carried out in the Proto machine with a Cu tube. The sample was prepared in the glovebox and a Kapton tape was put over it so that exposure to air/moisture is minimized. The sample was taken out from the glovebox and put in the instrument for measurement which was carried between 2 theta values of 10 - 90 degrees. The crystal density was measured using Rietveld refinement in the GSAS software suite. The crystal structure of  $\text{Na}[\text{Ni}_{1/2}\text{Mn}_{1/2}]\text{O}_2$  was used as a reference structure in the refinement.

#### 6.2.2.3 Scanning Electron Microscopy (SEM)

Top-view images of the hard carbon and NMST2488 electrodes were captured using an XL30 ESEM FEG (Phillips) with an accelerating voltage of 21 kV and a secondary electron detector. The mean particle radius of the electrodes was measured using ImageJ and spherical particle morphology was assumed.

#### 6.2.2.4 Optical Microscopy

Top-view images of the hard carbon and NMST2488 electrodes were captured using the Leica DCM8 3D digital microscope, using the confocal lens. The samples were then analysed using Leica Map software for visualising and analysing the electrode surface to obtain information about topology and particle size.

### 6.2.3 Electrochemical Characterisation

The electrochemical tests involved both a three-electrode configured PAT-Cell (EL-Cell) and a perfluoroalkoxy alkane (PFA) Swagelok<sup>TM</sup> half cell. The three-electrode cell was comprised of an 18 mm working and counter electrode, a 21.6 mm 250  $\mu\text{m}$  thick glass-fibre separator, a ring sodium reference electrode, with 150  $\mu\text{l}$  of electrolyte. The half-cell was comprised of a 12 mm working electrode, a 12 mm sodium disc counter electrode, 12.8 mm Celgard 2325 tri-layer separator (polypropylene/polyethylene/polypropylene) and 50  $\mu\text{l}$  of electrolyte. The electrolyte used was 1 mol  $\text{dm}^{-3}$   $\text{NaPF}_6$  in EC:DEC (1:1, v:v).<sup>86</sup> The electrochemical protocols were programmed on a VMP3 potentiostat (Bio-Logic). Electrochemical testing was preceded by two cycles of CCCV charge and CC discharge using the parameters outlined in Table 18. The tests were carried out at a controlled temperature of  $25 \pm 2$  °C.

Table 18. Voltage windows and formation parameters used for the three-electrode or two-electrode formation.

Configuration	Voltage Window	Formation current
Full cell	2.0 V to 4.2 V	10 mAh/g (3.33 mAh/g)
Positive electrode half cell	2.0 V to 4.2 V	10 mAh/g (3.33 mAh/g)
Negative electrode half cell	0.005 V to 2.0 V	15 mAh/g (5.00 mAh/g)

### 6.2.3.1 Galvanostatic Intermittent Titration Technique (GITT)

GITT was conducted in a three-electrode cell to evaluate the solid phase diffusion coefficients and electrode open circuit voltages (OCVs). The transient current and voltage windows used are outlined in Table 19. The transient duration was 600 seconds and the relaxation period was limited to 2 hours 30 minutes. The experiments were repeated for the individual electrodes in half cell configurations to understand electrode electrochemical behaviour beyond the stoichiometric range observed in the full cell.

Table 19. Voltage windows and current used for the three-electrode or two-electrode galvanostatic intermittent titration technique (GITT).

Configuration	Voltage Window	Transient current
Full cell	2.3 V to 4.2 V	15 mAh/g
Positive electrode half cell	2.3 V to 4.2 V	15 mAh/g
Negative electrode half cell	0.020 V to 1.5 V	15 mAh/g

### 6.2.3.2 Electrochemical Impedance Spectroscopy (EIS)

PEIS measurements were conducted at SoCs between 0% and 100% in a Swagelok half-cell. The sinusoidal current applied had an amplitude of 10 mV and a 10 mHz – 100 kHz frequency range. The data was analysed by fitting to an equivalent circuit model in Zview (Ametek).

### 6.2.3.3 Four-point Probe

Solid-phase electronic conductivity of the positive and negative electrodes was evaluated at temperatures using a four-point probe (Ossila Instruments). Both electrode coatings were delaminated using liquid gallium to dissolve the aluminium current collector and obtain the electrode coating undamaged. Small quantities of 1 mol dm<sup>-3</sup> hydrochloric acid and deionised water were used to remove the resulting gallium alloy. This methodology has been described in detail previously.<sup>166</sup> To measure the electronic conductivity of the electrodes a target current of 100  $\mu$ A was used, the voltage was stepped by 0.1 V until the target current had been reached.

Table 20. Summary of parameterization techniques.

	Technique	Parameter(s)	Details
Electrochemical characterisation	Galvanostatic intermittent titration technique	Diffusivity and open-circuit voltage	Three-electrode half cell
	Electrochemical impedance spectroscopy	Exchange current density	Two-electrode half cell
	Four-point probe	Electronic conductivity	Electrode laminate

### 6.2.3.4 Validation

The electrochemical model was validated using a discharge test in a three-electrode full cell. Before the experiment there is a two hour rest period to record the initial state. The cells were charged using a CCCV step with a 10 mA/g CC and a CV step with a 10 mA/g current cut-off for the CV step and discharged at 15 mA/g using a Bio-Logic VMP3

potentiostat. The voltage window used was 2.0 V - 4.2 V. The tests used the formation protocol outlined in Table 18.

#### **6.2.3.5 Simulations**

Simulations were conducted in the Python Battery Mathematical Modelling (PyBaMM) software package (using v0.4.0).<sup>109</sup> The equations for the electrochemical model are summarised in Table 3. In order to solve the model a finite volume scheme was used, with 30 grid points for each electrode and the separator, and 150 grid points for each particle; resulting in a system of 9092 ODEs and 150 algebraic equations. An exponential mesh was used to help with the convergence of the solver. To solve the system, a CasADI solver was used.<sup>167</sup>

### **6.3 Results & Discussion**

#### **6.3.1 Geometric Properties**

The geometric and microstructural information of the sodium-ion battery system were evaluated using gravimetric calculations and characterisation methods. The thicknesses of the aluminium current collector, and the positive electrode, and negative electrode were measured to be 16  $\mu\text{m}$ , 63  $\mu\text{m}$ , and 66  $\mu\text{m}$ . The chemical and physical properties of both electrodes are summarised in Table 18.

The particle radius is the most sensitive parameter used in the DFN model, this parameter has a significant impact on the model predictions so it is important that it is measured accurately. Imaged-based methods such as microscopy and X-ray CT are subject to inaccuracies due to small sampling sizes, two-dimensional representation, and difficulty contrasting particle boundaries. For this parameterisation the electrode powders can be characterised, this is the most accurate way to evaluate particle size. Although, changes to the active material during the electrode manufacturing such as cracking and agglomeration may cause morphological changes. Here, it is possible to compare the mean particle sizes obtained from the powder characterisation, SEM of the electrode, and optical microscopy of the electrode.

The  $D_{50}$  particle size and specific surface area of the hard carbon powder were known from the manufacturer datasheet provided by Kuraray for their Type I Hard Carbon. The  $D_{50}$  particle size for the hard carbon powder is 9  $\mu\text{m}$ , this is comparable to the 8.7  $\mu\text{m}$  measured using optical microscopy. The SEM images also illustrate a particle size of  $\sim 10 \mu\text{m}$  (Figure 56). The specific surface area of hard carbon was significantly higher than NMST2488 despite the larger particle radius, this is because of the pore-filled structure of the hard carbon.

The particle size distribution was of the synthesised NMST2488 (XRD pattern in Figure 54 to show chemical fingerprint) electrode powder was measured, with the  $D_{50}$  particle size and specific surface area measured to be 1.1  $\mu\text{m}$  and  $1.58 \text{ m}^2 \text{ g}^{-1}$  respectively. However, for the NMSTO the  $D_{50}$  particle size of the powder was measured to be 1.1  $\mu\text{m}$ , this is significantly different from the 4.46  $\mu\text{m}$  measured using optical microscopy. This difference is due to the agglomeration of micron-sized particles seen in the SEM images (Figure 56). This discrepancy would have a significant effect on the model predictions as

the particle size of the positive electrode is the most sensitive parameter in an electrochemical model.<sup>64</sup> This comparison demonstrates the differences of characterising the physical properties of the active material from the powder and electrode. For the model the powder particle size was taken as the true particle size, although there needs to be consideration in the model for the performance differences of distinct micro-sized particles and agglomerations of those particles.

The volume fractions and densities for the electrodes were calculated from the thicknesses, mass loadings, and crystal densities. For the NMST2488 electrode the laminate thickness was 63  $\mu\text{m}$  and an areal mass loading of 100  $\text{g m}^{-2}$ , this corresponded to a density of 1.58  $\text{g cm}^{-3}$ .

The crystal density of NMST2488 was calculated using Rietveld refinement, this is an O3-oxide NMST2488 material. Roberts *et al.* have reported other data on the structural characterisation of this material, including XPD and FT-IR.<sup>237</sup> The XRD pattern and the Rietveld refinement are shown in Figure 54. The lattice parameters were calculated from refining the crystal structure using  $\text{Na}[\text{Ni}_{1/2}\text{Mn}_{1/2}]\text{O}_2$  as a reference structure. The lattice parameters, outlined in Table 21, are used to calculate the unit cell volume. This unit cell volume is then used to calculate the unit cell volume  $V_c$  and the crystal density  $\rho$  from the following equation:

$$\rho = \frac{ZM_w}{V_c N_A} \quad [88]$$

The crystal density was calculated to be 3.90  $\text{g cm}^{-3}$ . The crystal density was used to calculate the volume fractions of the electrode by, from this the active material volume fraction was calculated to be 36.5% and the porosity was 54.7%. For the positive electrode the porosity is very high—this is likely due the micro-sized particles creating a lot of pores and the fact that the material was not calendered. The electrode was not calendered due to its thin electrode laminate.

Table 21. Lattice parameters and crystal structure properties of NMST2488 calculated from

Parameter	a / Å	b / Å	c / Å	Volume / Å <sup>3</sup>	Density / g cm <sup>-3</sup>
Value	3.009714	3.009714	16.028843	125.743	3.90
$\sigma$	0.000118	0.000118	0.000732	0.009	

For the hard carbon electrode, the laminate thickness was 66  $\mu\text{m}$  and an areal mass loading of 55  $\text{g m}^{-2}$ , this corresponded to a density of 0.83  $\text{g cm}^{-3}$ . Using a true density of 1.48  $\text{g cm}^{-3}$  for hard carbon the active material volume fraction was calculated to be 50.4%, while the porosity was 44.9%.

The tortuosity of both electrodes is assumed to be describe by the Bruggeman relationship with an Bruggeman constant  $b$  of 1.5:<sup>133</sup>

$$\tau = \varepsilon^{1-b} \quad [89]$$

The Bruggeman theory produces an exponent value of 1.5 for spherical particles, which aligns with the Bruggemann theory's prediction. This will be a limitation for hard carbon as the particle morphology is fragmented and non-spherical, however it is experimentally difficult to measure tortuosity using 3D imaging or mercury porosimetry.<sup>238</sup>

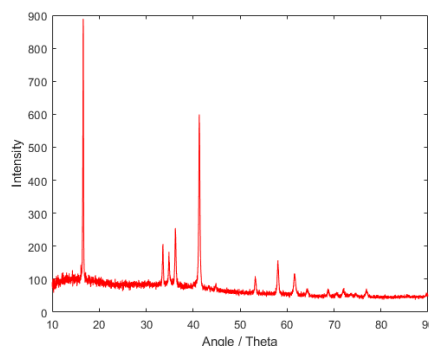


Figure 54. XRD pattern of the NMST2488 powder.

Table 22. Physical and chemical properties of the NMST2488 and hard carbon electrodes.\* denotes the particle sizes used in the model.

	Positive electrode	Negative Electrode
Active material	NMST2488	Hard carbon
Electrode laminate thickness / $\mu\text{m}$	63	66
D <sub>50</sub> particle size (powder) / $\mu\text{m}$	1.1*	9*
D <sub>50</sub> particle size (electrode) / $\mu\text{m}$	4.5	8.7
Current collector thickness / $\mu\text{m}$	16	16
Active volume fraction / %	36.5	50.4
Electrolyte volume fraction (porosity) / %	54.7	44.9
Inactive volume (binder and carbon) / %	8.8	4.6
Specific surface area / $\text{m}^2 \text{g}^{-1}$	1.58	4.0
Areal mass loading / $\text{g m}^{-2}$	100	55.5
Electrode density / $\text{g cm}^{-3}$	1.59	0.83
Crystal/True density/ $\text{g cm}^{-3}$	3.90	1.48

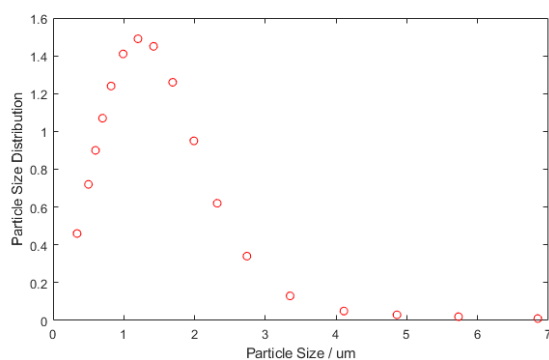


Figure 55. Particle size distributions for NMST2488, the D<sub>50</sub> is 1.1  $\mu\text{m}$  and specific surface area is 1.58  $\text{m}^2 \text{g}^{-1}$ . The data for the hard carbon was taken from the manufacturer datasheet.

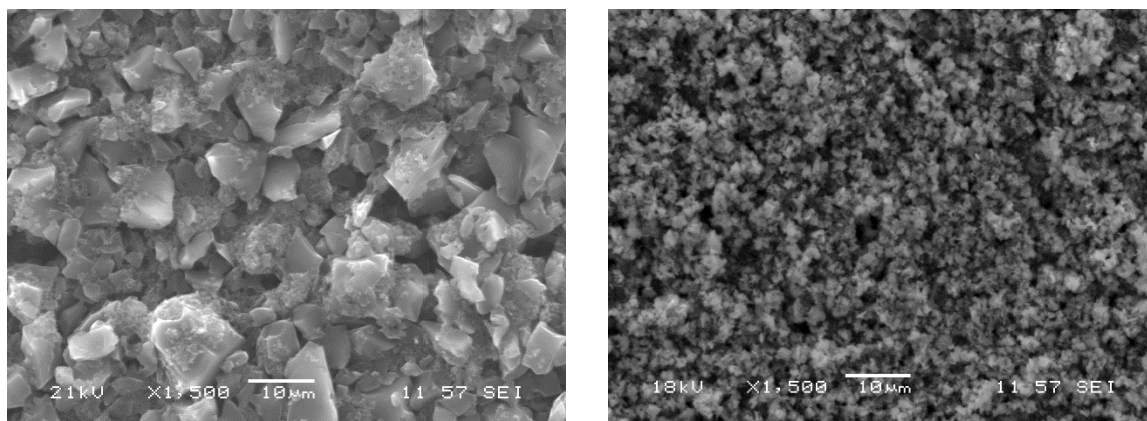


Figure 56. SEM images of the hard carbon powder (left) and NMST2488 (right) electrodes.

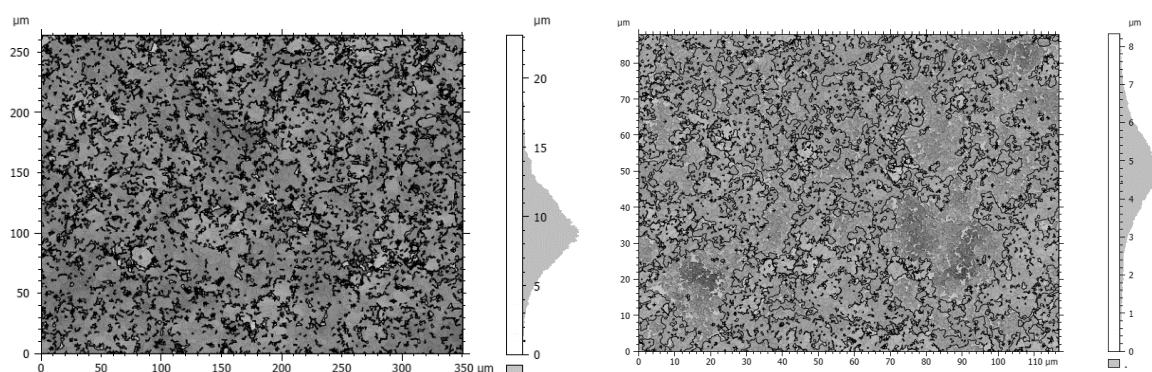


Figure 57. Optical microscopy of hard carbon powder (left) and NMST2488 (right) electrodes. The  $D_{50}$  particle sizes of the hard carbon and NMST2488 electrodes are 8.7  $\mu\text{m}$  and 4.5  $\mu\text{m}$  respectively.

### 6.3.2 Electrode Properties

The electrochemical properties of each material were evaluated from the average gravimetric capacities, first cycle losses and voltage profiles from half cell data. The electrochemical spectra are illustrated in Figure 58, with the electrochemical spectra of the positive electrode exhibiting a significant first cycle loss and high voltage hysteresis. The voltage profile of hard carbon does not have the voltage plateaus seen in graphite. These plateaus are due to the staging of graphite. Hard carbon has a sloped voltage profile due to the amorphous structure of carbon and a single plateau. The sloping region is due to sodium transport into the carbon layers and the plateau region is due to transport of sodium into the cavities.



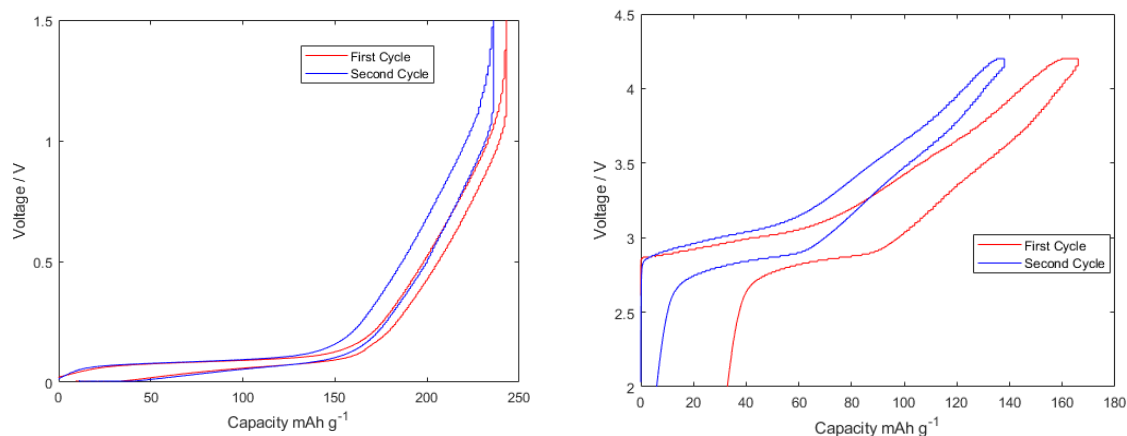


Figure 58. First cycle losses for each electrode during a formation of 15 mA/g of active material, hard carbon (left) and NMST2488 (right). Voltages recorded against Na/Na<sup>+</sup>.

For the positive electrode the capacity after the first cycle was measured to be 138 mAh g<sup>-1</sup> when cycled between 4.2 V and 2.0 V vs Na/Na<sup>+</sup>, this material experienced a 17% first cycle loss. This high first cycle loss can be attributed to the high surface and the fact that the material is made in-house and would have poorer quality.

For the negative electrode the capacity after the first cycle was calculated to be 243 mAh g<sup>-1</sup> when cycled between 1.5 V and 0.005 V vs Li/Li<sup>+</sup>, this material experienced a 3% first cycle loss. A lower first cycle loss is observed in the negative compared to the positive electrode because the manufacturing process has higher quality control.

The manufacturer datasheet states hard carbon has a charge capacity of 460 mAh g<sup>-1</sup> and a discharge capacity of 405 mAh g<sup>-1</sup>. The datasheet illustrates that ~50% of the capacity for hard carbon comes from the CV step. Figure 59 demonstrates that only 50 mAh g<sup>-1</sup> of capacity is extracted from the CV region, less than 75% than the manufacturer predicted. As the experimentally derived capacity does not reflect the full usable window, this discrepancy will need to be accounted for in the maximum concentration and stoichiometry calculations. This also demonstrates a methodological difference for sodium-ion compared to lithium-ion, a much lower current cut-off is needed for the CV step in hard carbon.. Due to the variable structure of hard carbons and the quantity of ions that can be stored in the cavities, the capacity ranges from 400 to 600 mAh g<sup>-1</sup>. This contrasts with graphite which has a theoretical capacity of 372 mAh g<sup>-1</sup>. For the characterisation of hard carbon in sodium-ion batteries it is important to fully evaluate the capacity so that sodium concentrations and stoichiometries can be calculated correctly.

Compared to the previous published sodium-ion parameterisation by Chayambuka et al. the materials in this chapter had significantly higher reversible capacities.<sup>5</sup> Achieving high reversible capacity is a prerequisite for a commercially viable energy system and therefore relevant parameterisation. In this chapter the reversible capacity of the positive and negative electrode were 138 mAh g<sup>-1</sup> and 243 mAh g<sup>-1</sup>, compared to the previously published 95 mAh g<sup>-1</sup> and 190 mAh g<sup>-1</sup>.

Cycling NMST2488 and hard carbon in a full cell configuration between 4.2 V and 2.0 V (defined as 0 to 100% SOC) achieves a capacity of  $1.32 \text{ mAh cm}^{-2}$  (Figure 59). This test was carried out in a three-electrode configuration to observe the individual voltage windows that the positive and negative electrode experience. This is important for properly mapping the change in the open-circuit voltage and other electrochemical properties as the battery is cycled. In the full cell there is a 25% first cycle loss, this is higher than the first cycle loss in both half cells and is likely due to a greater sodium loss in the positive electrode, the half cells have surplus sodium from the metal counter electrode.

The electrode conductivities were measured using a four-point probe to understand the electronic transport properties for NMST2488 and hard carbon materials. The electrodes were delaminated so that the electrode in-plane conductivity could be measured directly, this provided values of  $0.74 \text{ S m}^{-1}$  and  $18 \text{ S m}^{-1}$  for the NMST2488 and hard carbon respectively.

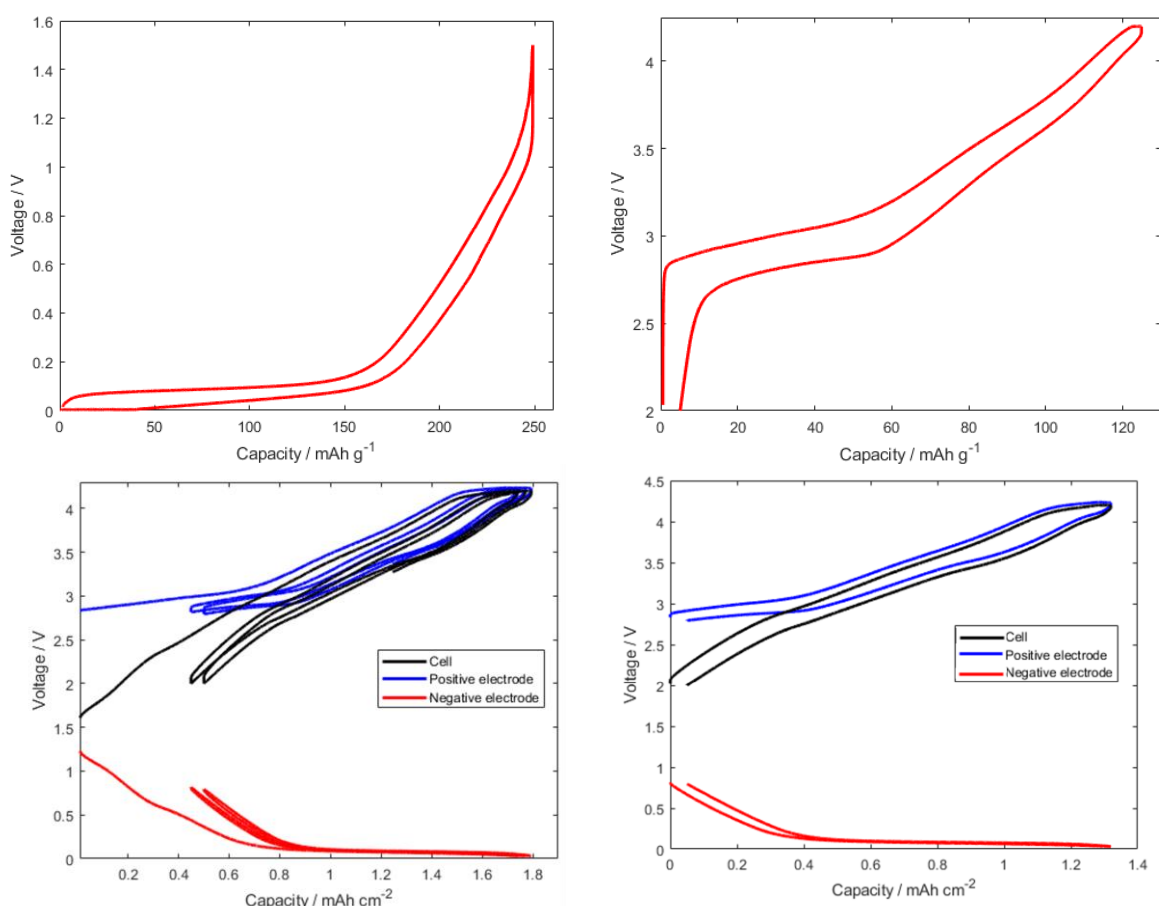
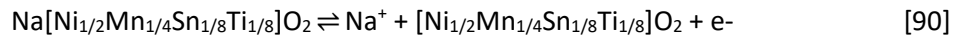


Figure 59. Gravimetric capacities of the hard carbon (top left) and NMST2488 (top right) electrodes measured in half cell figuration, and the first capacity loss (bottom left) for a three-electrode full cell, with the areal capacity of the second cycle (bottom right). Voltages recorded against  $\text{Na}/\text{Na}^+$ .

### 6.3.3 Stoichiometry & Maximum Concentration

The electrochemical properties of a sodium-ion battery are determined by the sodiation of the positive and negative electrode. This means that the occupation of sodium sites in the crystal lattices of the hard carbon and NMST2488 effects the material properties by influencing the electronic and ionic transport. Most notably, the solid phase diffusivity of sodium-ion materials can vary orders of magnitude across the stoichiometry range.<sup>239</sup> This means that the stoichiometry of these materials needs to be mapped as a function of voltage. This information can then be used to quantify the variability of the electrochemical properties that occur during cycling to enable more accurate model predictions compared to using constant parameter values.<sup>7</sup>

The redox reaction of the positive electrode is as follows:



A theoretical capacity of NMST2488 is calculated to be 227 mAh g<sup>-1</sup> from:

$$Q_{\text{theoretical}} = \frac{nF}{3600M_w} \quad [91]$$

The practical capacity of the material is 165 mAh g<sup>-1</sup>. The theoretical capacity of the commercial graphite can be calculated using the LiC<sub>6</sub> formula. However, determining the same for hard carbon employed in sodium-ion systems presents a more complex challenge due to its heterogeneous nature. The precise storage mechanism of hard carbon remains uncertain, and its exact structure is still unknown, primarily because it is influenced by the type of precursor and the conditions of carbonisation. These variables consequently yield materials with differing interlayer distances, crystal particle sizes, pore domains, among other properties. This means there is no general equation for the redox reaction. Instead of the theoretical capacity in hard carbon the maximum practical capacity stated on the manufacturer datasheet is used.

The maximum  $c_{1,m}^{\min}$  and minimum  $c_{1,m}^{\max}$  reversible sodium concentration can be calculated from the minimum and maximum reversible sodium capacities of the particles:<sup>87</sup>

$$c_{1,m}^{\min} = 3600 \frac{\rho_m Q_m^{\min}}{F} \quad [92]$$

$$c_{1,m}^{\max} = 3600 \frac{\rho_m Q_m^{\max}}{F} \quad [93]$$

$Q_m^{\min}$  is the non-extractable charge, this can be calculated from the difference in the reversible capacity and the theoretical capacity. This difference occurs due to the first cycle loss and the disparity between practical and theoretical capacity. Mapping electrode stoichiometry in commercial batteries excludes the first cycle loss as there is no

information about formation available. In these experiments the formation cycles have been recorded so the contribution of the irreversible sodium loss on formation can be calculated. The values needed to map stoichiometry are summarised in Table 23.

For the negative electrode the non-extractable charge  $Q_m^{min}$  is calculated to be 217 mAh g<sup>-1</sup> from the practical gravimetric capacity of 460 mAh g<sup>-1</sup> and a reversible capacity of 243 mAh g<sup>-1</sup>. Using a density of 830 g m<sup>-3</sup>, the  $c_{1,m}^{min}$  was calculated to be 6720 mol m<sup>-3</sup> and the  $c_{1,m}^{max}$  to be 14245 mol m<sup>-3</sup>.

For the positive electrode the non-extractable charge  $Q_m^{min}$  is calculated to be 89 mAh g<sup>-1</sup> from the theoretical gravimetric capacity of 227 mAh g<sup>-1</sup> and a reversible capacity of 138 mAh g<sup>-1</sup>. Using a density of 1580 g m<sup>-3</sup>, the  $c_{1,m}^{min}$  was calculated to be 5246 mol m<sup>-3</sup> and the  $c_{1,m}^{max}$  to be 13382 mol m<sup>-3</sup>.

Table 23. Parameters used to calculate stoichiometry limits for the electrodes in half cell configurations.

Parameter	Unit	Description	NMST2488	Hard carbon
$Q_m^{rev}$	mAh g <sup>-1</sup>	Reversible Capacity	138	243
$Q_m^{max}$	mAh g <sup>-1</sup>	Maximum Capacity	227	460
$Q_m^{min}$	mAh g <sup>-1</sup>	Non-extractable Charge	89	217
$c_{1,m}^{max}$	mol m <sup>-3</sup>	Maximum concentration	13382	14245
$c_{1,m}^{min}$	mol m <sup>-3</sup>	Minimum concentration	5246	6720
$S_m^{max}$	-	Maximum stoichiometric index	1	0.53
$S_m^{min}$	-	Minimum stoichiometric index	0.39	0

The sodium stoichiometries that each electrode experiences in a full cell can be evaluated by using three-electrode testing, and comparing data obtained in both half cell and full cell configurations. This requires mapping sodium stoichiometries across a known range, the stoichiometric indexes can be used to map the sodium concentrations for the half cells (in red) to calculate those for the full cell (in blue). For the hard carbon electrode, the half cell upper and lower voltage limits are defined as sodium stoichiometries of 0 and 0.53 respectively. The material is fully desodiated at the upper voltage window, but as the material did not have a CV step sufficiently long there is a significant amount of capacity from the material not being full sodiated.

From the fitting of the two voltage profiles, it can be observed that the stoichiometric range the NMST2488 electrode is cycled through in the full cell (2.5-4.2 V) is 0.39 to 1. Then the limits for the full cell these values correspond to 0% and 100% SoC respectively.

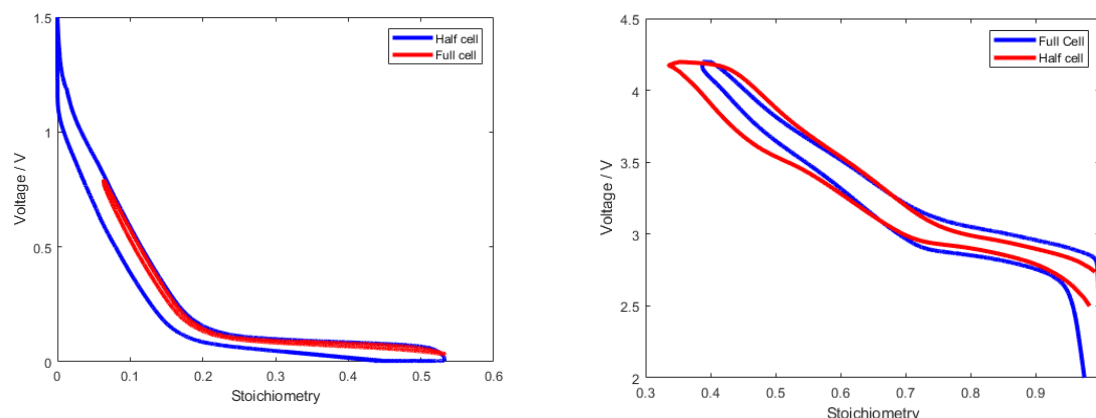


Figure 60. Three-electrode tests to map the sodium stoichiometry range that the hard carbon (left) and NMST2488 (right) electrodes undergo in a full cell (red) calculated by comparing to the half cell data (red). Voltages recorded against Na/Na<sup>+</sup>.

### 6.3.3.1 Open-circuit voltages

The open-circuit voltage is measured from galvanostatic intermittent titration technique (GITT) in a three-electrode configuration. The three-electrode cell of NMST2488 / Na / hard carbon provided the open-circuit voltage (OCV) points seen in Figure 61. The OCV profile was used to quantify the thermodynamic behaviour of the battery and is a critical parameter to predict the relationship between sodium concentration and voltage.

The hysteresis in the OCV provides further insight into the thermodynamic behaviour of the sodium-ion system. This is defined as the difference between OCV observed in sodiation and desodiation of the materials. For commercial viability of materials, it is important to find materials with low hysteresis as the property causes inaccuracies for state estimation and lowers the coulombic efficiency of the material. The hard carbon has negligible hysteresis for high degrees of sodiation (below 0.1 V), as sodium is removed the hysteresis increases. Similarly, the NMST2488 has low hysteresis below for high degrees of sodiation. In both cases the removal of sodium increases the hysteresis of each material, but most hysteresis can be attributed to the intrinsic properties of the material.

The stability and overpotentials can be observed in the GITT profiles, these are illustrated in Figure 61. The open-circuit voltage relaxation in both electrodes achieves  $<0.1 \text{ mV h}^{-1}$ , this is close to the electromotive force which is the voltage of the system at infinitely long rest. It is closely related to the OCV, which is the voltage measured across the terminals of a battery when it is not supplying any current; essentially, the OCV is a direct measurement of the electromotive force of the battery under no-load conditions.

The OCV and pseudo-OCV (pOCV) can be compared to understand the overpotentials during battery cycling, see Figure 62 for the comparison for both electrodes in a three-electrodes full cell. The pOCV is measured by application of a slow current so that the system does not reach open-circuit. GITT is used to reduce the hysteresis as it allows precise measurement of each electrode voltage, however if the overpotentials of the

material is low there is little difference between these two measurements. The comparison of these two voltage profiles for the positive electrode illustrates there is little difference between the voltage profile at open-circuit and under the application of a small current, there is a large intrinsic hysteresis in the NMST2488. This is also true for the hard carbon electrode, there is little observable difference between the OCV and pOCV.

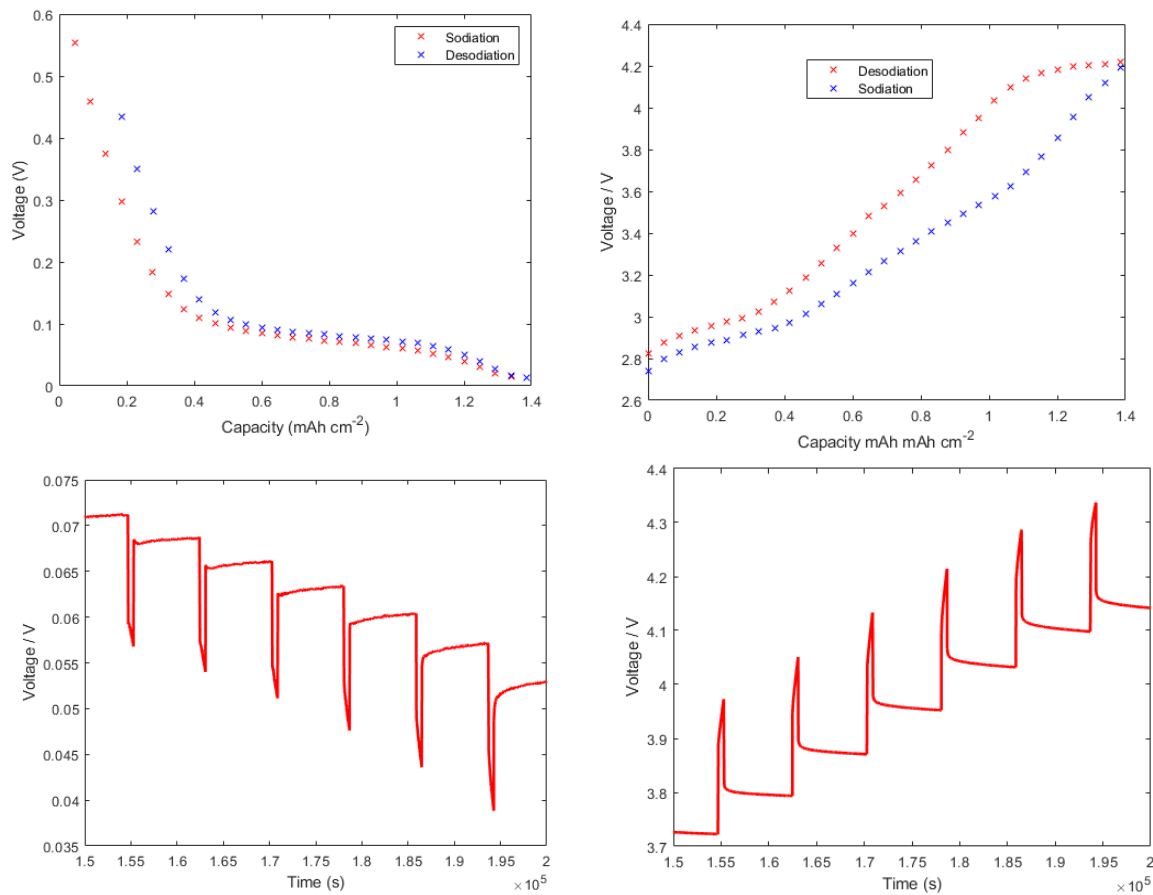


Figure 61. Open-circuit voltage of the hard carbon (top left) and NMST2488 electrodes (top right), measured using GITT in a three-electrode full cell. Voltages recorded against Na/Na<sup>+</sup>. The GITT profiles for the hard carbon (bottom left) and NMST2488 (bottom right) illustrate the stability and overpotentials during the measurement.

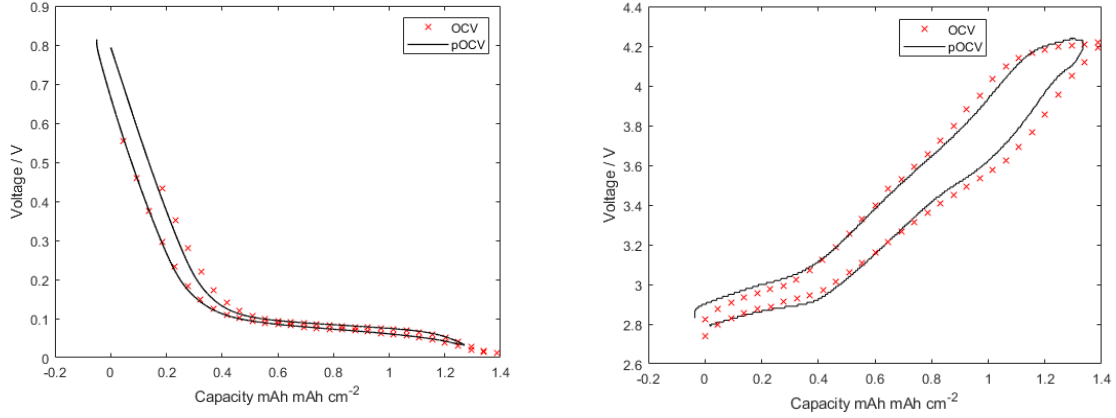


Figure 62. Comparison of the OCV and pOCV for the hard carbon (left) and NMST2488 (right) electrodes, measured using GITT in a three-electrode full cell. The voltage is measured against a Na/Na<sup>+</sup> reference.

### 6.3.3.2 Solid phase Diffusivity

GITT can also be used to determine the diffusion coefficient for the transport of sodium-ion within the active material. Traditionally, the diffusion coefficients can be calculated by:

$$D = \frac{4}{\pi\tau} \left( \frac{m_{AM} V_M}{M_{AM} S} \right)^2 \left( \frac{\Delta E_s}{\Delta E_t} \right)^2, \left( \tau \gg \frac{L^2}{D} \right) \quad [94]$$

As introduced by Weppner and Huggins.<sup>229</sup> Here  $\tau$  is the applied current interval ( $\tau = 600$  s),  $m_{AM}$  is the specific mass of the electrode,  $V_M$  is the molar volume,  $M_{AM}$  is the atomic weight of the active material,  $S$  is the active surface, and  $L$  is the electrode thickness. This equation has been adapted to use the Sand Equation as described in the Chen *et al.* paper.<sup>1</sup> This approach allows the fitting of multiple datapoints from the transient region and fitting the voltage profile to  $t^{1/2}$  rather than just four datapoints, improving the robustness of the measurement. The parameters needed to calculate solid-phase diffusivity using the Sand Equation include  $R$  as the particle radius,  $F$  as the Faraday constant,  $L$  is the electrode thickness, and  $\varepsilon_{act}$  as the active material fraction of the electrode. The physical properties of each electrode can be found in

Table 22.

Understanding the sodium diffusion process is important to be able to optimise the electrochemical performance of the resulting system. Relatively slow sodium diffusion in the pore networks of electrode can result in concentration depletion or excess sodium at the particle surface. This is observed as an overpotential and reduces performance. To examine the diffusion in each sodium ion material the diffusion as a function of sodium concentration in Figure 63 can be studied.

The solid-phase diffusion coefficients for hard carbon and NMST2488 for both materials are shown to vary orders of magnitude as a function of sodium concentration. The

measurements were taken in both three-electrode half cell and full configurations to evaluate the contribution of the sodium metal, the average values for each electrode are summarised in Table 24.

There is a difference between both the values and profiles for the solid-phase diffusivity in the half cell and full cell measurements. This is due to the presence of the sodium metal counter electrode in the half cell measurement, the shape of the diffusivity profile is caused by the instability of the voltage measurement in the half cell.

In hard carbon solid-phase diffusivity varies across between  $\sim 10^{-10}$  and  $\sim 10^{-12} \text{ cm}^2 \text{ s}^{-1}$ . In the full cell, the solid-phase diffusion coefficients have a largely consistent value in the order of  $\sim 10^{-10} \text{ cm}^2 \text{ s}^{-1}$ . However, in the half-cell the solid-phase diffusivity varies significantly for desodiation, this is due to the stripping of sodium on the counter electrode that could be causing dendrites or other electrochemical artefacts. The mean solid-phase diffusivity is nearly an order of magnitude lower in the half cell than the full cell. Solid-phase diffusivity values for hard carbon were previously outlined by Ledwoch *et al.* and were reported to be similarly in the range  $10^{-10} \text{ cm}^2 \text{ s}^{-1}$  and  $10^{-12} \text{ cm}^2 \text{ s}^{-1}$ .<sup>228</sup>

The measurement for the solid-phase diffusivity of NMST2488 positive electrode shows that this material is the rate limiting component in the sodium-ion system. The positive electrode had a significantly low mean solid-phase diffusivity in the order of  $10^{-13} \text{ cm}^2 \text{ s}^{-1}$  for both the half cell and full cell measurement. There is little research on similar layered oxide doped materials to compare diffusivity values.

Table 24. The mean solid-phase diffusion coefficients for both materials in the sodium-ion system extracted in three-electrode configurations. These values are provided for both Sodiation and desodiation.

Material	Full Cell / $\text{cm}^2 \text{ s}^{-1}$		Half Cell / $\text{cm}^2 \text{ s}^{-1}$	
	Sodiation	Desodiation	Sodiation	Desodiation
Hard Carbon	$1.161 \cdot 10^{-10}$	$1.051 \cdot 10^{-10}$	$3.144 \cdot 10^{-11}$	$5.271 \cdot 10^{-11}$
NMST2488	$2.960 \cdot 10^{-13}$	$5.274 \cdot 10^{-13}$	$3.332 \cdot 10^{-13}$	$5.660 \cdot 10^{-13}$

The key trends observed from the diffusivity measurements are:

- Significant difference between the positive and negative electrode solid-phase diffusivity, the mean value for the positive electrode is over 100x smaller than hard carbon. Smaller particles or more irregular shapes in the NMST2488 could lead to a higher tortuosity and therefore lower diffusivity, compared to larger or more uniform particles in the hard carbon.
- The diffusion limitation in sodium-ion systems primarily arises from the positive electrode (cathode) during charging. Slower diffusion rates for sodium ions in cathode materials, compared to lithium ions, result from their larger ionic radius and distinct thermodynamic and kinetic properties. These factors lead to higher diffusion resistance when sodium ions migrate from the anode to the cathode during charging. Such limitations impact the overall performance, energy efficiency, and rate capability of sodium-ion batteries.



- Hard carbon's solid-phase diffusivity is an order of magnitude lower in half-cells than full-cells, due to electrochemical artifacts on the sodium metal electrode. Half-cells exhibit higher overpotential and susceptibility to side reactions, like dendrite formation and electrolyte decomposition, compromising safety and performance. Capacity mismatch in half-cells leads to overestimation of specific energy and energy density in full-cells, highlighting the importance of validating half-cell results in full-cell configurations for practical applications.
- In most cases, for each electrode the solid-phase diffusion is higher for desodiation than sodiation. The solid-phase diffusion of ions in the electrode materials is influenced by factors such as crystal structure, thermodynamics, and kinetics of the intercalation and deintercalation processes. These factors can result in different diffusion rates during sodiation and desodiation. However, this is not a universal rule and may depend on the specific battery chemistry, electrode materials, and experimental conditions.

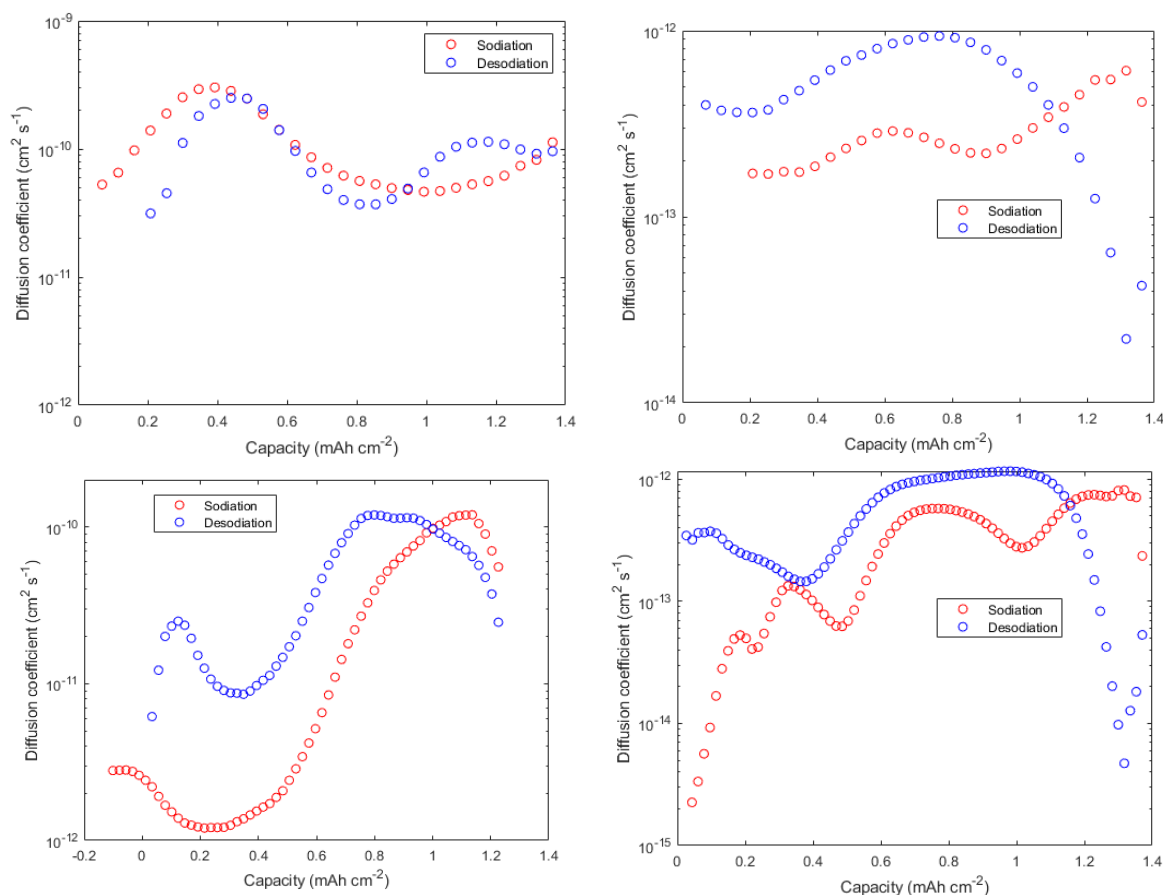


Figure 63. Sodium solid-phase diffusivity of the hard carbon (left) and NMST2488 electrodes, measured using GITT in three-electrode full cells (top) and three-electrode half cells (bottom).

### 6.3.3.3 Exchange Current Density

The exchange current density describes the electron transfer speed as ions transition between the electrolyte and the electrode. This is the current quantified at a zero overpotential and in the absence of any net charge transfer. It's feasible to determine this value via the charge transfer resistance, which is measured using electrochemical impedance spectroscopy (EIS).

To measure the exchange current density for both electrode, electrochemical impedance spectroscopy was used in a two-electrode set-up. From the EIS measurement the ohmic resistance, SEI (solid electrolyte interface) resistance and the charge transfer resistance can be investigated. These measurements were carried out for a NMST2488 and hard carbon electrodes in sodium metal half cells. The resistances were evaluated at 11 different states-of-charge (0, 10, 20, 30, 40, 50, 60, 70, 80, 90, 100%). The definition of state-of-charge for half cells is defined using the voltage windows summarised in Table 18.

The ohmic and interfacial resistances were evaluated by fitting an equivalent circuit model from carrying out potentiostatic EIS. The equivalent circuit used in the EIS analysis is outlined in Figure 64. In this circuit,  $R_{SEI}$  and  $CPE_{SEI}$  are related to the charge transfer across the solid electrolyte interphase. The exchange current density can be calculated from the charge transfer resistance ( $R_{ct}$ ), this is the larger of the two resistances parallelised with the CPE. The variation in the charge transfer resistance with respect to each electrode and state of charge can also be calculated.

The charge transfer resistance was calculated as a function of sodium stoichiometry for the NMST2488 and hard carbon electrodes, the values across this range are summarised in Table 25. The average value for the interfacial resistance was 227  $\Omega$  and 374  $\Omega$  for the hard carbon and the NMST2488 respectively. The large semi-circles correspond to a high resistance in the two-electrode set-up. This resistance is due to the sodium metal contacting the electrolyte and forming a thick SEI film. The thick SEI film is formed as a result of sodium metal reacting with the electrolyte upon contact, leading to the accumulation of insulating layers on the electrode surface. This thick SEI creates a large transfer resistance in comparison to lithium-ion batteries, with the sodium-ion system phenomena being reported previously in research.<sup>230</sup> Three-electrode configurations can be used to reduce this resistance contribution, although there are often artefacts observed that make analysis difficult.<sup>96</sup>

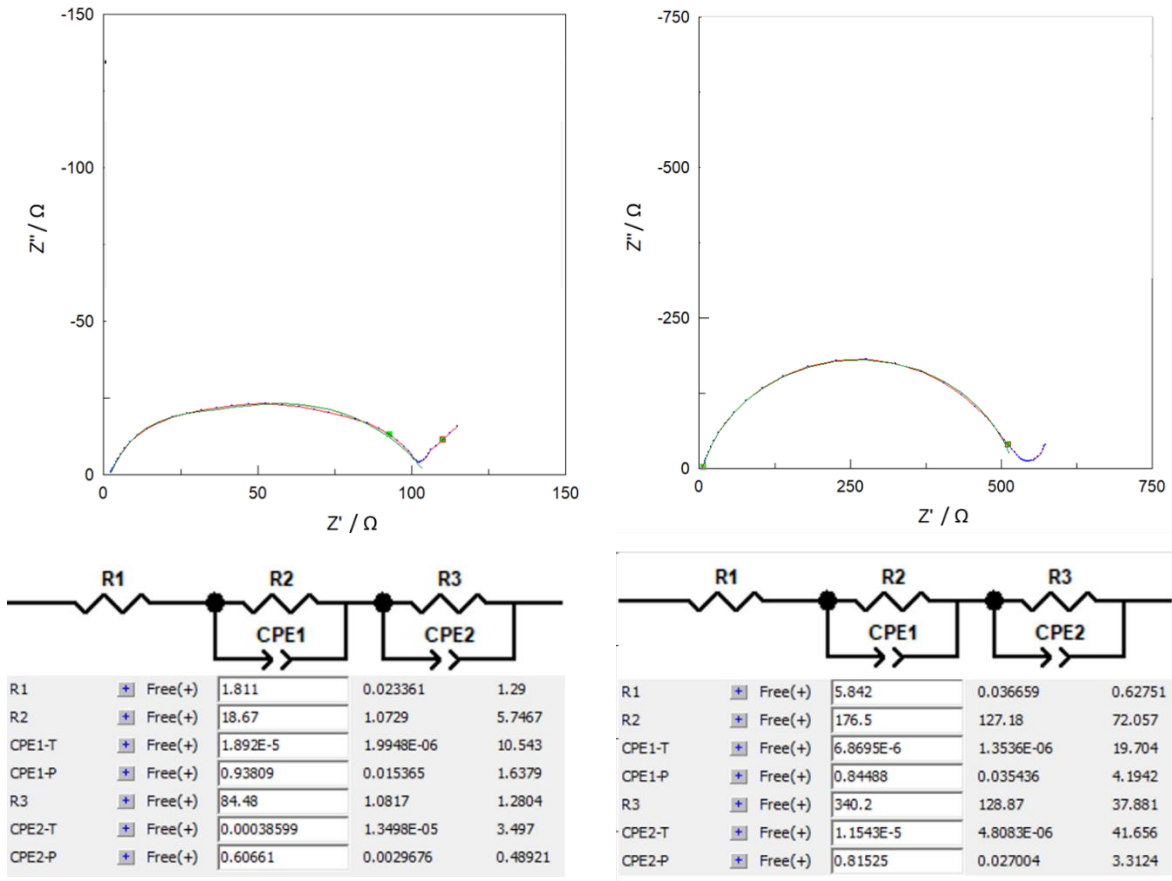


Figure 64. Nyquist plot data fitted to an equivalent circuit model for the negative (top left) and positive electrodes (top right), plus the corresponding fitting parameters with errors for the resistance and capacitance values (bottom).

Table 25. Interfacial resistances ( $R_{CT}$ ) across the stoichiometric range measured in a half cell configuration.

SoC	0%	10%	20%	30%	40%	50%	60%	70%	80%	90%	100%
Hard Carbon $R_{CT} / \Omega$	1040	342	195	130	130	96.6	83.8	91.5	102	97.3	99.8
NMST2488 $R_{CT} / \Omega$	593	353	333	344	379	365	316	360	360	340	314

Following this, the exchange current density  $j_o$  can be evaluated by using the charge transfer resistance  $R_{ct}$ :

$$j_o = \frac{RT}{R_{ct}SF} \quad [95]$$

Here  $R$ ,  $S$ ,  $T$ , and  $F$  are the gas constant, the surface area density, temperature in Kelvin, and the Faradaic constant. For this calculation  $S$  can be calculated from the specific surface volume ( $A \times L$ ) of active material, the active material volume fraction  $\varepsilon_{act}$ , and the active material mass radius  $r$

$$S = \frac{3V\varepsilon_{act}}{r} \quad [96]$$

For hard carbon the specific volume is  $7.46 \cdot 10^{-9} \text{ m}^3$ , the active material volume fraction is 50.4%, and the radius is  $9 \cdot 10^{-6} \text{ m}^3$ . This equates to  $0.001253 \text{ m}^2$ . For NMST2488 the specific volume is  $7.10 \cdot 10^{-9} \text{ m}^3$ , the active material volume fraction is 36.5%, and the radius is  $1.1 \cdot 10^{-6} \text{ m}^3$ . This equates to  $0.00709 \text{ m}^2$ . This equates to  $0.0119 \text{ m}^2$ . Following Equation [77] the exchange current densities can be calculated and are summarised in Table 26. The average values of the exchange current densities for the hard carbon and NMST2488 electrodes are  $1.60 \cdot 10^{-1} \text{ A m}^{-2}$  and  $9.95 \cdot 10^{-2} \text{ A m}^{-2}$  respectively, these are the values used in the model. However, the data in Table 26 can be used to map the exchange current density as a function of sodium concentration to account for this parameter dependency, previous research has mapped the dependency using a Butler-Volmer expression.<sup>7</sup>

Table 26. Exchange current densities calculated across the stoichiometric range for both electrodes.

SoC	0%	10%	20%	30%	40%	50%	60%	70%	80%	90%	100%
Hard Carbon / $\text{A m}^{-2}$	0.0197	0.0599	0.1051	0.1576	0.2121	0.2445	0.2239	0.2009	0.2106	0.2053	0.0197
NMST2488 / $\text{A m}^{-2}$	0.0061	0.0103	0.0109	0.0105	0.0096	0.0099	0.0115	0.0101	0.0101	0.0107	0.0061

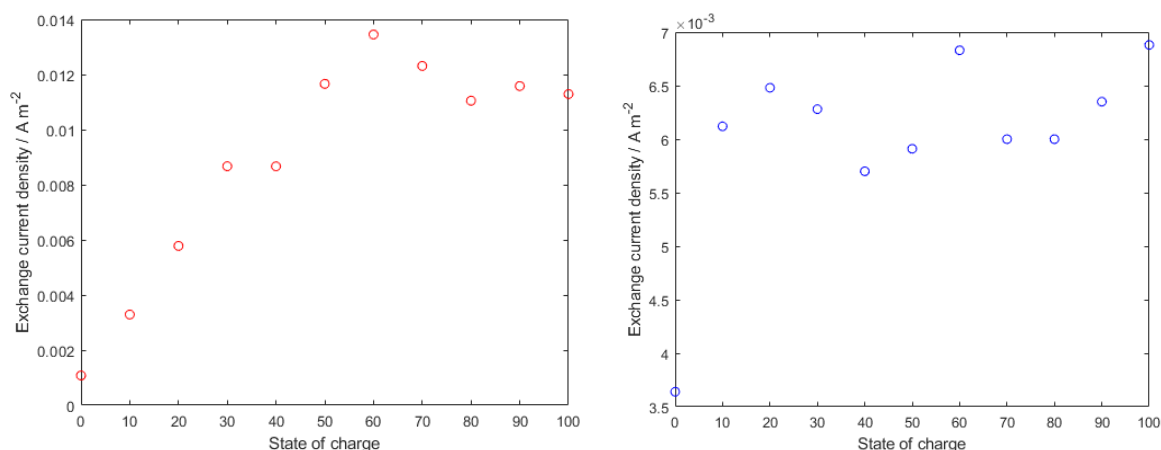


Figure 65. Exchange current densities measured from EIS as a function of state-of-charge (SOC) for hard carbon (left) and NMST488 (right), measured in half cell configurations. These values are used to observe the parabolic Butler-Volmer behaviour and to evaluate the mean exchange current density.

### 6.3.4 Electrolyte properties

It's important to note that the upcoming equations and properties were not developed by the author of this thesis. They are included here to ensure a complete and well-rounded understanding of the topic. Full credit for these equations and properties goes to the original researchers, as indicated by the proper citations and references in the text. The last set of properties for the full electrochemical parameterisation relate to the electrolyte and separator. For this investigation an electrolyte composition of a previously characterised electrolyte was chosen, this electrolyte was  $\text{NaPF}_6$  in EC:DEC (1:1, v:v). The electrolyte properties measured include the ionic conductivity, ionic diffusivity, transference number, and thermodynamic factor.<sup>86</sup> The electrolyte properties

are each dependent on concentration (for these relationships the units of concentration should be mol l<sup>-1</sup>).

Ionic conductivity:

$$\kappa(c) = 61.2 \cdot c \cdot \frac{1 - 0.732 \cdot \sqrt{c} + 0.0857 \cdot c}{1 + \exp(0.374 \cdot c^2)} \cdot \frac{mS}{cm} \quad [97]$$

Ionic diffusivity (note: this expression has been corrected from the original publication due to a typographical error that had a second multiple of 10<sup>-6</sup>):

$$D_{\pm} = 4.07 \cdot 10^{-6} \cdot \exp(-0.367 \cdot c) \cdot 10^{-6} \cdot \frac{cm^2}{s} \quad [98]$$

Transference number:

$$t_+(c) = 0.526 - 0.132 \cdot c \quad [99]$$

Thermodynamic factor:

$$TDF = 1.24 + 0.306 \cdot c \quad [100]$$

The validation experiments were carried out in an EL-Cell using the separator FS-5P (Freudenberg Viledon FS 2226E + Lydall Solupor 5P09B). This separator is 220 µm, the properties are described in Table 27. The FS-5P separator is bi-layered, comprising of two materials with different porosities and thicknesses, the porosity of the separator is evaluated to be 70.5% by averaging across the individual thicknesses and porosities of each separator. The Freudenberg Viledon FS 2226E and Lydall Solupor 5P09B separators had thicknesses and porosities of 182 µm and 67%, plus 38 µm and 86% respectively. With the electrode, electrolyte, and separator properties quantified and summarised in Table 29, it is now possible to conduct validation through a comparison of experimental and simulated data.

Table 27. Physical properties of the separator in the electrolyte domain. 1 = assumed according the Bruggeman relationship. 2 = averaged across both separator materials and weighted as thickness.

Name	Description	Thickness / µm	Porosity	Tortuosity
FS/5P	PP fiber/PE membrane	220	70.5	1.5 <sup>1</sup>

### 6.3.5 Validation

The key differences between electrochemical parameterization of lithium-ion and sodium-ion batteries stem from the distinct structural properties, materials, and transport mechanisms associated with each system. For sodium-ion parameterization, hard carbon demands extensive characterization due to its unique structure and capacity, which affects stoichiometry and maximum concentration calculations. In contrast, lithium-ion batteries typically use LFP or NMC materials.

Additionally, sodium-ion cathode materials require XRD and Rietveld refinement for accurate characterization, as sodium systems exhibit greater crystal inhomogeneity compared to lithium-ion systems. Furthermore, sodium-ion modelling demands new equations to extend the standard DFN framework, accounting for different transport mechanisms in sodium-ion batteries.

Lastly, sodium-ion parameterization involves in-house materials development due to limited commercially available cells. This introduces more experimental error as manufacturing tolerances are harder to control at a small scale, compared to the well-established lithium-ion battery materials and manufacturing processes. Building on the unique challenges of sodium-ion battery parameterization, our validation methodology adopts a three-electrode configuration to accurately parameterise these systems.

The three-electrode configuration used in validation enables the positive and negative electrode potentials to be used to accurately tune individual parameters. Deconvoluting the individual potentials allows improved tuning of the stoichiometry and maximum concentrations of each electrode as the changes of parameters can be seen directly for an individual electrode voltage, rather than their contribution to the battery terminal voltage.

To improve the accuracy of the simulated sodium-ion battery model, it was necessary to fine-tune the model parameters by adjusting the maximum concentrations of the positive and negative electrodes by factors of 1.135x and 0.79x, respectively. These adjustments were carried out by comparing the discharge profiles on the individual electrode potentials as seen in Figure 66. These adjustments are summarised in Table 28.

This improved the Root Mean Square Error (RMSE) to an average of 9.7 mV, which is significantly better than the automotive requirement of less than an average of 30 mV across the cycle. This outcome demonstrates the effectiveness of our parameterization methodology, which incorporates a new process for calculating the thermodynamic and kinetic parameters.

However, one limitation of this approach is that it only considers a slow discharge current, while ignoring the charge, drive cycles, and the temperature dependency of parameters. To further enhance the model's accuracy and applicability, future work should address these additional factors.

Table 28. Table outlining the tuning of parameters for the physics-based model.

Parameter	Positive Electrode Maximum Concentration / mol m <sup>-3</sup>	Negative Electrode Maximum Concentration / mol m <sup>-3</sup>
Old Value	13382	14245
New Value	15188	11253
Tuning / %	13.5%	21%

The experimental validation in this research is limited to only a slow discharge to prove the novel parameterization methodologies for sodium-ion batteries. However, this provides future scope to improve the robustness of methods with wider validation data. Future validation, including different temperatures, different C-rates, and dynamic drive cycles, will improve the experiments' validity to widen to results to different applications. The full list of parameters is summarised in Table 29, with parameters tuned from their measured values highlighted.

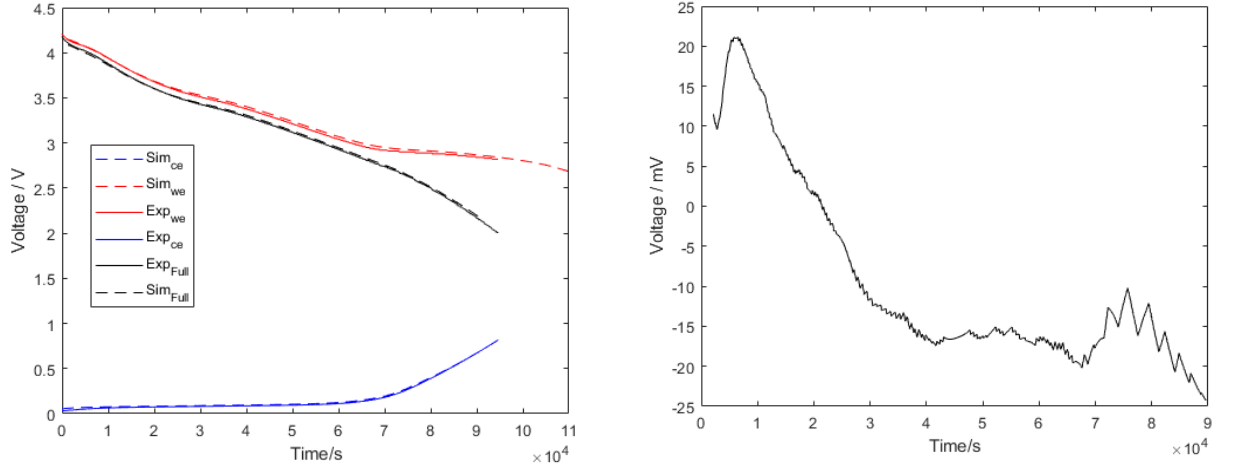


Figure 66. Plots for the working and counter simulated and experimental discharges voltage profiles from a three-electrode cell (left) and the root mean square error (RMSE) between the simulated and experimental terminal voltages (right), these voltage profiles were measured at C/20.

Table 29. Sodium-ion battery parameters required for the Doyle-Fuller-Newman (DFN) model.

	Parameter	Unit	Positive electrode ( $k = p$ )	Separator ( $k = s$ )	Negative electrode ( $k = n$ )
	Active material		NMST2488	FS-5P	Hard Carbon
Design specifications	Current collector thickness	m	$16 \cdot 10^{-6}$	-	$16 \cdot 10^{-6}$
	Electrode thickness ( $L_k$ )	m	$63 \cdot 10^{-6}$	$220 \cdot 10^{-6}$	$66.0 \cdot 10^{-6}$
	Mean particle radius ( $R_k$ )	m	$1.1 \cdot 10^{-6}$	-	$9.0 \cdot 10^{-6}$
	Electrode volume fraction ( $\epsilon_{act,k}$ )	%	36.5	70.5	50.4
	Electrolyte volume fraction ( $\epsilon_k$ )	%	54.7	29.5	44.9
	Bruggeman exponent ( $b$ )	-	1.5	1.5	1.5
Electrode	Open Circuit Voltages ( $U_k$ )	V	Figure 61	-	Figure 61
	Solid phase sodium diffusivity ( $D_{s,k}$ )	$\text{m}^2 \text{s}^{-1}$	Figure 63	-	Figure 63
	Solid phase electronic conductivity ( $\sigma_{s,k}$ )	$\text{S m}^{-1}$	0.74	-	18
	Maximum concentration ( $c_{s,k}^{\max}$ )	$\text{mol m}^{-3}$	13382	-	14245
	Exchange Current Density	$\text{A m}^{-2}$	$1.6 \cdot 10^{-1}$	-	$9.95 \cdot 10^{-2}$
	Stoichiometry at 0% SoC	-	0.364	-	0.127
	Stoichiometry at 100% SoC	-	0.984	-	1.000
Electrolyte	Electrolyte ionic conductivity ( $\sigma_{e,k}$ )	$\text{mS cm}^{-1}$	Equation [84] <sup>86</sup>		
	Electrolyte ionic diffusivity ( $D_{e,k}$ )	$\text{m}^2 \text{s}^{-1}$	Equation [98] <sup>86</sup>		
	Transference number ( $t^+$ )	-	Equation [99] <sup>86</sup>		
	Thermodynamic factor		Equation [100] <sup>86</sup>		
	Initial electrolyte concentration ( $c_{e0}$ )	$\text{mol m}^{-3}$	1000		

## 6.4 Conclusions

A methodology for parameterizing a sodium-ion system physics-based model is presented, focusing on measuring, or deriving the properties of the electrode and electrolyte. These parameters are relevant to the popular Doyle Fuller Newman (DFN) model, specifically outlining the physical (particle radius, porosity, etc.), thermodynamic (open-circuit voltage), and kinetic (solid-phase diffusivity, exchange current density, and ionic conductivity) properties for hard carbon and  $\text{Na}[\text{Ni}_{1/2}\text{Mn}_{1/4}\text{Sn}_{1/8}\text{Ti}_{1/8}]\text{O}_2$  (NMST2488). These materials were chosen due to their high specific energy, making them relevant for commercializing sodium-ion batteries in stationary energy storage applications.

The primary experimental approaches employed were electrochemical galvanostatic cycling, electrochemical impedance spectroscopy (EIS), and galvanostatic intermittent titration technique (GITT) to quantify electrode thermodynamic and kinetic properties. A three-electrode testing configuration improved measurement reproducibility, reduced sodium metal intrinsic hysteresis effects, and facilitated better validation by observing individual electrode potentials.

Key observations include the identification of methodological differences between lithium-ion and sodium-ion systems in the parameterization process. These differences involved more detailed characterization of hard carbon and positive electrode materials. For hard carbon, the theoretical capacity and physical properties were evaluated due to the variable ionic ratio  $\text{NaC}_x$ . Hard carbon's structure significantly differs from graphite, causing changes in theoretical capacity. For the positive electrode, X-ray diffraction determined crystal density, as R&D materials can have vastly different crystal structures. Additionally, electrochemical protocols were modified for characterizing hard carbon, requiring a much lower current cut-off during the constant voltage step due to approximately 50% of hard carbon capacity extraction in this region. The first cycle loss during electrode formation was also considered when mapping stoichiometry, more pronounced in sodium-ion systems and R&D materials not optimized for performance. Lastly, kinetic parameters, such as solid-phase diffusivity, needed adjustments in the model to account for sodium insertion mechanisms beyond intercalation.

This comprehensive set of parameters for a sodium-ion system enhances understanding of the impact of design changes on thermodynamic and kinetic properties, facilitating faster commercialization of high-energy sodium-ion materials. These parameters can be used to optimize sodium-ion battery design and application for stationary energy storage, including modifying cell parameters to increase energy density or employing degradation models to understand material limits. These parameters are available in the PyBaMM modelling platform for further research.

Future work for improving sodium-ion battery modelling involves several key focus areas: incorporating plating and stripping equations to enhance model equations for mass and charge transport, better mapping electrode stoichiometry using  $dQ/dV$  plots to improve quantification of irreversible sodium loss, extending experimental validation to include



various temperatures and cycling conditions, and incorporating the effects of agglomerations in the positive electrode to compare with the simplification of a single particle with the same volume.

## **6.5 Data Availability**

The parameter set in Table 29 has been made uploaded into the PyBaMM software package. This open-source software is a development platform for physics-based modelling tools.<sup>109</sup> The parameters will be open-sourced under 'ORegan2023' after final corrections for this thesis.

## Chapter 7: About:Energy - Exploring the Business Case for Parameterisation and Modelling

This chapter outlines the motivation and process of commercialising the research in this thesis. The physics-based model parameterisation in previous chapters was brought into and licensed by a spin-out company between the University of Birmingham and Imperial College London.

### 7.1 Problem

The development of new battery technologies involves significant investment, timelines, and risk (Figure 67). These factors stem from the need for data to improve batteries, which must be extracted from physical prototypes to inform better design. To acquire this data, companies must build laboratories and hire relevant expertise for physical testing. Building sufficient R&D capabilities for testing can require investments in the millions of pounds for testing channels, thermal chambers, and gloveboxes. It can take years due to supply chain lead times and difficulties in hiring relevant expertise due to a skills shortage. Additionally, it is often away from the critical path of a company and poses a risk of failure to commercialize a product.

Ultimately this risk is taken so that companies can create value through customer jobs. These include cell manufacturers build batteries, automotive OEMs designing systems, and data analytics companies predicting lifetime of batteries in the field. Building testing capacity and developing methodologies is not on their critical path but is a consequence of their industry.

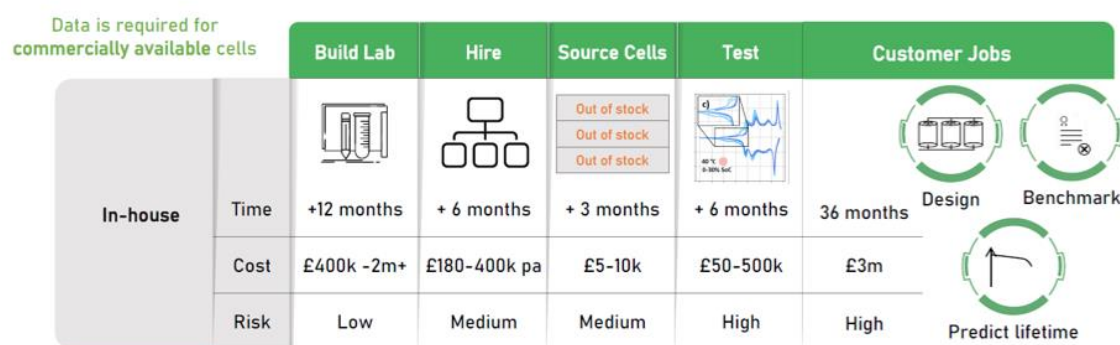


Figure 67. The different stages and costs to extract data and to develop models needed to design better batteries. This data has been obtained from first-hand experience of activities and projects.

Battery models (or digital twins) can be used to speed up battery development. Models provide a virtual representation of the battery so that experiments can be simulated rather than carried out physically. This accelerates battery development to lower both risk and cost.

## 7.2 Solution

These models are a simplification of a real battery and allow the prediction of one or a subset of its behaviours. Battery behaviour involves electrical, thermal, electrochemical, and ageing processes (Figure 68). Models that utilise each of these behaviours are chosen depending on the use case.

Modelling is used in several battery industries, including manufacturing, technology development, automotive, grid storage, and aerospace. Electrical, electrochemical, and thermal models provide significant value in battery development. However, each model requires significantly different expertise and facilities to evaluate the relevant parameters. The requirement to parameterise multiple cells and cell models has meant that many companies are seeking to outsource this activity, developing the facilities and expertise in-house is considerably expensive.

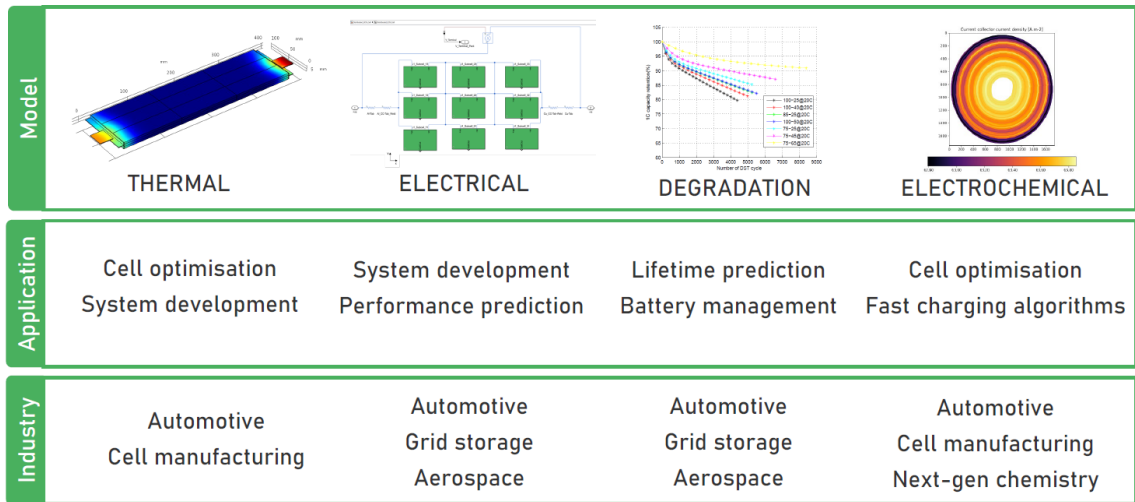


Figure 68. The different battery models used, the activities they are used for, and the industries they are used in.

The availability of parameters of commercially available batteries (LG, Samsung, or Sony) poses one of the main hurdles in the implementation of models in battery development and application. Companies that want to use models to select the best cell for their application, design battery packs, or build battery management systems must buy many physical batteries and test them in-house. However, there is still a question about the accuracy of these models as in-house research and expertise is needed.

Software platforms including Ansys, COMSOL, PyBaMM, and Simulink are used widely in industry to simulate batteries, but the value of these platforms is dependent on the parameterisation capabilities of a company (Figure 69). Parameters are unique to a cell type due to the chemistry, anatomy, and microstructure being tailored for a specific application. As companies often develop or implement several commercial/bespoke cells, each would have to be parameterised to be able to simulate its behaviour.

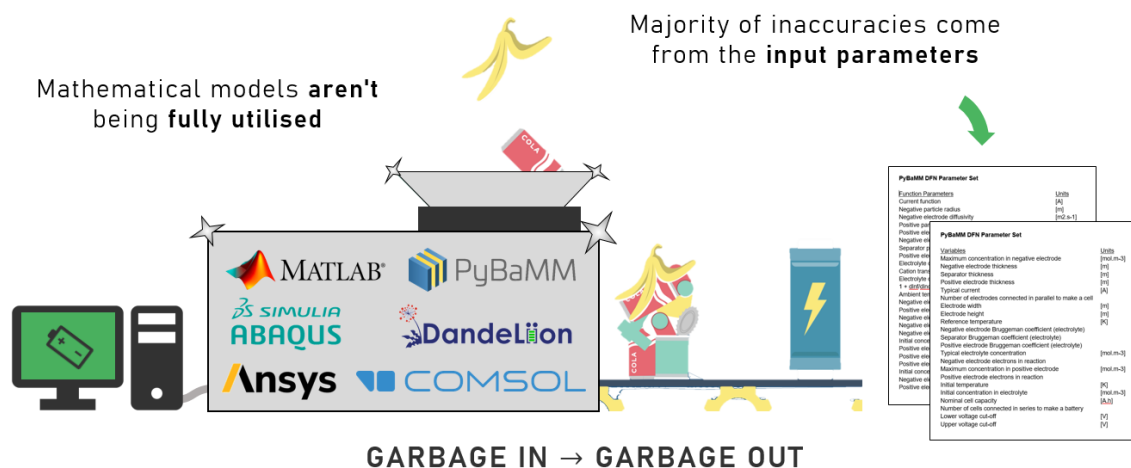


Figure 69. The practical limitation of battery models is the quality of the input parameters.

About:Energy was created as an end-to-end battery modelling company to help customers build better battery systems. The core capability and intellectual property of About:Energy is the parameterisation of different cell models (Figure 70). The parameters are then optimised and packaged into a model to be delivered to a customer. The high accuracy battery models can then be used as for cell selection, as design tools, in battery management systems, or to predict performance. Models are not a holistic solution to battery development but can be used to complement existing lab-based activities, allowing customers to be less reliant on the expensive experimental design processes. About:Energy centralises this activity allowing companies to focus on their product development.

About:Energy's intellectual property was jointly developed by University of Birmingham and Imperial College London under The Faraday Institution "Multi-Scale Modelling" research project. This project involved the world-leading model parameterisation methods for physics-based and equivalent circuit-based models, including a patented process to determine a battery's thermal properties. The parameterisation capabilities provide value to industry by being integrated into models of commercial batteries and then are made available in a software platform, called "The Voltt".

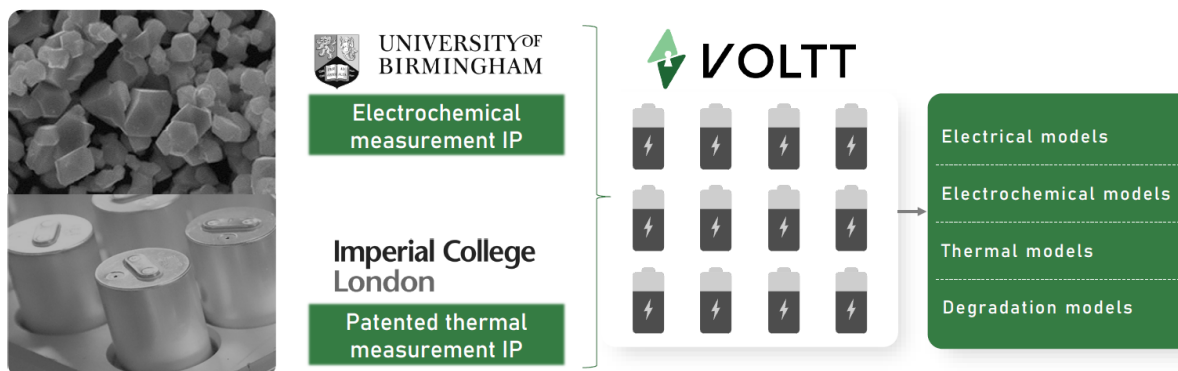


Figure 70. Combining intellectual property in the parameterisation of several models with the aim to reduce the cost of turning a physical cell into a battery model by 90%. This activity will be used to populate a database with data and models from commercial cells.

## 7.3 Technology

About:Energy's technologies involve intellectual property relating to the measurement of batteries. The innovations relate to more accurately extracting parameters and validation data for physics-based models and equivalent circuit-based. Improving the measurement of batteries helps companies lower the cost and timescales to bring new products to market through better modelling and design. The technologies being brought into the company relate to several key publications and patents published by the Co-Founders of the company, these cover different areas of battery modelling:

- Electrical:
  - i. Hardware using Peltier elements (thermoelectric cooling) was developed to provide more accurate temperature control compared to commonly used thermal chambers. This is used alongside a mature and adaptable PID controller to maintain surface temperature of any battery under test to  $\pm 0.05$  °C.<sup>231</sup>
- Electrochemical:
  - i. Methods of battery disassembly to take samples of commercial electrodes, allowing the measurement of their chemical and mechanical properties to generate model parameters.<sup>1</sup>
  - ii. Methods that allow the measurement of the thermal properties of individual components to allow thermal coupling of an electrochemical model. Improves accuracy by including temperature dependence of the kinetics and thermodynamics.<sup>7</sup>
- Thermal:
  - i. Patent enabling battery thermal conductivity to be measured with high accuracy. Current industry methods have experimental errors up to 50%. Leading to unreliable prediction of the battery model outputs, specifically regarding heat and temperature (patent application number 2116173.2).<sup>232</sup>
  - ii. Developed the cell cooling coefficient as a method to define heat rejection capability and shows how geometric changes in pouch cells affect thermal performance. The study finds that increasing tab thickness by 34% can enhance tab cooling performance by 20% with a minimal reduction in specific energy.<sup>21</sup>
- Ageing:
  - i. Developing a design of experiments (DOE) to accurately evaluate battery ageing. This research provides a path to more efficiently parameterise degradation models to predict battery lifetime.<sup>233</sup>

About:Energy's future intellectual property relates to three main areas: parameterisation, modelling, and products. By combining expertise in these three areas, it is possible to create specific battery models and scale them to many industries.

## 7.4 Market Research

About:Energy has engaged with over 100 companies across several industries during market research to understand competition and find differentiation. This included companies both in the UK and internationally. These companies were chosen to primarily represent our beachhead market of automotive (>60%) and the other industries that battery technologies are used in. The others represented incumbent/emerging industries that map out different markets for the future, including next-generation batteries (silicon or sodium) and new industries (aerospace and advanced BMS).

From market research, About:Energy's business model changed from providing consultancy services to populating an internet database with commercial cell models. Through relationships with market leaders and a UK battery distributor most popular commercial cells used in the market were evaluated. This means that models can be made for a few specific cells, and then the models can be sold multiple times. This database will eventually be offered to customers as a subscription service i.e. software-as-a-service (SaaS). Delivering battery models to strategic partners in key industries will still be a core activity to fund the business in the short-term, provide insight into new industry trends, and a test platform to develop technologies relevant to these growing industries.

This enabled us to identify competition and separated into two categories (Figure 71):

- Incumbents – companies that have widely used cross-industry modelling platforms.
- Emerging – companies beginning to build libraries of battery models for specific cells.

Incumbents includes companies such as Altair, Ansys, and AVL, they make software platforms that allow battery modelling, their main limitation is that leave it is the responsibility of the user to collect data for modelling. These companies provide a sales channel and potential partnerships if we can make our data available in their platforms. Several companies offer physics-informed or “*black-box*” models of batteries for cell selection and system design, the limitation for these platforms is that “*black-box*” means they are unable to be integrated into every workflow. These solutions also have limited use for material developers and cell manufacturers as they do not provide the ability to model the electrochemical processes within the battery.

The “*black-box*” approach was identified as a significant customer pain point to solve with our platform. Many automotive and application-based customers were wanting to move away from these models. “*Black-box*” models do not provide information on cell parameters and (Figure 72), this makes it difficult to implement into a bespoke workflow and to understand the cell properties, this is important for BMS and cell optimisation.

Implementation required by custom






Company	Employees	Valuation	Lifetime prediction	BMS control	Cell design	System design	Vertically integrated with labs	Flexibility to work in other platforms	Library of commercial cells
 ABOUT:ENERGY	12	-	●	●	●	●	●	●	●
 BATEMO <small>UNDERSTANDING BATTERIES</small>	12	-	◐	●		◐	◐	●	●
 TWAICE	110	~\$300m	●	●		◐	◐		●
 Ansys	6,335	~\$31b	◐	◐	●	●		◐	
 COMSOL	500	~\$500m	◐	◐	●	●		◐	

Figure 71. Analysis of incumbent and emerging companies in the battery software and modelling industries

This research suggested that making a greater diversity of models which incorporate the physical, electrochemical, and thermal properties, would provide the ability to tap into the value chain. The core parameterisation expertise delivers value to customers through various models/products, but making these solutions have the following attributes makes the offering more competitive:

1. 'White-box':

Complete visibility of the model parameters and framework help customers use the model in their workflow. There is no white-box solution available on the market currently. Competitors offer a black-box solution (Figure 72). This approach creates an information asymmetry between those defining the battery model and those using it, creating uncertainty in the thermal performance, where parameterisation is difficult.

2. Multi-scale:

Providing solutions that span material, cell, and system level provides value to R&D across the entire value chain and assists companies on a 15-year commercial journey, from ideation to end-of-life (Figure 73).

3. Multi-behaviour:

Providing models that predict electrical, thermal, ageing, and electrochemical properties of a battery provides new products, including advanced BMS algorithms and cell optimisation software.

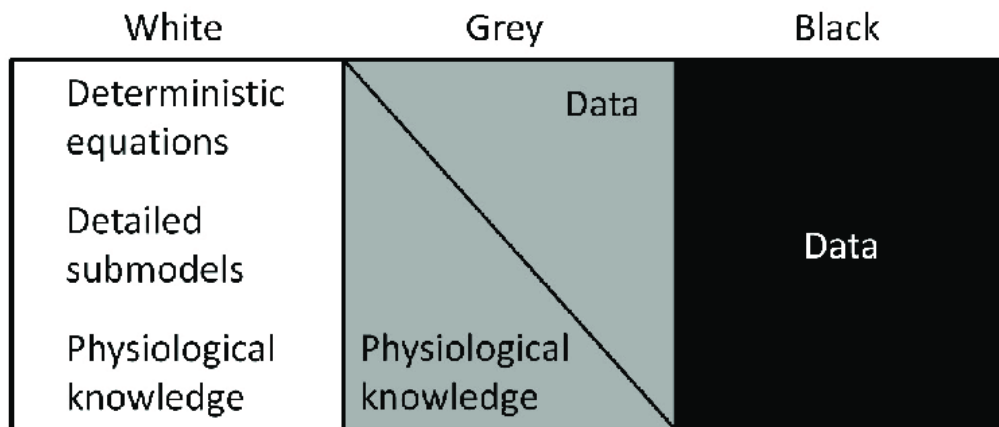


Figure 72. Schematic to show the difference between “black-box” and “white-box” models.

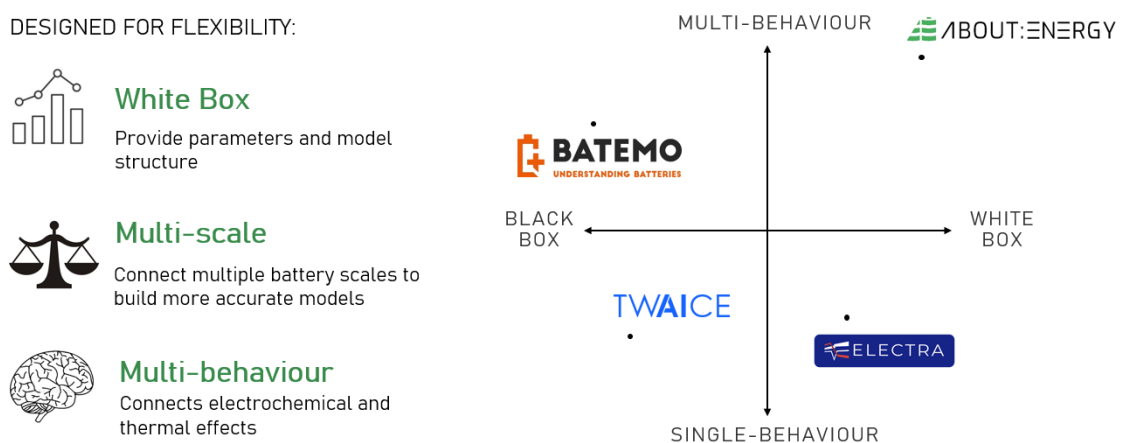


Figure 73. Positioning in the market, key differentiators are the different model classes being offered and the “white box” implementation.

However, it was clear that these existing services did not meet customer needs completely. ‘Black-box’ models meaning customers would not be able to customise/understand it. Another company, Electra offers models that can be integrated into vehicle systems. Both Electra and Twaice focus on modelling the electrochemical behaviour of the cell, and we see them as potential collaborators so that they can outsource their parameterisation and develop models for vehicle systems and fleet analytics. The three companies largely focus on automotive cell chemistries such as NMC. For About:Energy there is huge value in other industries including stationary energy storage and emerging chemistries such as LFP and lithium metal.

The market research also identified a long-term technology strategy that would involve About:Energy being the technology provider to companies across the value chain. The focus of most companies in the electrification transition is developing products, such as building electric vehicles and gigafactories, and new chemistries. Ultimately, the interest of these industries is to develop better characterization and modelling capabilities in-house because of the need to improve their products, but it is not their critical path. The



research investment required to develop these new technologies is considerable, and often companies only reap the rewards once. About:Energy can significantly invest in developing these technologies for a greater return on investment by delivering them to many companies (Figure 74).

The recommendations from the market research can be summarised as follows:

- Business Model: Building a database of commercial battery models and deliver through a software subscription model to many industries.
- Competitive edge: Developing products that are “white-box”, multi-scale, and multi-behaviour to satisfy industry pain points.
- Go-to-market: Partnerships with incumbent modelling platforms to provide data to be used by their existing customer base.

Technology strategy: focus on developing “deep technologies” to be the technology provider for companies across the value chain.

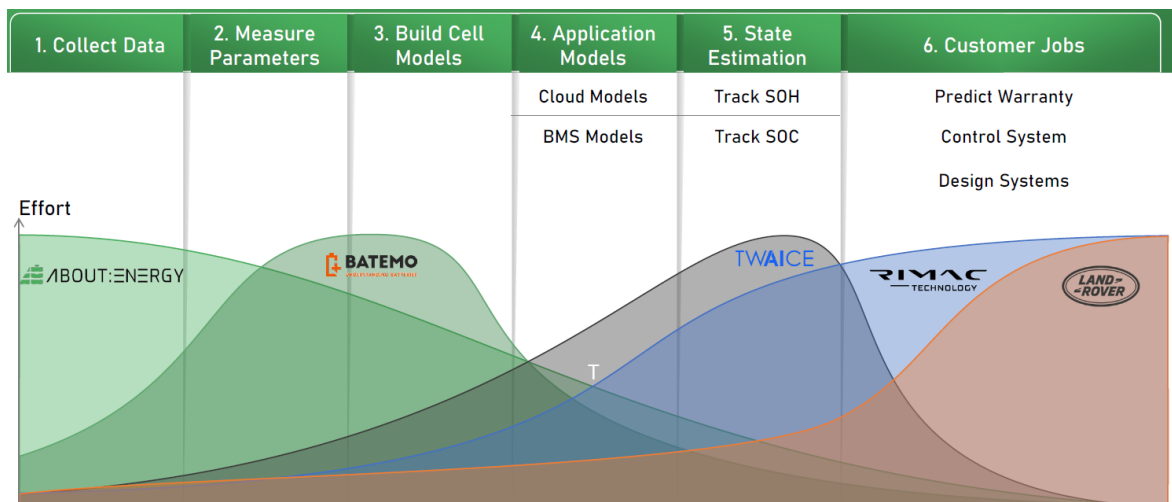


Figure 74. Illustration to show technology map, from data collection to using tools to deliver value.

## 7.5 Business Model

*“The Voltt”* delivers value to companies by providing access to a library of commercial cells to centralise significant parts of their R&D by outsourcing the creation and development of the datasets and models needed for:

- Cell Selection – evaluating best cell for an application based on pack specification.
- Benchmarking – comparing cells with in-house technologies.
- System Design – developing optimal pack configuration.
- Cell Design – improving cell design.
- Lifetime prediction – evaluating the state-of-health
- Supply Chain – insights into the cost and sustainability of batteries.
- Data Sharing – sharing data through a secure cloud-based database.

*“The Voltt”* generates revenue and delivers value to B2B customers (business-to-business) through services and software subscriptions. Different subscription tiers have been designed to cater to different industries and sized companies:

- B2B Software

Software that includes model and data of commercially available cells for companies to purchase and download through our web platform. Commercial batteries from a few manufacturers are used by most automotive companies, a few cells can cater to most of the industry (Figure 75):

- B2B Services

Services for companies developing technologies that are not commercially available. This requires our products being tailored for proprietary cells that may be novel chemistries and formats, the data is confidential but hosted within our platform.

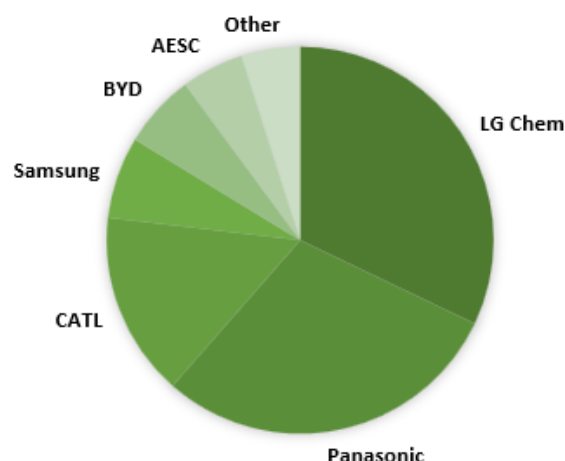


Figure 75. Global electric vehicle battery production for Q1 2020 (Source data: ev-volumes.com).

The technologies we have developed allows About:Energy to measure a suite of parameters that relate to the different properties in our “*Advanced Datasheet*” (Figure 76):

- Manufacturer data stating the operating conditions of the battery.
- Electrical data to understand the voltage-current behaviour.
- Chemical information on the components within the battery.
- Electrochemical data for the thermodynamic and kinetic properties.
- Thermal data to understand heat generation and transport.
- Techno-economic data to connect chemical composition with supply chain.

These parameters are useful for understand the commercial battery landscape. The value of these parameters is integrating them into the various models to accelerate battery development. These validated models can be downloaded and delivered directly into the workflow of companies e.g. Ansys, Simulink, and COMSOL.

The route to market for “*The Voltt*” involves providing beginning of life lithium-ion batteries for companies within automotive to design systems. Through research programmes we are developing new technologies to cater to new markets, this includes next-generation chemistries and other industries:

- Chemistries – Sodium-ion, silicon, and solid-state.
- Industries - Aerospace, grid storage, and commercial vehicles.

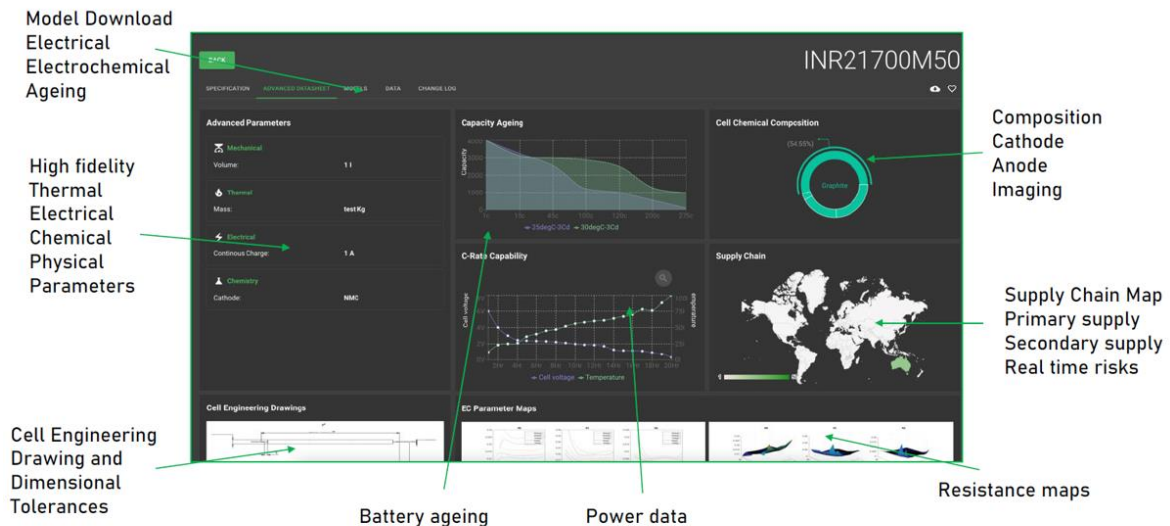


Figure 76. “Advanced Datasheet” outlining measured parameters in different categories.

## 7.6 Market Size

Evaluating the size of a market can be completed through a top-down or bottom-up approach. The top-down approach refers to the larger market or industry, and then breaking it down into smaller segments. It begins by estimating the total size of the market or industry, then breaking it down into smaller segments. For About:Energy this involves evaluating the total size of the global battery. Benchmark Mineral Intelligence estimate an additional 343 gigafactories to be built by 2030, which represents a seven-fold increase in capacity from today 7,500GWh. The battery capacity presents a market opportunity by being split into two categories (Figure 77):

- Pre-deployment: The decisions made before a battery is in operation, this includes design.
- Post-deployment: The decisions made after a battery is in operation, this includes battery management, warranty estimation, and recycling.

These markets represent \$424 billion and \$1,534 in 2030. For pre-deployment this number is based on the number of batteries being manufactured in 2030 and the R&D investment needed to bring those to market, for post-deployment the number refers to the cumulative amount of batteries in the field. From these market sizes we can calculate our total addressable market size (TAM) by assuming a typical B2B software-as-a-service penetration rate of 15% to 20%, this measures the value we can add to the industry. Then revenue is calculated from the assumption. This analysis provides a potential TAM of \$37 billion for About:Energy by 2030 based on sizing the entire battery industry.

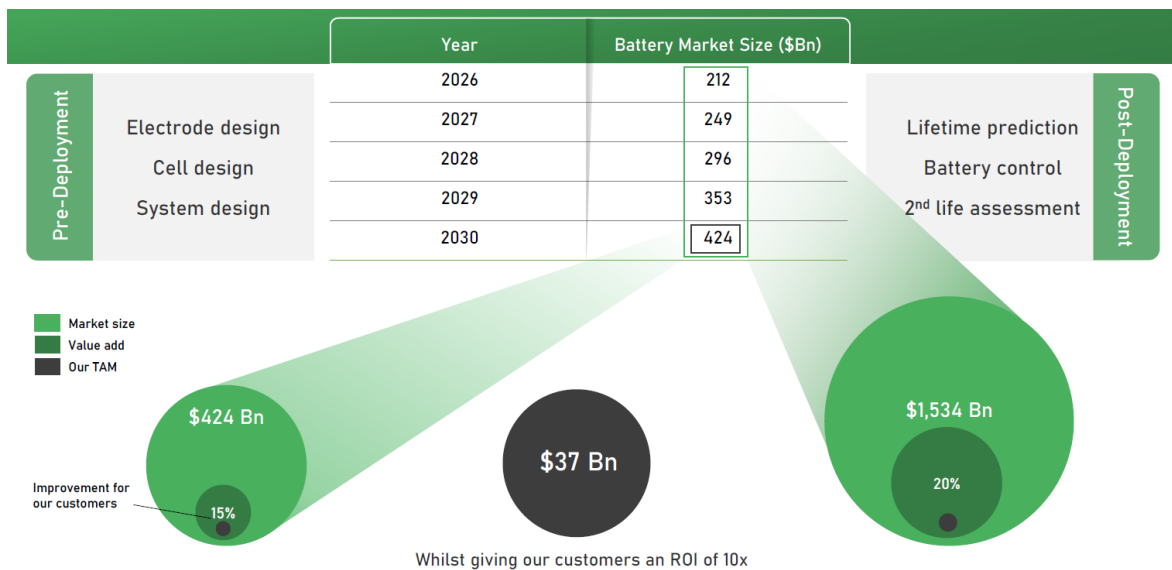
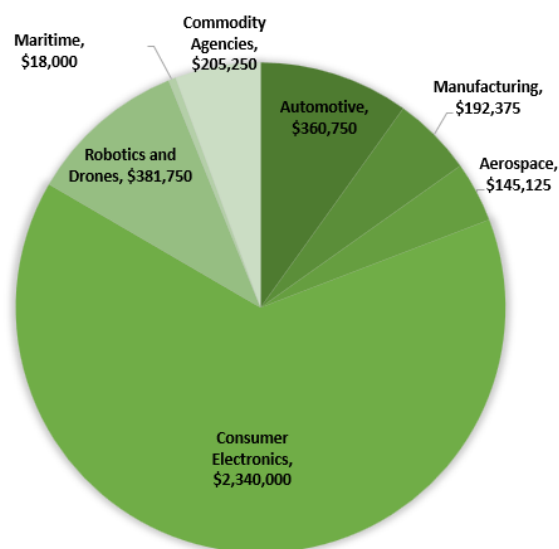


Figure 77. Top-down analysis: Growth of the battery market size between 2021 and 2030 based on (Source data: Benchmark Mineral Intelligence)



## 7.7 Outlook

About:Energy's core intellectual property is related to the measurement of battery performance and was developed through research programmes at the University of Birmingham and Imperial College London. This involves the testing methodologies developed within this PhD thesis which accurately capture the fundamental physics (thermodynamic and kinetic) properties of batteries.

The parameterisation provides the ability to measure the chemical, electrochemical, thermal, and ageing performances of a battery, involving activities ranging from cell teardown to carefully controlled cell-level parameterisation. This data can then be packaged into battery models that allow the prediction of performance and the ability to conduct virtual experiments. These simulations provide a path to significantly lower the cost and timelines required to develop batteries and to improve performance in operation.

Market research provided insight into how to develop the commercial and technical roadmaps to deliver maximum value from the technologies. This market research was initially UK-focussed to utilise immediate networks but includes international battery companies. Further plans to exploit opportunities in different geographies involved a visit to Tokyo through the Global Business Innovation Programme and commercial relationships being developed with companies in the US and India.

The automotive industry has been identified as the beachhead market, due to the wide adoption of battery models, significant R&D budgets, and willingness to innovate. While this segment presents significant value, future markets require further commercial and technology developments to enter. This would involve understanding the pain points of these industries to deliver products, or to develop technologies that would allow us to model new battery types. As described in *Chapter 6*, new chemistries including sodium-ion require developments in the way we characterise and model these systems. The methods we develop are largely application/chemistry agnostic, but they need to optimise. Existing UK research projects relating to solid-state and sodium-ion batteries will help in the development of new battery models for these emerging technologies (Figure 79).

"The Voltt" software platform is being developed to centralise the creation of data and tools that are needed to carry out activities across the value chain. These activities include cell selection, system design, cell optimisation and many others. This database would involve the parameters and models for 100s of commercial batteries to reduce the in-house testing carried out by companies and providing them access to state-of-the-art battery models. The business model for the "The Voltt" is a software-as-a-service model with recurring value being delivered to customers through the continual development of technologies to improve existing products and new products to enable other activities.

Future products include analytics/visualisations to provide more insight into the commercial landscape for industry participants, investors, and policymakers. This would help identify emerging battery trends and areas of battery performance that have not

been improved so policy/investment could aid in development. A cloud-based cell optimisation tool called “The Foundry” to customise battery design to reduce the cost of development. This would enable companies to virtual design batteries with respect to energy, power, lifetime, cost and carbon footprint.

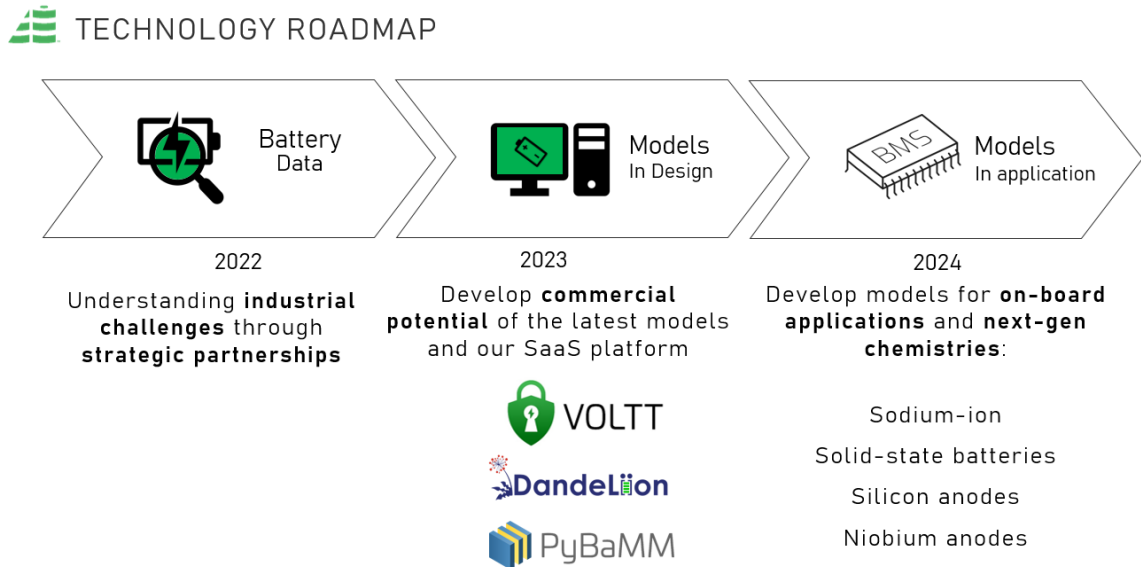


Figure 79. Projected revenue for the business divided between the services and software business models.

# Chapter 8: Conclusions and Future Work

## 8.1 Conclusions

The motivation behind this research was to improve physics-based battery modelling, particularly for commercially relevant cells like lithium-ion and sodium-ion batteries. This improvement could be related to enhancing model accuracy or reducing computational costs, for instance, by finding better ways to approximate input parameters, or by understanding which assumptions can be justifiably made. These models can significantly enhance the performance, longevity, and efficiency of battery systems. By focusing on battery parameterisation methodologies and extending them to various chemistries, the research aimed to offer a more comprehensive understanding of battery systems and their complex electrochemical behaviours.

An important aspect of this motivation was to lower the barriers to entry for industries seeking to adopt and utilize these advanced modelling tools. By simplifying the process and making it more accessible, a wider range of stakeholders can benefit from the improved battery designs and applications. This approach not only fosters the growth of existing markets, such as the automotive industry, but also enables the development of new and emerging applications for advanced battery systems.

The research also seeks to provide a foundation for future advancements in battery technologies, such as solid-state and sodium-ion batteries. By offering a robust and versatile methodology for parameterization and model development, this work can support the ongoing optimization of these emerging technologies, ensuring that they reach their full potential in terms of performance, safety, and cost-effectiveness.

This thesis presents a comprehensive study of battery parameterisation methodologies for physics-based models, focusing on lithium-ion batteries and extending to sodium-ion systems. It highlights the importance of obtaining accurate input parameters in model application. Key to this is understanding the effects of temperature and state-of-charge on these parameters.

In Chapter 4, a complete parameter set for a commercial lithium-ion cell was developed and validated. The research highlighted the importance of careful teardown and delamination procedures to extract materials from the cell with minimal degradation. It also emphasized the need for accurate image-based techniques to characterize the 3D microstructural properties of the electrode. The successful implementation of these methodologies resulted in only five out of 37 values requiring tuning to achieve low error between DFN model simulations and experimental data.

Chapter 5 outlined the parameterisation methodology for a 3D thermal-electrochemical model for a high energy lithium-ion battery, mapping the electrochemical and thermal relationships in a high energy density cylindrical cell. The research provided insight into the limiting electrodes and the parameter variability caused by local and global changes in temperature or lithium concentration. These findings can be applied to different cell



types to increase the availability of 3D thermal-electrochemical parameters and optimize battery design and application.

In Chapter 6, a methodology to parameterize a sodium-ion system physics-based model was presented. The research identified key methodological differences between lithium-ion and sodium-ion systems in the parameterization process. The complete set of parameters for a sodium-ion system allowed for a better understanding of the impact of design changes on thermodynamic and kinetic properties. These parameters can be utilized to optimize the design and application of sodium-ion batteries for stationary energy storage applications, including modifying cell parameters to increase energy density or utilizing degradation models to comprehend the limits of these materials.

Chapter 7 detailed the commercialization of the research, focusing on the development of a software platform called "The Voltt" that centralizes the creation of data and tools needed for various activities across the value chain. The automotive industry was identified as the beachhead market due to its wide adoption of battery models and willingness to innovate. The software-as-a-service business model provides recurring value to customers through the continual development of technologies to improve existing products and new products to enable other activities.

This research has identified specific limitations within the approximations of kinetics and ion transport within the model, particularly in terms of solid-phase diffusivity and exchange current density. These limitations are intrinsically linked to shortcomings in experimental methods such as galvanostatic intermittent titration technique (GITT) and electrochemical impedance spectroscopy (EIS), as well as to the foundational assumptions underpinning these models. The findings underscore a need for revisiting and refining the experimental approaches to better capture the nuances of ion transport and kinetic reactions within battery systems. This highlights areas for theoretical advancement but also calls for an improvement in experimental methodologies, paving the way for a dual-front improvement in both theoretical and practical aspects of battery research. Such advancements could lead to more accurate models that are essential for predicting battery behaviour under various operational conditions.

Overall, this thesis demonstrates the importance and complementarity of practical methods in aiding model development and understanding, advancing the field of battery modelling by proposing a framework for ongoing refinement as new data becomes available. The methodologies developed and validated have been commercialized and will be further developed to provide various industries with expertise in parameterization and model development. This research lays the groundwork for the optimization of battery performance in various applications and paves the way for more advanced battery technologies, such as solid-state and sodium-ion batteries, to be efficiently modelled and optimized in the future.

## **8.2 Future Work**

While this thesis provides a comprehensive understanding of the electrochemical and thermal behaviour of battery systems, there is still scope for further research in this field,

particularly beyond the science in more widely applying the results of this thesis for real-world impact. Several key areas of future work are identified based on the findings of the thesis:

- **Application to new chemistries:** The methodology presented to other battery chemistries, including niobium batteries and other emerging technologies. Further development of these physics-based models can lead to a better understanding of the behaviour of different battery systems to accelerate their time to market.
- **Addition of new mathematics:** The model equations for mass and charge transport can be improved by incorporating lithium or sodium plating and stripping equations. This will improve the accuracy of the models and enable a more accurate prediction of the behaviour of different battery systems.
- **Improved experimental analysis:** The mapping of the stoichiometry of each electrode using  $dQ/dV$  plots can be improved to better quantify the irreversible loss of sodium. This will enable a more accurate prediction of the long-term performance of sodium-ion batteries.
- **Extending experimental validation:** Including *various* temperatures and different cycling conditions in the validation process will ensure the robustness and versatility of the developed methodologies.
- **Accounting for microstructural inhomogeneities:** Incorporating the effects of agglomerations in the positive electrode to compare to the simplification of one particle with the same volume will help refine the models and improve their accuracy.

### 8.3 Impact

The impact of this research extends across various industries, including automotive, stationary energy storage, and consumer electronics, by providing improved methodologies for battery parameterization and model development. The optimized battery designs and applications will help meet the growing demand for efficient energy storage solutions, promoting the adoption of electric vehicles and renewable energy systems.

The popularity of the LG M50 parameter set and novel research in modelling commercially relevant cells highlights the significance of this work in the battery research community. The impact is further enhanced by the establishment of About:Energy, a start-up company founded from the research in this PhD. About:Energy's aim is to lower the barrier to entry for industry using advanced predictive models for battery design, enabling companies to develop and optimize batteries more efficiently and cost-effectively.

The "The Voltt" software platform, developed as part of this research, allows industry participants to access state-of-the-art battery models and reduce in-house testing, resulting in significant cost and time savings in battery development. The platform also provides policymakers and investors with valuable insights into the commercial

landscape and emerging battery trends, enabling them to make informed decisions on policy and investment to support the growth of the battery industry.

## References

- 1 C.-H. Chen, F. Brosa Planella, K. O'Regan, D. Gastol, W. D. Widanage and E. Kendrick, *J Electrochem Soc*, 2020, **167**, 080534.
- 2 T. G. Tranter, R. Timms, T. M. M. Heenan, S. G. Marquis, V. Sulzer, A. Jnawali, M. D. R. Kok, C. P. Please, S. J. Chapman, P. R. Shearing and D. J. L. Brett, *J Electrochem Soc*, 2020, **167**, 110538.
- 3 F. Brosa Planella, M. Sheikh and W. D. Widanage, *Electrochim Acta*, 2021, **388**, 138524.
- 4 W. Ai, N. Kirkaldy, Y. Jiang, G. Offer, H. Wang and B. Wu, *J Power Sources*, 2022, **527**, 231142.
- 5 A. A. Wang, S. E. J. O'Kane, F. Brosa Planella, J. Le Houx, K. O'Regan, M. Zyskin, J. Edge, C. W. Monroe, S. J. Cooper, D. A. Howey, E. Kendrick and J. M. Foster, *Progress in Energy*, 2022, **4**, 032004.
- 6 L. M. Morgan, M. M. Islam, H. Yang, K. O'Regan, A. N. Patel, A. Ghosh, E. Kendrick, M. Marinescu, G. J. Offer, B. J. Morgan, M. S. Islam, J. Edge and A. Walsh, *ACS Energy Lett*, 2022, **7**, 108–122.
- 7 K. O'Regan, F. B. Planella, W. D. Widanage and E. Kendrick, *Electrochim Acta*, 2022, 140700.
- 8 S. Arrhenius, *The London, Edinburgh, and Dublin Philosophical Magazine and Journal of Science*, 1896, **41**, 237–276.
- 9 J. B. Goodenough and K. S. Park, *J Am Chem Soc*, 2013, **135**, 1167–1176.
- 10 H. Bajolle, M. Lagadic and N. Louvet, *Energy Res Soc Sci*, 2022, **93**, 102850.
- 11 J. M. Tarascon and M. Armand, *Nature*, 2001, **414**, 359–67.
- 12 V. Lundaev, A. A. Solomon, T. Le, A. Lohrmann and C. Breyer, *Miner Eng*, 2023, 203.
- 13 K. Pan, F. Zou, M. Canova, Y. Zhu and J. H. Kim, *J Power Sources*, 2019, **413**, 20–28.
- 14 J. B. Goodenough, *Journal of Solid State Electrochemistry*, 2012, **16**, 2019–2029.
- 15 J. B. Goodenough, *Acc Chem Res*, 2013, **46**, 1053–1061.
- 16 K. Märker, P. J. Reeves, C. Xu, K. J. Griffith and C. P. Grey, *Chemistry of Materials*, 2019, **31**, 2545–2554.
- 17 A. Manthiram, *Nat Commun*, 2020, **11**, 1550.
- 18 X. Zuo, J. Zhu, P. Müller-Buschbaum and Y. J. Cheng, *Nano Energy*, 2017, **31**, 113–143.

- 19 X. Lu, A. Bertei, D. P. Finegan, C. Tan, S. R. Daemi, J. S. Weaving, K. B. O'Regan, T. M. M. Heenan, G. Hinds, E. Kendrick, D. J. L. Brett and P. R. Shearing, *Nat Commun*, 2020, **11**, 2079.
- 20 D. Gastol, M. Capener, C. Reynolds, C. Constable and E. Kendrick, *Mater Des*, 2021, **205**, 109720.
- 21 A. Hales, L. B. Diaz, M. W. Marzook, Y. Zhao, Y. Patel and G. Offer, *J Electrochem Soc*, 2019, **166**, A2383–A2395.
- 22 T. G. Tranter, R. Timms, P. R. Shearing and D. J. L. Brett, *J Electrochem Soc*, 2020, **167**, 160544.
- 23 G. Y. Kim, S. R. Park and J. S. Yu, 2021, 1–16.
- 24 L. Shui, F. Chen, A. Garg, X. Peng, N. Bao and J. Zhang, 2018, 331–347.
- 25 J. B. Goodenough and Y. Kim, *Chemistry of Materials*, 2010, **22**, 587–603.
- 26 M. Ue, K. Sakaushi and K. Uosaki, *Mater Horiz*, 2020, **7**, 1937–1954.
- 27 D. A. Howey, S. A. Roberts, V. Viswanathan, A. Mistry, M. Beuse, E. Khoo, S. C. Decaluwe and V. Sulzer, *Electrochemical Society Interface*, 2020, **29**, 30–34.
- 28 W. Weppner and R. A. Huggins, *J Electrochem Soc*, 1977, **124**, 1569.
- 29 P. Peljo and H. H. Girault, *Energy Environ Sci*, 2018, **11**, 2306–2309.
- 30 J. Newman and W. Tiedemann, *AIChE Journal*, 1975, **21**, 25–41.
- 31 M. Doyle, T. Fuller and J. Newman, *J Electrochem Soc*, 1993, **140**, 1526.
- 32 R. Darling, *J Electrochem Soc*, 1997, **144**, 4201.
- 33 J. Christensen and J. Newman, *Proceedings - Electrochemical Society*, 2003, **20**, 85–94.
- 34 P. Albertus, J. Christensen and J. Newman, *J Electrochem Soc*, 2009, **156**, A606.
- 35 M. Tang, P. Albertus and J. Newman, *J Electrochem Soc*, 2009, **156**, A390.
- 36 A. Fotouhi, D. J. Auger, K. Propp, S. Longo and M. Wild, *Renewable and Sustainable Energy Reviews*, 2016, **56**, 1008–1021.
- 37 S. M. Mousavi G. and M. Nikdel, *Renewable and Sustainable Energy Reviews*, 2014, **32**, 477–485.
- 38 M. K. Tran, M. Mathew, S. Janhunen, S. Panchal, K. Raahemifar, R. Fraser and M. Fowler, *J Energy Storage*, 2021, **43**, 103252.
- 39 J. Le Houx and D. Kramer, 2020, **6**, 1–9.
- 40 J. Newman and W. Tiedemann, *J Electrochem Soc*, 1993, **140**, 1961–1968.

- 41 H. Arunachalam and S. Onori, *Proceedings of the IEEE Conference on Decision and Control*, 2019, **2018-Decem**, 5702–5707.
- 42 S. G. Marquis, V. Sulzer, R. Timms, C. P. Please and S. J. Chapman, *J Electrochem Soc*, 2019, **166**, A3693–A3706.
- 43 S. Goutam, A. Nikolian, J. Jaguemont, J. Smekens, N. Omar, P. Van Dan Bossche and J. Van Mierlo, *Appl Therm Eng*, 2017, **126**, 796–808.
- 44 G. Liebig, U. Kirstein, S. Geißendörfer, F. Schuldts and C. Agert, *Batteries*, 2020, **6**, 3.
- 45 M. V. Morganti, S. Longo, M. Tirovic, C. Y. Blaise and G. Forostovsky, *IEEE Trans Veh Technol*, 2019, **68**, 10594–10606.
- 46 C. R. Birkl, M. R. Roberts, E. McTurk, P. G. Bruce and D. A. Howey, *J Power Sources*, 2017, **341**, 373–386.
- 47 K. Uddin, S. Perera, W. Widanage, L. Somerville and J. Marco, *Batteries*, 2016, **2**, 13.
- 48 B. Ng, P. T. Coman, E. Faegh, X. Peng, S. G. Karakalos, X. Jin, W. E. Mustain and R. E. White, *ACS Appl Energy Mater*, 2020, **3**, 3653–3664.
- 49 X. G. Yang, Y. Leng, G. Zhang, S. Ge and C. Y. Wang, *J Power Sources*, 2017, **360**, 28–40.
- 50 S. Atalay, M. Sheikh, A. Mariani, Y. Merla, E. Bower and W. D. Widanage, *J Power Sources*, 2020, **478**, 229026.
- 51 J. M. Reniers, G. Mulder and D. A. Howey, *J Electrochem Soc*, 2019, **166**, A3189–A3200.
- 52 J. Li, K. Adewuyi, N. Lotfi, R. G. Landers and J. Park, *Appl Energy*, 2018, **212**, 1178–1190.
- 53 A. Mauger, M. Armand, C. M. Julien and K. Zaghib, *J Power Sources*, 2017, **353**, 333–342.
- 54 M. D. Slater, D. Kim, E. Lee and C. S. Johnson, *Adv Funct Mater*, 2013, **23**, 947–958.
- 55 N. Tapia-ruiz, A. R. Armstrong, H. Alptekin, M. A. Amores, H. Au, J. Barker, R. Boston, W. R. Brant, J. M. Brittain, Y. Chen, M. Chhowalla, Y. Choi, S. I. R. Costa, M. C. Ribadeneyra, S. A. M. Dickson, E. I. Eweka, J. D. Forero-saboya, C. P. Grey, Z. Li, S. F. L. Mertens, R. Mogensen, L. Monconduit, D. M. C. Ould, R. G. Palgrave, P. Poizot, A. Ponrouch, S. Renault, E. M. Reynolds, A. Rudola, R. Sayers, D. O. Scanlon, S. Sen, V. R. Seymour, B. Silv, G. S. Stone, C. I. Thomas, M. Titirici, J. Tong, T. J. Wood, D. S. Wright and R. Younesi, *Journal of Physics: Energy*, 2021, **3**, 031503.
- 56 G. Åvall, J. Mindemark, D. Brandell and P. Johansson, *Adv Energy Mater*, 2018, **8**, 1–22.
- 57 S. Roberts and E. Kendrick, *Nanotechnol Sci Appl*, 2018, **Volume 11**, 23–33.

- 58 L. Li, Y. Ren, K. O'Regan, U. R. Koleti, E. Kendrick, W. D. Widanage and J. Marco, *J Energy Storage*, 2021, **44**, 103324.
- 59 A. Zülke, I. Korotkin, J. M. Foster, M. Nagarathinam, H. Hoster and G. Richardson, *J Electrochem Soc*, 2021, **168**, 120522.
- 60 F. J. Günter and N. Wassiliadis, *J Electrochem Soc*, 2022, **169**, 030515.
- 61 M. Ecker, P. Dechent, T. K. D. Tran, A. Warnecke, S. Käbitz and D. U. Sauer, *J Electrochem Soc*, 2015, **162**, A1836–A1848.
- 62 J. Schmalstieg, C. Rahe, M. Ecker and D. U. Sauer, *J Electrochem Soc*, 2018, **165**, A3799–A3810.
- 63 G. Liebig, G. Gupta, U. Kirstein, F. Schuldt and C. Agert, *Batteries*, 2019, **5**, 62.
- 64 W. Li, D. Cao, D. Jöst, F. Ringbeck, M. Kuipers, F. Frie and D. U. Sauer, *Appl Energy*, 2020, **269**, 115104.
- 65 A. Nickol, T. Schied, C. Heubner, M. Schneider, A. Michaelis, M. Bobeth and G. Cuniberti, *J Electrochem Soc*, 2020, **167**, 090546.
- 66 Y. Chen, J. Key, K. O'Regan, T. Song, Y. Han and E. Kendrick, *Chemical Engineering Journal*, 2022, **450**, 138275.
- 67 R. Raccichini, M. Amores and G. Hinds, *Batteries*, 2019, **5**, 12.
- 68 S. S. Zhang, *J Electrochem Soc*, 2020, **167**, 100510.
- 69 M. Ender, A. Weber and E. Ivers-Tiffée, *J Electrochem Soc*, 2012, **159**, A128.
- 70 J. Costard, M. Ender, M. Weiss and E. Ivers-Tiffée, *J Electrochem Soc*, 2017, **164**, A80–A87.
- 71 T. S. Pathan, M. Rashid, M. Walker, W. D. Widanage and E. Kendrick, *Journal of Physics: Energy*, 2019, **1**, 044003.
- 72 T. M. Bandhauer, S. Garimella and T. F. Fuller, *J Electrochem Soc*, 2011, **158**, R1.
- 73 S. Wang, *Chinese Physics B*, 2016, **25**, 010509.
- 74 M. Ecker, P. Dechent, T. K. D. Tran, A. Warnecke, S. Käbitz and D. U. Sauer, *J Electrochem Soc*, 2015, **162**, A1836–A1848.
- 75 J. Sturm, A. Rheinfeld, I. Zilberman, F. B. Spingler, S. Kosch, F. Frie and A. Jossen, *J Power Sources*, 2019, **412**, 204–223.
- 76 A. Zülke, I. Korotkin, J. M. Foster, M. Nagarathinam, H. Hoster and G. Richardson, *J Electrochem Soc*, 2021, **168**, 120522.
- 77 I. D. Campbell, M. Marzook, M. Marinescu and G. J. Offer, *J Electrochem Soc*, 2019, **166**, A725–A739.

- 78 Xing Jin, A. P. Vora, V. Hoshing, T. Saha, G. M. Shaver, R. E. Garcia, O. Wasynczuk and S. Varigonda, in *2017 American Control Conference (ACC)*, IEEE, 2017, pp. 80–85.
- 79 G. Liebig, G. Gupta, U. Kirstein, F. Schuldt and C. Agert, *Batteries*, 2019, **5**, 62.
- 80 J. S. Edge, S. O’Kane, R. Prosser, N. D. Kirkaldy, A. N. Patel, A. Hales, A. Ghosh, W. Ai, J. Chen, J. Yang, S. Li, M.-C. Pang, L. Bravo Diaz, A. Tomaszewska, M. W. Marzook, K. N. Radhakrishnan, H. Wang, Y. Patel, B. Wu and G. J. Offer, *Physical Chemistry Chemical Physics*, 2021, **23**, 8200–8221.
- 81 J. Stadler, C. Krupp, M. Ecker, J. Bandlow, B. Spier and A. Latz, *J Power Sources*, 2022, **521**, 230952.
- 82 T. Gewald and M. Lienkamp, *Forschung im Ingenieurwesen/Engineering Research*, 2019, **83**, 831–841.
- 83 B. Rumberg, B. Epding, I. Stradtman and A. Kwade, *J Energy Storage*, 2019, **25**, 100890.
- 84 J. P. Fath, D. Dragicevic, L. Bittel, A. Nuhic, J. Sieg, S. Hahn, L. Alsheimer, B. Spier and T. Wetzel, *J Energy Storage*, 2019, **25**, 100813.
- 85 Kovachev, Schröttner, Gstrein, Aiello, Hanzu, Wilkening, Foitzik, Wellm, Sinz and Ellersdorfer, *Batteries*, 2019, **5**, 67.
- 86 J. Landesfeind, T. Hosaka, M. Graf, K. Kubota, S. Komaba and H. A. Gasteiger, *J Electrochem Soc*, 2021, **168**, 040538.
- 87 K. Chayambuka, G. Mulder, D. L. Danilov and P. H. L. Notten, *Journal of Power Sources Advances*, 2021, **9**, 100056.
- 88 K. Chayambuka, M. Jiang, G. Mulder, D. L. Danilov and P. H. L. Notten, *Electrochim Acta*, 2022, **404**, 139726.
- 89 K. Chayambuka, G. Mulder, D. L. Danilov and P. H. L. Notten, *Electrochim Acta*, 2022, **404**, 139764.
- 90 R. Guo, L. Lu, M. Ouyang and X. Feng, *Sci Rep*, 2016, **6**, 1–9.
- 91 D. M. Poojary and A. Clearfield, *Acc Chem Res*, 1997, **30**, 414–422.
- 92 J. I. Langford, D. Louër and P. Scardi, *J Appl Crystallogr*, 2000, **33**, 964–974.
- 93 M. F. Hasan, C.-F. Chen, C. E. Shaffer and P. P. Mukherjee, *J Electrochem Soc*, 2015, **162**, A1382–A1395.
- 94 D. Y. W. Yu, C. Fietzek, W. Weydanz, K. Donoue, T. Inoue, H. Kurokawa and S. Fujitani, *J Electrochem Soc*, 2007, 253–257.
- 95 V. S. Mironov, J. K. Kim, M. Park, S. Lim and W. K. Cho, *Polym Test*, 2007, **26**, 547–555.



- 96 N. Meddings, M. Heinrich, F. Overney, J.-S. Lee, V. Ruiz, E. Napolitano, S. Seitz, G. Hinds, R. Raccichini, M. Gaberšček and J. Park, *J Power Sources*, 2020, **480**, 228742.
- 97 T. L. Kirk, A. Lewis-Douglas, D. Howey, C. P. Please and S. Jon Chapman, *J Electrochem Soc*, 2023, **170**, 010514.
- 98 M. Dubarry, V. Svoboda, R. Hwu and B. Y. Liaw, *J Power Sources*, 2007, **174**, 1121–1125.
- 99 M. Dubarry, V. Svoboda, R. Hwu and B. Y. Liaw, *Electrochemical and Solid-State Letters*, 2006, **9**, 454–457.
- 100 M. Dubarry, V. Svoboda, R. Hwu and B. Y. Liaw, *J Power Sources*, 2007, **165**, 566–572.
- 101 M. Rashid, T. S. Pathan, A. McGordon, E. Kendrick and W. D. Widanage, *J Power Sources*, 2019, **440**, 227153.
- 102 A. J. Bard and L. R. Faulkner, *Electrochemical Methods: Fundamentals and Applications*, Wiley, New York, 2nd ed., 2001.
- 103 A. Loges, S. Herberger, P. Seegert and T. Wetzel, *J Power Sources*, 2016, **336**, 341–350.
- 104 H. Maleki, *J Electrochem Soc*, 1999, **146**, 947.
- 105 J. Hartmann, O. Nilsson and J. Fricke, *High Temperatures. High Pressures (Print)*, 1993, **25**, 403–410.
- 106 S. S. Madani, E. Schaltz and S. K. Kær, *Batteries*, 2018, **4**, 1–16.
- 107 S. Basu, R. S. Patil, S. Ramachandran, K. S. Hariharan, S. M. Kolake, T. Song, D. Oh, T. Yeo and S. Doo, *J Power Sources*, 2015, **283**, 132–150.
- 108 M. Maures, Y. Zhang, C. Martin, J. Delétage, J. Vinassa and O. Briat, *Microelectronics Reliability*, 2019, **100–101**, 113364.
- 109 V. Sulzer, S. G. Marquis, R. Timms, M. Robinson and S. J. Chapman, *J Open Res Softw*, 2021, **9**, 14.
- 110 Y. Merla, B. Wu, V. Yufit, R. F. Martinez-Botas and G. J. Offer, *J Power Sources*, 2018, **384**, 66–79.
- 111 J. Schmalstieg and D. U. Sauer, *J Electrochem Soc*, 2018, **165**, A3811–A3819.
- 112 M. Ecker, S. Käbitz, I. Laresgoiti and D. U. Sauer, *J Electrochem Soc*, 2015, **162**, A1849–A1857.
- 113 D. C. Weisenberger, K. Harrison, T. Bernthaler, G. Schneider and V. Knoblauch, *Practical Metallography*, 2020, **57**, 176–198.
- 114 B. Y. Liaw, G. Nagasubramanian, R. G. Jungst and D. H. Doughty, in *Solid State Ionics*, 2004, vol. 175, pp. 835–839.

- 115 G.-H. Kim, K. Smith, K.-J. Lee, S. Santhanagopalan and A. Pesaran, *J Electrochem Soc*, 2011, **158**, A955.
- 116 M. Ebner and V. Wood, *J Electrochem Soc*, 2014, **162**, A3064–A3070.
- 117 P. R. Shearing, L. E. Howard, P. S. Jørgensen, N. P. Brandon and S. J. Harris, *Electrochem commun*, 2010, **12**, 374–377.
- 118 A. U. Schmid, M. Kurka and K. P. Birke, *J Energy Storage*, 2019, **24**, 100732.
- 119 M. Ecker, T. K. D. Tran, P. Dechent, S. Kabitz, A. Warnecke and D. U. Sauer, *J Electrochem Soc*, 2015, **162**, A1836–A1848.
- 120 S. F. Gorman, T. S. Pathan and E. Kendrick, *Phil. Trans. R. Soc. A*, 2019, **377**, 1–19.
- 121 A. Bottino, G. Capannelli, S. Munari and A. Turturro, *J Polym Sci B Polym Phys*, 1988, **26**, 785–794.
- 122 R. Zhu, J. Feng and Z. Guo, *J Electrochem Soc*, 2019, **166**, A1107–A1113.
- 123 A. Schilling, S. Wiemers-Meyer, V. Winkler, S. Nowak, B. Hoppe, H. H. Heimes, K. Dröder and M. Winter, *Energy Technology*, , DOI:10.1002/ente.201900078.
- 124 L. Yu, Y. Jin and Y. S. Lin, *RSC Adv*, 2016, **6**, 40002–40009.
- 125 M. Baunach, S. Jaiser, S. Schmelzle, H. Nirschl, P. Scharfer and W. Schabel, *Drying Technology*, 2016, **34**, 462–473.
- 126 S. Morelly, M. Tang and N. Alvarez, *Polymers (Basel)*, 2017, **9**, 461.
- 127 M. Ender, J. Joos, T. Carraro and E. Ivers-Tiffée, *Electrochem commun*, 2011, **13**, 166–168.
- 128 S. R. Daemi, C. Tan, T. Volkenandt, S. J. Cooper, A. Palacios-Padros, J. Cookson, D. J. L. Brett and P. R. Shearing, *ACS Appl Energy Mater*, 2018, **1**, 3702–3710.
- 129 L. Li, X. Li, Z. Wang, H. Guo, P. Yue, W. Chen and L. Wu, *J Alloys Compd*, 2010, **507**, 172–177.
- 130 T. Carraro, A. Weber, B. Rüger, M. Ender, J. Joos, E. Ivers-Tiffée, T. Carraro, M. Ender, B. Rüger, A. Weber and E. Ivers-Tiffée, *ECS Trans*, 2011, **35**, 2357–2368.
- 131 M. Ebner, D. W. Chung, R. E. García and V. Wood, *Adv Energy Mater*, 2014, **4**, 1–6.
- 132 B. Suthar, J. Landesfeind, A. Eldiven and H. A. Gasteiger, *J Electrochem Soc*, 2018, **165**, A2008–A2018.
- 133 T. DuBeshter, P. K. Sinha, A. Sakars, G. W. Fly and J. Jorne, *J Electrochem Soc*, 2014, **161**, A599–A605.
- 134 M. S. Hossain, L. I. Stephens, M. Hatami, M. Ghavidel, D. Chhin, J. I. G. Dawkins, L. Savignac, J. Mauzeroll and S. B. Schougaard, *ACS Appl Energy Mater*, 2020, **3**, 440–446.

- 135 T. Hutzenlaub, S. Thiele, R. Zengerle and C. Ziegler, *Electrochemical and Solid-State Letters*, 2011, **15**, A33.
- 136 J. Landesfeind, M. Ebner, A. Eldiven, V. Wood and H. A. Gasteiger, *J Electrochem Soc*, 2018, **165**, A469–A476.
- 137 D. Kehrwald, P. R. Shearing, N. P. Brandon, P. K. Sinha and S. J. Harris, *J Electrochem Soc*, 2011, **158**, A1393.
- 138 T.-T. Nguyen, A. Demortière, B. Fleutot, B. Delobel, C. Delacourt and S. J. Cooper, *NPJ Comput Mater*, 2020, **6**, 123.
- 139 W. Li, E. M. Erickson and A. Manthiram, *Nat Energy*, 2020, **5**, 26–34.
- 140 D. Ren, Y. Yang, L. Shen, R. Zeng and H. D. Abruña, *J Power Sources*, 2020, **447**, 6–10.
- 141 M. A. Roscher, O. Bohlen and J. Vetter, *International Journal of Electrochemistry*, 2011, **2011**, 1–6.
- 142 W. M. Dose, M. J. Piernas-Muñoz, V. A. Maroni, S. E. Trask, I. Bloom and C. S. Johnson, *Chemical Communications*, 2018, **54**, 3586–3589.
- 143 A. Marongiu, F. G. W. Nußbaum, W. Waag, M. Garmendia and D. U. Sauer, *Appl Energy*, 2016, **171**, 629–645.
- 144 H. G. Schweiger, O. Obeidi, O. Komesker, A. Raschke, M. Schiemann, C. Zehner, M. Gehnen, M. Keller and P. Birke, *Sensors*, 2010, **10**, 5604–5625.
- 145 S. Tan, Y. J. Ji, Z. R. Zhang and Y. Yang, *ChemPhysChem*, 2014, **15**, 1956–1969.
- 146 V. J. Ovejas and A. Cuadras, *Sci Rep*, 2019, **9**, 1–9.
- 147 S. Ernst, T. P. Heins, N. Schlüter and U. Schröder, *Front Energy Res*, 2019, **7**, 1–13.
- 148 M. Otero, C. Heim, E. P. M. Leiva, N. Wagner and A. Friedrich, *Sci Rep*, 2018, **8**, 1–10.
- 149 O. Capron, R. Gopalakrishnan, J. Jaguemont, P. Van Den Bossche, N. Omar and J. Van Mierlo, *Materials*, 2018, **11**, 176.
- 150 M. D. Levi and D. Aurbach, *Journal of Physical Chemistry B*, 1997, **101**, 4641–4647.
- 151 M. M. Forouzan, B. A. Mazzeo and D. R. Wheeler, *J Electrochem Soc*, 2018, **165**, A2127–A2144.
- 152 R. Amin and Y.-M. Chiang, *J Electrochem Soc*, 2016, **163**, A1512–A1517.
- 153 K. R. Kim, S. Y. Choi, J. G. Kim, S. Paek and W. I. Goh, *Int J Electrochem Sci*, 2015, **10**, 7660–7670.
- 154 A. Verma, K. Smith, S. Santhanagopalan, D. Abraham, K. P. Yao and P. P. Mukherjee, *J Electrochem Soc*, 2017, **164**, A3380–A3392.

- 155 A. Swiderska-Mocek and A. Lewandowski, *Journal of Solid State Electrochemistry*, 2017, **21**, 1365–1372.
- 156 W. Waag, S. Käbitz and D. U. Sauer, *Appl Energy*, 2013, **102**, 885–897.
- 157 P. C. Tsai, B. Wen, M. Wolfman, M. J. Choe, M. S. Pan, L. Su, K. Thornton, J. Cabana and Y. M. Chiang, *Energy Environ Sci*, 2018, **11**, 860–871.
- 158 A. Nyman, M. Behm and G. Lindbergh, *Electrochim Acta*, 2008, **53**, 6356–6365.
- 159 P. Bai and M. Z. Bazant, *Nat Commun*, 2014, **5**, 1–7.
- 160 M. J. Hunt, F. Brosa Planella, F. Theil and W. D. Widanage, *J Eng Math*, 2020, **122**, 31–57.
- 161 M. J. Lain, J. Brandon and E. Kendrick, *Batteries*, 2019, **5**, 64.
- 162 M. J. Lain and E. Kendrick, *J Power Sources*, 2021, **493**, 229690.
- 163 J. Sturm, A. Rheinfeld, I. Zilberman, F. B. Spingler, S. Kosch, F. Frie and A. Jossen, *J Power Sources*, 2019, **412**, 204–223.
- 164 C. Bhat and J. Channegowda, *Energy Storage*, 2021, 1–9.
- 165 H. Lundgren, P. Svens, H. Ekström, C. Tengstedt, J. Lindström, M. Behm and G. Lindbergh, *J Electrochem Soc*, 2016, **163**, A309–A317.
- 166 N. A. Zacharias, D. R. Nevers, C. Skelton, K. Knackstedt, D. E. Stephenson and D. R. Wheeler, *J Electrochem Soc*, 2013, **160**, A306–A311.
- 167 J. A. E. Andersson, J. Gillis, G. Horn, J. B. Rawlings and M. Diehl, *Math Program Comput*, 2019, **11**, 1–36.
- 168 T. G. Tranter, R. Timms, T. M. M. Heenan, S. G. Marquis, V. Sulzer, A. Jnawali, M. D. R. Kok, C. P. Please, S. J. Chapman, P. R. Shearing and D. J. L. Brett, *J Electrochem Soc*, 2020, **167**, 110538.
- 169 T. R. B. G.F. Hewitt, G.L. Shires, *Process Heat Transfer*, CRC Press, London, 1993.
- 170 P. Bohn, G. Liebig, L. Komsiyiska and G. Wittstock, *J Power Sources*, 2016, **313**, 30–36.
- 171 G. Liebig, U. Kirstein, S. Geißendörfer, F. Schuldt and C. Agert, *Batteries*, 2020, **6**, 3.
- 172 R. Kantharaj and A. M. Marconnet, *Nanoscale and Microscale Thermophysical Engineering*, 2019, **23**, 128–156.
- 173 C. Chen, A. Verma and P. P. Mukherjee, *J Electrochem Soc*, 2017, **164**, E3146–E3158.
- 174 P. Bohn, G. Liebig, L. Komsiyiska and G. Wittstock, *J Power Sources*, 2016, **313**, 30–36.

- 175 P. Gotcu, W. Pfleging, P. Smyrek and H. J. Seifert, *Physical Chemistry Chemical Physics*, 2017, **19**, 11920–11930.
- 176 G. R. Stewart, *Review of Scientific Instruments*, 1983, **54**, 1–11.
- 177 T. R. B. G.F. Hewitt, G.L. Shires, *Process Heat Transfer*, CRC Press, London, 1993.
- 178 S. Bak, E. Hu, Y. Zhou, X. Yu, S. D. Senanayake, S. Cho, K. Kim, K. Y. Chung, X. Yang and K. Nam, *ACS Appl Mater Interfaces*, 2014, **6**, 22594–22601.
- 179 L. Wei, Z. Lu, F. Cao, L. Zhang, X. Yang, X. Yu and L. Jin, *Int J Energy Res*, 2020, **44**, 9466–9478.
- 180 S. C. Chen, C. C. Wan and Y. Y. Wang, *J Power Sources*, 2005, **140**, 111–124.
- 181 C. Chen, A. Verma and P. P. Mukherjee, *J Electrochem Soc*, 2017, **164**, E3146–E3158.
- 182 W. Mei, H. Chen, J. Sun and Q. Wang, *Sustain Energy Fuels*, 2019, **3**, 148–165.
- 183 L. Wei, Z. Lu, F. Cao, L. Zhang, X. Yang, X. Yu and L. Jin, *Int J Energy Res*, 2020, **44**, 9466–9478.
- 184 H.-K. Kim, J. H. Choi and K.-J. Lee, *J Electrochem Soc*, 2019, **166**, A1769–A1778.
- 185 G.-H. Kim, K. Smith, K.-J. Lee, S. Santhanagopalan and A. Pesaran, *J Electrochem Soc*, 2011, **158**, A955.
- 186 S. C. Chen, C. C. Wan and Y. Y. Wang, *J Power Sources*, 2005, **140**, 111–124.
- 187 K. Takano, Y. Saito, K. Kanari, K. Nozaki, K. Kato, A. Negishi and T. Kato, *J Appl Electrochem*, 2002, **32**, 251–258.
- 188 F. Reuter, A. Baasner, J. Pampel, M. Piwko, S. Dörfler, H. Althues and S. Kaskel, *J Electrochem Soc*, 2019, **166**, A3265–A3271.
- 189 W. Weppner and R. A. Huggins, *J Electrochem Soc*, 1977, **124**, 1569–1578.
- 190 L. Stolz, G. Homann, M. Winter and J. Kasnatscheew, *Materials Today*, 2021, **44**, 9–14.
- 191 D. Sauerteig, N. Hanselmann, A. Arzberger, H. Reinshagen, S. Ivanov and A. Bund, *J Power Sources*, 2018, **378**, 235–247.
- 192 K. Pan, F. Zou, M. Canova, Y. Zhu and J. H. Kim, *J Power Sources*, 2019, **413**, 20–28.
- 193 M. A. Cabañero, N. Boaretto, M. Röder, J. Müller, J. Kallo and A. Latz, *J Electrochem Soc*, 2018, **165**, A847–A855.
- 194 R. Jung, M. Metzger, F. Maglia, C. Stinner and H. A. Gasteiger, *J Electrochem Soc*, 2017, **164**, A1361–A1377.
- 195 M. Winter, J. O. Besenhard, M. E. Spahr and P. Novák, *Advanced Materials*, 1998, **10**, 725–763.

- 196 M. A. Cabañero, N. Boaretto, M. Röder, J. Müller, J. Kallo and A. Latz, *J Electrochem Soc*, 2018, **165**, A847–A855.
- 197 W. Lee, S. Muhammad, T. Kim, H. Kim, E. Lee, M. Jeong, S. Son, J. H. Ryou and W. S. Yoon, *Adv Energy Mater*, 2018, **8**, 1–12.
- 198 A. Latz, T. Danner, B. Horstmann and T. Jahnke, *Chem Ing Tech*, 2019, **91**, 758–768.
- 199 J. Lück and A. Latz, *Physical Chemistry Chemical Physics*, 2018, **20**, 27804–27821.
- 200 N. Takami, *J Electrochem Soc*, 1995, **142**, 371.
- 201 T. L. Kulova, A. M. Skundin, E. A. Nizhnikovskii and A. V. Fesenko, *Russian Journal of Electrochemistry*, 2006, **42**, 259–262.
- 202 I. Umegaki, S. Kawauchi, H. Sawada, H. Nozaki, Y. Higuchi, K. Miwa, Y. Kondo, M. Månsson, M. Telling, F. C. Coomer, S. P. Cottrell, T. Sasaki, T. Kobayashi and J. Sugiyama, *Phys. Chem. Chem. Phys.*, 2017, **19**, 19058–19066.
- 203 K. Märker, P. J. Reeves, C. Xu, K. J. Griffith and C. P. Grey, *Chemistry of Materials*, 2019, **31**, 2545–2554.
- 204 N. Jin, D. L. Danilov, P. M. J. Van den Hof and M. C. F. Donkers, *Int J Energy Res*, 2018, **42**, 2417–2430.
- 205 T. R. Jow, M. B. Marx and J. L. Allen, *J Electrochem Soc*, 2012, **159**, A604–A612.
- 206 M. C. Smart and B. V. Ratnakumar, *J Electrochem Soc*, 2011, **158**, A379.
- 207 A. S. Keefe, S. Buteau, I. G. Hill and J. R. Dahn, *J Electrochem Soc*, 2019, **166**, A3272–A3279.
- 208 E. Antolini, *Solid State Ion*, 2004, **170**, 159–171.
- 209 R. Amin and Y.-M. Chiang, *J Electrochem Soc*, 2016, **163**, A1512–A1517.
- 210 S. Chacko and Y. M. Chung, *J Power Sources*, 2012, **213**, 296–303.
- 211 X. Zhang, *Electrochim Acta*, 2011, **56**, 1246–1255.
- 212 J. Hong, H. Maleki, S. Al Hallaj, L. Redey and J. R. Selman, *J Electrochem Soc*, 1998, **145**, 1489–1501.
- 213 V. V. Viswanathan, D. Choi, D. Wang, W. Xu, S. Towne, R. E. Williford, J. G. Zhang, J. Liu and Z. Yang, *J Power Sources*, 2010, **195**, 3720–3729.
- 214 Y. Reynier, R. Yazami and B. Fultz, *J Power Sources*, 2003, **119–121**, 850–855.
- 215 J. Sturm, A. Rheinfeld, I. Zilberman, F. B. Spingler, S. Kosch, F. Frie and A. Jossen, *J Power Sources*, 2019, **412**, 204–223.
- 216 V. V. Viswanathan, D. Choi, D. Wang, W. Xu, S. Towne, R. E. Williford, J. G. Zhang, J. Liu and Z. Yang, *J Power Sources*, 2010, **195**, 3720–3729.

- 217 L. Gu, J. Y. Gui, J. V. Wang, G. Zhu and J. Kang, *Energy*, 2019, **178**, 21–32.
- 218 J. Landesfeind, A. Ehrl, M. Graf, W. A. Wall and H. A. Gasteiger, *J Electrochem Soc*, 2016, **163**, A1254–A1264.
- 219 J. Landesfeind and H. A. Gasteiger, *J Electrochem Soc*, 2019, **166**, A3079–A3097.
- 220 F. Brosa Planella, M. Sheikh and W. D. Widanage, *Electrochim Acta*, 2021, **388**, 138524.
- 221 T. Kirk, J. Evans, C. Please and J. Chapman, *ArXiv:2006.12208*.
- 222 V. Sulzer, S. G. Marquis, R. Timms, M. Robinson and S. J. Chapman, *J Open Res Softw*, 2021, **9**, 14.
- 223 H. Au, H. Alptekin, A. C. S. Jensen, E. Olsson, C. A. O’Keefe, T. Smith, M. Crespo-Ribadeneyra, T. F. Headen, C. P. Grey, Q. Cai, A. J. Drew and M. M. Titirici, *Energy Environ Sci*, 2020, **13**, 3469–3479.
- 224 S. Hein, T. Danner and A. Latz, *ACS Appl Energy Mater*, 2020, **3**, 8519–8531.
- 225 J. M. Bray, C. L. Doswell, G. E. Pavlovskaya, L. Chen, B. Kishore, H. Au, H. Alptekin, E. Kendrick, M.-M. Titirici, T. Meersmann and M. M. Britton, *Nat Commun*, 2020, **11**, 2083.
- 226 S. Roberts, L. Chen, B. Kishore, C. E. J. Dancer, M. J. H. Simmons and E. Kendrick, *J Colloid Interface Sci*, 2022, **627**, 427–437.
- 227 F. L. E. Usseglio-Viretta, A. Colclasure, A. N. Mistry, K. P. Y. Claver, F. Pouraghajan, D. P. Finegan, T. M. M. Heenan, D. Abraham, P. P. Mukherjee, D. Wheeler, P. Shearing, S. J. Cooper and K. Smith, *J Electrochem Soc*, 2018, **165**, A3403–A3426.
- 228 D. Ledwoch, J. B. Robinson, D. Gastol, K. Smith, P. R. Shearing, D. J. L. Brett and E. Kendrick, *Batter Supercaps*, 2021, **4**, 163–172.
- 229 W. Weppner and R. A. Huggins, *Annual Review of Materials Science*, 1978, **8**, 269–311.
- 230 B. Kishore and M. Nookala, *Journal of Electroanalytical Chemistry*, 2017, **799**, 134–141.
- 231 M. A. Samieian, A. Hales and Y. Patel, *Batteries*, 2022, **8**, 125.
- 232 G. White, A. Hales, Y. Patel and G. Offer, *Appl Therm Eng*, 2022, **212**, 118573.
- 233 N. Kirkaldy, M. A. Samieian, G. J. Offer, M. Marinescu and Y. Patel, *ACS Appl Energy Mater*, 2022, **5**, 13367–13376.

## Supporting Information

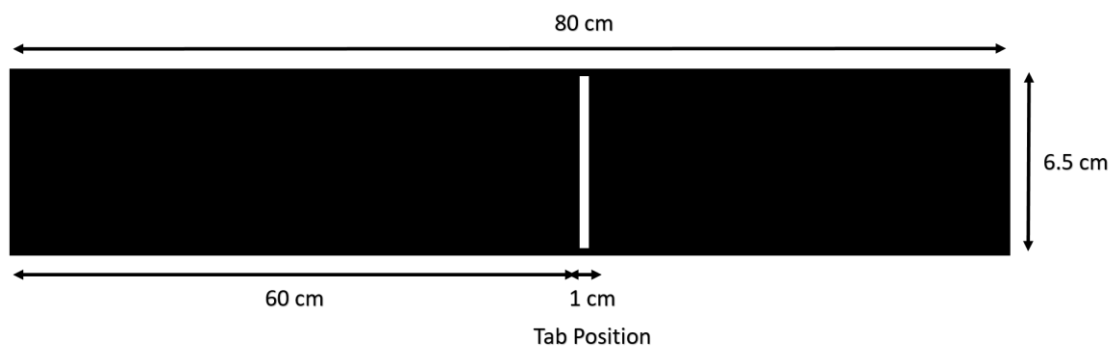


Figure S1. Illustration to show positive electrode coating on the aluminium current collector. The coating was symmetrical.

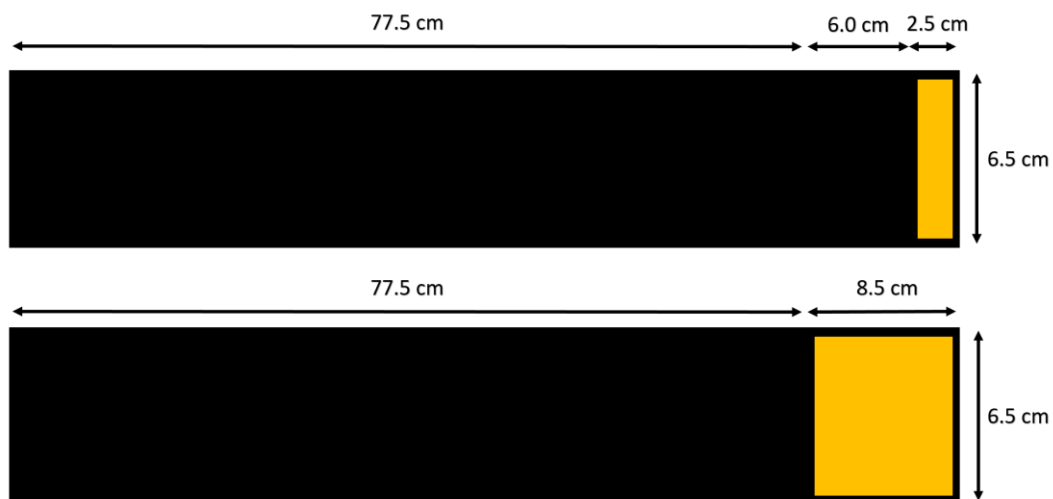


Figure S2. Illustration to show negative electrode coating on the copper current collector.



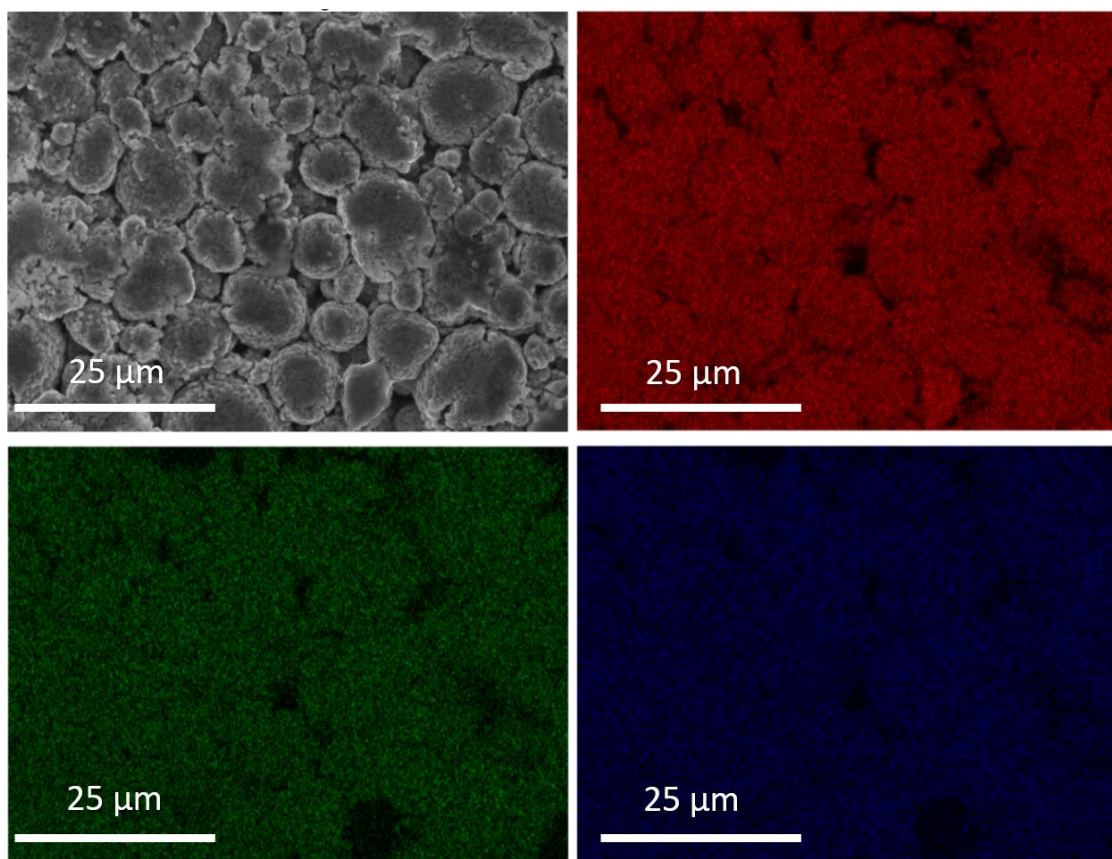


Figure S3. Top-view EDS images of the positive electrode illustrating the nickel (red), cobalt (green), and manganese (blue) contents.

### Cell data sheet

Table S1.Details of the LG M50 battery.<sup>1t</sup>

Parameter	Value
Manufacturer	LG Chem
Geometry	Cylindrical 21700
Dimensions	Ø 21 mm x 70 mm
Model	M50
Chemistry*	LiNi <sub>0.8</sub> Co <sub>0.1</sub> Mn <sub>0.1</sub> O <sub>2</sub> & SiO <sub>y</sub> -graphite
Nominal voltage (V)	3.63
Nominal capacity (Ah)	5
Nominal energy (Wh)	18.2
Maximum charge voltage (V)	4.2
Cut off voltage (V)	2.5
Max discharge current 5-45 °C (A)	7.23 (1.5C)
Operating temperature during charge (°C)	0 ~ 50
Operating temperature during discharge (°C)	-30 ~ 60
Storage temperature 1 year (°C)	-20 ~ 20
Weight (g)	68.3

# Physical properties of cell

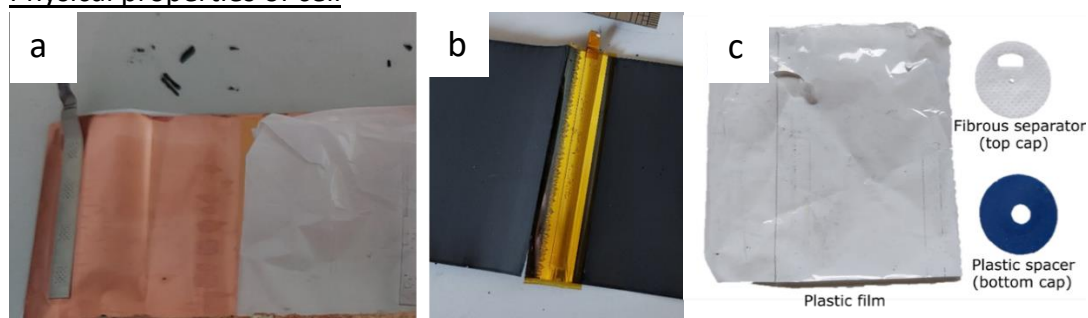


Figure S4. (a) The negative electrode tab, (b) positive electrode tab, and (c) plastic film covering, top cap and bottom spacer components within the cell.

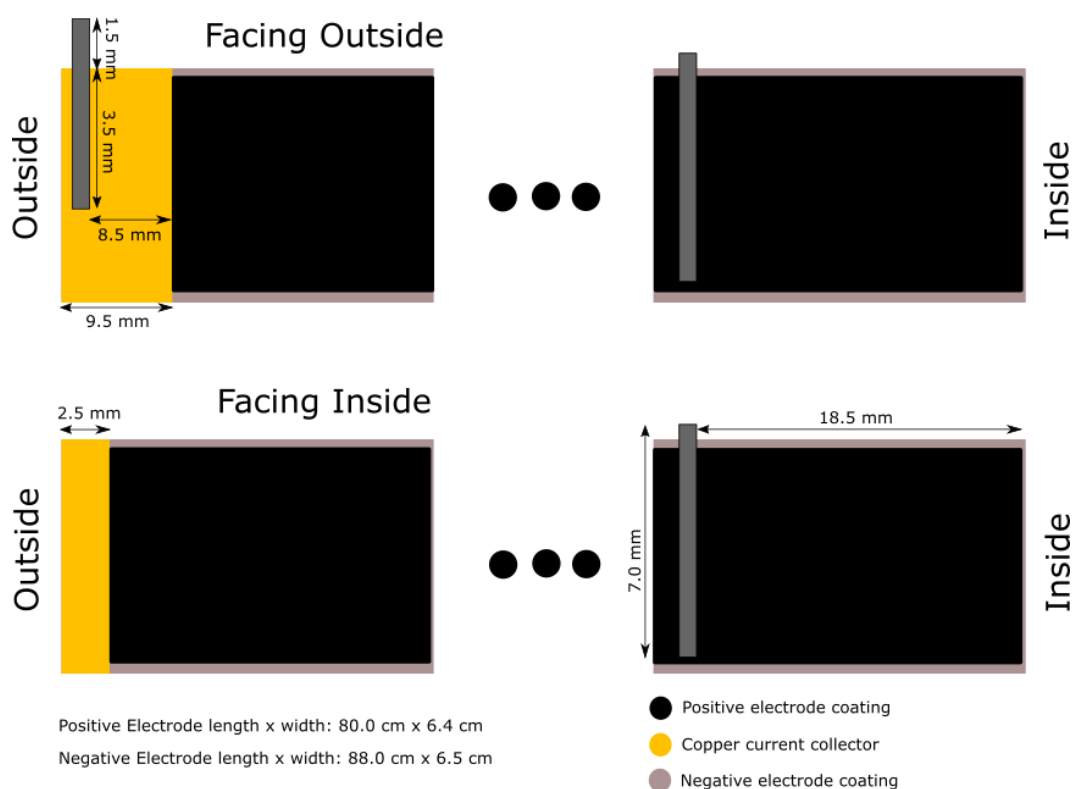


Figure S5. Sketches of the electrode winds.

## Thermal properties

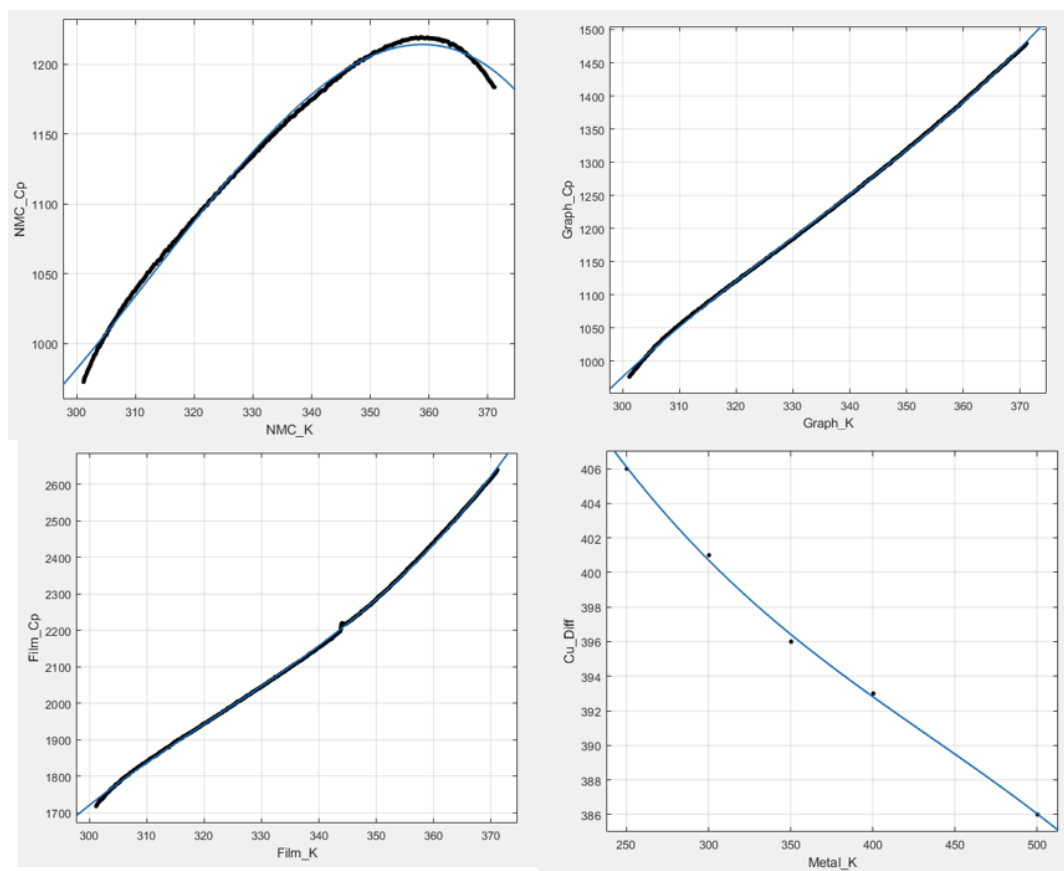


Figure S6. Third order polynomial fits of the specific heat capacity data (as a function of temperature in Kelvin) for NMC powder (top left), graphite powder (top right), the separator (bottom left), and copper (bottom right).

## Diffusion Properties

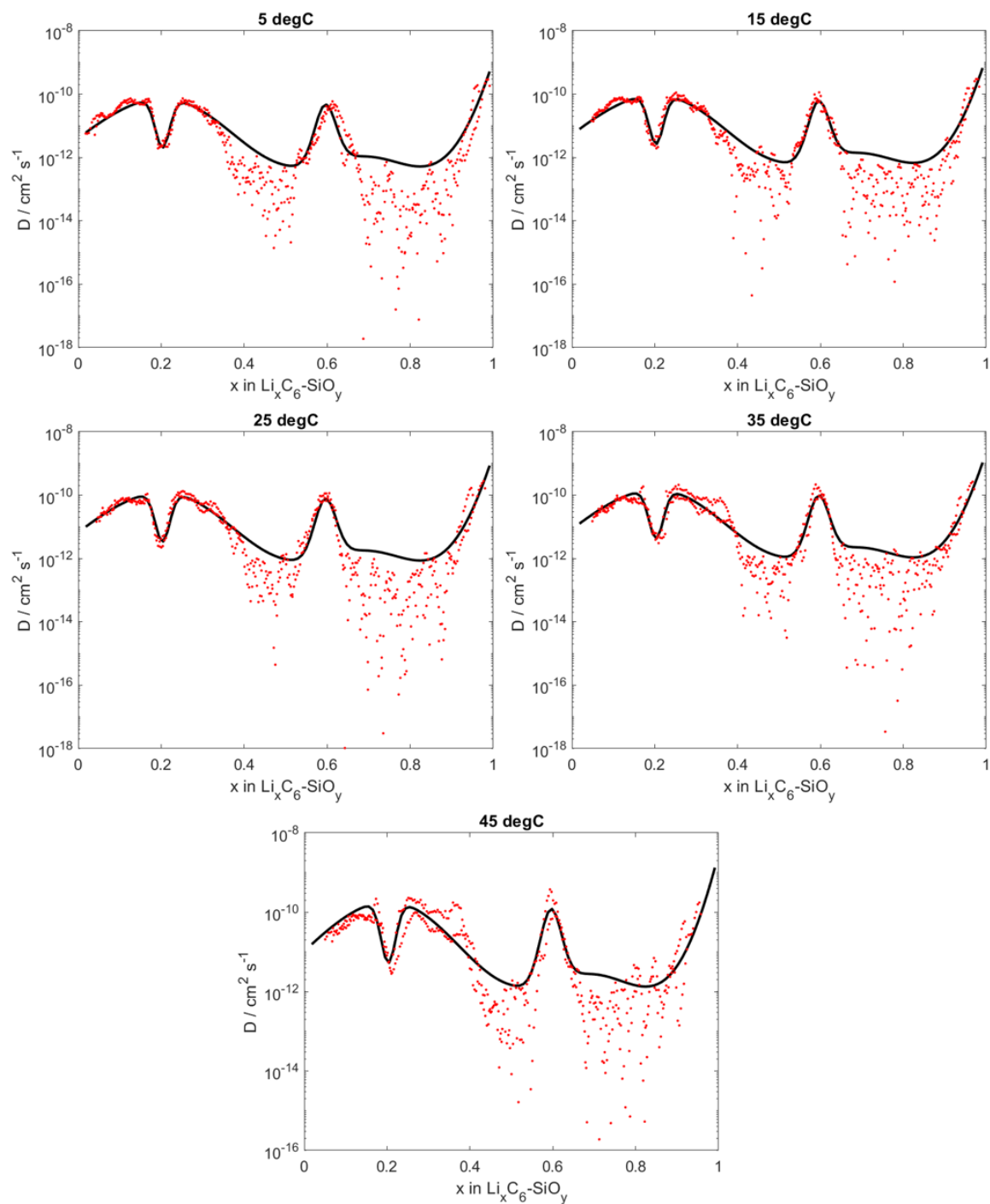


Figure S7. Average fit for the two diffusivity profiles of the negative electrode at 5 °C, 15 °C, 25 °C, 35 °C, and 45 °C.

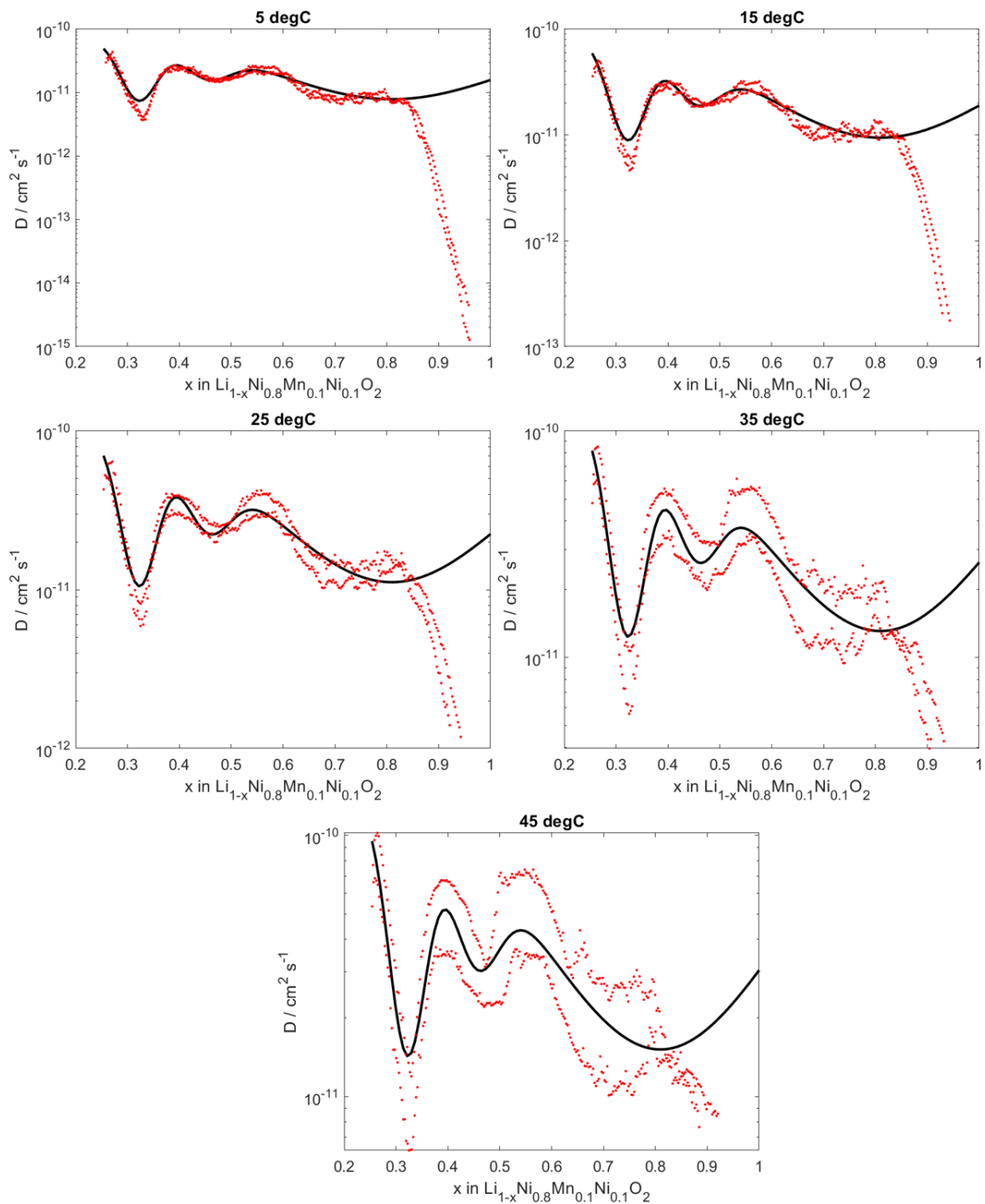


Figure S8. Average fit for the two diffusivity profiles of the positive electrode at 5 °C, 15 °C, 25 °C, 35 °C, and 45 °C.

### Exchange current density, open circuit voltage and diffusivity fitting

Table S2. Fitting parameters for the function describing solid-phase electrode diffusivity and 95% confidence intervals. A “-” means that the term including that parameter has not been included.

Fitting Parameter	Positive Electrode	Negative Electrode
$a_0$	-	11.17 (8.645, 13.69)
$a_1$	-0.9231 (-0.9958, -0.8504)	-1.553 (-1.633, -1.473)
$a_2$	-0.4066 (-0.4475, -0.3656)	-6.136 (-7.511, -4.76)
$a_3$	-0.993 (-1.124, -0.8623)	-9.725 (-11.53, -7.923)
$a_4$	-	1.85 (1.725, 1.976)
$b_0$	-13.96 (-14.09, -13.83)	-15.11 (-15.2, -15.01)
$b_1$	0.3216 (0.3199, 0.3233)	0.2031 (0.2021, 0.2041)
$b_2$	0.4532 (0.4506, 0.4559)	0.5375 (0.5083, 0.5668)
$b_3$	0.8098 (0.798, 0.8216)	0.9144 (0.8901, 0.9387)
$b_4$	-	0.5953 (0.5941, 0.5966)
$c_1$	0.002534 (0.002113, 0.002956)	0.0006091 (0.00053, 0.0006882)
$c_2$	0.003926 (0.003287, 0.004565)	0.06438 (0.04902, 0.07973)
$c_3$	0.09924 (0.07619, 0.1223)	0.0578 (0.04712, 0.06848)
$c_4$	-	0.001356 (0.001144, 0.001567)
$E_a$	12047 (11415, 12679)	17393 (15647, 19139)

Table S3. Fitting parameters for the function describing exchange current density.

Fitting Parameter	Positive Electrode	Negative Electrode
$k_0$	0.0005028 (0.0004312, 0.0005744)	0.0002668 (0.0002225, 0.0003111)
$\alpha$	0.43 (0.3136, 0.5464)	0.792 (0.7252, 0.8589)
$Ea$	$2.401 \cdot 10^4$ ( $1.676 \cdot 10^4$ , $3.126 \cdot 10^4$ )	$4e \cdot 10^4$ ( $3.263 \cdot 10^4$ , $4.737 \cdot 10^4$ )

Table S4. Fitting parameters for the function describing entropic term and 95% confidence intervals. A “-” means that the term including that parameter has not been included.

Fitting Parameter	Positive Electrode	Negative Electrode
$a_0$	-	-0.111 (-0.1535, -0.06846)
$a_1$	0.04006 (-2.578e+07, 2.578e+07)	0.3562 (0.3231, 0.3892)
$a_2$	-0.06656 (-0.08762, -0.04551)	-
$b_0$	-	0.02901 (-0.003796, 0.06182)
$b_1$	0.2828 (-2.466e+07, 2.466e+07)	0.08308 (0.07159, 0.09456)
$b_2$	0.8032 (0.7687, 0.8376)	-
$c_1$	0.0009855 (-4.924e+05, 4.924e+05)	0.004621 (0.001368, 0.007874)
$c_2$	0.02179 (0.003508, 0.04007)	-

### Electrode Open Circuit Voltages

The OCV curve for the positive electrode is:

$$\begin{aligned}
 U_+(x) = & -0.8090x + 4.4875 - 0.0428 \tanh(18.5138(x - 0.5542)) \\
 & - 17.7326 \tanh(15.7890(x - 0.3117)) \\
 & + 17.5842 \tanh(15.9308(x - 0.3120))
 \end{aligned}
 \quad [S1]$$

The OCV curve for the negative electrode is:

$$U_{-}(x) = 1.9793e^{-39.3631x} + 0.2482 - 0.0909 \tanh(29.8538(x - 0.1234)) - 0.04478 \tanh(14.9159(x - 0.2769)) - 0.0205 \tanh(30.4444(x - 0.6103)). \quad [S2]$$

### Nyquist diagrams and fitting exchange current

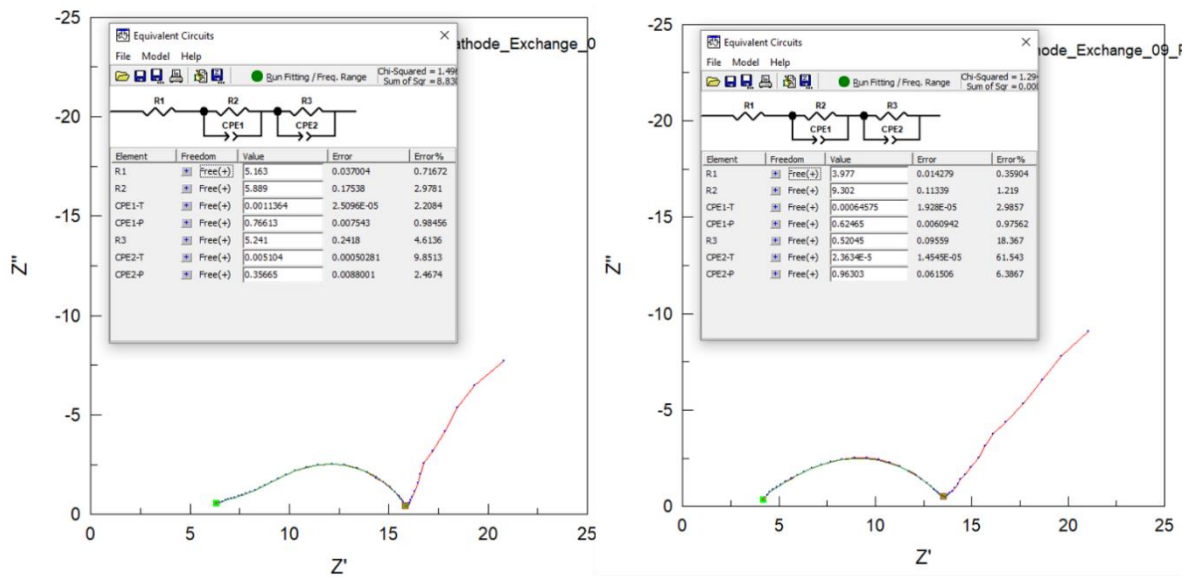


Figure S9. Example equivalent circuit fitting result for the positive electrode (left) and negative electrode (right), with corresponding resistance and capacitance values, with respective errors below.

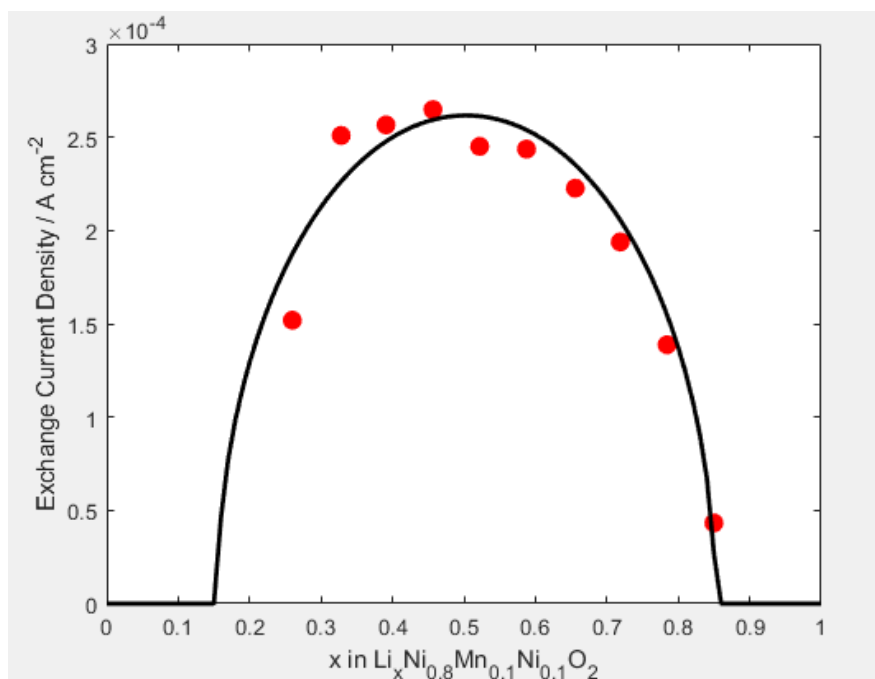


Figure S10. Alternative fit for the exchange current density results based on an empirical fit using a semi-ellipse with the exchange current density fitted to be 0 at lithium, stoichiometries of 0 and 0.95.